

THE UNIVERSITY
of EDINBURGH

This thesis has been submitted in fulfilment of the requirements for a postgraduate degree (e.g. PhD, MPhil, DClinPsychol) at the University of Edinburgh. Please note the following terms and conditions of use:

This work is protected by copyright and other intellectual property rights, which are retained by the thesis author, unless otherwise stated.
A copy can be downloaded for personal non-commercial research or study, without prior permission or charge.
This thesis cannot be reproduced or quoted extensively from without first obtaining permission in writing from the author.
The content must not be changed in any way or sold commercially in any format or medium without the formal permission of the author.
When referring to this work, full bibliographic details including the author, title, awarding institution and date of the thesis must be given.

Mass imbalance and climate sensitivity of Arctic glaciers and ice caps

Paul Tepes



Submitted for the degree of Doctor of Philosophy

The University of Edinburgh

2020

"'Each animal knows way more than you do,' a Koyukon Indian elder was fond of telling me." ∼ Richard Nelson, 1993

Abstract

Glaciers and ice caps are prominent features in the landscapes surrounding the Greenland Ice Sheet and in the archipelagos of the Arctic seas. Their dynamic response in mass and flow to climate variability makes them a visible and important expression of the changes that are affecting the Earth's climate system. Arctic glaciers and ice caps are losing mass rapidly, a trend sustained over recent decades and that is expected to continue into the 21^{st} century driven by climatic change and exacerbated by the amplification of polar warming relative to the planetary mean. Mass imbalance of Arctic land ice is a source of major concern given its impact on global sea level rise, ocean circulation, regional hydrology, and on the local ecosystems and communities, which are also impacted by these changes, with increased ecological, socio-economic and geopolitical pressures afflicting the region. To effectively mitigate and adapt to these environmental changes, the large-scale, continuous monitoring of the Arctic cryosphere has become essential, and satellite geodesy is a critical tool for estimating glacier and ice cap mass balance.

In this thesis, seven years of CryoSat-2 high-resolution swath interferometric altimetry were utilised to investigate changes in the volume of Arctic glaciers and ice caps outside of Greenland between 2010 and 2017. From these data, a pan-Arctic assessment of mass imbalance was produced, and losses partitioned into signals associated with atmospheric processes and glacier dynamics. The sampled satellite observations provide a detailed picture of the response of Arctic glaciers and ice caps to climate forcing, eliciting contrasting patterns of change

that are driven by a combination of oceanic and atmospheric forcing and by internal instabilities (glacier surges). Results show that between 2010 and 2017, Arctic glaciers and ice caps lost 609±7 gigatonnes of ice, contributing 0.240±0.007 millimetres per year to global sea level rise. While surface ablation is responsible for 87 % of losses across the Arctic, dynamic imbalance is increasing in the Barents and Kara Sea region where it now accounts for almost half of the total ice loss. This dynamic imbalance is associated with a northward shift of Atlantic climate and is sustained by a range of climate-dynamic feedbacks and processes that have been amplified in areas adjacent to the archipelagos of the Eurasian Shelf.

The thesis builds on these initial pan-Arctic findings to further investigate, in Chapter 5, the processes that shape the current response to forcing of the glaciers and ice caps in the Eurasian High Arctic, with a particular focus on glacier fluctuations in the Russian archipelagos of Novaya Zemlya and Severnaya Zemlya. Time series of surface elevation change between 2010 and 2018 in conjunction with concurrent climate anomaly trends provide insights into the contrasting cryospheric changes affecting these two regions, as well as their association with contemporary atmospheric and oceanic forcing. While both frontal ablation of tidewater glaciers and surface melt are found to jointly contribute to volume changes in Novaya Zemlya, ice dynamics are entirely responsible for the recent net ice loss from Severnaya Zemlya. A quasi-linear relationship between coupled ocean-atmosphere forcing and volumetric changes in Novaya Zemlya is found to be appropriate in explaining the overall regional trends in ice loss at decadal scale, in agreement with previous findings from tidewater glaciers in east Greenland. In Severnaya Zemlya, the role of ocean warming is found to be the key factor in driving dynamic ice loss, owing to the intrusion of warmer Atlantic Water circulating along the Eurasian continental margin.

Together these results suggest that meteorological processes will continue to dominate glacier loss throughout the Arctic, while warming of the Arctic Ocean will increasingly affect the dynamic stability of tidewater glaciers in the Barents and Kara Sea regions, with unpredictable and possibly abrupt shifts in mass bal-

ance. In this region, as well as globally, ice dynamics represent the largest source of uncertainty in climate models predicting how land ice will respond to future climatic fluctuations. The findings from this thesis support the principle that linear relationships between environmental forcings and glacier change may be sufficiently accurate to parametrise ice loss in regions where synchronous, coupled ocean-atmospheric forcing prevails. The results therefore provide important support to current efforts aimed at estimating future ice loss, freshwater budgets, and sea level contributions from Arctic glaciers and ice caps in a changing climate.

Lay Summary

Glaciers and ice caps are prominent features in the coastal landscapes of Greenland and in the archipelagos of the Arctic seas. Their response to 21^{st} century global warming makes them a visible and important expression of the changes that are affecting the Earth's climate system. Arctic glaciers and ice caps are losing mass rapidly, a trend sustained over recent decades and that is expected to continue in the foreseeable future driven by climatic change and exacerbated by stronger warming in the northern polar regions compared to the planetary mean. Sustained mass loss from Arctic land ice is a source of major concern given its impact on global sea level rise, ocean circulation, regional hydrology, and on the local ecosystems and communities, which are also impacted by these changes, with increased ecological, socio-economic and geopolitical pressures afflicting the region. To effectively mitigate and adapt to these environmental changes, the large-scale, continuous monitoring of Arctic glacier systems has become essential, and satellite geodesy currently provides new and innovative ways for estimating glacier and ice cap mass balance.

In this thesis, seven years of CryoSat-2 high-resolution measurements were utilised to investigate changes in the volume and mass of Arctic glaciers and ice caps outside of Greenland between 2010 and 2017. From these data, an Arctic-wide assessment of annual mean mass loss was produced, together with a partitioning between losses that are associated with surface melt, and those caused by enhanced ice flow into the ocean. The sampled satellite observations provide a detailed picture of the response of Arctic glaciers and ice caps to environmental

forcing, eliciting contrasting patterns of change driven by both meteorology and oceanic processes. Results show that between 2010 and 2017, Arctic glaciers and ice caps lost 609 ± 7 gigatonnes of ice, contributing 0.240 ± 0.007 millimetres per year to global sea level rise. While surface melt is responsible for 87 % of losses across the Arctic, both iceberg calving and submarine melting at glacier fronts are accelerating in the Barents and Kara Sea region where they now account for almost half of the total ice loss. Glacier acceleration and increased calving rates are associated with a northward shift of Atlantic climate and sustained by a range of processes that are amplified by temperature increases in both the ocean and the atmosphere around the glaciated islands of the Eurasian Shelf.

The thesis builds on these initial pan-Arctic findings to further investigate, in Chapter 5, the processes that shape the current response to warming of glaciers and ice caps in the Eurasian High Arctic, with a particular focus on the Russian archipelagos of Novaya Zemlya and Severnaya Zemlya. Time series of surface elevation change between 2010 and 2018 in conjunction with concurrent climate data analyses provide insights into the contrasting forcing mechanisms and glacier responses affecting these two regions. While both frontal ablation of tidewater glaciers and surface melt contribute to mass changes in Novaya Zemlya, enhanced ice flow is entirely responsible for the recent net ice loss in Severnaya Zemlya. A simple, linear relationship between coupled ocean-atmosphere warming and mass change over Novaya Zemlya is found to describe appropriately the decadal trend in ice loss at regional scale, in agreement with previous findings over Greenland. In Severnaya Zemlya, ocean warming is found to be the key factor influencing glacier velocities, owing to the intrusion of warm Atlantic Water along the Eurasian continental margin and reaching the archipelago's tidewater glacier fronts where it drives dynamic thinning.

Together these results suggest that meteorological processes will continue to dominate glacier loss throughout the Arctic, while warming of the Arctic Ocean will increasingly affect the dynamic stability of tidewater glaciers in the Barents and Kara Sea region, with unpredictable and possibly abrupt shifts in mass

balance. In this particular region and globally, rapid changes in glacier speed represent the largest source of uncertainty in climate models predicting how land ice will respond to future climate transitions. The findings from this thesis demonstrate that radar altimetry and swath processing can be used effectively to improve significantly upon these uncertainties. Finally, evidence is provided to support the principle that simple relationships between environmental forcings and glacier change are sufficiently accurate to describe ice loss in regions where synchronous, coupled ocean-atmospheric warming prevails. Overall the thesis provides critical advances for estimating future ice loss, freshwater budgets, and sea level contributions from Arctic glaciers and ice caps in a changing climate.

Declaration

I declare that this thesis has been composed solely by myself, and that it contains only my work except where otherwise specified, or where the work is explicitly indicated below to have formed part of a jointly-authored publication. This work has not been submitted for any other degree or professional qualification.

Paul Tepes

July 2020

Acknowledgements

This work was funded by the European Space Agency and the University of Edinburgh School of GeoSciences.

I would firstly like to thank warmheartedly Pete Nienow and Rob Bingham for helping me navigate through the many challenges that I faced during this project. Steering a steady course and making headway through the rough seas encountered during this PhD was a herculean task, and this thesis would be in a very different state without Pete's and Rob's engagement, guidance, and skill.

I would like to thank Noel Gourmelen for offering me the great opportunity to embark on this cutting edge polar science and earth observation project. The project provided me with incredible learning opportunities, including multidisciplinary training in the use and analysis of climatic and glaciological data, teaching responsibilities, and support to attend several international conferences. Overall, I have learnt a great deal, on and off the Command Line and the Arctic maps. My thanks extend to all academic staff in the Glaciology Department in Drummond Street, and to all those who contributed to the different chapters in this thesis.

Many thanks to all colleagues from Upper and Lower Lewis who supported and encouraged me. I'd like to thank Luca Foresta and Flora Weissgerber in particular, for their technical guidance, their spirit of collegiality, and for supporting me through the good and the bad. Thanks to Ashley and Conrad for their kindness, for the Monday afternoon runs around *Arthur's Seat*, and for all the great times we shared together after work at the *Salt Horse* and in the Highlands. Thanks also to Richard, Monika, Amit and Penny for their friendship and

great sense of humour.

A special thank you to the UK Polar Network, APECS Russia, and the Kola Science Center Of The Russian Academy Of Sciences for organising and offering an unforgettable experience at the inter-disciplinary fieldwork course *Arctis 2019* in the Russian Arctic.

I would like to express all my gratitude to my wife and road companion Michelle for her patience, relentless encouragements, and unconditional support. Your open-minded spirit, lightheartedness, and forbearance were invaluable during these long years in which I was committed to this project.

And finally thank you to my parents and my sister Alina, for always being there no matter what.

Contents

Abstract iii

Lay Summary vi

Declaration ix

Acknowledgements x

List of Figures xv

List of Tables xviii

Glossary xix

1 Introduction 1
- 1.1 Mapping the Arctic in a time of rapid change . . . 3
- 1.2 Thesis aims and overview . . . 5

2 Background 7
- 2.1 Land ice fluctuations and sea level change . . . 7
- 2.2 Uncertainties . . . 8
- 2.3 Monitoring Arctic land ice fluctuations . . . 10
  - 2.3.1 Mass balance . . . 10
  - 2.3.2 CryoSat-2 swath interferometry and mass balance . . . 14
  - 2.3.3 Global assessments of glacier and ice cap mass balance . . . 19
- 2.4 Climatic controls on Arctic ice mass imbalance . . . 20
  - 2.4.1 Arctic climate trends . . . 22
  - 2.4.2 Svalbard . . . 24
  - 2.4.3 The Russian Arctic . . . 25
  - 2.4.4 Iceland . . . 26
  - 2.4.5 The Canadian Arctic . . . 27
  - 2.4.6 Alaska . . . 29
- 2.5 Longer-term Arctic climate records and land ice change . . . 29
- 2.6 Projections of future mass loss . . . 32
- 2.7 Summary of knowledge gaps . . . 35
- 2.8 Research questions and thesis structure . . . 36

2.9 Appendices 39

3 Methods **42**
3.1 Study region: Arctic glacier inventory 42
3.2 Swath processing 45
3.2.1 Waveform filtering 46
3.2.2 Phase unwrapping 48
3.3 Gridded maps of surface elevation change 51
3.4 Time series of surface elevation change 52
3.5 Validation of CryoSat-2 swath products 54
3.6 Spatial coverage and data gaps 55
3.6.1 Spurious elevation changes from 'ground truth' 56
3.6.2 Receiver Operating Characteristic (ROC) function 58
3.6.3 Errors from changes in the scattering horizon 60
3.7 Volume change 60
3.7.1 Hypsometric averaging 63
3.7.2 Upscaling of volume change 63
3.8 Mass balance 66
3.8.1 Ice density assumptions 67
3.8.2 Sensitivity analysis 67
3.8.3 Partitioning between surface ablation and ice discharge . . 68
3.8.4 Validation of the SMB parametrisation 70
3.8.5 Contribution to sea level rise (SLR) 73
3.8.6 Error calculation 73
3.9 Discussion on measurement uncertainty 76
3.10 Summary of Methods 78
3.11 Appendices 80

4 Changes in elevation and mass of Arctic glaciers and ice caps (2010-2017) **93**
4.1 Abstract 93
4.2 Introduction 94
4.3 Pan-Arctic view of GIC thinning 95
4.4 Arctic GIC mass balance 98
4.5 Surface mass balance and glacier dynamics 100
4.6 Atmospheric and oceanic drivers of ice loss 103
4.7 Conclusions 105
4.8 Appendices 107
4.8.1 Mass balance of Arctic GIC 107
4.8.2 Atmospheric and oceanic forcing anomalies 108
4.8.3 Data availability 109
4.8.4 Acknowledgements 109

5 Russian Arctic glacier and ice cap response to accelerated warming (2010-2018) 111
5.1 Abstract . . . 111
5.2 Introduction . . . 112
5.3 Methods . . . 114
5.4 Results . . . 117
5.4.1 Spatial patterns of surface elevation change . . . 117
5.4.2 Time series of surface elevation change . . . 119
5.4.3 Mass balance . . . 123
5.4.4 Climatic trends in the BKS region . . . 125
5.5 Discussion . . . 129
5.5.1 Novaya Zemlya's ice mass response to atmospheric and oceanic warming . . . 129
5.5.2 Atlantic Ocean fingerprints on Severnaya Zemlya's dynamic imbalance . . . 131
5.5.3 Coupled versus decoupled climatic forcing . . . 133
5.6 Summary and conclusions . . . 139
5.7 Appendices . . . 141
5.8 Data availability statement . . . 154
5.9 Acknowledgments . . . 154

6 Conclusions 156
6.1 Synthesis of findings . . . 157
6.2 Advances on key knowledge gaps . . . 160
6.2.1 High-definition swath interferometry for the direct assessment of global ice mass balance . . . 161
6.2.2 Partitioning between surface mass balance anomalies and dynamic imbalance . . . 162
6.2.3 Climate sensitivity of glaciers and ice caps in an Arctic warming 'hotspot' . . . 163
6.3 Limitations and opportunities for future research . . . 165
6.4 Final remarks . . . 168

Bibliography 171

List of Figures

1.1 *Septentrionalium terrarum descriptio* (1595) 2
1.2 The Arctic viewed from space 4

2.1 Global mean sea level contributions and measurement 8
2.2 Global total cumulative GIC and ice sheet mass loss 9
2.3 CryoSat-2 sampling resolution in SARIn mode 16
2.4 CryoSat-2 sampling modes according to a geographic mode mask 16
2.5 CryoSat-2 POCA and swath processing 17
2.6 CryoSat-2 coverage over a smoothly sloped ice cap 18
2.7 CryoSat-2 coverage along ice margins with rough topography . . . 18
2.8 Regional glacier and ice cap mass budgets and surface areas . . . 20
2.9 Conceptual model of "Atlantification" 23
2.10 GIC surface elevation change over Svalbard (ICESat, 2003-2009) . 24
2.11 GIC surface elevation change over the Russian Arctic (ICESat, 2003-2009) 26
2.12 Icelandic ice caps and their mass balance 27
2.13 Canadian Arctic GIC and their time series of mass change (ICESat, 2003-2009) 28
2.14 Projected land ice loss from different Arctic regions in 2030 and 2080 under RCP4.5 and RCP8.5 34
2.15 Projected changes in near surface air temperature 39

3.1 Thesis main workflow 43
3.2 RGI 6.0 land- versus marine-terminating glacier basin misallocations over Svalbard 45
3.3 Example of a CryoSat-2 echo waveform with applied power and coherence filter thresholds 47
3.4 Example of CryoSat-2 swath altimetry over extreme topography . 48
3.5 Critical slope angle resulting in interferometric phase ambiguities, geospatial positioning, and elevation errors 49
3.6 Swath-processed elevation changes using different reference DEMs 50
3.7 Time series of surface elevation change over Vil'kitskogo southern glacier basin, Novaya Zemlya (Russian Arctic) 53
3.8 Validation of CryoSat-2 swath products using NASA Operation Ice Bridge (OIB) measurements 55

3.9 CryoSat-2 - OIB surface elevation change bias . . . 56
3.10 Selection of parameters for noise detection . . . 57
3.11 ROC functions for the selection of suitable noise classifiers . . . 58
3.12 Spatial distribution of spurious elevation change samples over Barnes Ice Cap on Baffin Island, Arctic Canada . . . 59
3.13 Iterative volume change computation and typical convergence, example of Novaya Zemlya, Russian Arctic . . . 61
3.14 Surface elevation change over Vatnajökull Ice Cap, Iceland . . . 62
3.15 Hypsometric averaging over Bylot Island and over Barnes and Penny Ice Caps, Arctic Canada . . . 64
3.16 CryoSat-2 swath elevation change maps, hypsometry and coverage over Austfonna Ice Cap, Svalbard, and over Academy of Sciences Ice Cap, Severnaya Zemlya, Russian Arctic . . . 65
3.17 RACMO2.3 cumulative SMB between 01/2011 and 12/2017 . . . 70
3.18 CryoSat-2 SMB parametrisation: comparison with RACMO2.3 . . . 71
3.19 Maps of surface elevation change (2010-2017) east of Greenland . 80
3.20 Map of surface elevation change (2010-2017) over Svalbard . . . 81
3.21 Map of surface elevation change (2010-2017) over Novaya Zemlya, Russian Arctic . . . 82
3.22 Map of surface elevation change (2010-2017) over Franz Josef Land, Russian Arctic . . . 83
3.23 Map of surface elevation change (2010-2017) over Severnaya Zemlya, Russian Arctic . . . 84
3.24 Maps of surface elevation change (2010-2017) over Icelandic ice caps 85
3.25 Surface elevation change (2010-2017) in the Canadian Arctic . . . 86
3.26 Maps of surface elevation change (2010-2017) over Bylot Island, and Barnes and Penny Ice Caps . . . 87
3.27 Map of surface elevation change (2010-2017) over Devon Ice Cap . 88
3.28 Maps of surface elevation change (2010-2017) over Manson and Sydkap Ice Caps . . . 89
3.29 Map of surface elevation change (2010-2017) over Prince of Wales Ice Field . . . 90
3.30 Maps of surface elevation change (2010-2017) over Muller and Steacie Ice Caps . . . 91
3.31 Maps of surface elevation change (2010-2017) over Northern Ellesmere ice fields and Agassiz Ice Cap . . . 92

4.1 CryoSat-2 swath-processed surface elevation change fields and mass balance of Arctic GIC, 2010-2017 . . . 96
4.2 Arctic GIC 2010-2017 area-specific SMB and discharge D from CryoSat-2 swath altimetry . . . 101
4.3 Arctic climate forcing anomalies . . . 104
4.4 Arctic-wide T_{2m} decadal anomalies (ERA-Interim) . . . 108
4.5 Arctic-wide SST decadal anomalies (ERA-Interim) . . . 108
4.6 Arctic-wide SOT decadal anomalies (TOPAZ) . . . 108

4.7 Arctic-wide SIC decadal anomalies (NASA Team) 109

5.1 Study region: Eurasian Arctic with major ocean currents and ocean bathymetry 113
5.2 Maps of surface elevation change and mass budgets over Novaya Zemlya and Severnaya Zemlya, Russian Arctic, 2010-2018 118
5.3 Time series of cumulative surface elevation change 121
5.4 Near surface air temperature and sea ice concentration anomalies in the Barents and Kara Sea region 127
5.5 Sea surface and subsurface temperature anomalies in the Barents and Kara Sea region 128
5.6 Time series of normalised forcing anomalies and surface elevation change for Novaya Zemlya and Severnaya Zemlya 136
5.7 R^2 statistics as a measure of linear fit between environmental forcing and surface elevation change $\dot{h}$ 137
5.8 Schematic illustrating heat fluxes in the BKS region 138
5.9 T_{2m} (ERA5) seasonal anomaly trends 2003-2018 141
5.10 SIC (GLORYS) seasonal anomaly trends 2003-2018 141
5.11 SST (ERA5) seasonal anomaly trends 2003-2018 142
5.12 $SOTF_1$ (GLORYS) seasonal anomaly trends 2003-2018 142
5.13 $SOTF_2$ (GLORYS) seasonal anomaly trends 2003-2018 143
5.14 $SOTF_3$ (GLORYS) seasonal anomaly trends 2003-2018 143
5.15 Arctic Ocean mean annual (1979-2014) vertical Ekman transport . 144
5.16 Maps of annual mean vertical Ekman velocity 1979-1989, 1990-1999, 2000-2009 144
5.17 Time lag cross-correlation analysis 145
5.18 Regression analysis of glacier response to forcing 146
5.19 Arctic Oscillation Index 148
5.21 Franz Josef Land $\dot{h}$ maps and time series 151
5.22 Ocean bathymetry around Franz Josef Land 152

List of Tables

2.1 Regional breakdown of global GIC mass budgets and glaciated areas after Gardner et al. (2013) 21
2.2 Number of glacier basins, glaciated area, ice volume and sea level equivalent by region 40
2.3 Global land ice contributions to sea level rise during 2004-2010 . . 41

3.1 Classifier thresholds for volume change computation 62
3.2 CryoSat-2 SMB parametrisation coefficients 69
3.3 CryoSat-2 SMB parametrisation over Svalbard 73

4.1 Summary table of Arctic GIC mass budgets 99
4.2 Summary table of Arctic glacier and ice cap discharge D 102
4.3 Arctic climate anomalies during 2010-2017 relative to 1990-2009 means 104
4.4 Mass balance of Arctic glaciers and ice caps from CryoSat-2 swath altimetry, 2010-2017 107

5.1 GIC mass balance (2010-2018) across Novaya Zemlya and Severnaya Zemlya from CryoSat-2 swath altimetry 124

Glossary

AIS - Antarctic Ice Sheet.
AO - Arctic Oscillation.
AR5 - Fifth Assessment Report.
ATM - Airborne Topographic Mapper.
AWI - Atlantic Water Inflows.

BKS - Barents and Kara Seas.
BMB - Basal Mass Balance.

CAA - Canadian Arctic Archipelagos.
CAA-N - Northern Canadian Arctic Archipelagos.
CAA-S - Southern Canadian Arctic Archipelagos.
CMIP5 - Coupled Model Intercomparison Project Phase 5.

D - Ice Discharge.
DEM - Digital Elevation Model.

ECMWF - European Centre for Medium-Range Weather Forecasts.
EGM96 - Earth Gravitational Model 1996.
ENSO - El Niño Southern Oscillation.
ESA - European Space Agency.

FJL - Franz Josef Land.
FPR - False Positive Rate.

GDAL - Geospatial Data Abstraction Library.
GIC - Glaciers and Ice Caps.
GLIMS - Global Land Ice Measurements from Space.
GMSL - Global Mean Sea Level.
GRACE - Gravity Recovery and Climate Experiment.
GrIS - Greenland Ice Sheet.

Ic - Iceland.
ICESat - Ice, Cloud, and land Elevation Satellite.
InSAR - Synthetic Aperture Radar Interferometry.
IPCC - Intergovernmental Panel on Climate Change.

LIA - Little Ice Age.

LRM - CryoSat-2 Low Resolution Mode.

MAR - Modèle Atmosphérique Régional.

NAO - North Atlantic Oscillation.
NASA - National Aeronautics and Space Administration.
NPI - Norwegian Polar Institute.
NZ - Novaya Zemlya.

OIB - Operation Ice Bridge.

POCA - Point Of Closest Approach.

RAA - Russian Arctic Archipelagos.
RACMO - Regional Atmospheric Climate Model.
RGI - Randolph Glacier Inventory.
ROC - Receiver Operating Characteristics function.

SAR - Synthetic Aperture Radar.
SARIn - SAR Interferometric mode.
SAT - Surface Air Temperature.
SIC - Sea Ice Concentration.
SIRAL - SAR Interferometric Radar Altimeter.
SLE - Sea Level Equivalent.
SLR - Sea Level Rise.
SMB - Surface Mass Balance.
SOT - Subsurface Ocean Temperature.
SOTF - Subsurface Ocean Temperature Forcing.
SSH - Sea Surface Height.
SST - Sea Surface Temperature.
Sv - Svalbard.
SZ - Severnaya Zemlya.

TPR - True Positive Rate.

WGI - World Glacier Inventory.
WGS84 - World Geodetic System 1984.

Chapter 1

Introduction

The Arctic is the northernmost region on Earth. Its name comes from the Greek *arktikos*, which means "near the northern bear", in reference to the constellation *Alpha Ursae Minoris* and its brightest star *Polaris*, or North Star, which is located near the north celestial pole. The Arctic has fascinated humanity since ancient times due to its remoteness, the capability of the indigenous people to adapt to its cold and extreme conditions, and the possibilities of new discoveries, resources, and the interest in new trade routes (e.g. Berton, 1988).

One of the earliest maps indicating an open water route across the Arctic was by Gerardus Mercator (Figure 1.1). At the time, some believed that water from the adjacent oceans flowed northwards between the islands of the Arctic, and to the centre of the Earth. As much as this perception is of a distant past, it is much less equivocal than it may seem at first sight. As modern scientific advances have shown, poleward transport of Atlantic Ocean water, and its overturning in the Arctic where it sinks to the ocean floor is not an abstruse phenomenon, but a key climatic mechanism, and a central component of the modern Earth System (Caesar et al., 2018; Thornalley et al., 2018). Equally important are the islands and archipelagos of the Arctic, which lock up significant amounts of ice, exhibiting both high sensitivity to environmental change, and a strong impact globally on climate (Church et al., 2013; Zemp et al., 2019). Paleoclimatic

studies have shown for example, how Atlantic Water advection into the Arctic influences glacier dynamics (Bartels et al., 2017), and how changes affecting the Arctic cryosphere during cycles of warming and glaciation are directly linked to the state of the Earth's climate system at deep timescales (e.g. Brigham-Grette et al., 2013, and references within).



Figure 1.1: *Septentrionalium terrarum descriptio* (1595) by Gerardus Mercator (1512-1594). Description: "Circular copper plate engraving map of the Northern Hemisphere from the Arctic Pole to latitude 60° North. The map contains four circular insets, one containing the map title and statement, '*Per Gerardum Mercatorem Cum Privilegio*'. The other three insets contain detailed depictions of islands from the larger map." Source: open.library.ubc.ca/collections/manuscripts/items/1.0224509, accessed on 19/7/2020.

Owing to unprecedented rates of human population growth, energy consumption and land-use, and the concomitant increase in atmospheric carbon dioxide and other greenhouse gases, the Arctic's continental ice masses are currently ex-

posed to the amplified effects of polar warming (Screen and Simmonds, 2010), resulting from both anthropogenic forcing and natural variability (Ding et al., 2014; Marzeion et al., 2014). It is predicted that the Arctic Ocean could become largely free of sea ice during the summer months before 2040 (Barber et al., 2017). The imminent opening of northern routes for maritime transport is believed to have profound implications for the global economy and the geopolitical power balance in a globalised world. In view of these changes, the Arctic is receiving growing attention and pressure as global warming accelerates, ice masses shrink, new resources are discovered, and disputed territories are claimed. Monitoring, mapping, and projecting the Arctic's rapidly changing landscape, and in particular its declining land- and sea ice cover is thus of utter importance today, as it was five hundred years ago, to policymakers, traders and the scientific community.

1.1 Mapping the Arctic in a time of rapid change

The advance of space science transformed observation of the Earth in unprecedented ways, allowing for the measurement of processes and rates of change at its surface with an ever-increasing degree of accuracy. It replaced long and perilous travel to, and slow gathering of geographic information from the world's remotest regions, with monitoring campaigns from satellites hundreds of kilometres away in space. Looking down on the Arctic from these orbiting instruments before the onset of the snow season, land that is covered in ice stands out prominently, in strong contrast to the surrounding environment, which includes the substantial presence of ocean water (Figure 1.2). Alaskan mountains, and a number of islands east and west of heavily glaciated Greenland hold approximately 58 % of the global land ice volume external to the Greenland and Antarctic Ice Sheets, which corresponds to 236 ± 23 mm of sea level equivalent (Farinotti et al., 2019). Although small in size when compared to the two ice sheets, they are currently responsible for 24 % of the observed increase in global mean sea level between 2004 and 2010 (Box and Sharp, 2017). The Arctic archipelagos' glaciers and

ice caps are especially vulnerable to environmental change, as they are exposed simultaneously to fluctuations in atmospheric, oceanic and sea ice conditions, driven by polar amplification of climate warming (Barber et al., 2017).

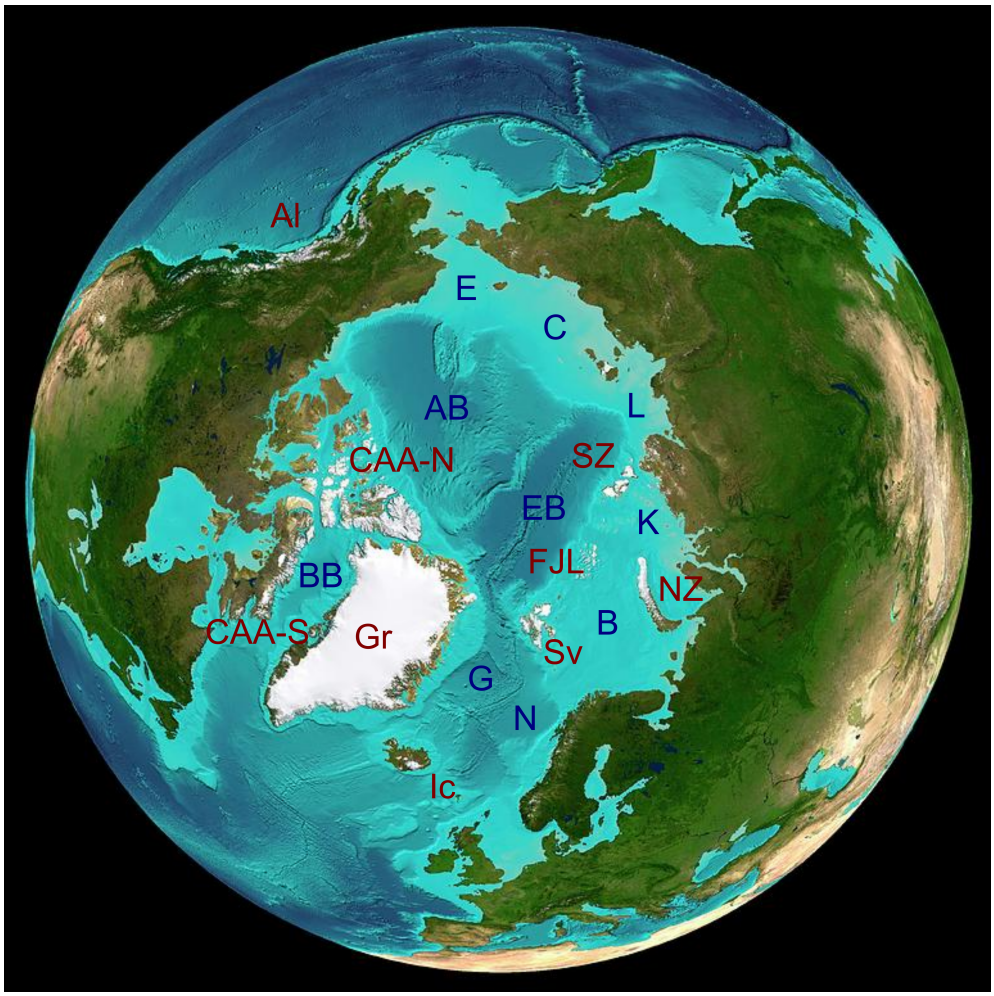


Figure 1.2: The Arctic viewed from space. Map centred on the North Pole, with the main land based ice masses located on Greenland (Gr), the southern and northern Canadian Arctic (CAA-S and CAA-N, respectively), Alaska (Al), Svalbard (Sv), Novaya Zemlya (NZ), Franz Josef Land (FJL), Severnaya Zemlya (SZ), and Iceland (Ic). The principal Arctic Ocean basins, bays and shelf seas are: Amerasian Basin (AB), Eurasian Basin (EB), Baffin Bay (BB), East Siberian Sea (E), Chukchi Sea (C), Laptev Sea (L), Kara Sea (K), Barents Sea (B), Norwegian Sea (N), and Greenland Sea (G). Ocean bathymetry is from the International Bathymetric Chart of the Arctic Ocean (IBCAO) and Earth Topography (ETOPO2-2) altimetry. The land areas use data from the Blue Marble satellite mosaic. Source: Martin Jacobsson, Science Photo Library, sciencephoto.com/media/166939/view, accessed on 19/7/2020.

Despite the profound advances in earth observation technologies, Arctic glaciers

and ice caps still present considerable challenges for satellite observation and monitoring, due primarily to their complex topography (Gardner et al., 2013; Jacob et al., 2012). For example, mapping glaciers from optical satellite imagery, such as in Figure 1.2, is not straightforward, and the end products are generally derived from a composite of snapshots taken at different points in time, including data shifts and gaps (Schuler et al., 2020), as optical instruments rely heavily on the presence of sunlight, and on the absence of cloud cover. This makes optical measurement alone of limited use in the continuous, long-term monitoring of the important ice dynamical and surface processes that occur at seasonal, interannual, and decadal timescales. At present, the joint use of geodetic, altimetric, gravimetric, and in situ observations has proven to be the most robust way of making global, quantitative assessments of cryospheric change (Gardner et al., 2013; Schuler et al., 2020). Amongst these, radar interferometry has been increasingly effective and accurate in tracking subtle change at the ice surface, independently of meteorology and Earth rotation. The CryoSat-2 satellite in particular, launched in 2010, was specifically designed to measure ice thickness very precisely. However, given the vast volumes of data sampled by this satellite, significant quantities of data have not yet been processed over extensive regions, including over many Arctic glaciers and ice caps, which are critically exposed to external forcings. These datasets are essential for providing robust evidence of local and regional trends in diminishing polar ice cover in a warming Arctic, while at the same time improving our understanding of the complex relationships between ice and global climate.

1.2 Thesis aims and overview

Against this background, the overall aim of this thesis is to identify, test and use CryoSat-2 measurements and novel processing techniques to provide a comprehensive assessment of recent land ice change across the Arctic since the launch of the satellite, quantify these changes, and understand their drivers. Chapter

2 provides essential background information underlining the role of the Arctic cryosphere in the Earth System while focusing on the regional specificities of current Arctic glacier mass loss and its drivers, which is the central focus of this thesis. Chapter 2 also elucidates in detail the ability of the CryoSat-2 interferometric altimeter in continuously monitoring cryospheric change, and its capacity to measure Arctic glaciers and ice caps at high spatial and temporal resolution. After identifying a series of key gaps in the present state of knowledge regarding Arctic glacier and ice cap mass imbalance and the evaluation of its sensitivity to climate, the chapter concludes with a list of key research questions and aims, which are then addressed individually in the results Chapters 3-5. Chapter 6 provides a synthesis of the findings, highlights their significance and limitations, gives an overview of how the aims of the thesis have been met, and includes a list of recommendations for future research.

Chapter 2

Background

2.1 Land ice fluctuations and sea level change

The cryosphere is a constituent of the Earth System characterised by the presence of land ice, sea ice, snow and permafrost (Slaymaker and Kelly, 2007), and forms an integral part of the hydrological cycle in which the different cryospheric components interact over different time scales. Continental ice is stored during periods of glaciation through net ocean-to-land mass transfer resulting from an imbalance between precipitation as snowfall and ice melt. The ice is presently stored in the Greenland and Antarctic Ice Sheets (GrIS and AIS, respectively), a number of comparatively small glaciers and ice caps (GICs) at their periphery and in the archipelagos of the Arctic, and across a multitude of mid-to-high latitude mountain glaciers and ice fields, which are clustered primarily along the American Cordillera, from Alaska to Patagonia, and in the Himalayas, a region sometimes referred to as the 'Third Pole' (Qiu, 2008). In the polar regions, any substantial changes affecting the cryosphere are believed to have long-lasting impacts on global energy balance and climate (Cohen et al., 2014). In the Arctic in particular, increased melting of the seasonal snowpack and ongoing reductions in sea ice are currently thought to enhance an observed planetary warming trend that has been accelerating since the ending of the interval commonly referred to

as the Little Ice Age (e.g. Matthews and Briffa, 2005).

Global eustatic sea level rise, dominated by land ice loss and ocean thermal expansion (Figure 2.1a), is one of the clearest expressions of this warming trend, with lasting impacts on coastal communities worldwide. Global sea level can be estimated instrumentally from satellite altimetry directly, or alternatively as the sum of ocean mass and thermosteric change, which are retrieved from the Gravity Recovery and Climate Experiment (GRACE) (Tapley et al., 2004) and the Argo float programme (Roemmich et al., 2012), respectively (Figure 2.1b).

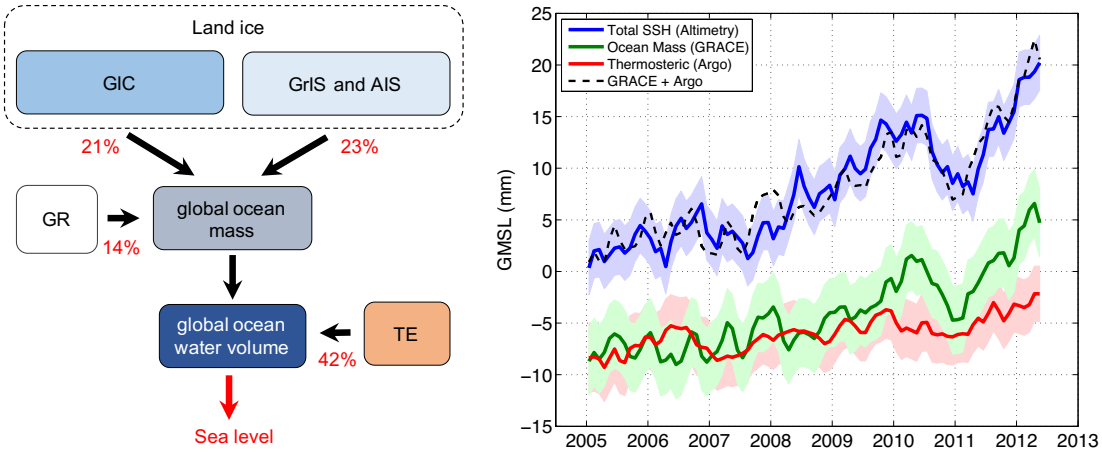


Figure 2.1: Global mean sea level (GMSL) contributions (left) and measurement (right) using different methodologies. Acronyms: GIC = glaciers and ice caps, GrIS = Greenland Ice Sheet, AIS = Antarctic Ice Sheet, TE = thermal expansion, GR = groundwater and reservoirs, SSH = sea surface height. Source: Church et al., 2013

2.2 Uncertainties

Although sea level changes can be monitored from space, the relative input from individual freshwater sources is poorly constrained. Partitioning hydrological losses into contributions from ice sheets, glaciers and ice caps, and ground water reservoirs is challenging, and the respective driving mechanisms of these mass transfers remain poorly understood. Between 1993 and 2018, it is estimated that glaciers and ice caps contributed 21 % to eustatic sea level rise compared to 23

% from the Greenland and Antarctic Ice Sheets, with thermal expansion and groundwater reservoirs contributing 42 % and 14 % respectively during the same time period (Figure 2.1a) (WCRP Global Sea Level Budget Group, 2018). Nevertheless, these estimates are associated with large uncertainties, in particular those contributions stemming from glacier and ice cap mass loss (Vaughan et al., 2013) (Figure 2.2a). This can be largely explained by the fact that in the early stages of earth observation, and until recently, satellite instruments were primarily designed to sample measurements from the Greenland and Antarctic Ice Sheets, with limited application over glaciers and ice caps owing to their small surface area and complex topography. However, glacier and ice caps' current input to sea level change is significant and is expected to accelerate over the next century and beyond (Gardner et al., 2013), particularly in the Arctic, where mean annual surface temperatures have been increasing faster than the global average (Park et al., 2018; Screen and Simmonds, 2010).

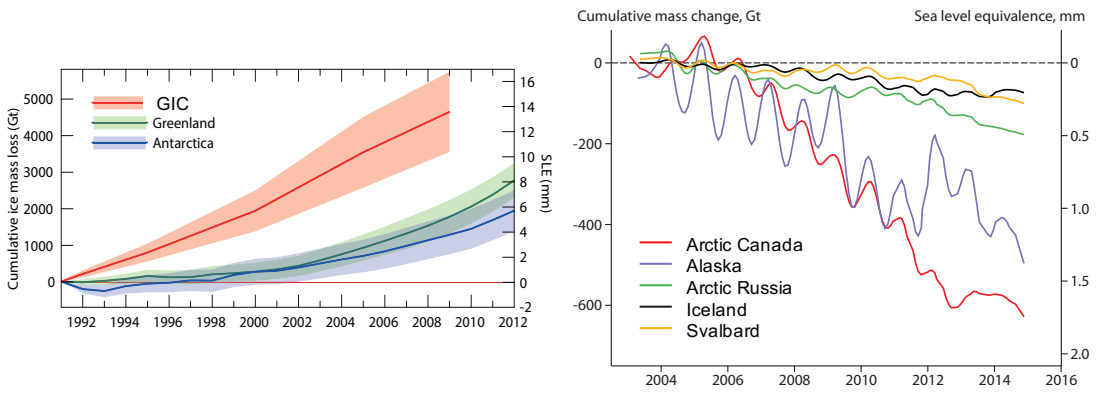


Figure 2.2: Cumulative ice mass loss from the world's glaciers and ice caps (GIC) and the two ice sheets. Source: Vaughan et al. (2013) (left) and Box and Sharp (2017) (right).

A significant proportion of the losses from the world's $\sim 10^5$ smaller glaciers and ice caps since 2003 is from the archipelagos of the Canadian High Arctic, Alaska, the Russian High Arctic, Svalbard and Iceland (Figure 2.2b). Overall, glaciers and ice caps extend over a total of 7.3×10^5 km^2 and one third of this total is located in the Arctic (Gardner et al., 2013). The Arctic archipelagos alone

store approximately 44 % of the world's glacier ice volume, excluding ice locked up in the Greenland and Antarctic Ice Sheets (Farinotti et al., 2019), although the two ice sheets dominate the land ice segment of the global freshwater reservoir ($>$ 95 % of total area and $>$ 99 % of total volume).

2.3 Monitoring Arctic land ice fluctuations

Given the rate at which the cryosphere is changing and its importance for sea level rise, ocean circulation, and climate, accurate monitoring of rates of volume and mass change is becoming increasingly important. A variety of instruments and techniques have been developed for measuring glacier change since the onset of glaciology as a scientific field. Historically, because of the difficulty in accessing most of the world's glaciers, the standard approach was to measure changes in glacier length by reconstructing glacial chronologies of advance and retreat from terminus position and moraine sequences (Grove, 1988). Photography, including from airborne platforms, was key for recording and processing information on glacier changes (e.g. Benn and Evans, 2010).

The most direct and reliable method for evaluating the status or 'health' of glaciers, however, is to determine their mass balance. The advent of satellites has been central to the constant development and improvement of mass balance measurement techniques by allowing the cyclical acquisition of information about the world's ice masses, extending observations made locally to monitoring at the global scale.

2.3.1 Mass balance

Glacier shape and size are controlled by the accumulation of snowfall, surface and subglacial melt, frontal ablation or calving, and by flow carrying ice from regions of net accumulation to regions of net ablation. Hence, glacier velocity and ice thickness variations, in addition to snowfall and ice melt, are good indicators

of glacier mass budgets measured over an annual cycle. They can be utilised to describe the dynamic behaviour of glacier ice during short periods of time (Cuffey and Paterson, 2010):

$$\dot{H} = \frac{\partial H}{\partial t} = \underbrace{\frac{\dot{b}_S}{\rho_S}}_{SMB} + \underbrace{\frac{\dot{b}_B}{\rho_B}}_{BMB} + \underbrace{\int_B^S \frac{\dot{\mu}_i}{\rho} dz}_{englacial\ melt} - \underbrace{\nabla \cdot \vec{q}}_{\substack{mass\ flux \\ divergence}} - \underbrace{\int_B^S \frac{1}{\rho} \frac{D\rho}{Dt} dz}_{densification} \quad (2.1)$$

where $\dot{H}$ (m a^{-1}) represent changes in ice thickness (H) over time (t) resulting from **(a)** mass losses or gains at the ice surface (surface mass balance *SMB*), at the glacier bed (basal mass balance, *BMB*), and throughout the ice column (*englacial melt*), **(b)** from the vertical and horizontal movement of ice (*mass flux divergence*), and **(c)** from changes in the density of glacier ice and firn (*densification*). The terms $\dot{b}_S$ and $\dot{b}_B$ denote the area-specific surface- and basal mass balance (kg m^{-2} a^{-1}), respectively, and ρ_S and ρ_B are the corresponding densities of ice at the glacier surface (S) and at the bed (B). Englacial melt is related to the deformational work per unit volume and is described in Equation 2.1 as the rate $\dot{\mu}_i$ of mass loss by melt, divided by the density of ice (ρ) and integrated over the glacier depth (z). Mass flux divergence ($\nabla \cdot \vec{q}$) is generally described as a function of depth-averaged velocity multiplied by ice thickness.

In most cases basal and englacial mass balance are considered to be negligible, and ice density is assumed to be constant across the entire volume of a glacier or ice cap. These approximations are acceptable for large ice sheets, and in analyses of long-term mass fluctuations and steady-state dynamics. For an ice cap with 500 m total ice thickness and a 40 m firn layer, the induced error in mass change is about 2 %, according to Cuffey and Paterson (2010). After accounting for these simplifications, the remaining terms in equation 2.1 are surface mass balance and flux divergence, the former directly related to climate, and the latter describing ice thinning through the spreading of glacier mass (Cuffey and Paterson, 2010):

$$\dot{h} = \frac{\partial h}{\partial t} = \frac{\dot{b}_S}{\rho_S} - \nabla \cdot \vec{q} \tag{2.2}$$

Surface elevation changes ($\dot{h}$) are thus a visible and potentially measurable expression of the competition between climate and ice flow (Cuffey and Paterson, 2010).

The following main techniques are commonly applied to measure changes in glacier mass:

- The **glaciological** method, a traditional in situ measurement technique carried out by means of ablation stakes and accumulation pits, with data on surface wastage, accumulation of snowfall, and ice and firn density used to estimate surface mass balance;
- The **hydrological** method, which relies on the measurement of precipitation and runoff over entire hydrological catchments;
- The **geodetic** method derives ice thickness changes indirectly from satellite altimetry by comparing digitised topographic maps measured at different points in time, with time differences ranging from years to decades. Digital elevation maps are generally based on aerial photographs, optical stereo or interferometric radar (InSAR) imagery, and are applied at regional level, with a high spatial resolution;
- The **altimetric** and interferometric methods use cross-over or repeat-track optical (laser) altimetry, or radar (SARIn) interferometric altimetry to derive mass balance directly from measurements of surface elevation change (e.g. ICESat, CryoSat-2);
- The **input-output** method calculates mass balance as the sum of surface mass balance (input) and ice discharge (output), which are estimated separately. Surface mass balance is derived from regional climate models (e.g. RACMO, MAR) coupled with snow and firn models, while discharge is computed from satellite optical and radar (InSAR) imagery-based velocity fields and ice thickness profiles at the grounding line;

- The **gravimetric** method measures mass changes directly from the inversion of measured satellite gravity fields (e.g. GRACE). Gravimetry has no vertical component and hence mass changes from ice and snow, surface and underground water, and changes within the solid Earth are not distinguished. Measurements need to be corrected for the influence of the glacial isostatic rebound and non-glacial hydrological and lithospheric changes.

The glaciological method provides glacier-wide mass changes extrapolated from single point measurements, and hence carry large uncertainties. Nonetheless, they form an essential observational baseline for comparison with estimates from other methods (Marzeion et al., 2015; Zemp et al., 2019). In situ glaciological datasets extend back over more than a century for some glaciers, and thus provide critical long-term evidence of change. The hydrological method is ideally adapted for studies of river basin hydrology and downstream water supply (e.g. Immerzeel et al., 2010), and is not further discussed in this thesis.

Satellite geodesy has revolutionised mass balance assessments, with vast volumes of data allowing for a continuous, large-scale monitoring of globally distributed ice masses, thereby opening new possibilities for the evaluation of glacier responses to climate variability and change. Since the early 2000s, the concomitant development of satellite gravimetry, altimetry and interferometry has led to multiple global assessments of land ice to ocean mass transfer. To date however, most efforts have been directed towards the observation of the Greenland and Antarctic Ice Sheets (e.g. Shepherd and Wingham, 2007; Shepherd et al., 2012; The IMBIE Team, 2018, 2020), with smaller glaciers and ice caps receiving growing attention only during the last decade (Gardner et al., 2011, 2013; Gray et al., 2015; Jacob et al., 2012; Moholdt et al., 2012b). This is due in large part to the limited spatial and temporal resolution of the available observation techniques, which remain challenged when sampling over complex terrain, with steep topographic gradients, and small ice extent. For example, data from the Gravimetry Recovery and Climate Experiment GRACE, launched in 2002, has a spatial resolution of approximately 400 km, leaving individual glaciers and small ice caps

unresolved. The input-output method relies on ice thickness profiles which, outside Antarctica and Greenland, are either unavailable or associated with large uncertainties, with velocity fields and time series having only started to emerge recently at the global scale (e.g. Dehecq et al., 2015; Dehecq et al., 2019). ICESat's laser altimeter sampled measurements from 2003 to 2009 along relatively sparse satellite orbits (Nilsson et al., 2015a), leaving large areas unmeasured.

Radar altimetry is particularly well suited for tracking volumetric changes due to its all-weather year-round capability of observing the ice surface, and conventional radar altimeters have been collecting measurements for over more than 35 years (e.g. Elachi and Zyl, 2006). Early altimeter missions however also suffered from a variety of limiting factors, including relatively large pulse- and beam-limited footprints and wide ground track interspacing, the inability to locate the return signal over sloping terrain, and preferential sampling from topographic highs, leaving many glacier valleys and ice fields unmapped (Gourmelen et al., 2018). It is only with the emergence of swath interferometric altimetry (Hawley et al., 2009) that continuous, high-resolution assessments of mass change started to be conceivable at global scale. This thesis utilises this potential to present the first attempt to perform a pan-Arctic mass balance computation based on this novel, direct measurement technique, for which a more detailed description is provided in the following section.

2.3.2 CryoSat-2 swath interferometry and mass balance

The SAR Interferometric Radar Altimeter (SIRAL) onboard the European Space Agency's (ESA) CryoSat-2 satellite (Wingham et al., 2006) is designed to map changes in surface elevation over sub-ice sheet scale ice masses such as Arctic glaciers and ice caps. SIRAL is a beam forming, active microwave radar altimeter containing two Cassegrain nadir-looking antennas that are mounted perpendicular to the flight direction. It is designed to acquire data continuously while the satellite is orbiting around the planet, with a maximum imaging range (beam-

limited footprint) of $\sim$ 15 km on the ground (Figure 2.3a). The sensor emits Ku-band pulses, which reduce the footprint to $\sim$ 1.6 km within the beam, and also restrict signal penetration in the snowpack compared to microwave instruments operating at C or X-band frequencies (Foresta et al., 2018). Over Arctic glaciers and ice caps, CryoSat-2 operates in SARIn mode (Figure 2.4), using its dual receive antennas for both along-track aperture synthesis and cross-track interferometry (Wingham et al., 2006). Synthetic aperture processing takes multiple looks in flight direction by handling the pulse-limited return signal within single adjacent Doppler cells or sub-beams, thereby increasing the along-track resolution to $\sim$ 380 m (Figure 2.3b-c). Differences in the interferometric phase between the antennas are extracted to map the lateral positioning of the footprint centre.

Level 1b, baseline C altimetry from CryoSat-2 is provided by the ESA ground segment as a sequence of delay-Doppler radar echoes sampled along the satellite track. The data bundles consist of single power, interferometric phase and corresponding coherence waveforms for each along-track location (Gourmelen et al., 2018). Conventional processing of *level 1b* altimetry uses a retracker algorithm designed to extract single measurements from each waveform based on the shape of the power signal. Typically, retracking retrieves elevations at the Point of Closest Approach (POCA), which is located at the shortest distance between the satellite and the ground (Figure 2.5). The relatively recent development of swath altimetry (Hawley et al., 2009) expands the retracking technique to exploit the entire radar waveform well beyond POCA, retrieving dense swaths of elevation measurements that cover large areas across the satellite ground track (e.g. Christie et al., 2016; Foresta et al., 2016; Gourmelen et al., 2018; Gray et al., 2013; Ignéczi et al., 2016) (Figure 2.5). Swath altimetry thus represents a breakthrough in radar echo sampling, providing one to two orders of magnitude more elevation measurements compared with POCA. To retrieve swath elevations from the echo waveforms, conventional POCA retracking is replaced by a combination of normalised power and coherence thresholds applied to the signal (see Chapter

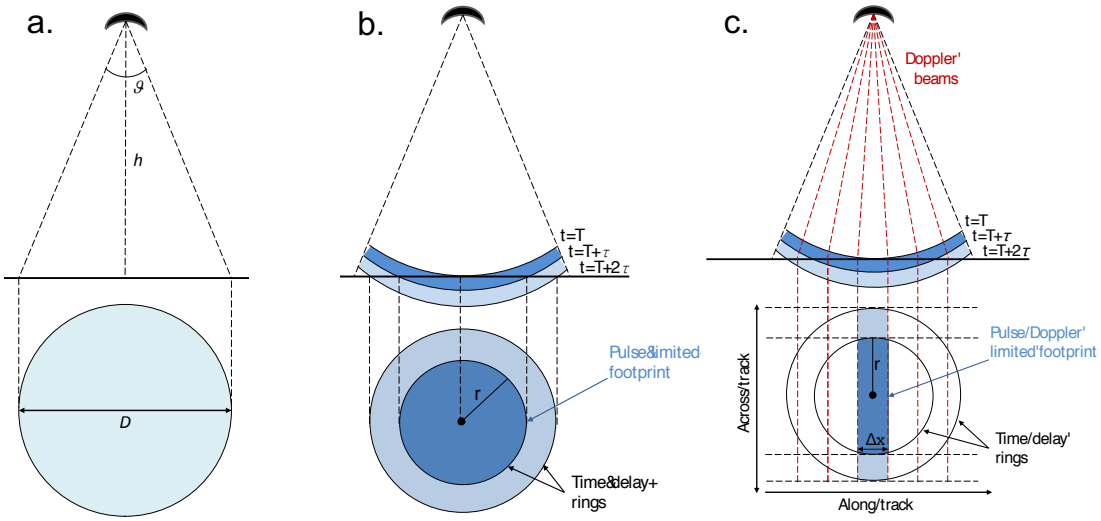


Figure 2.3: CryoSat-2 sampling resolution in SARIn mode. (a) beam-limited footprint, with D $\sim$ 15 km in the northern polar regions, **(b)** pulse-limited footprint, with r $\sim$ 1.6 km (t, T, τ), and **(c)** Doppler-limited footprint, with $\Delta x \sim$ 380 m in flight direction. Source: Bouzinac (2012).

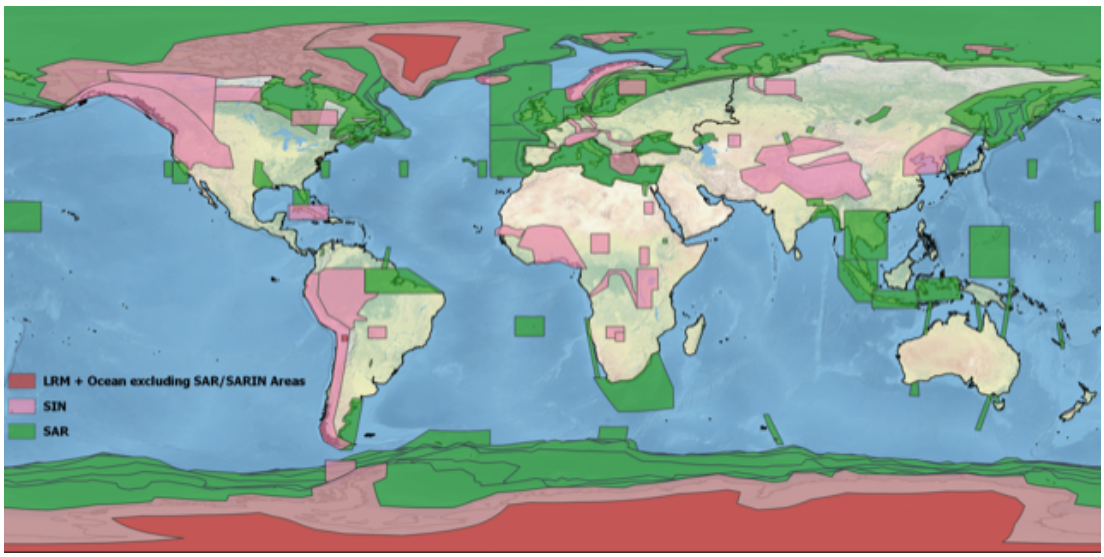


Figure 2.4: CryoSat-2 sampling modes according to a geographic mode mask. Synthetic Aperture Radar (SAR) (green) is operated mainly over ocean basins affected by sea ice; SAR Interferometric (pink) mode is used in regions of extreme topography, such as ice caps, mountain glaciers and steep-sloping ice-sheet margins; Low Resolution Mode (LRM) is operated over the smoothly-sloped continental ice sheet segments (red), and over areas not covered by the other modes. Source: `://earth.esa.int/web/guest/-/geographical-mode-mask-7107` (accessed on 15/06/2020).

3, Section 3.2.1). These thresholds were previously established through empirical analysis (Gourmelen et al., 2018; Gray et al., 2013).

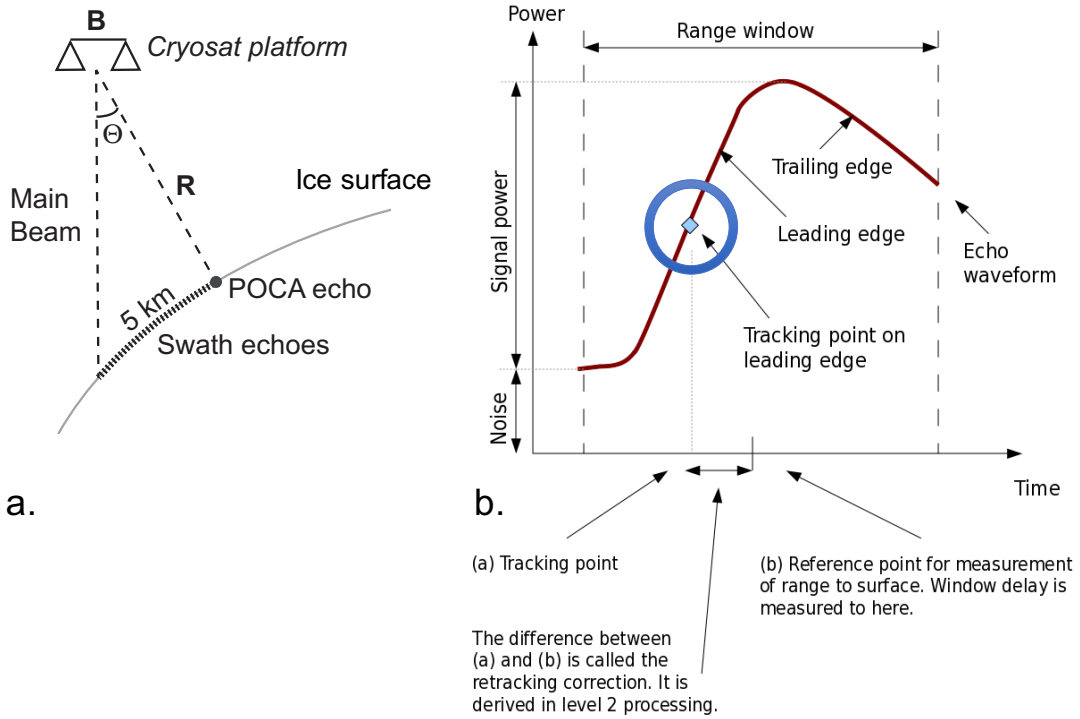


Figure 2.5: CryoSat-2 POCA and swath processing. Schematic showing across-track interferometric sampling **(a)**, and return signal power waveform nomenclature **(b)**. The interferometric baseline B is the distance between the Cassegrain antennas, R is the slant range, and Θ is the look angle. Source: Gourmelen et al. (2018) and Bouzinac (2012).

Swath altimetry not only allows for a much larger but also more homogeneous coverage of the ice surface (Foresta et al., 2016, 2018). Considering the example of Langjökull, a relatively small Icelandic ice cap, POCA typically tends to concentrate the sampling along surface heights and ice divides (Figure 2.6b), whereas swath processing samples elevations across the entire ice cap and in particular at low elevations, where much of the ice thinning occurs (Figure 2.6c-d). Swath altimetry has been successfully tested over Austfonna Ice Cap (Hawley et al., 2009), Devon Ice Cap (Gray et al., 2013), the Bellingshausen margin of West Antarctica (Christie et al., 2016), Icelandic ice caps (Foresta et al., 2016), and the southern and northern Patagonian ice fields (Foresta et al., 2018). Additionally, swath processing has been applied to identify surface depressions on ice surfaces resulting from the formation of supraglacial lakes (Gray et al., 2017; Ignéczi et al., 2016) or subglacial lake drainage (Smith et al., 2017). A fundamental step-increase in

data quality from swath processing compared to other sampling techniques provides, as highlighted previously, the capability to sense surface changes that occur over the convoluted ice surfaces at the ice cap margins and near glacier termini where mass losses are enhanced and important ice-climate interactions take place (Figure 2.7).

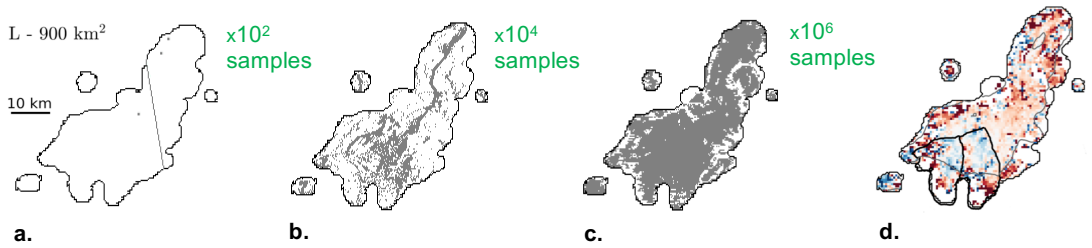


Figure 2.6: CryoSat-2 coverage over a smoothly sloped ice cap using different sampling methods. Measurement density **(a-c)** and gridded elevation change **(d)** over Langjökull Ice Cap, Iceland from **(a)** ICESat (2003-2009) for reference, **(b)** CryoSat-2 POCA and **(c, d)** CryoSat-2 swath. Source: (a) adapted from Nilsson et al. (2015a) and (b-d) Foresta et al. (2016).

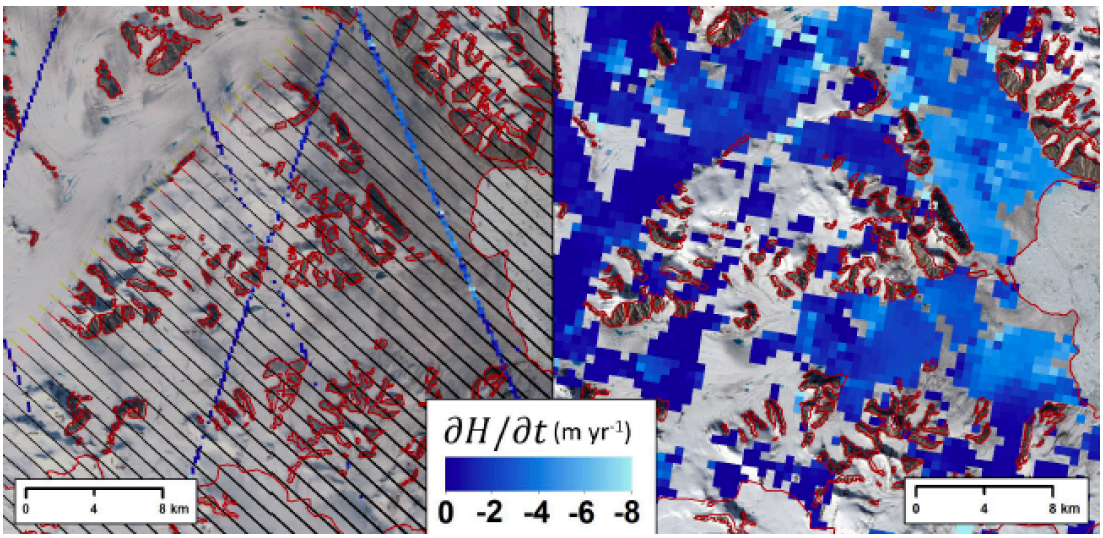


Figure 2.7: CryoSat-2 coverage along ice margins with rough topography. Gridded surface elevation change, $\dot{h}$, over Trinity-Wykeham Glacier, Nunavut, Canada. ICESat, 2003-2009 (left panel) for reference, and CryoSat-2, 2010-2017 (right panel). Source: Harcourt et al. (2019).

In addition to optimised satellite instrumentation and swath processing, CryoSat's orbital characteristics offer another critical advantage over alternative satellite platforms for the high-resolution surveying of land ice surfaces. CryoSat-2

orbits the Earth with a 369-day repeat period formed by the successive shift of a 30-day sub-cycle. The satellite has an inclination of 92° and a rapid increase in orbit cross-over density towards the poles, from 7.5 km inter-track distance at the Equator to less than 1.6 km at latitudes higher than ∼70° N/S (Gourmelen et al., 2018; Wingham et al., 2006). Altogether, sensor, orbital setup, swath altimetry, and the all-weather sampling capability of radar technology turn CryoSat-2 into a powerful tool for continuous large-scale high-resolution measurement of polar land ice. Despite this potential, swath altimetry has not been successfully applied previously at the pan-Arctic scale, an ambition that this thesis aims to rectify.

2.3.3 Global assessments of glacier and ice cap mass balance

At the start of this thesis in 2016, the most recent and comprehensive assessment of global glacier and ice cap mass change was by Gardner et al. (2013). The study reconciles altimetric, gravimetric and glaciological datasets for all regions worldwide (Figure 2.8).

Gardner et al. (2013) show that glacier and ice cap loss was ubiquitous during 2003–2009, with largest contributions from Arctic Canada (60 ± 6 Gt a^{-1} at 411 ± 39 kg m^{-2} a^{-1}), Alaska (50 ± 17 Gt a^{-1} at 570 ± 200 kg m^{-2} a^{-1}), coastal Greenland (38 ± 7 Gt a^{-1} at 420 ± 70 kg m^{-2} a^{-1}), the Andes (29 ± 10 Gt a^{-1} at 990 ± 360 kg m^{-2} a^{-1}), the Himalayas (26 ± 12 Gt a^{-1} at 220 ± 100 kg m^{-2} a^{-1}), Arctic Russia (11 ± 4 Gt a^{-1} at 210 ± 80 kg m^{-2} a^{-1}), Iceland (10 ± 2 Gt a^{-1} at 911 ± 150 kg m^{-2} a^{-1}) and Svalbard (5 ± 2 Gt a^{-1} at 130 ± 60 kg m^{-2} a^{-1}) (Table 2.1). Over this period, the global glacier and ice cap mass budget (including Greenland and Antarctic periphery) was -259 ± 28 Gt a^{-1} at -350 ± 40 kg m^{-2} a^{-1}, accounting for 29 ± 13 % of the observed sea level rise, equivalent to the combined contribution from both Greenland and Antarctic Ice Sheets during this time period (Gardner et al., 2013). The Arctic archipelagos' 2003-2009 mass imbalance represents 33 % of this total, 53 % if Alaska's losses

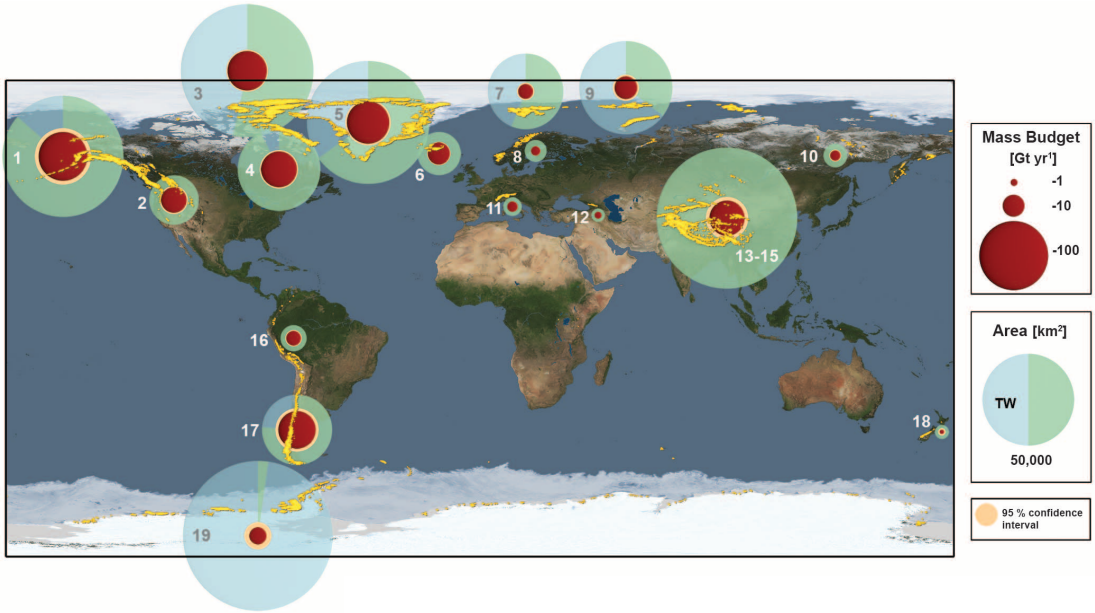


Figure 2.8: Regional glacier and ice cap mass budgets and surface areas. Yellow contours on the map denote areas covered by glaciers and ice caps - 19 glacier regions defined containing a total glaciated area of $\sim 729,400$ km^2 (Randolph Glacier Inventory, RGIv3, year 2000). Red circles show 2003-2009 regional glacier mass budgets with the corresponding 95 % confidence interval represented by the surrounding peach coloured halos (only visible for regions with large uncertainties). Pale blue/ green circles show regional glaciated areas with tidewater basin fractions (TW) in pale blue. Source: Gardner et al. (2013).

are added to the calculation (Table 2.1). Accelerated warming during the 2010s (Overland et al., 2017), in particular in the Barents and Kara Sea region (Lind et al., 2018) has likely reinforced the observed 2003-2009 Arctic glacier and ice cap mass imbalance. The next sections examine in more detail regional climate trends and the recent evolution of glaciers and ice caps across the Arctic.

2.4 Climatic controls on Arctic ice mass imbalance

Mass change across glaciers and ice caps is controlled by a range of driving mechanisms which can be revealed through the analysis of time series of ice mass change in conjunction with environmental data. Controls on glacier mass bal-

Table 2.1: Regional breakdown of glacier and ice cap mass budgets and glaciated areas. Numbers represent best 2003-2009 estimates with the 95 % confidence interval selected from the most suitable sampling methods for each region: GRACE (G), ICESat (I), glaciological (gl). For corresponding references see Gardner et al. (2013).

	Region	Total area (km^2)	Tidewater area (km^2)	Mass budget ($kg\ m^{-2}\ year^{-1}$)	Mass budget ($Gt\ year^{-1}$)	Method
1	Alaska	87,100	11900	−570 ± 200	−50 ± 17	G
2	Western Canada/United States	14,600	0	−930 ± 230	−14 ± 3	gl
3	Arctic Canada north	104,900	48,800	−310 ± 40	−33 ± 4	I, G
4	Arctic Canada south	40,900	3,000	−660 ± 110	−27 ± 4	I, G
5	Greenland	89,700	31,300	−420 ± 70	−38 ± 7	I
6	Iceland	11,100	0	−910 ± 150	−10 ± 2	G, gl
7	Svalbard	34,000	14,900	−130 ± 60	−5 ± 2	I, G
8	Scandinavia	2,900	0	−610 ± 140	−2 ± 0	gl
9	Russian Arctic	51,600	33,400	−210 ± 80	−11 ± 4	I, G
10	North Asia	3,400	0	− 630 ± 310	−2 ± 1	gl
11	Central Europe	2,100	0	−1060 ± 170	−2 ± 0	gl
12	Caucasus and Middle East	1,100	0	−900 ± 160	−1 ± 0	gl
13–15	HMA	118,200	0	−220 ± 100	−26 ± 12	I, G
16	Low latitudes	4,100	0	−1080 ± 360	−4 ± 1	gl
17	Southern Andes	29,400	7,000	−990 ± 360	−29 ± 10	G
18	New Zealand	1,200	0	−320 ± 780	0 ± 1	gl
19	Antarctic and sub–Antarctic	133,200	130,200	−50 ± 70	−6 ± 10	I
Total, excluding Greenland and Antarctic		506,600	119,000	−420 ± 50	−215 ± 26	
Global total		729,400	280,500	−350 ± 40	−259 ± 28	

ance range from internal dynamics to changes in boundary conditions at: **(a)** the ice-ocean interface via submarine melting and calving; **(b)** the ice surface and the atmospheric boundary layer through accumulation of snowfall and loss by surface melting and sublimation; and **(c)** the adjacent land margins such as at the ice bedrock interface where changes in friction and dynamic force balance can lead to variability in both melt rates and ice flow. It has been shown that seasonal surface melt input to the beds of glaciers via moulins and the occasional drainage of supraglacial lakes regulates basal water pressure and hence ice motion via hydrodynamic coupling (Das et al., 2008; Iken and Bindschadler, 1986; Tedstone et al., 2015). Furthermore, subglacial discharge reaching tidewater glacier fronts is thought to accelerate calving through enhancing submarine melt rates driven by convective plumes operating along the ice face of tidewater glacier termini (Straneo and Heimbach, 2013).

2.4.1 Arctic climate trends

According to the aforementioned mechanisms of ice loss, trends in air, sea surface and subsurface ocean temperatures are all potential forcing factors influencing surface, basal and frontal ablation and ice dynamics. Sea ice concentrations and the presence of ice mélange have also been implicated to impact calving rates and promote the acceleration of ice flow (Robel, 2017).

The Arctic region receives relatively low amounts of energy from the sun compared with low- and mid-latitudes. Snow, land- and sea ice play an important role in the region's radiative balance by reflecting back to space most of the incoming energy. Arctic sea ice volume and concentration have been declining over the past two decades, allowing for more solar heat to be absorbed by the ice-ocean system (Barber et al., 2017). Minimum Arctic sea ice extents in 2012 and 2016, and long periods of open water in the Barents and Kara Sea region were the result of increasing energy fluxes sourced from the Atlantic Ocean and reaching the Arctic Ocean's basins, bays and shelf seas (Barber et al., 2017).

The Arctic Ocean operates as a global heat pump, drawing in warm ocean water from the mid-latitudes, cooling it, and sinking it to the bottom of the ocean, thereby acting as a key driver of the thermohaline ocean circulation (e.g. AMAP, 2017; Weaver et al., 1999). Meltwater sources such as sea ice and glaciers and ice caps increase the freshwater budget of the Arctic Ocean, an imbalance that is transferred towards the Labrador Sea where freshening of the mixed surface layer slows down deep-ocean circulation by hampering density-driven subsidence and bottom-water formation (Thornalley et al., 2018; Yang et al., 2016). Finally, northward shift of Atlantic climate, or "Atlantification" (Figure 2.9), is currently accelerating (Årthun et al., 2012), promoting zonal and vertical heat fluxes, which are weakening ocean stratification (Polyakov et al., 2017).

Observations in recent decades show a clear link between rising global surface air temperatures and land and sea ice loss, a correlation that is particularly significant for regions north of the 60°N (AMAP, 2017). Meteorological records

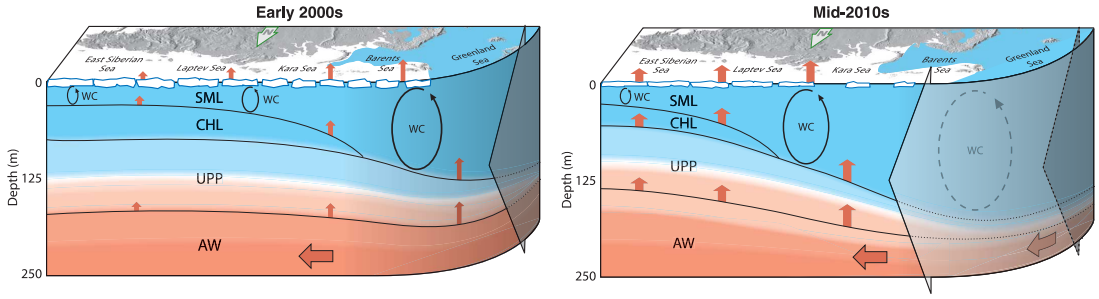


Figure 2.9: Conceptual model of "Atlantification". The black arrow extending from the right side across the vertical section shows the north-eastward progression, along the Eurasian continental slope, of a suite of processes associated with the northward shift of Atlantic Ocean forcing: (i) increased penetration of depth and surface signature Atlantic Water, (ii) reduction in sea ice cover (iii) greater vertical heat fluxes (red arrows) and ocean-atmosphere coupling. Acronyms denote ocean layers, processes or water masses, notably the surface mixed layer (SML), winter convection (WC) and Atlantic Water (AW). After Polyakov et al. (2017).

and atmospheric general circulation models show that mean annual surface temperatures in the Arctic have been increasing twice as fast as the global mean (Screen and Simmonds, 2010). This preferential warming trend known as polar temperature amplification (Park et al., 2018) is associated with a reduction in sea ice extent, decreasing land snow cover, earlier onset of the melt season, aerosols forcing, radiative effects in the atmosphere, and associated dynamic feedbacks (Park et al., 2018; Screen et al., 2012; Shindell and Faluvegi, 2009). In the Barents and Kara Sea region, self-perpetuating ice-ocean-atmosphere feedback loops have been acting to form a large Arctic warming hotspot (Lind et al., 2018), with average near surface air temperatures in excess of 7°C in January 2016 relative to 1981-2010 means (Overland et al., 2017), and ocean heat content in the upper 100 m increasing at 39 ± 9 MJ m^{-2} a^{-1} during 2010-2016 (Lind et al., 2018). The most prominent tropospheric warming in the Arctic since the beginning of the satellite era has occurred over Greenland and the Eastern Canadian Arctic (Ding et al., 2014). Much of this warming may be related to anomalous El Niño Southern Ocean (ENSO) activity (Ding et al., 2014). The following section summarises climatic trends and current assessments of ice loss briefly for each Arctic region.

2.4.2 Svalbard

Svalbard is an Arctic Archipelago located on the eastern flank of Fram Strait, between the Arctic Ocean, the Barents and the Greenland Seas (Figure 1.2). It is formed of five major islands, Spitzbergen, Nordaustlandet, Edgeøya, Baretsøya and Kvitøya, which have a large number of tidewater and valley glaciers, a few extensive ice fields, and eight ice caps, of which Austfonna on Nordaustlandet is the largest.

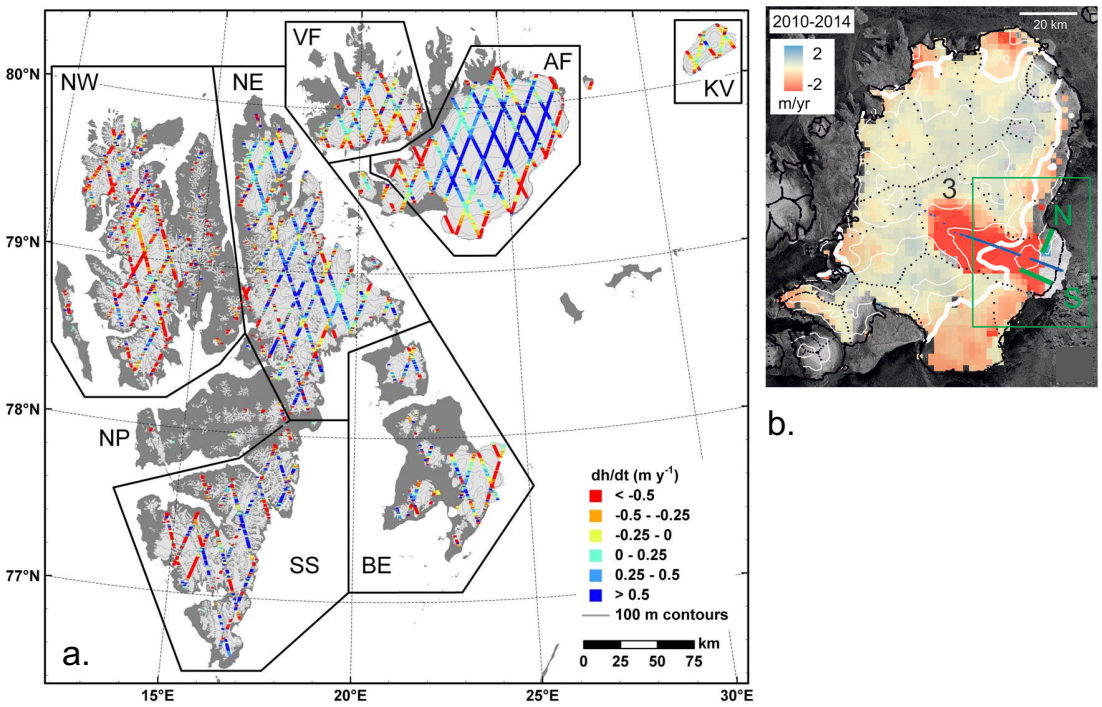


Figure 2.10: Svalbard's glaciers and ice cap surface elevation change measured from space. ICESat 2003-2009 tracks **(a)**, and CryoSat-2 2010-2014 swath over Austfonna **(b)**. Austfonna's Basin 3 is denoted with the number (3). Source: McMillan et al. (2014) and Moholdt et al. (2010).

Spitzbergen is the most alpine of the Svalbard islands with a maximum elevation of 1717 m above sea level, while the ice caps are marked by smooth surface slopes with maximum elevations between 450 and 800 m above sea level. Svalbard's glaciers and ice caps are considered to be polythermal (Björnsson et al., 1996), with 60 % of the ice masses draining into tidewater glaciers (Blaszczyk et al., 2009), which often terminate in elongated fjords and embayments. Glacier

mass balance is controlled by both surface processes and marine forcing and was estimated at -5 ± 2 Gt a^{-1} between 2003 and 2009 from gravimetry (GRACE) (Jacob et al., 2012) and laser altimetry (ICESat) (Moholdt et al., 2010) (Table 2.1). There is high interannual variability in surface mass balance across the archipelago, driven mainly by weather patterns associated with modes of large-scale atmospheric circulation, principally the Arctic (AO) and the North Atlantic Oscillation (NAO), whereby summer melting rather than winter accumulation is the main factor controlling variability (Box and Sharp, 2017). A number of flow instabilities have been observed at some of Svalbard's marine-terminating ice cap margins, most notably Austfonna's Basin 3 (Figure 2.10b), which experienced a 45-fold increase in discharge since the mid 1990s, with maximum rates of thinning > 25 m a^{-1} across the basin (McMillan et al., 2014).

2.4.3 The Russian Arctic

The Russian Arctic comprises three archipelagos, Novaya Zemlya, Franz Josef Land and Severnaya Zemlya (Figure 2.11). Novaya Zemlya's elongated shape forms a natural border between the Barents and the Kara Seas to the west and east, respectively. Its northernmost island, Severny, is covered by a large ice cap and numerous mountain glaciers and is separated from the largely ice-free Yuzhny Island further south by the narrow Matochkin Strait. Franz Josef Land and Severnaya Zemlya are composed of several islands, with both archipelagos stretching south of the continental margin between the Eurasian Shelf Seas and the Eurasian Basin of the Arctic Ocean (Figure 1.2).

The region is marked by a strong east-west temperature and precipitation gradient, with a warmer and wetter climate in the southwest becoming progressively colder and drier moving northeast (Moholdt et al., 2012b). Accordingly, mass imbalance between 2004 and 2009 was more negative in Novaya Zemlya (-7.1 ± 1.2 Gt a^{-1} at -321 ± 54 kg m^{-2} a^{-1}) compared with Severnaya Zemlya (-1.4 ± 0.9 Gt a^{-1} at -84 ± 54 kg m^{-2} a^{-1}) and Franz Josef Land (-0.6 ± 0.9 Gt a^{-1} at -47 ± 71

kg m^{-2} a^{-1}) (Moholdt et al., 2012b). During the 2000s, Novaya Zemlya was the region with the greatest ice mass loss from the entire Eurasian Arctic. Russian Arctic glaciers and ice caps are experiencing currently rapid climate transitions due to ongoing Atlantification (Lind et al., 2018; Polyakov et al., 2017), are one of the most understudied regions of the Arctic, and are the focus of Chapter 5 in this thesis.

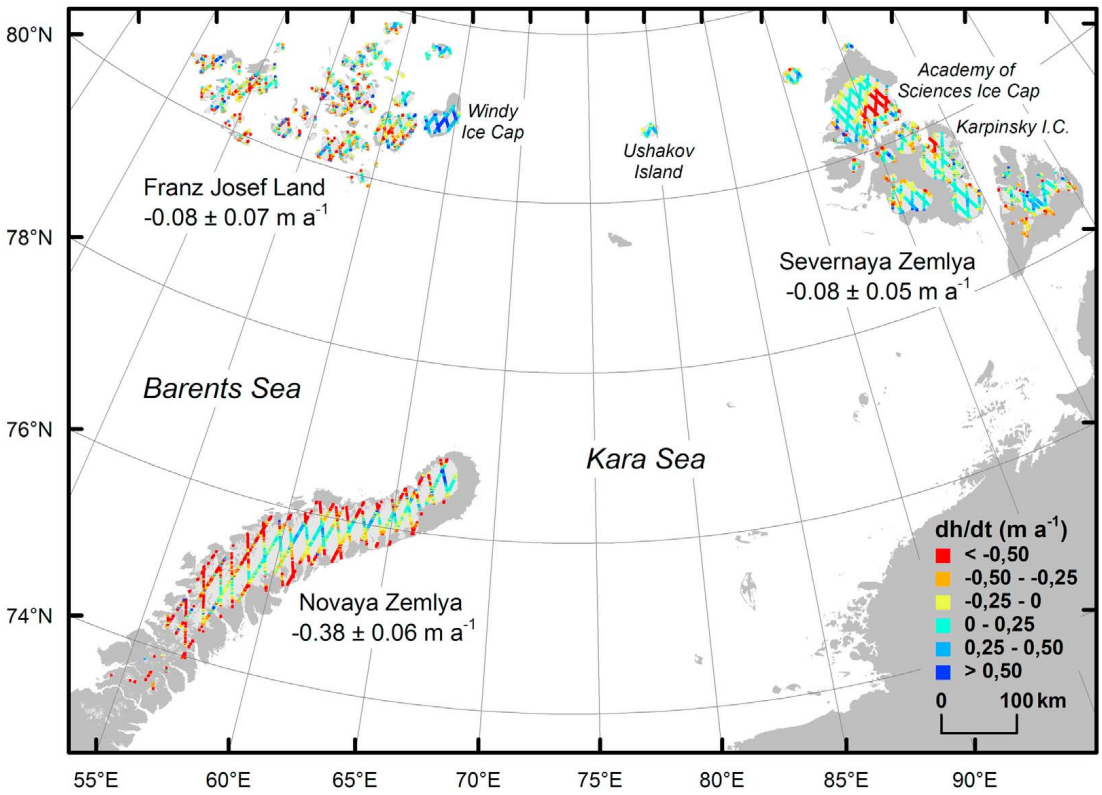


Figure 2.11: The Russian Arctic's 2003-2009 glacier and ice cap surface elevation change from ICESat. Source: Moholdt et al. (2012b).

2.4.4 Iceland

Owing to Iceland's geographic location in the subpolar North Atlantic, the island's six main ice caps are under the influence of strong maritime climate patterns, characterised mainly by large annual rates of accumulation (Figure 2.12). This position makes the ice caps highly sensitive to shifts in both Arctic and Atlantic climate. Mass balance fluctuations are driven largely by surface processes,

which are superimposed on episodes of glacier surging, and dynamic and ablative ice loss triggered by subglacial volcanic activity and geothermal heat convection (Foresta et al., 2016).

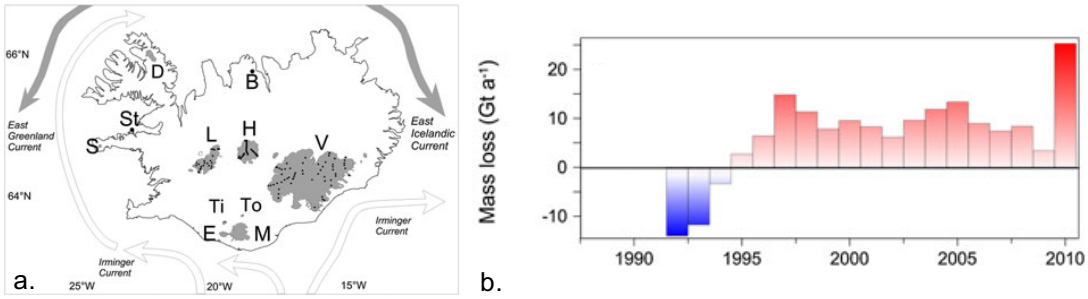


Figure 2.12: Icelandic ice caps (a) and their mass balance (b). Icelandic ice caps are: Vatnajökull (V), Langjökull (L), Hofsjökull (H), Mýrdalsjökull (M), Eyafjallajökull (E), Drangajökull (D). After Björnsson et al. (2013)

Estimates of glacier mass change between 2003 and 2009 from spatial interpolation of glaciological and local geodetic measurements by (Cogley, 2009) (-9 ± 2 Gt a^{-1}) agree well with gravimetric records by (Jacob et al., 2012) (-11 ± 3 Gt a^{-1}) from the same time period (Gardner et al., 2013). Foresta et al. (2016), using CryoSat-2 swath altimetry, estimated a rate of loss from 2010 to 2016 of 5.8 ± 0.7 Gt a^{-1}, equating to a ~ 40 % decrease compared to the ICESat period (Gardner et al., 2013) (Table 2.1).

2.4.5 The Canadian Arctic

The Canadian Arctic Archipelago is an extensive glaciated region located off the western and northwestern shores of Greenland (Figures 2.13 and 1.2). Its large ice caps, ice fields and mountain glaciers contain 39 % of the global volume of land ice outside Greenland and Antarctica (Farinotti et al., 2019).

The region experiences minimal interannual variability in precipitation and hence ice loss is largely dominated by summer air surface temperatures, with only small contributions (8-10 %) from ice discharge (Gardner et al., 2011; Millan et al., 2017). This is in strong contrast to forcings and mechanisms of ice loss across the Eurasian part of the Arctic, where complex climate dynamics involving sea

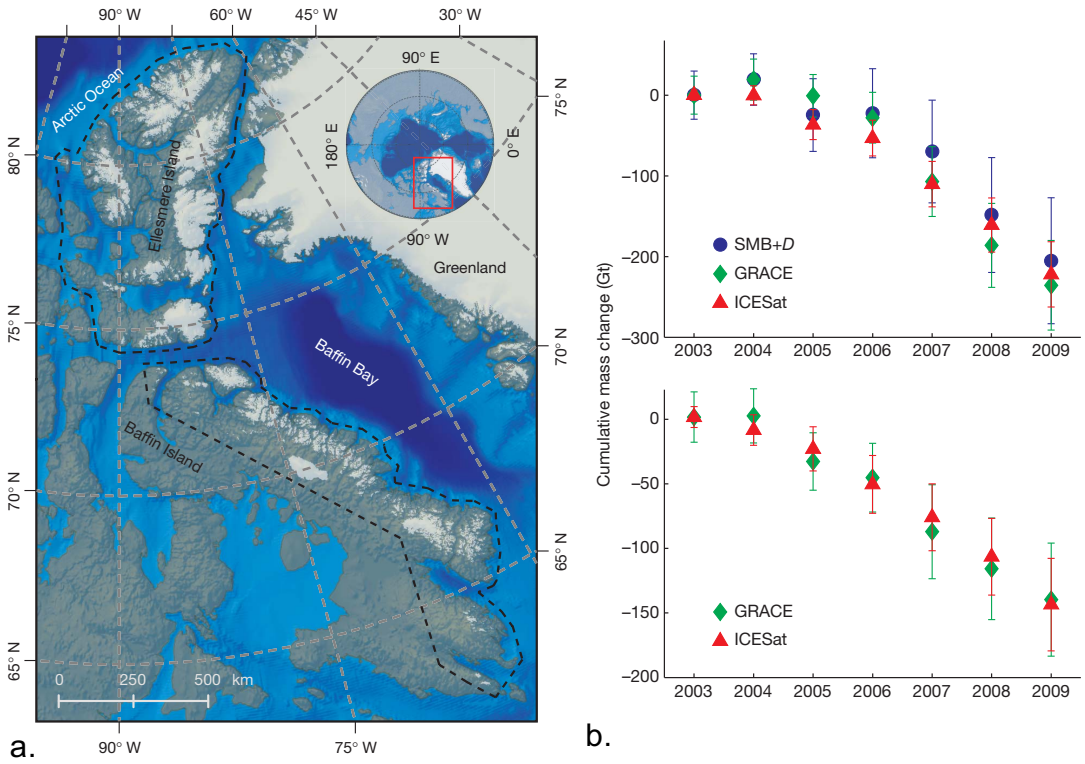


Figure 2.13: Canadian Arctic glaciers and ice caps (a) and time series of mass change (b), 2003–2009. After Gardner et al. (2011).

ice behaviour, meteorology and ocean currents are all factors playing a key role in inter-annual and decadal mass balance fluctuations. It has been demonstrated that the Arctic and North Atlantic Oscillations are correlated with July surface air temperatures and ice cap mass budgets in the Canadian Arctic (Gardner and Sharp, 2006). Modelling experiments have also shown that mean tropospheric warming in northeast Canada and Greenland are likely impacted by circulation anomalies extending from the tropical Pacific to Greenland and driven by an ENSO signature in sea surface temperatures (Ding et al., 2014). There is a strong negative trend in mass balance observed after 2005 (Figure 2.13b), which is in direct response to a shift towards warmer surface air temperatures during summer (Gardner et al., 2011). Mass imbalance in the northern and southern Canadian Arctic was -310 ± 40 kg m^{-2} a^{-1} and -660 ± 110 kg m^{-2} a^{-1} respectively during 2003-2009 (Gardner et al., 2013), reflecting a strong latitudinal control on air temperatures and ice loss.

2.4.6 Alaska

Alaskan glaciers and ice fields are among the Earth's continental ice masses with the highest rates of annual loss. According to Gardner et al. (2013), these were on average 50 ± 17 Gt a^{-1} at 570 ± 200 kg m^{-2} a^{-1} between 2003 and 2009 (Table 2.1), although estimates vary considerably depending on the sampling instrument and method applied. For example, there are large differences between glaciological (72 ± 22 Gt a^{-1}) and gravimetric estimates of loss (42 ± 11 Gt a^{-1}) for the same time period. These disparities reflect the sparse data and large satellite footprints (Gardner et al., 2013). Alaska and the North American Cordillera are an example of ice masses characterised by extreme topography with steep surface gradients, which presents significant challenges for satellite altimetry, including CryoSat-2. Due to these issues with poor data coverage, this region was not considered for processing and analysis in this thesis.

2.5 Longer-term Arctic climate records and land ice change

The Arctic has experienced rapid acceleration of ice loss over the past few decades (Slater et al., 2021). Determining the extent to which this trend is anomalous with respect to longer-term climate variability is essential in order to gain a broader understanding of the evolution of Arctic glaciers and ice caps.

The history of glaciation since the end of the Pleistocene (12 ka before present) reconstructed from radiocarbon, terrestrial cosmogenic nuclide, and optically stimulated luminescence geochronology, indicates rapid glacier retreat in Svalbard during the early Holocene ($12.0 - 11.0$ ka before present), followed by a period of ca. $6.0 - 7.0$ ka characterised by reduced fjord glaciation and numerous ice-free basins (Farnsworth et al., 2020). Subsequently, increased sedimentation rates and sediment transport from a large number of catchments, from 4.0 to 0.5 ka before present, are associated with late Holocene glacier expansion over

Svalbard (Farnsworth et al., 2020). This is consistent with upper and northern tree line reconstructions (Nicolussi and Schlüchter, 2012; Öberg and Kullman, 2011) suggesting widespread, long-term glacier advances across the entire northern hemisphere during the second half of the Holocene (Solomina et al., 2015). Holocene glacier fluctuations in the northern hemisphere are believed to be primarily driven by orbital forcing superimposed by higher frequency forcing such as periods of low solar- and increased volcanic activity during the mid-to late Holocene (Solomina et al., 2015).

Neoglacial glacier advances culminated during the Little Ice Age (LIA, ca. 1300-1850, e.g. Grove, 1988), followed by a period of warming and unusual glacier behaviour during the last century. Over the last few decades in particular, persistent Arctic-wide glacier retreat has been inconsistent with the current interval of orbital forcing, which favours mass gains rather than ubiquitous ice losses (Solomina et al., 2015). For example, paleoclimate reconstructions from ice core data indicate that mass loss from Arctic Canada's ice caps has been higher since the 1990s than at any time during the last 4200 years (Fisher et al., 2012). Some studies argue that current melt rates in Arctic Canada may not have been exceeded since the interval of rapid deglaciation following the Younger Dryas ca. $11.5-9.0$ ka before present (Kaufman et al., 2004; Miller et al., 2013). In the Eurasian Arctic, ice core records are available from the archipelagos of Severnaya Zemlya (e.g. Opel et al., 2013), Franz Josef Land (Henderson, 2002) and Svalbard (Isaksson et al., 2001; Watanabe et al., 2001). The $\delta^{18}O$ record from the Akademii Nauk ice core (Severnaya Zemlya, Russian Arctic) shows evidence of episodic decadal temperature changes over the last 1100 years in the Barents-Kara Sea region, superimposed on a multi-century, late Holocene cooling trend, which ended during the final stages of the LIA around 1800 (Opel et al., 2013). The relatively short-lived cycles marked by abrupt shifts in surface air temperature trends may have been caused by changes in Atlantic water transport, atmospheric circulation patterns and sea ice feedbacks (Opel et al., 2013).

The more recent evolution of Arctic glaciers and ice caps is documented by

glaciological measurements starting roughly after the first International Polar Year in 1882-1883, during a time when Svalbard increasingly became a natural laboratory for glaciological studies (Farnsworth et al., 2020), although earlier records of frontal advance and retreat also exist (Zeeberg and Forman, 2001, e.g. Petersen Glacier, Novaya Zemlya, 1871–1993). Mass balance time series starting in the 1930s, and more consistently after the second World War, were constructed from in situ measurements of a large number of Arctic glaciers and ice caps, such as: Austre Brøggerbreen, Finsterwalderbreen and Bertilbreen (Svalbard); Decade Glacier, Meighen Ice Cap, Devon Ice Cap and White Glacier (Arctic Canada); Obruchev Glacier, Shokal'skogo Glacier, Vavilov Ice Cap (Arctic Russia); Hofsjökull and Tungnarjökull (Iceland) (Dowdeswell et al., 1997).

Generally, mass balance trends and terminus position sequences across the Arctic are consistent with concurrent surface air temperature records indicating a general warming trend since the end of the Little Ice Age, and accelerated warming since roughly the 1990s (Solomina et al., 2015). Intense and sustained melt rates across Greenland and Canada's Queen Elizabeth Islands during the early 21^{st} century were caused by the most prominent tropospheric warming in the Arctic since 1979 (Ding et al., 2014). This warming trend is likely due to the presence of sustained high atmospheric pressure systems (Bezeau et al., 2015; McLeod and Mote, 2016; Rajewicz and Marshall, 2014), driven primarily by a negative trend in the North Atlantic Oscillation (NAO) phase index (Ding et al., 2014). This pattern could not be reproduced by Coupled Model Intercomparison Project Phase 5 (CMIP5) simulations prescribed with anthropogenic forcing (Box and Sharp, 2017; Ding et al., 2014), suggesting that a considerable fraction of recent accelerated warming in this region results from natural climate variability (Ding et al., 2014).

In the Eurasian Arctic, land ice change and climate dynamics are modulated by the presence of sea ice and by North Atlantic oceanic heat flux, in addition to NAO-related atmospheric circulation (Bartels et al., 2017; Zeeberg et al., 2003). Similar to the surface air temperature trend in Greenland and Nunavut Canada,

the eastern Arctic experienced strong warming since the early 2000s compared to the preceding decades (e.g. Lind et al., 2018). For example, Novaya Zemlya's glaciated area was reduced significantly, by 812.6 ± 2.7 km^2, between 1952 and 2015, with losses from both land- and marine terminating ice cap basins. Accelerated warming since the early 2000s caused Novaya Zemlya's areal retreat rate to double during 2001-2015 (20.3 km^2 a^{-1}) compared to the period between 1952 and 2001 (10.8 km^2 a^{-1}) (Box and Sharp, 2017). The $\delta^{18}O$ data from Akademii Nauk ice core in Severnaya Zemlya reveal significant warming at the beginning of the 20^{th} century, with surface air temperatures reaching a maximum in the 1930s (Opel et al., 2009). Since 1930, increased warming during the melt season in particular resulted in a decrease in sea ice extent and amplified regional evaporation from the Kara Sea (Opel et al., 2009), which likely led to enhanced accumulation rates over Severnaya Zemlya's ice caps (Sánchez-Gámez et al., 2019). In Svalbard, a comparison between surface elevation changes from satellite altimetry and losses derived from older topographic maps indicates rates of mass loss up to two times higher from 1990 to 2005 compared to the period between 1936 and 1990, depending on the region (Nuth et al., 2010). Since the end of the Little Ice Age, Icelandic ice caps experienced relatively high loss rates during the 1930s and 1940s, followed by a four-decade long slowdown and a substantial acceleration after the mid-1990s (Björnsson et al., 2013).

2.6 Projections of future mass loss

Mean sea level is projected to continue to rise during the 21^{st} century due to global warming, with large contributions from both thermal expansion and glacier and ice cap shrinkage (Meier et al., 2007), and smaller contributions from the Greenland and Antarctic Ice Sheets (Gardner et al., 2013; Raper and Braithwaite, 2006), although revisions now suggest that Greenland is likely to become the main contributor to 2000-2100 sea level rise under both RCP4.5 and RCP8.5 climate scenarios (Box and Colgan, 2017). The Barents and Kara Sea region is

expected to continue to experience highest rates of warming in the Arctic under both scenarios, with surface air temperature changes during winters of the 2050s decade > 7°C compared to 1986-2005 baseline means (Appendices, Figure 2.15).

Projections are forced according to estimated future greenhouse gas emissions and climate change scenarios. For climate models to correctly forecast continental ice response to these parametrised forcings, it is essential that parameters playing a key role in the mechanisms of ice loss are correctly represented. Incomplete bed topography and fjord bathymetry, two essential elements for constraining the physical boundaries of the ice masses both for modelling their flow and determining the impact of ocean circulation on tidewater glacier dynamics are lacking at the global scale (Box and Sharp, 2017). The largest uncertainties currently leading to a wide spectrum of modelled ice responses to climate fluctuations are due to poor understanding of glacier dynamics and its drivers (Enderlin et al., 2014; Nick et al., 2013; Pfeffer et al., 2008). While surface mass balance has been successfully modelled (see review article by Lenaerts et al., 2019) over Greenland (Fettweis et al., 2013; Noël et al., 2016), the Canadian Arctic (Lenaerts et al., 2013), Patagonia (Lenaerts et al., 2014), and Antarctica (Agosta et al., 2019) using RACMO and MAR regional climate models, the mechanisms controlling variations in ice discharge remain elusive (Straneo and Heimbach, 2013), and the future relative contributions of ice dynamics versus surface mass balance to total mass loss are therefore highly uncertain (McMillan et al., 2014; Pfeffer et al., 2008). Until recently, most studies advocated that surface processes likely dominated mass loss over discharge and calving both presently and into the future (Enderlin et al., 2014; Nick et al., 2013; Price et al., 2011). More recently however, Mouginot et al. (2019) have postulated that glacier dynamics controlled 66 % of Greenland mass loss during 1972-2018, with surface mass balance responsible for the remaining 34 %. This emphasises a potentially even higher error factor associated with future sea level projections and highlights once more the importance of correct parametrisation of ice flow in climate models for reducing these uncertainties.

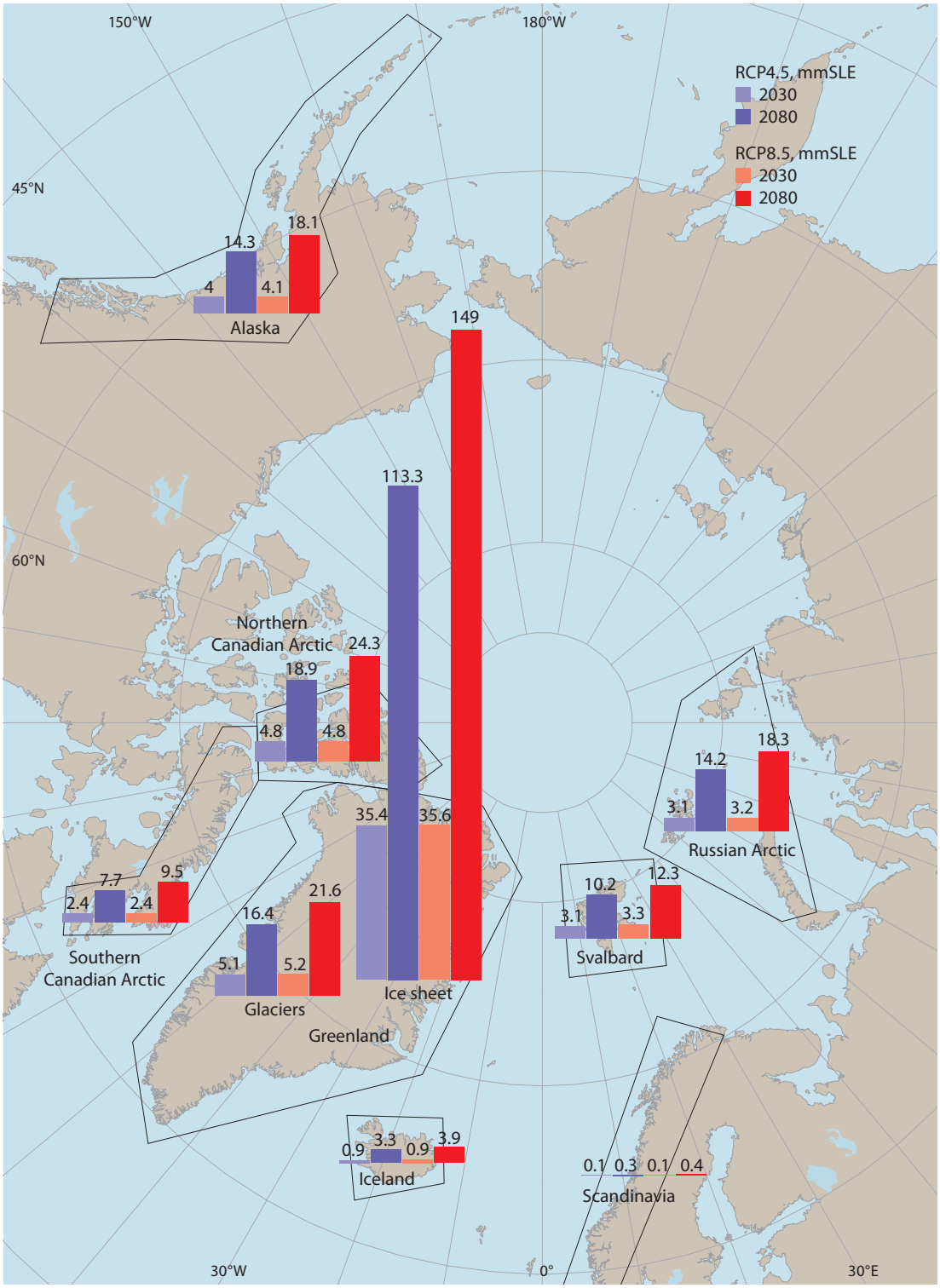


Figure 2.14: Projected land ice loss from different Arctic regions in 2030 and 2080 under RCP4.5 and RCP8.5 climate scenarios. Future ice losses are expressed in millimetres sea level equivalent (SLE). After Box and Colgan (2017).

2.7 Summary of knowledge gaps

Recent scientific advances show that the temporal and regional disparities in the rates and drivers of cryospheric change in the Arctic are poorly constrained. A range of specific gaps in knowledge related to these rates and drivers were identified in the previous sections of this chapter.

Sections 2.1 and 2.2 highlighted the important contribution of glaciers and ice caps to ongoing sea level change and identified Arctic land ice outside of Greenland as a key component of ice loss and meltwater delivery to the world's oceans. A quantitative assessment of this contribution from smaller Arctic ice masses is associated with large uncertainties due to large data gaps resulting from incomplete satellite coverage.

Section 2.3 identified swath interferometric altimetry and CryoSat-2's dense orbital tracks as a potentially groundbreaking approach for estimating high-resolution mass balance at a pan-Arctic scale, including over many areas characterised by rough topography. If successful, this novel approach provides a potential step-change in our ability to drastically reduce uncertainties on mass budget trends through obtaining unprecedented measurements at high density of ice surface elevation and mass change.

Section 2.4 described the Arctic climate system with a breakdown by sub-region and identified important links between observed mass imbalance and decadal climate trends and anomalies, in particular in the archipelagos of the Barents and Kara Seas. This is a region witnessing complex interactions between the cryosphere, the ocean and the atmosphere over different time scales, and with a high degree of regional variability and uncertainty over the relative impact that each of these Arctic climate system components have on environmental change. Elucidating some of these complexities is necessary to better apprehend regional and temporal variability in response of land ice to forcing, to better predict future climate transitions, and to identify potential tipping elements in the Earth's climate system.

Section 2.6 reviewed the current limitations of climate models in projecting future sea level rise. Partitioning continental ice loss into surface ablation and ice discharge is an essential gap in knowledge that needs to be addressed in order to improve parametrisations of dynamic flow in ice sheet models. Ice dynamics have led to massive destabilisations of glacier and ice cap basins in the Eurasian Arctic over the past decade. Associated acceleration and thinning are currently difficult to predict and are likely to increase in number and scale in a warming Arctic, with possibly abrupt shifts in mass balance, and significant future contributions to sea level rise.

2.8 Research questions and thesis structure

This project aims to address these knowledge gaps in an attempt to better quantify and improve our understanding of Arctic glaciers and ice cap evolution and drivers. By processing and analysing new satellite altimetry acquisitions and climate data, the thesis seeks to address the following critical questions and objectives:

- Investigate to what extent swath interferometry can be exploited and applied to Arctic glaciers and ice caps, with the purpose of improving both spatial and temporal sampling density at the ice surface, and hence drastically reduce uncertainties in the estimation of mass imbalance and sea level change (Chapter 3);
- Produce high-resolution maps of surface elevation change over areas sampled by the CryoSat-2 satellite, thereby providing a detailed picture of the response of glaciers and ice caps to climate forcing across the Arctic (Chapter 4);
- Generate an unprecedented record of high-resolution mass budget of Arctic land ice outside of Greenland (Chapter 4);
- Investigate how the high-density measurements of mass change can be used to separate the mechanisms of mass loss into either surface processes or ice

dynamics (Chapter 4);

- Produce, for the first time, robust, high-resolution time series of surface elevation change over the Russian Arctic's glaciers and ice caps, an understudied region that is critically exposed to current Arctic climate transitions (Chapter 5);
- Analyse time series of elevation change in conjunction with climate data reanalyses to investigate the potential impact of Arctic climate variability on the evolution of glaciers and ice caps in the Barents and Kara Sea region (Chapter 5).

To address these questions individually, the following thesis structure is proposed:

Chapter 3 describes in detail all the methodologies developed and applied to collect, process and analyse CryoSat-2 altimetry. This includes swath processing and CryoSat-2 product validation, data filtering and noise reduction, gridding, time series, volume change and mass balance computations, error analysis, quality control, evaluation and assembly of supplementary material such as glacier outlines, digital elevation products and regional climate models. Methodology related specifically to climate data analysis is detailed in Chapters 4 and 5.

Chapter 4 uses a novel swath algorithm to process CryoSat-2 interferometric altimetry and produce Arctic-wide maps of mean 2010-2017 ice surface elevation change. Elevation change rates from seven Arctic regions (southern and northern Canadian Arctic, Novaya Zemlya, Severnaya Zemlya, Franz Josef Land, Svalbard, and Iceland) are used individually to calculate volume change and estimate mass balance over the sampling period. The high-density measurement field is utilised further to partition ice losses into contributions from land- and marine-terminating glacier basins, and into signals associated with meteorology and ice flow. The chapter finally discusses possible connections between Arctic glacier change and concurrent Arctic-wide climatic trends.

Chapter 5 explores further the relationship between Arctic climate dynamics and decadal ice thinning and mass loss in the Eurasian Arctic, a region currently

undergoing rapid climatic transitions. The chapter builds on the methodologies developed for the pan-Arctic assessment in Chapter 4, and one year of additional satellite measurements to build 90-day sequences of surface elevation change for GICs in Novaya Zemlya and Severnaya Zemlya, in the Russian Arctic. These are analysed in conjunction with anomalies and trends in near surface air and ocean temperatures, as well as sea ice concentrations, to gain a more in-depth understanding of how climate change relates to ice mass loss in the Barents and Kara Sea region. The work in Chapter 5 is entirely my own, with advice and guidance from Professor Pete Nienow. George Malczyk implemented important improvements to the time series calculation method.

Chapter 6 synthesises the main findings of the thesis, reviews the main limitations of the research conducted in Chapters 3-5, and offers recommendations for future work.

In addition to the material presented in Chapters 3-5, I also contributed with data acquisition and processing, as well as edits to the following peer-reviewed articles:

Slater, T., Lawrence, I. R., Otosaka, I. N., Shepherd, A., Gourmelen, N., Jakob, L., Tepes, P., Gilbert, L., and Nienow, P. (2021). Review Article: Earth's ice imbalance. In: *Cryosphere*, 15, 233-246. doi.org/10.5194/tc-15-233-2021.

Harcourt, W. D., Palmer, S. J., Mansell, D. T., Brocq, A. Le, Bartlett, O., Gourmelen, N., Tepes, P., et al. (2019). Subglacial controls on dynamic thinning at Trinity-Wykeham Glacier, Prince of Wales Ice Field, Canadian Arctic. In: *International Journal of Remote Sensing*, 41(3), 1191-1213. doi.org/10.1080/01431161.2019.1658238.

Zheng, W., Pritchard, M. E., Willis, M. J., Tepes, P., Gourmelen, N., Benham, T. J., and Dowdeswell, J. A. (2018). Accelerating glacier mass loss on Franz Josef Land, Russian Arctic. In: *Remote Sensing of Environment*, 211, 357-375. doi.org/10.1016/j.rse.2018.04.004.

2.9 Appendices

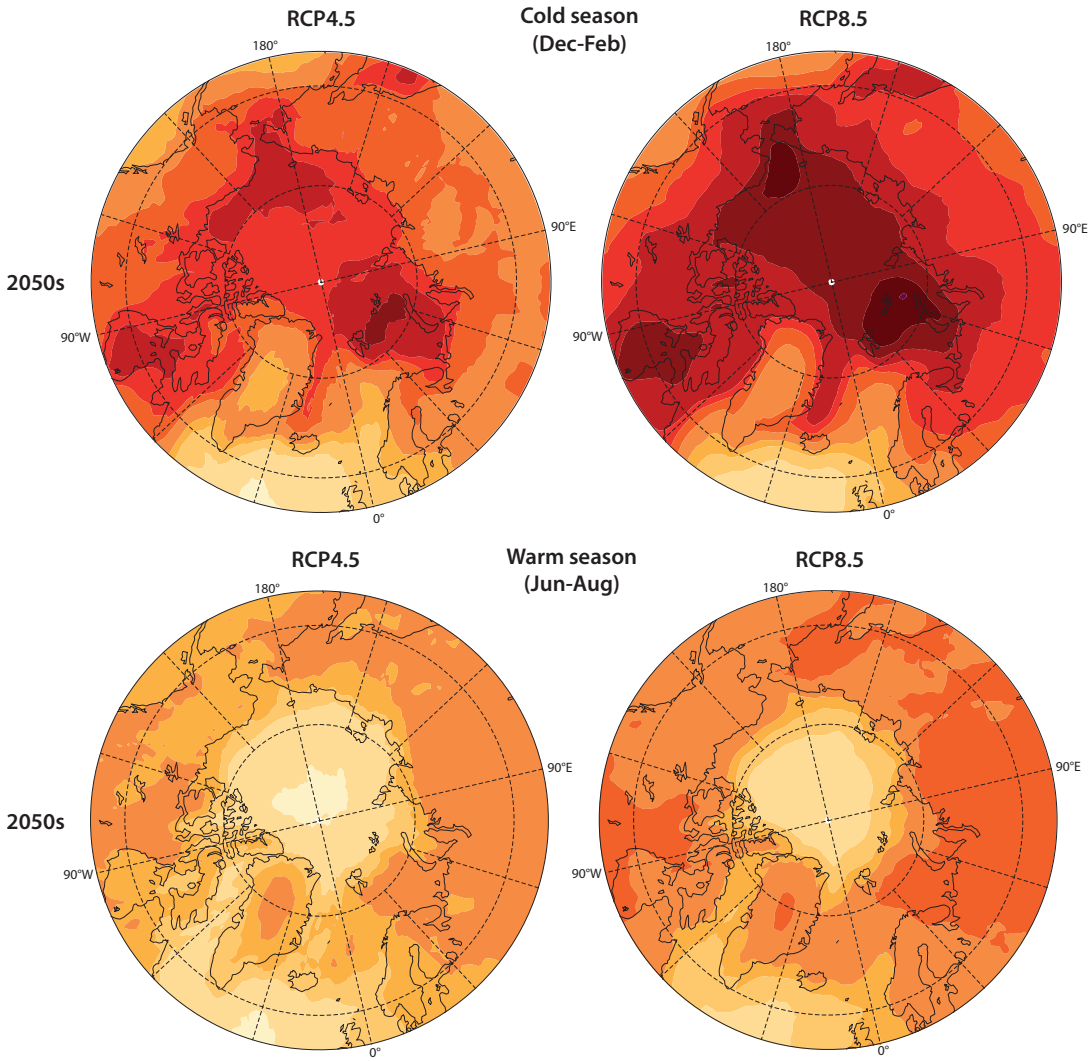


Figure 2.15: Projected changes in near surface air temperature. Projections are for the 2050s relative to the 1986-2005 baseline under different RCP climate scenarios. After Overland et al. (2017).

Table 2.2: Number of glaciers, area, ice volume and sea level equivalent (SLE) by region. After Farinotti et al. (2019).

Table 1 | Regionally aggregated summary statistics for the provided results

RGI region	*N*	*A* (km²)	*V* (10^3 km³)	$\bar{h}$ (m)	SLE (mm)	BSL (%)
01 Alaska	27,108	86,677	18.98 ± 4.92	218	43.3 ± 11.2	5.4
02 Western Canada and United States	18,862	14,629	1.06 ± 0.27	72	2.6 ± 0.7	0.0
03 Arctic Canada North	4,549	104,920	28.33 ± 7.35	270	64.8 ± 16.8	5.3
04 Arctic Canada South	7,422	40,860	8.61 ± 2.23	210	20.5 ± 5.3	1.3
05 Greenland periphery	19,306	89,651	15.69 ± 4.07	175	33.6 ± 8.7	11.3
06 Iceland	567	11,052	3.77 ± 0.98	341	9.1 ± 2.4	0.2
07 Svalbard	1,615	33,932	7.47 ± 1.94	220	17.3 ± 4.5	4.1
08 Scandinavia	3,417	2,947	0.30 ± 0.08	101	0.7 ± 0.2	0.0
09 Russian Arctic	1,069	51,551	14.64 ± 3.80	283	32.0 ± 8.3	9.5
10 North Asia	5,144	2,399	0.14 ± 0.04	56	0.3 ± 0.1	0.0
11 Central Europe	3,927	2,091	0.13 ± 0.03	61	0.3 ± 0.1	0.0
12 Caucasus and Middle East	1,887	1,305	0.06 ± 0.02	48	0.2 ± 0.0	0.0
13 Central Asia	54,429	49,295	3.27 ± 0.85	66	7.9 ± 2.0	0.0
14 South Asia West	27,986	33,561	2.87 ± 0.74	85	6.9 ± 1.8	0.0
15 South Asia East	13,119	14,734	0.88 ± 0.23	59	2.1 ± 0.5	0.0
16 Low latitudes	2,940	2,341	0.10 ± 0.03	42	0.2 ± 0.1	0.0
17 Southern Andes	15,908	29,368	5.34 ± 1.39	181	12.8 ± 3.3	0.7
18 New Zealand	3,537	1,161	0.07 ± 0.02	63	0.2 ± 0.0	0.0
19 Antarctic and subantarctic[a]	2,751	132,771	46.47 ± 12.06	349	69.4 ± 18.0	38.1
Total	215,543	705,253	158.17 ± 41.03	224	324.3 ± 84.1	15.1

[a]As the Antarctic ice sheet is not included in this region, we refer to it as to the Antarctic periphery throughout the manuscript. The number of considered glaciers (*N*) and their area (*A*) is given together with the regional glacier volume (*V*) and the corresponding average ice thickness ($\bar{h}$). The potential sea-level equivalent (SLE) accounts for the ice portion presently located below sea level (BSL). All numbers refer to the composite solution.

Table 2.3: Global land ice contributions to sea level rise during 2004-2010. After Box and Colgan (2017).

Region	Mass balance, Gt/y	Uncertainty, Gt/y	Global fraction	Start year	End year	Method(s)	Source
Greenland ice sheet	-225	26	40.8%	2005	2010	altimetry, gravimetry, input-output	Shepherd et al. (2012) Gardner et al. (2013)
Canadian Arctic (3,4)	-60	8	10.9%	2003	2009	altimetry	Gardner et al. (2013)
Alaska (1)	-50	17	9.1%	2003	2009	altimetry	Gardner et al. (2013)
Greenland glaciers (5)	-38	7	6.9%	2003	2008	altimetry	Gardner et al. (2013)
Iceland (6)	-10	2	1.8%	2004	2011	altimetry	Matsuo and Heki (2013), Gardner et al. (2013), uncertainties from latter
Russian Arctic (9)	-7	4	1.3%	2004	2012	altimetry	Matsuo and Heki (2013), uncertainties from latter
Svalbard (7)	-4	2	0.7%	2004	2012	altimetry	Matsuo and Heki (2013), uncertainties from latter
Scandinavia (8)	-2	0	0.4%	2003	2009	altimetry	Gardner et al. (2013)
Arctic ice	-396	66	71.7%				
West Antarctic ice sheet	-102	18	18.5%	2005	2010	altimetry, gravimetry, input-output	Shepherd et al. (2012)
Antarctic peninsula	-36	10	6.5%	2005	2010	altimetry, gravimetry	Shepherd et al. (2012)
East Antarctic ice sheet	58	31	-10.5%	2005	2010	altimetry, gravimetry, input-output	Shepherd et al. (2012)
Non-Arctic or Antarctic glaciers (10–18)	-76	25	13.8%	2003	2009	altimetry	Gardner et al. (2013)
Non-Arctic ice	-156	84	28.3%	2004	2010	average	Gardner et al. (2013)
Global, Gt/y	-552	150					
Global, mm/y	-1.5	0.4					

Chapter 3

Methods

This chapter presents in detail the methodological steps developed and implemented during the course of the thesis. Elements developed by third parties prior to or during the thesis are also described where necessary to guide the reader in understanding workflow and data processing (Figure 3.1). Additional methodological information specific to analyses undertaken in Chapters 4 and 5 is provided directly in those chapters.

All computational processes were run on a local server with the exception of the swath processing, which was performed on the University of Edinburgh supercomputing cluster.

3.1 Study region: Arctic glacier inventory

At the start of the thesis, glaciers and ice caps of the following Arctic and sub-Arctic regions were considered for study: Iceland (Ic), Svalbard (Sv), the Russian Arctic Archipelagos of Novaya Zemlya (NZ), Severnaya Zemlya (SZ) and Franz Josef Land (FJL), the southern and northern Canadian Arctic Archipelagos of Nunavut (CAA-S and CAA-N), the glaciers and ice fields of Alaska (Al), and the mountain glaciers of the American Cordillera (AA). The last two regions (Al and AA) were subsequently excluded from any detailed analysis due to their relatively poor CryoSat-2 data coverage (see Section 3.2.1). The following Arctic

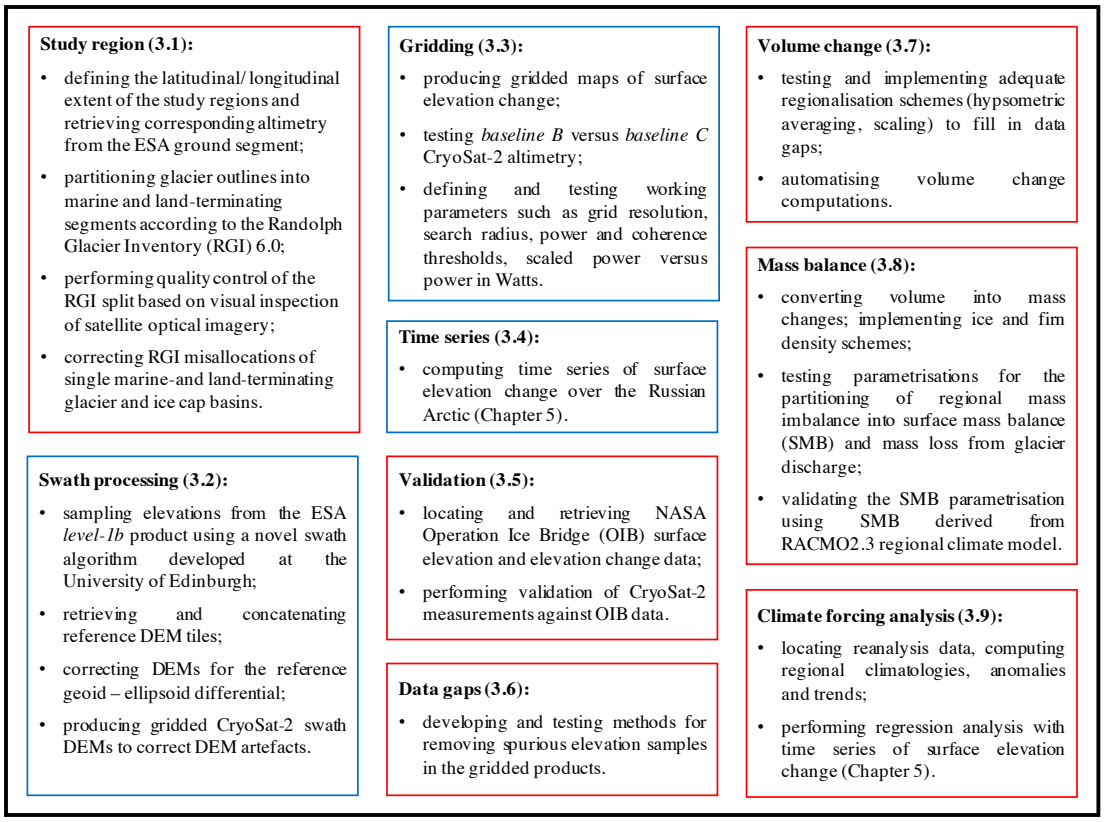


Figure 3.1: Thesis main workflow. Boxes corresponds to the major steps in the thesis research programme regarding data acquisition and processing. Red boxes correspond to methodology entirely developed and validated as part of this thesis while blue boxes correspond to data processing segments tested and carried out (applied to the Arctic) during this thesis but were developed by other parties. Red boxes correspond to methodology entirely developed and validated as part of this thesis. Numbers in parenthesis correspond to the chapter subsections where the content of the blocks is further detailed.

glaciers and ice caps were also not included in the thesis due to lack of coverage by CryoSat-2 (the satellite does not operate in SARIn mode at their location, see Figure 2.4): Jan Mayen Island (Norway), Kvitøya Ice Cap (Svalbard), Victoria Ice Cap (Franz Josef Land), Ushakov Ice Cap (Russian High Arctic) and Schmidt Ice Cap (Severnaya Zemlya). Together, these ice masses extend over a relatively small glaciated area ($\sim$1600 km^2). The De Long Islands ice caps (East-Siberian Sea) exhibiting a total glaciated area $<$ 80 km^2 (Glazovskiy, 1996) were also excluded due to their relatively small size. For all study regions, it is assumed that the glaciated area remains constant over the total period of measurement.

Glacier outlines from the Randolph Glacier Inventory (RGI 6.0), available in vector (*shp*) format at Global Land Ice Measurements from Space (GLIMS), were converted to gridded ice masks at 500 m resolution to delimit the areas of bare ground and ocean water from those covered in land ice in the CryoSat-2 derived gridded products (Section 3.3). In addition, RGI 6.0 single glacier metadata was used to compute ice masks separately for land- and marine-terminating basins. Initial partitioning between mountain and tidewater glaciers revealed existing misallocations in the RGI 6.0 database for some regions. The most substantial adjustments needed to be made for Svalbard, where a number of land-terminating basins were re-allocated as marine-terminating based on visual inspection of online maps from the Norwegian Polar Institute (NPI) available at www.npolar.no. Regions particularly affected were Westfonna Ice Cap, Haakon VII Land (NW Spitzbergen), Olav V Land (NE Spitzbergen) and Edgeøya Island (Figure 3.2). The detailed reallocation over Svalbard was made for the following glacier and ice cap basins: Augnebreen, Aldousbreen, Besselsbreen, Bragebreen, Chydeniusbreen, Deltabreen, Duckwitzbreen, Fjortende Julibreen, Franklinbreen N and S, Frazerbreen, Gimlebreen, Hayesbreen, Hinlopenbreen, Hochstetterbreen, Idunbreen, Infantfonna, Ingerbreen, Innifonna, Johansenbreen, Kongsbreen, Kongsvegen, Kronebreen, Kosterbreen, Mayerbreen, Mittag-Lefflerbreen, Monacobreen, Negribreen, Nordenskiöldbreen, Nordsysselbreen, Oslobreen, Paulabreen, Perseibreen, Petermannbreen, Polarisbreen, Recherchebreen, Richardsbreen, Scheibreen, Sidevegen, Spælbreen, Stonebreen, Tunabreen, Vaigattbreen. The total glaciated area of these misrepresented glacier basins equates to 7,120 km^2, which is 21 % of the total area covered by glaciers and ice caps in Svalbard. The corrected tidewater glacier area for Svalbard is 22,020 km^2 and needs to replace previously published data, such as in Gardner et al. (2013) (14,900 km^2, see Table 2.1).

The result of the reallocation is shown graphically in Figure 3.2. A few minor reallocations were also made for Novaya Zemlya, Severnaya Zemlya and the Canadian Arctic over a total area < 500 km^2 for both land- and marine-terminating basins.

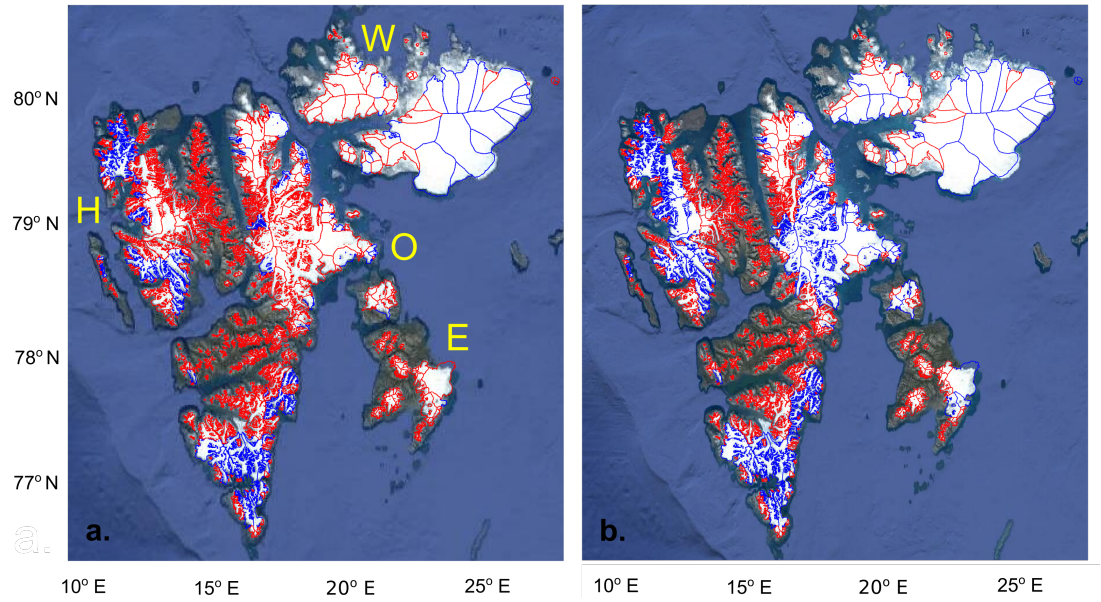


Figure 3.2: Land (red) and marine-terminating (blue) glacier basins in Svalbard. Partitioning according to RGI 6.0 (a) and after reallocation (b). E denotes Edgeøya Island, H denotes Haakon VII Land, O denotes Olav V Land, W denotes Westfonna Ice Cap.

Some of the misrepresentations in RGI 6.0 may be due to changes in glacier area extents resulting from the rapid advance and retreat of ice masses, such as tidewater glaciers retreating on land, and/or previously land-terminating glaciers now terminating in marine waters. However, the large majority seem to stem from inconsistent database updates and incomplete or erroneous metadata provided by RGI due to limited resources (Pfeffer et al., 2014, Dr. Geir Moholdt, personal communication). This is evidenced by the large number of inaccuracies, in particular over Svalbard, with examples of well-studied tidewater glaciers, for example Tunabreen, Stonebreen or Kronebreen, which were incorrectly classified as land-terminating glaciers in RGI 6.0.

3.2 Swath processing

CryoSat-2 *level 1b*, baseline B altimetry was downloaded from the ESA *ftp* server, and later, during July-September 2017, replaced with baseline C altimetry, which represents an upgrade of the *level 1b* product (Bouffard. et al., 2015; Gourmelen

et al., 2018).

3.2.1 Waveform filtering

The swath algorithm used in this thesis to sample CryoSat-2 elevations is based on a version that was in a testing phase at the start of the thesis. It was applied successfully over Icelandic ice caps by Foresta et al. (2016) and is described in detail in Gourmelen et al. (2018). The algorithm extracts from each power, phase and associated coherence waveform integral to the *level 1b* product a range of elevations h, together with their corresponding geographic location (x, y), and the time of measurement t. It essentially filters out waveforms based on a combination of power and coherence thresholds previously established by empirical analysis (Christie et al., 2016; Foresta et al., 2016; Gourmelen et al., 2018; Gray et al., 2013; Ignéczi et al., 2016). To optimise the sampling over Arctic glaciers and ice caps, a series of qualitative tests was performed, using a range of thresholds in conjunction with the implementation of baseline C altimetry, which was available within six months after the start of the thesis. The best signal was obtained when sampling the swath elevations with normalised power, scaled over the entire power range within single waveforms $> 10^4$ and coherence > 0.8 (Figure 3.3).

Swath processing copes relatively well with the challenge of surveying ice surfaces over rough terrain (Chapter 2). Good coverage is obtained over both smooth ice cap slopes and in regions characterised by a rough topographic landscape, such as mountain ranges in the Canadian High Arctic (Figure 2.7). In regions of extreme elevation gradients however, the radar return signal is backscattered with a high degree of dispersion, preferentially from mountain peaks and crests, and with weak echoes from valley glaciers, which are often entirely missed out (Dehecq et al., 2013; Gray et al., 2015). Extreme topographic relief is characterised by surface gradients typically $>$ 1000 m in elevation over distances shorter than the satellite's along-track footprint ($\sim$380 m), with glacier hypsometries nearly perpendicular to the flight track. This leads to frequent loss-of-lock occurrences

in the altimetric record, that is a temporary inability of the altimeter in adjusting its range window to track the ice surface (Dehecq et al., 2013; Foresta et al., 2018). Typical regions of extreme topography are the Karakoram, Himalayas, Alaska, the American Cordillera and the Andes (Figure 3.4).

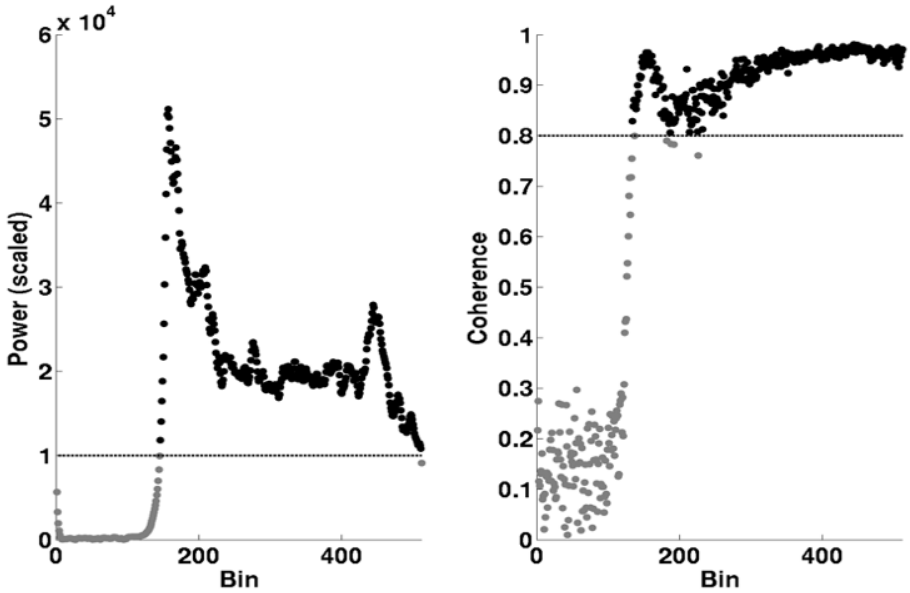


Figure 3.3: Example of a CryoSat-2 echo waveform and applied power and coherence filter thresholds. Source: Foresta (2015).

Under these circumstances, the implementation of thresholds on power and coherence needs to be complemented by the analysis of the interferometric phase, all three elements being needed in order to achieve sufficient sampling on valley glaciers. This procedure, initially developed for (InSAR) radar image processing (Weissgerber, 2016), was shown to increase substantially the number of swath elevations sampled over Jakobshavn Glacier, Greenland (Weissgerber and Gourmelen, 2017), and was used further to improve the signal over Patagonian Icefields (Foresta et al., 2018). However, at the start of this thesis, this procedure had not yet been tested, and hence, due to a relatively weak signal-to-noise ratio over Alaska and the American Cordillera, it was decided to focus the research on the remaining seven Arctic regions, namely: Iceland, Svalbard, Novaya Zemlya, Severnaya Zemlya, Franz Josef Land, and the southern and northern archipelagos

of the Canadian Arctic.

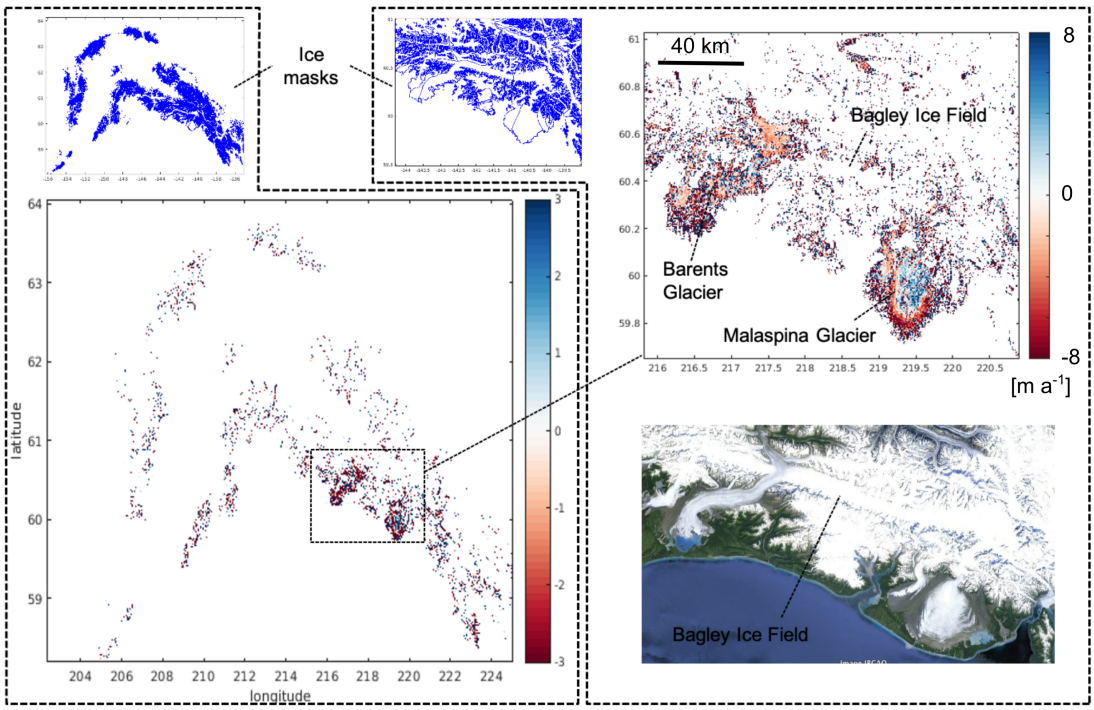


Figure 3.4: Example of CryoSat-2 swath altimetry over extreme topography. Maps of elevation change over the Alaskan range and corresponding ice mask. Detail map (right) shows the area surrounding the St Elias mountain range, the only region that is relatively well-covered by CryoSat-2, including Malaspina and Barents glaciers. The signal over the adjacent Bagley Ice Field is shadowed as a result of extreme elevation gradients between the ice surface and surrounding mountain tops and crests.

3.2.2 Phase unwrapping

Interferometric phase differentials between the two receiving Cassegrain antennas (Chapter 2, Section 2.3.2) are primarily used for the lateral positioning of the footprint centre in the presence of a surface gradient (Figure 3.5). Phase differences $> 2\pi$ within single echo waveforms are common for small surface slopes with an angle $< 0.54°$, and are corrected using a local phase unwrapping procedure implemented in the swath algorithm (Gourmelen et al., 2018). In areas of moderate to extreme topography where the surface angle is $>> 0.54°$, such as over ice cap margins and mountain glaciers, phase ambiguities may affect entire waveforms, causing errors in gridded elevation of tens of metres, and significant inaccuracies

in the positioning of the return signal on the ground (Gourmelen et al., 2018). To remedy such ambiguities in the signal caused by 2π phase wrapping of entire waveforms, the implementation of an external topographic reference, such as a digital surface elevation model (DEM), is therefore required to guide the interferometric swath processing.

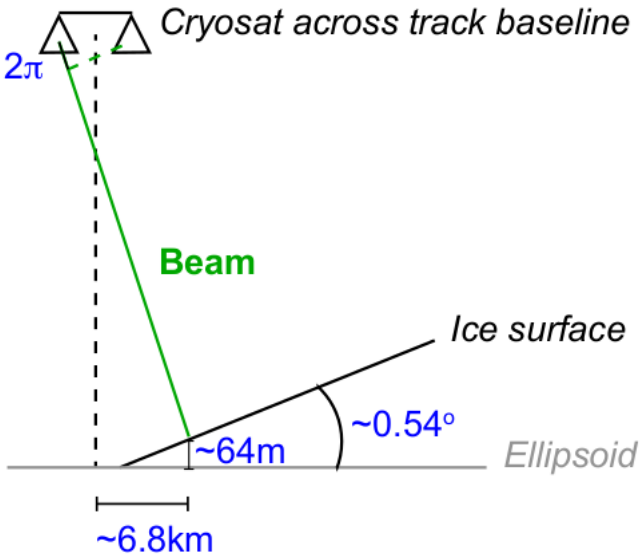


Figure 3.5: Critical slope angle resulting in interferometric phase ambiguities, geospatial positioning and h (x, y) errors. Source: Foresta (2015).

At the start of the thesis, a viable source providing digitised topographic maps of the Arctic was Viewfinder Panoramas (Ferranti, 2014). Digital elevation models from this source are built from 1:200,000 digitised topographic maps of the Russian High Arctic surveyed by the Soviet military from the 1960s to 1980s, Norwegian Polar Institute 1:100,000 maps for Svalbard, and a range of maps from National Resources Canada for the Canadian Arctic (de Ferranti, 2017, personal communication). For Iceland, a DEM from the National Land Survey of Iceland (Landmælingar Íslands) was used, as in Foresta et al. (2016). The implemented DEMs are referenced to the EGM96 geoid, while geospatial positioning of CryoSat-2 and altimetry is expressed relative to the WGS84 ellipsoid. The necessary adjustment was made to reference DEM elevations using the Geospatial Data Abstraction Library (GDAL), so that satellite and reference DEM measurements

were both expressed relative to WGS84.

Due to the large time spans separating the corresponding sampling periods, reference DEMs may differ substantially from the topography measured using CryoSat-2 swath elevations. Differences between the swath and the reference topography are acceptable to a certain degree, although the level of accuracy depends on the region's topographic complexity and is difficult to estimate (Gourmelen et al., 2018). In one instance, these differences appeared to be too large, namely over a section in the northern extremities of Severny Ice Cap, Novaya Zemlya (Russian Arctic), where the unwrapping could not be completed, resulting in data breaches in the gridded products (Figure 3.6). The Viewfinder Panoramas reference DEM therefore had to be corrected locally using gridded elevations from a CryoSat-2 swath-generated DEM, which was generated using time stamps from the very first CryoSat-2 records in July 2010. Later, Viewfinder Panoramas DEMs were replaced by the more recently published ArcticDEM (Porter et al., 2018), which supported the analysis of Russian Arctic glaciers and ice caps in Chapter 5.

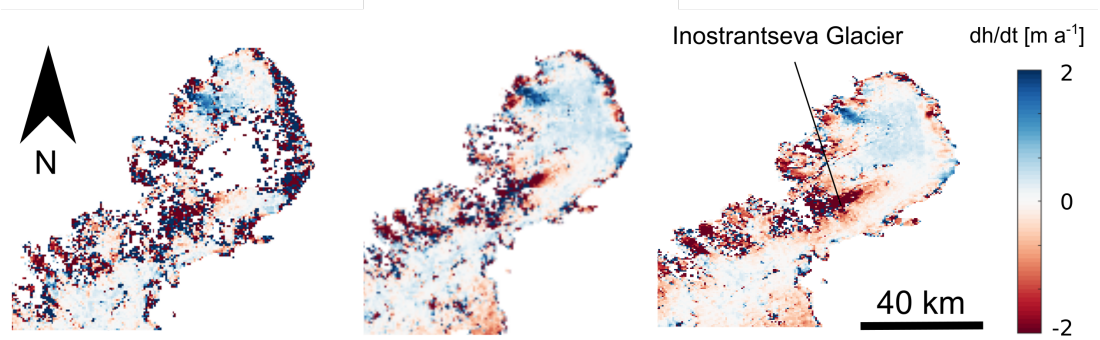


Figure 3.6: Swath-processed elevation changes using different reference DEMs. Example of Severny Island Ice Cap, Novaya Zemlya, Russian Arctic (see also Chapter 5). Viewfinder Panoramas with apparent data gap **(a)**, Viewfinder Panoramas corrected with CryoSat-2 swath DEM **(b)**, ArcticDEM (2010-2018) **(c)**.

3.3 Gridded maps of surface elevation change

Gridded maps of surface elevation change $\dot{h}$ are extracted using a linear plane-fit algorithm (Foresta et al., 2016) applied to all swath elevations sampled within a predefined search radius from each pixel centre and covering the entire measurement period from 2010 to 2017. The algorithm assumes a linear relationship between the swath elevations h, longitude x, latitude y, and time of measurement t, thereby solving for both the temporal and the spatial components of surface elevation change:

$$\mathbf{h}(x, y, t) = c_0\mathbf{x} + c_1\mathbf{y} + c_2\mathbf{t} + c_3 = \nabla\mathbf{h}(x, y) + \dot{\mathbf{h}}\mathbf{t} + c \tag{3.1}$$

with

$$\nabla\mathbf{h}(x, y) = \frac{\partial h}{\partial x}x + \frac{\partial h}{\partial y}y \tag{3.2}$$

and

$$\dot{\mathbf{h}} = \frac{\partial h}{\partial t} \tag{3.3}$$

$\nabla h(x, y)$ is the ice surface gradient, and the time-dependent coefficient c_2 retrieved from the parametrisation is the rate of surface elevation change $\dot{h}$. The coefficients c_n are determined from the parametrisation matrix M = [x y t 1] after assigning each swath elevation with a weight according to the corresponding echo power field (Foresta et al., 2018):

$$\mathbf{c}_n = [\mathbf{M}^T\ w\ \mathbf{M}]^{-1}\ \mathbf{M}^T\ w\ \mathbf{h} \tag{3.4}$$

where M^T is the transposed parametrisation matrix and w the diagonal matrix of the power weights. The gridded elevations h_p (x_p,y_p) are fitted to the measurement field around each pixel centre using an iterative 3σ-filter at each step until all outliers are removed (Foresta et al., 2016).

The grid cell size was chosen based on instrument resolution and empirical testing. Measurement swaths orthogonal to the satellite tracks expand over sev-

eral kilometres (typically $\sim$ 5 km) beyond POCA (Figure 2.5). The (x y) position of each individual swath measurement on the ground is determined from the smoothed phase interferogram (Gray et al., 2013). The resulting cross-track sampling precision depends on the local incidence angle θ ($\sim$ 143 m for $\theta = 1°$) of each swath measurement, and is generally much smaller compared to the footprint of conventional POCA (Gray et al., 2013). In flight direction, the satellite resolution is optimised by doppler pulses with a footprint of $\sim$ 380 m (see Chapter 2, Section 2.3.2). According to these sampling characteristics and owing to the dense elevation fields h (x, y, t) obtained, gridding with a maximum cell resolution on the order of the Doppler-limited footprint is achievable. A series of qualitative tests showed that a cell resolution of 500 $\times$ 500 m with a search radius of 500 m from each pixel centre ensures sufficient spatial detail while maximising the number of observations in each resolution cell across a broad range of topographic settings in the Arctic. A 500 $\times$ 500 m grid resolution was previously applied successfully over Icelandic Ice Caps (Foresta et al., 2016), and later over the Patagonian Ice Fields (Foresta et al., 2018) (examples in Figure 2.6d and Figure 2.7).

3.4 Time series of surface elevation change

Owing to CryoSat's dense ground track network and the overlapping swaths of measurements between adjacent satellite tracks, the high-density swath elevation field can be exploited not only in space but also in time to generate robust time series of elevation change $\dot{h}$, with time intervals down to 90 days. The methodology applied in this thesis to compute elevation changes between consecutive time intervals is based on Gray et al. (2015) and was further developed by Foresta et al. (2016) and Malczyk et al. (2019) to fit the University of Edinburgh swath algorithm procedures. Surface elevation changes between time interval t_n and the subsequent time interval t_{n+1} are calculated as the average difference between measurements in t_n and measurements in t_{n+1} located at a maximum distance of 400 m from each measurement in t_n. This search radius is chosen to correspond

approximately to the along-track sampling resolution of CryoSat-2 (Gray et al., 2015). A reference elevation model (ArcticDEM, Porter et al., 2018) is used in the algorithm to correct for existing spatial gradients between measurements in t_n and those in t_{n+1}.

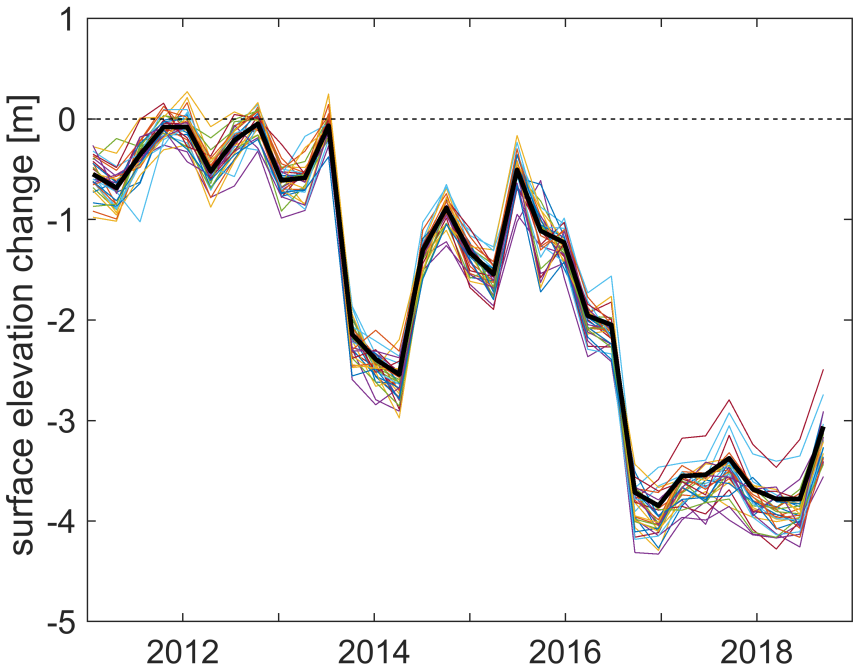


Figure 3.7: Time series of surface elevation change over Vil'kitskogo southern glacier basin, Novaya Zemlya, Russian Arctic. Time series resulting from permutations of time interval pairings (coloured) and median time series of elevation change (black, bold).

To add robustness to the time series, elevation changes between two given time periods are calculated multiple times using all possible permutations of time interval pairings (Foresta et al., 2018). For example, the mean difference in elevation h_{13} between the time intervals t_1 and t_3 can be calculated either directly as h_{13}, or as the sum of h_{12} and h_{23}, or as the difference between h_{14} and h_{34}, etc. This approach also ensures that possible biases associated with temporal differences in penetration of the radar signal into surface ice and snowpack are minimised (see Chapter 2, Section 2.3.2). The final product is calculated as the median difference in elevation between these permutations (Figure 3.7). In this thesis, time series

of elevation change were computed for the Russian Arctic archipelagos of Novaya Zemlya, Severnaya Zemlya and Franz Josef Land at catchment scale (Chapter 5).

3.5 Validation of CryoSat-2 swath products

CryoSat-2 elevation changes were validated against airborne measurements of $\dot{h}$ from the NASA Operation Ice Bridge (OIB) Airborne Topographic Mapper (ATM), a scanning laser altimeter (Studinger, 2014). Two validation test sites were located in the Arctic outside of Greenland, one over Barnes Ice Cap on Baffin Island, and one over Devon Ice Cap in the Canadian High Arctic (Figure 3.8). The OIB product used for validation is ATM L4 Surface Elevation Rate of Change, Version1 (Studinger, 2014), with measurements sampled along extensive repeat flight paths in 2010 and 2015. ATM acquisitions of surface elevation were made with 74 cm horizontal and 6.6 cm vertical accuracy, with no existing penetration bias of the laser beam over ice and snow (Martin et al., 2012). For each 2010-2015 CryoSat-2 gridded elevation change sample, the selection of corresponding validation measurements was made based on their location < 250 m from each grid cell centre of the CryoSat-2 swath product. Biases were calculated as the median value of the difference between CryoSat-2 and OIB measurements:

$$\mathbf{\Delta \dot{h}} = median(\mathbf{\dot{h}}_{CryoSat} - \mathbf{\dot{h}}_{OIB}) \tag{3.5}$$

A minimal bias of 0.05 m $a^{-1} \pm 0.26$ m a^{-1} and 0.00 m $a^{-1} \pm 0.13$ m a^{-1} was found respectively for Barnes and Devon Ice Caps (Figure 3.8). This can be explained by differences in the precision of echo geolocation, signal properties, and penetration bias. Other comparisons between CryoSat-2 and OIB swath elevation changes over Jacobshavn Isbrae glacier (Greenland) and the Amundsen Sea Sector (Antarctica) yield a bias of 0.04 m a^{-1}, with a measurement dispersion of 1.15 and 0.92 m a^{-1}, respectively (Gourmelen et al., 2018). Finally, six independent CryoSat-2 POCA elevation products used for comparison in a col-

laborative validation exercise with 2016 CryoVex measurements over Svalbard (Sørensen et al., 2018) yield biases ranging between -1.11 m and +2.04 m, with differences depending on the CryoSat-2 processing scheme. CryoVex is ESA's dedicated validation campaign for the CryoSat-2 mission.

Because the climate and snow characteristics differ between regions, caution is needed when transferring the results from these validation procedures to other locations in the Arctic.

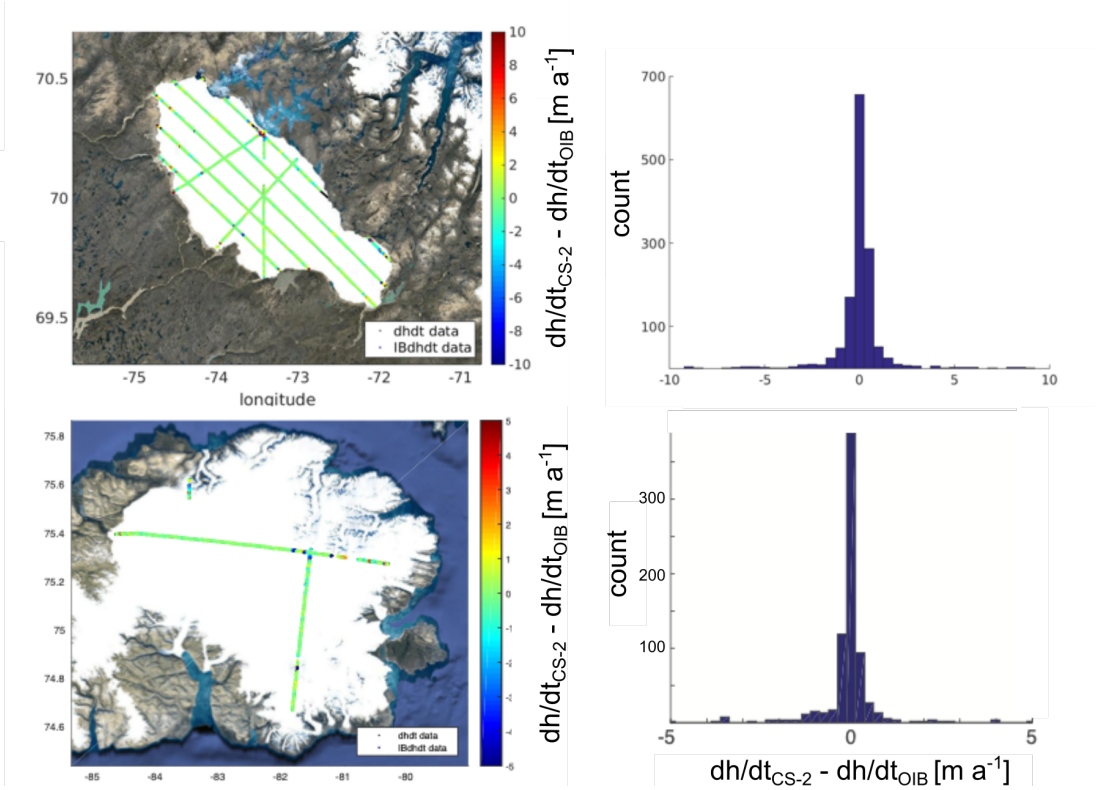


Figure 3.8: Validation of CryoSat-2 (CS-2) rates of surface elevation change $\dot{h}$ (dh/dt) against NASA Operation Ice Bridge (OIB): Barnes Ice Cap (top panels), and the Devon Ice Cap (bottom panels) with differences of 0.05 ± 0.26 m a^{-1} and 0.00 ± 0.13 m a^{-1} respectively for Barnes and Devon Ice Caps.

3.6 Spatial coverage and data gaps

As described earlier, a series of data filtering steps are needed during the swath processing to generate gridded surface elevation change from *level 1b* altimetry.

These are: **(1)** waveform selection/ filtering based on pre-established scaled power and coherence thresholds (Section 3.2.1); **(2)** 3σ clipping of spurious elevations from the plane-fitted grid elevations (Section 3.3); and **(3)** identification and removal of remaining spurious elevations in the gridded maps. This third and last step is discussed in detail in Section 3.6.1.

3.6.1 Spurious elevation changes from 'ground truth'

The raw gridded products (see Section 3.3 and Appendices, Figures 3.19 - 3.31) are examined in terms of their signal-to-noise ratio using 'ground truth' information from the performed validation against OIB data. Spurious samples are defined conservatively as grid cells with values of h larger than the maximum dispersion on the CryoSat-2 – OIB $\Delta\dot{h}$ bias, that is $\sim$ 1 m a^{-1} (Section 3.5).

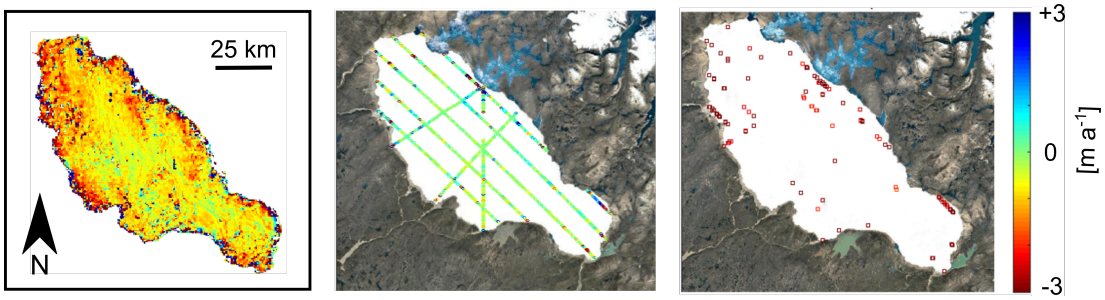


Figure 3.9: CryoSat-2 - OIB bias in surface elevation change. (a) $\dot{h}$ CryoSat-2 (b) $\Delta\dot{h}$ bias between CryoSat-2 and OIB and (c) 'ground-truth' - based noise.

Over the areas covered by OIB flight tracks, the 1 m a^{-1} threshold can be applied directly to isolate spurious elevation changes (Figure 3.9). However, over the rest of the glaciated area, and in Arctic regions where ground information is unavailable a supplementary methodology is needed for noise detection and removal. Typically, smoothing functions are applied to the gridded products, whereby pixels with original rates more than 3σ larger than the smoothed values are discarded (e.g. Foresta et al., 2016, 2018; Zheng et al., 2018). Alternatively, a series of parameters related to the changes in ice topography can be used for filtering. Foresta et al. (2016) for example, used thresholds on the errors $\epsilon_{\dot{h}}$ on $\dot{h}$ extracted from the plane-fit parametrisation, minimum/ maximum values of

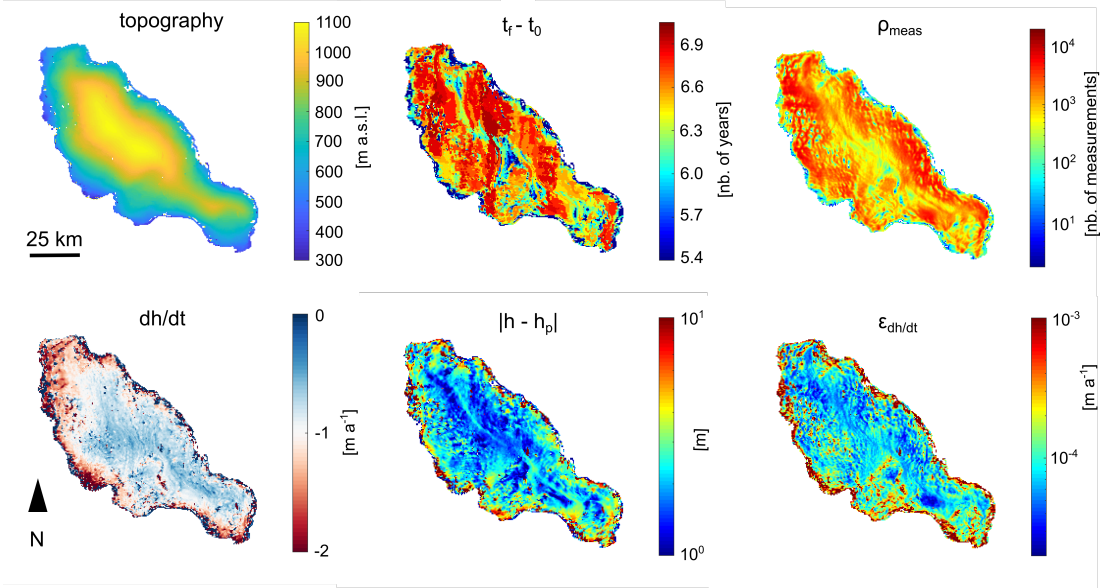


Figure 3.10: Selection of parameters for noise detection in gridded format, example from Barnes Ice Cap on Baffin Island, Nunavut, Canada. From top-left to bottom-right: elevation (h), CryoSat-2 time stamps ($t_f - t_0$), measurement density ρ_{meas}, surface elevation change ($\dot{h}$), differences between measured and parametrised elevation $|h - h_p|$, error $\epsilon_{\dot{h}}$ on $\dot{h}$.

$\dot{h}$, maximum differences between measured and parametrised elevation $|h - h_p|$, and minimum time stamps $(t_f - t_0)$ on CryoSat-2 sampling to identify spurious values of $\dot{h}$ in the gridded maps. These parameters are all derivative products of swath processing and are associated with surface elevation change rates in each grid cell (Figure 3.10). However, the applied thresholds are, for each of the parameters, based on empirical knowledge and testing over specific regions, in the cited case over the Icelandic ice caps (Foresta et al., 2016) and the Patagonian ice fields (Foresta et al., 2018). Because in this thesis a pan-Arctic assessment is undertaken, a more robust approach for identifying spurious elevation changes over the entire Arctic needed to be developed, which is the subject of Section 3.6.2. The methodology described in Section 3.6.2 has, to the best of my knowledge, not been applied elsewhere with the purpose of isolating spurious altimetric measurements over land ice.

3.6.2 Receiver Operating Characteristic (ROC) function

An effective tool for assessing the suitability of a specific parameter in detecting noise is provided by the so-called Receiver Operating Characteristics (ROC) function (James et al., 2015). ROC functions describe, for a set of thresholds applied to a given parameter or classifier, the ratio of true positive rate (TPR), that is the fraction of samples – in the present case of $\dot{h}$ - correctly identified as noise, to false positive rate (FPR), which is the fraction of valid samples erroneously classified as noise (Figure 3.11). Whether the identification is correct or erroneous at any given threshold can be directly inferred over regions where 'ground truth' information is available (Weissgerber, 2016). Here, the ROC functions were computed using surface elevation change over the OIB flight ground tracks (Figure 3.9b).

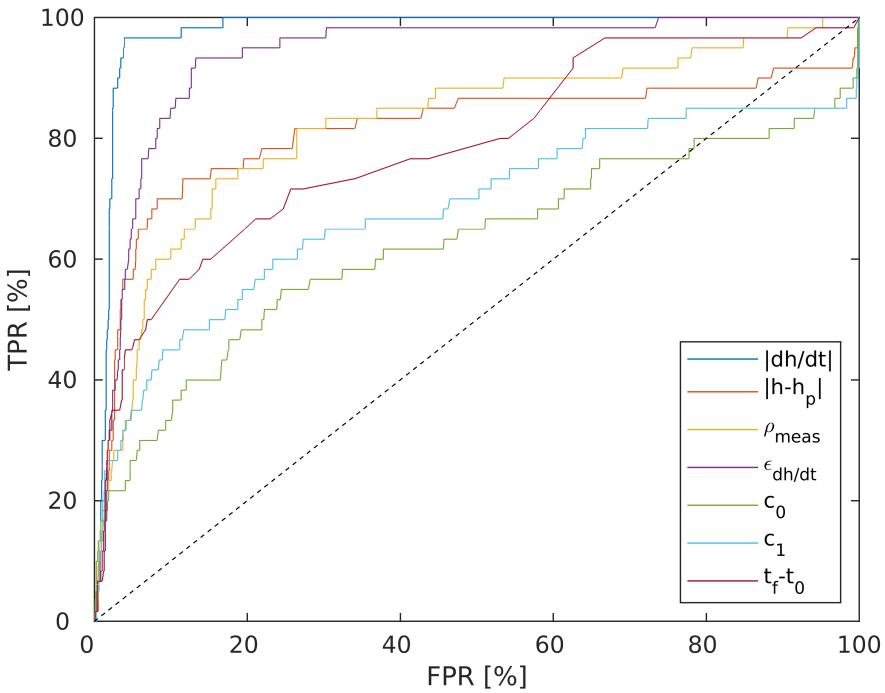


Figure 3.11: ROC functions for the selection of suitable noise classifiers, including those shown in 3.6.1 (Figure 3.10): absolute values of $\dot{h}$ (dh/dt), standard deviation between elevation samples and polynomial fit $|h - h_p|$, measurement density ρ_{meas} after 3σ-clipping, error $\epsilon_{\dot{h}}$ on $\dot{h}$ extracted from the parametrisation co-variance matrix, the (x, y) coefficients c_0 and c_1, and maximum time span between measurement samples $(t_f - t_0)$.

The overall performance of a parameter, summarised over all possible thresholds, is measured by the area under the ROC function, with an optimal classifier tending to hug the top left corner of the ROC plot (James et al., 2015; Weissgerber, 2016). In the present case, the best classifiers are minimum and maximum thresholds on $\dot{h}$ and on the corresponding error field $\epsilon_{\dot{h}}$ (Figure 3.11). The latter is extracted for each grid cell from the covariance matrix of the plane-fit algorithm (see Section 3.8.6). Likewise, the ROC functions in Figure 3.11 also highlight those parameters that are less suited as classifiers, in particular $|h - h_p|$, and the parametrisation coefficients c_0 and c_1, for which the test rules against the diagnosis, since for a range of thresholds the ratio of TPR-to-FPR is smaller than 1. Finally, the performance of each of the main classifiers identified in the ROC diagram can be evaluated from visual inspection of the spatial distribution of detected noise over the entire ice cap at different TPR/FPR combinations (Figure 3.10 and Figure 3.12). These confirm the choice of $\dot{h}$ and $\epsilon_{\dot{h}}$ as main classifiers.

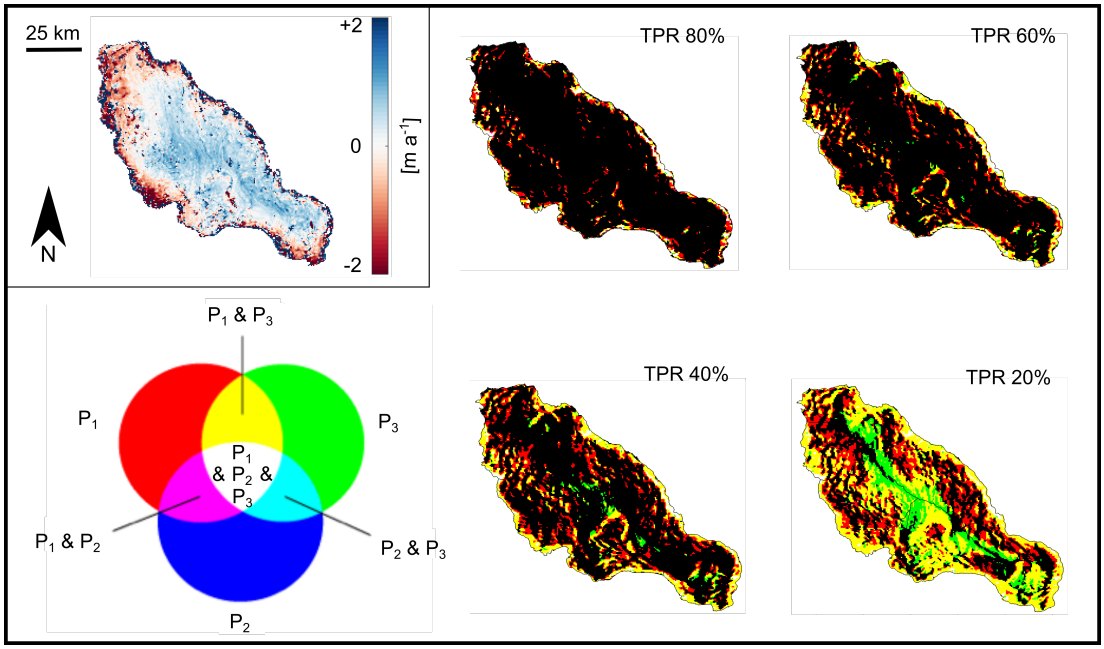


Figure 3.12: Spatial distribution of spurious $\dot{h}$ samples over Barnes Ice Cap. Insert (upper left) shows map of measured $\dot{h}$ before denoising. The four maps on the right show detected noise from a combination of the three main classifiers P_1 ($\dot{h}$), P_2 ($\epsilon_{\dot{h}}$), and P_3 (ρ_{meas}) at TPR 80 %, 60 %, 40 % and 20 %. Black samples correspond to valid measurements.

Once the classifiers were identified, denoising was performed individually for each of the seven Arctic regions and for single ice caps by removing grid cells with $|\dot{h}| > \delta$, and with errors $\epsilon_{\dot{h}}$ above a certain threshold. Thresholds applied to both $|\dot{h}|$ and $\epsilon_{\dot{h}}$ are specific to each study region/ ice cap and were established following an iterative volume change computation, which is described in Section 3.7.

3.6.3 Errors from changes in the scattering horizon

Generally, seasonal cycles in backscatter depth resulting from varying snowpack liquid water content, density, and surface roughness are not expected to have a significant impact on decadal trends in surface elevation change (McMillan et al., 2016). However, occasional changes in surface conditions may lead to transient artefacts in the altimetry record (McMillan et al., 2016; Nilsson et al., 2015b). To ensure that time series of surface elevation change are not affected by such biases, a waveform deconvolution procedure can be applied, for example, to the data record to determine echo power as a function of depth (McMillan et al., 2016). In the absence of known, widespread melt events outside of Greenland since the launch of CryoSat-2, however, the procedure applied in this thesis was limited to the inspection of time series of elevation change (see Section 3.4). The analysis of single-basin 90-day time step series over the Russian Arctic, a region not covered by CryoSat-2 validation campaigns, reveals no unexpected jumps in the time series (Figure 3.7 and Chapter 5), suggesting that biases on $\dot{h}$ induced by changing depth of the scattering horizon in this region are likely small for measurements made between 2010 and 2018.

3.7 Volume change

Mean annual volume change $\dot{V}$ is computed for each region as the sum of surface elevation change in each grid cell of the denoised $\dot{h}$ map multiplied by the

pixel area A_{pixel} as defined by the posting (0.25 km^2).The computation is done iteratively by increasing the threshold on $\epsilon_{\dot{h}}$ (Section 3.6.2) at each step until $\dot{V}$ converges towards a plateau value, $\dot{V}_{denoised}$:

$$\dot{\mathbf{V}}_{denoised} = \mathbf{A}_{pixel} \sum \dot{\mathbf{h}}_{denoised} \tag{3.6}$$

The $\epsilon_{\dot{h}}$ threshold is chosen so that the number of outliers is minimised after $\dot{V}_{denoised}$ levels out (Figure 3.13). Error $\epsilon_{\dot{h}}$ thresholds are 2.1 ± 0.5 m a^{-1} and vary by region. Thresholds δ on the second classifier ($\dot{h}$) are applied during the first iteration such that $|\dot{h}| > \delta$, with δ varying between 10 m a^{-1} and 25 m a^{-1}, and defined for each region individually based on typical thinning rates from recent literature and visual inspection of the $\dot{h}$ maps (see Appendices, Figures 3.19 - 3.31). A summary of the thresholds applied for each region is provided in Table 3.1.

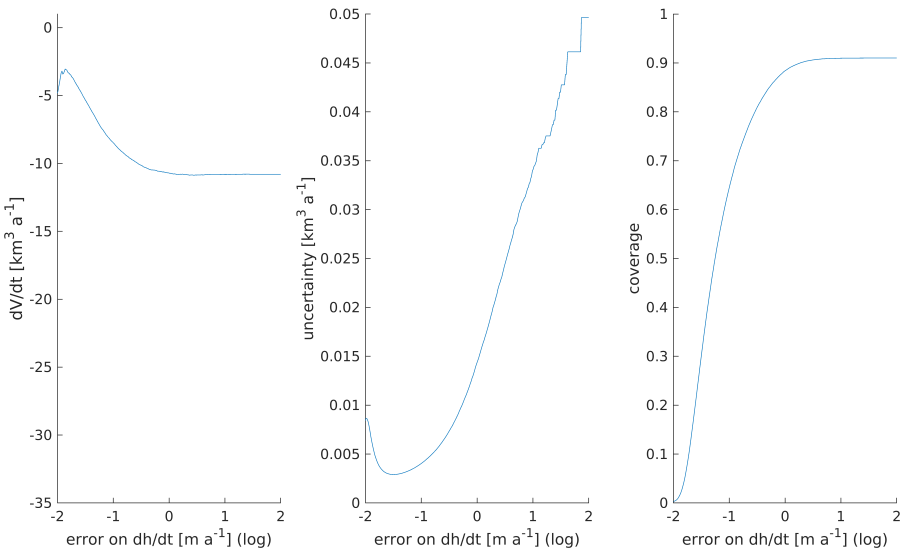


Figure 3.13: Iterative volume change computation and typical convergence, example of Novaya Zemlya, Russian Arctic. Error thresholds $\epsilon_{\dot{h}}$ on $\dot{h}$ (middle) are increased stepwise until $\dot{V}$ (dV/dt) reaches a plateau value (left) and coverage is maximised (right). Error thresholds (x-axis) are shown on a logarithmic scale. Coverage on the y-axis (right) is the fraction of total glaciated area after removal of outliers, with values converging towards the total measured area.

To calculate total volume change $\dot{V}$ over the entire glacial extent of the Arctic

Table 3.1: Classifier thresholds for the removal of spurious elevation change samples by region.

Region	$\dot{\varepsilon}_{h,thres}$ [m a^{-1}]	$\dot{h}_{min}$ [m a^{-1}]	$\dot{h}_{max}$ [m a^{-1}]
FJL	2.5	-20	+20
NZ	0.7	-15	+15
SZ	0.6	-25	+25
Sv	2.1	-25	+25
Ic	2.5	-20	+20
CAA-N	0.8	-10	+10
CAA-S	2.5	-10	+10

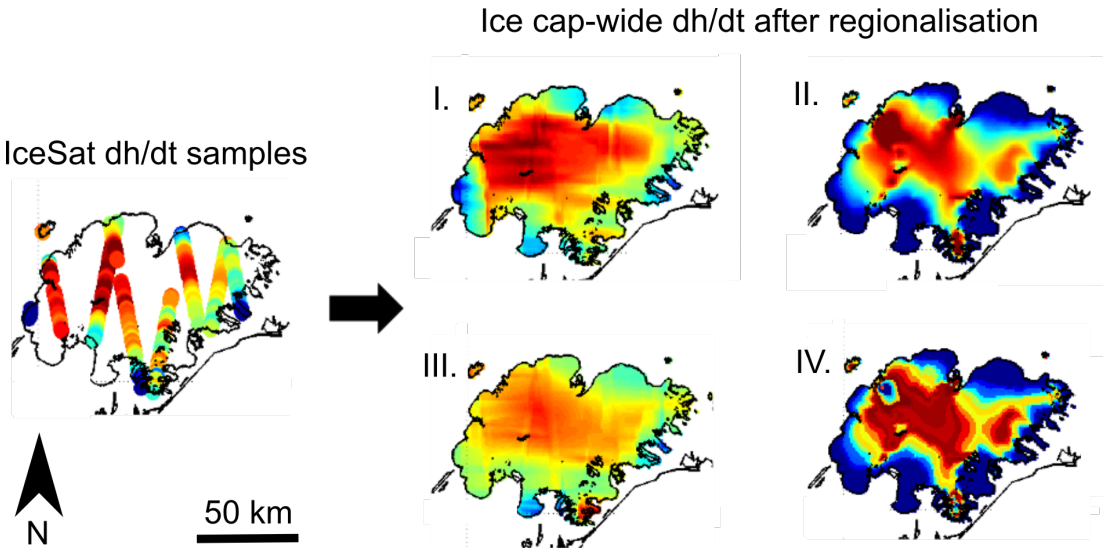


Figure 3.14: Surface elevation change over Vatnajökull Ice Cap, Iceland. From ground track measurement (left) to ice cap-wide regionalisation of change (right). The four examples (I-IV) of regionalised $\dot{h}$ - maps are based either on smoothing (spatial interpolation, I and III) or hypsometric averaging (extrapolation, II and IV). Ice thinning is displayed in blue, thickening in red, and stable areas are in green. Source: Nilsson et al. (2015a).

glaciers and ice caps, certain assumptions were applied in order to fill data gaps over both unsampled areas and those resulting from the removal of spurious measurements. A range of regionalisation schemes are typically applied to the reduced maps of elevation change with spatial interpolation and hypsometric averaging (e.g. Nilsson et al., 2015a) typically the preferred options (Figure 3.14). Because of the large-scale, Arctic-wide assessment of volume and mass change carried out in this thesis, careful consideration of the regional specificities in ice

loss is needed before applying a particular regionalisation method.

3.7.1 Hypsometric averaging

Over land-terminating basins, it can be assumed that surface processes dominate the overall mass budget, with ice losses controlled mainly by precipitation gradients, latitude, and the tropospheric temperature lapse rate (-6.5 °C / 1000 m). At small regional scales such as across single land-terminating ice caps or small clusters of mountain glaciers, volume changes are mainly a function of elevation, implying that hypsometric averaging is an appropriate regionalisation scheme to fill data gaps (Moholdt et al., 2010; Nilsson et al., 2015a).

Hypsometric averaging involves establishing a statistical relationship between rates of surface elevation change and elevation using a polynomial fit (Figure 3.15). The methodology described in Foresta et al. (2018) is applied individually for each single Arctic region or ice cap, whereby the order of the best possible polynomial describing the relationship is iteratively determined by an F-test. This involves a stepwise increase in the order of the polynomial at each iteration until a 99 % confidence level (by measure of the residual sum of squares of the fit) is reached.

Individual grid cells with no measurement are ascribed values of $\dot{h}$ based on their elevation and the coefficients from the polynomial fit. To reduce the impact of potential outliers introduced by the polynomial fitting, total volume change $\dot{V}$ is calculated as the sum of the product between median elevation change ($\widetilde{\dot{h}}_j$) and the corresponding glaciated area A_j within each 50 m elevation band j:

$$\dot{\mathbf{V}} = \sum_j \widetilde{\dot{\mathbf{h}}}_j \cdot \mathbf{A}_j \tag{3.7}$$

3.7.2 Upscaling of volume change

Hypsometric averaging is problematic when applied to larger areas where latitudinal or longitudinal gradients impact mass loss, over surging basins, and where

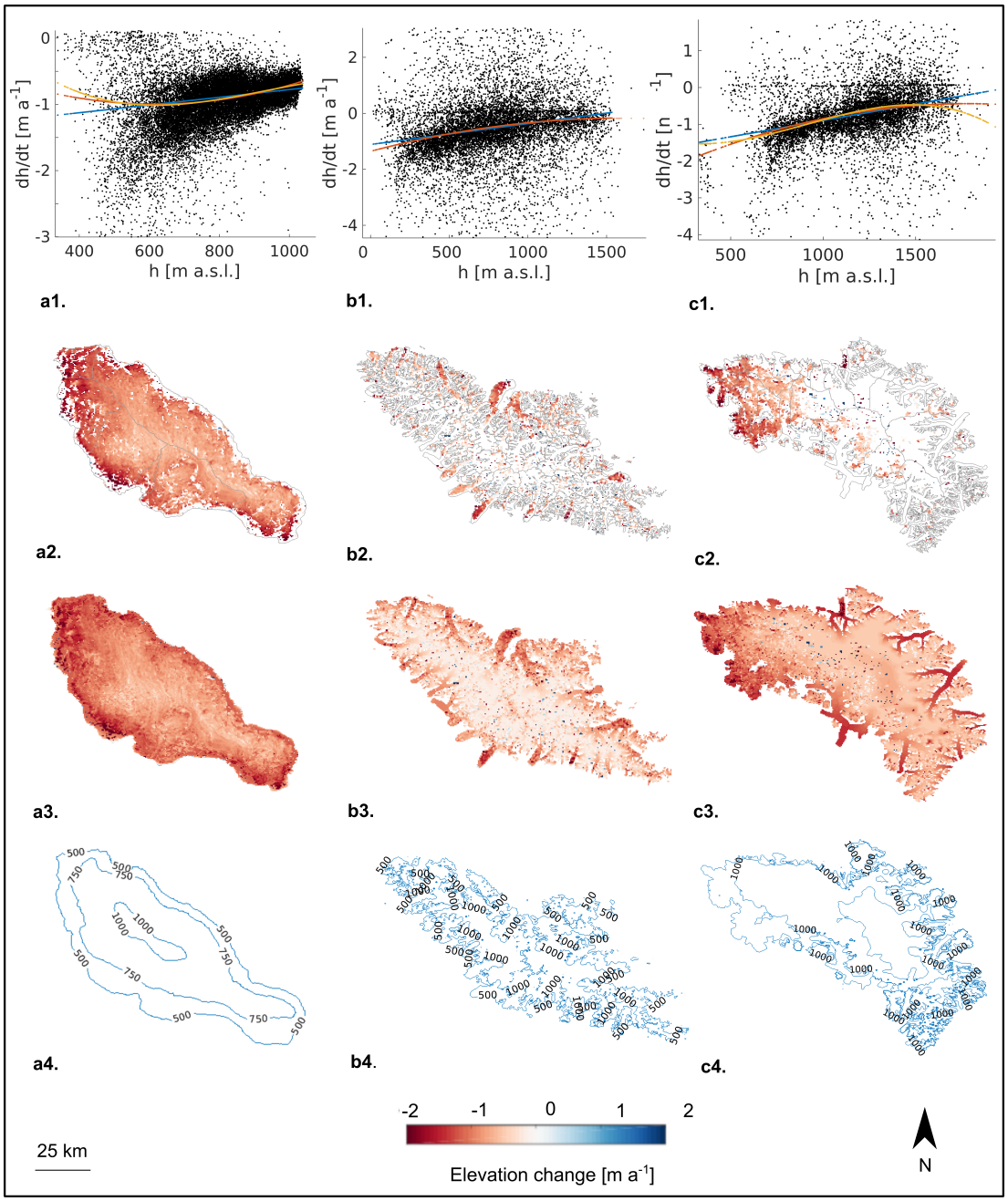


Figure 3.15: Hypsometric averaging over the southern Canadian Arctic. Barnes Ice Cap **(left)**, Bylot Island **(centre)**, and Penny Ice Cap **(right)**: $\dot{h}$ versus elevation h and polynomial fits of different orders (a1-c1), maps of measured $\dot{h}$ after denoising (a2-c2), maps of $\dot{h}$ after applying hypsometric averaging (a3-c3), and reference DEM contour lines (numbers denote m a. s. l.) (a4-c4). The difference in CryoSat-2 coverage is evident between a smooth ice cap surface (e.g. Barnes Ice Cap or the western areas of Penny Ice Cap) and rough topography (northern and eastern areas of Penny Ice Cap and central Bylot Island).

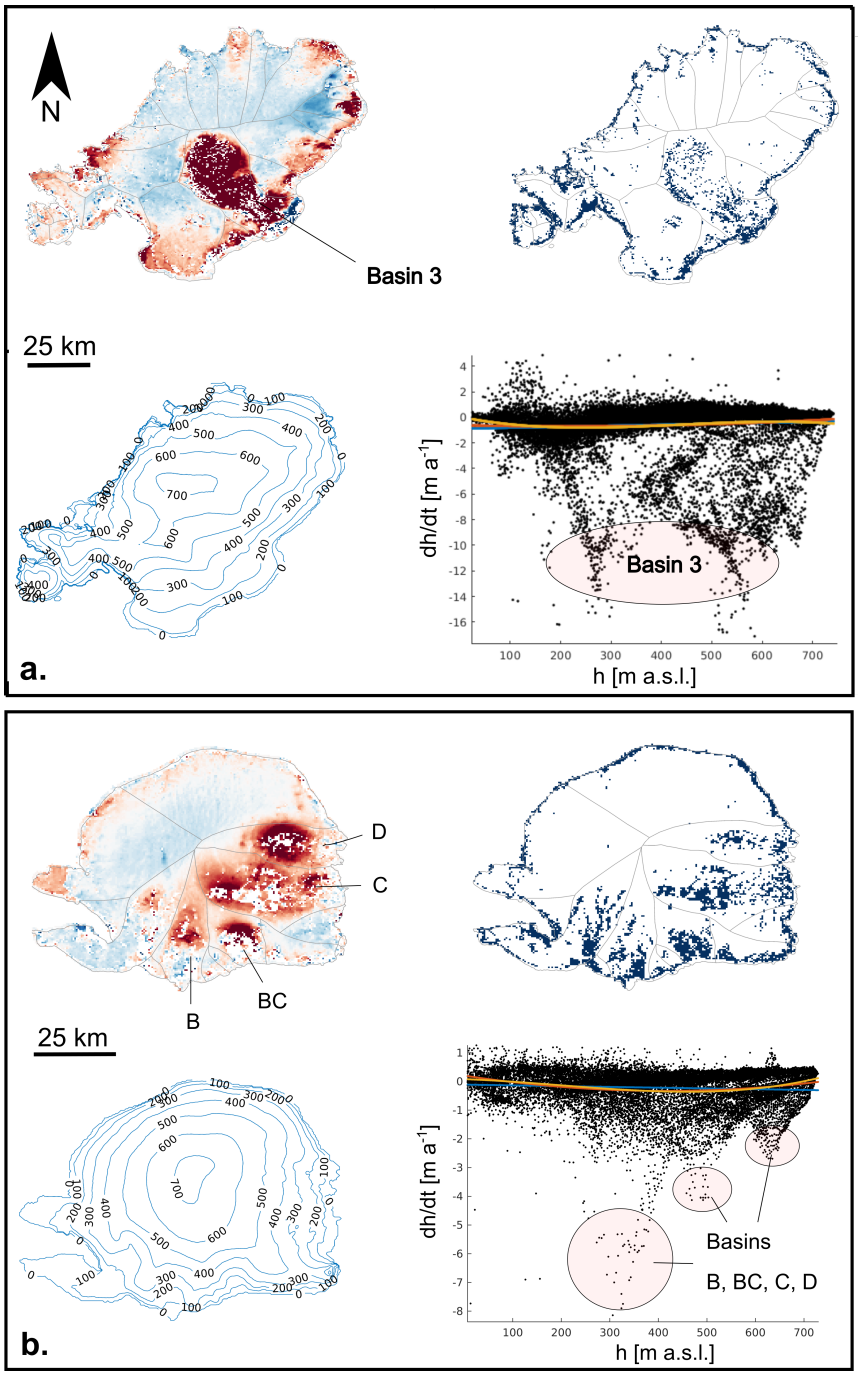


Figure 3.16: CryoSat-2 swath elevation change maps, hypsometry and coverage over (a) Austfonna Ice Cap, Svalbard and (b) Academy of Sciences Ice Cap, Severnaya Zemlya, Russian Arctic. CryoSat-2 2010-2017 swath-processed maps of elevation change $\dot{h}$ after denoising (see Chapter 4), spurious samples (blued dots), reference DEM contour lines (100 m elevation bands), and plots of $\dot{h}$ vs. h with 1^{st}, 2^{nd}, and 3^{rd} order polylines.

dynamic processes (typically associated with tidewater glaciers) lead to significant geometric changes over the ice surface that are decoupled from the local surface mass balance. In the Arctic region, dynamic instabilities after 2010 were mainly observed over marine-terminating basins such as basins B, C, BC and D on the Academy of Sciences Ice Cap, Severnaya Zemlya (Sánchez-Gámez et al., 2019), or Basin 3 in Austfonna, Svalbard (McMillan et al., 2014) (Figure 3.16). As can be inferred from Figure 3.16, strong thinning in some basins is independent of elevation, and hence a simple relationship between $\dot{h}$ and elevation is not sufficiently accurate to extrapolate volume loss estimates to areas without data.

In these cases, and more generally over all marine-terminating sectors of Franz Josef Land, Novaya Zemlya, Severnaya Zemlya and Svalbard, the high measurement density provided by CryoSat-2 (see Chapter 4, Appendices, Table 4.4) allows for the computation of volume change by simply upscaling $\dot{V}_{denoised}$ using the ratio of total-to-measured grid cell samples:

$$\dot{\mathbf{V}} = \frac{\mathbf{n}_{total}}{\mathbf{n}_{denoised}} \cdot \dot{\mathbf{V}}_{denoised} \tag{3.8}$$

where n_{total} is the total number of grid cells and $\mathrm{n}_{denoised}$ the number of pixels after removal of outliers in the $\dot{h}$ product.

3.8 Mass balance

The appropriate regionalisation scheme is chosen according to the criteria discussed in Section 3.7, that is upscaling for marine-terminating basins, and hypsometric averaging over land-terminating sectors. Regionalised volume changes are then converted to mass changes $\dot{m}_l$ and $\dot{m}_m$ for each of the seven Arctic regions' land- and marine-terminating segments, respectively.

3.8.1 Ice density assumptions

The conversion from volume- to mass change is performed using a constant density of ice ρ_{ice} equal to 850 ± 60 kg m^{-3}. This is slightly lower than the 900 kg m^{-3} typically used for conversion (e.g. Gardner et al., 2013) to better account for the wide range of near surface conditions typical across the entire Arctic (Huss, 2013). Total ice cap or regional mass balance $\dot{m}$ is calculated as the sum of the corresponding land- and marine-terminating mass budget segments:

$$\dot{\mathbf{m}} = \dot{\mathbf{m}}_l + \dot{\mathbf{m}}_m \tag{3.9}$$

A detailed pan-Arctic mass balance assessment is provided by region and type of basin in a summary table in Chapter 4, Appendices, Table 4.4.

3.8.2 Sensitivity analysis

In order to test the validity of the upscaling method, a sensitivity test was performed between upscaling and hypsometric averaging over the sum of land-terminating basins in Arctic Canada, where the ice masses are characterised by relatively low data coverage (e.g. only 44 % over Penny Ice Cap) compared to other Arctic regions (up to 95 % in the Russian Arctic). The comparison reveals that total land-terminating mass change is 6 % and 2 % more negative when hypsometric averaging is applied over the elevation field compared to upscaling (see Chapter 4, Appendices, Table 4.4). Given the much higher CryoSat-2 coverage in the other Arctic regions, including over areas of high loss such as Austfonna and Vavilov Ice Caps (see Chapter 4, Appendices, Table 4.4), the results suggest that upscaling is a relatively accurate regionalisation scheme across the marine-terminating segments of each of the seven Arctic regions considered in this thesis.

Because $\dot{h} - h$ dependency varies regionally as a function of local climate, hypsometric averaging is ideally applied over single ice caps rather than over larger areas. A second sensitivity test was therefore performed comparing mass balance over single land-terminating ice caps with mass balance obtained when

hypsometric averaging was applied to the entire glaciated area of a particular Arctic region. The comparison reveals no significant disparities (< 4 %) between the two approaches (see Chapter 4, Appendices, Table 4.4), with differences well within error margins. In the case of the southern and northern Canadian Arctic archipelagos, this is consistent with previous findings by Gardner et al. (2011).

To account for differences in characteristic ice/ firn conditions below and above the equilibrium line, a third sensitivity test was performed, whereby total mass balance was calculated using different density schemes for the ablation (900 kg m^{-3}) and the accumulation (650 kg m^{-3}) areas. The test was run over the Russian and the Canadian Arctic, with assumed equilibrium line altitudes at 500 m a.s.l. (Melkonian et al., 2016) and 1200 m a. s. l. (Gardner et al., 2012), respectively. The two-density scheme has no significant impact on the overall mass balance calculation in either the Russian (< 1 %) or the Canadian Arctic (< 3 %) compared with a one density scheme (850 ± 60 kg m^{-3}).

3.8.3 Partitioning between surface ablation and ice discharge

Surface elevation changes are the result of both surface mass balance (SMB) processes and the advection of ice mass or ice discharge (D), and are described by the kinematic relation for $\dot{h}$ (equation 2.1). Over land-terminating glaciers and ice caps not affected by surges, it can be assumed that surface processes dominate the mass loss, and dynamic thickness changes are either negligible, or cancelling out when integrated over the entire glaciated area A_l. Hence, elevation change rates $\dot{h}_l$ over land-terminating basins can be related directly to the local SMB anomaly, with equation 2.2 resulting in:

$$\dot{\mathbf{h}}_\mathbf{l} = \frac{\partial \mathbf{h}_l}{\partial t} = \frac{\dot{b}_{S,l}}{\rho_S} = \frac{SMB_l}{A_l \cdot \rho_S} \tag{3.10}$$

To quantify the relative contribution of SMB and D to the overall mass loss plane-fitted elevation change ($\dot{h}$) and gridded elevations h_l (x_l, y_l, t) over land-

terminating glaciers and ice cap basins are used to calculate the elevation (h_l) hessian a_0 and gradient a_1, the longitudinal (x_l) and latitudinal (y_l) gradients a_2 and a_3, and the coefficient a_4 for each of the seven Arctic regions:

$$\dot{\mathbf{h}}_\mathbf{l}(x_l, y_l, h_l) \approx a_0\mathbf{h}_l^3 + a_1\mathbf{h}_l^2 + a_2\mathbf{h}_l + a_3\mathbf{x}_l + a_4\mathbf{y}_l + a_5 \tag{3.11}$$

The function describes the direct influence of elevation, latitude and longitude on SMBl-related elevation change $\dot{h}_l$. The coefficients a_i (Table 3.2) and gridded elevations $h_l(x_l,y_l,t)$ and $h_m(x_m,y_m,t)$ over land- and marine-terminating sectors are used, respectively, to calculate parametrised $\dot{h}_{p_l}$ and $\dot{h}_{p_m}$, separately for both types of basins. Bulk marine-terminating SMB_m is derived as follows:

$$\mathbf{SMB}_m = \mathbf{SMB}_l \cdot \sum_{n_m} \dot{h}_{p_m} / \sum_{n_l} \dot{h}_{p_l} \tag{3.12}$$

where SMB_l is equal to the total mass balance $\dot{m}_l$ of land-terminating glacier and ice cap basins (see Chapter 4, Appendices, Table 4.4), and n_l and n_m are the number of pixels in the gridded $\dot{h}_{p_l}$ and $\dot{h}_{p_m}$ maps, respectively. Discharge D is then calculated by subtracting SMB_m from the total mass balance $\dot{m}_l$ of marine-terminating glacier and ice cap basins.

Table 3.2: SMB parametrisation coefficients in [10^{-3} a^{-1}] and RMSE [m a^{-1}]. Numbers in brackets for each region indicate the latitude (lat_*ts*) and longitude (lon_*0*) at natural origin, which are used in the local polar stereographic projection to calculate the x and y components of the parametrisation of $\dot{h}$.

Region	a_0	a_1	a_2	a_3	a_4
FJL [80.5 55.0]	1.7 e^{-5}	-1.4 e^{-2}	4.5	1.4 e^{-3}	2.0 e^{-3}
NZ [75.5 61]	-2.9 e^{-6}	4.2 e^{-3}	-0.5	1.7 e^{-3}	0.3 e^{-3}
SZ [79.5 99]	-7.3 e^{-7}	-1.6 e^{-3}	2.0	-1.0 e^{-3}	0.2 e^{-3}
Sv [78.5 20]	6.3 e^{-7}	-2.9 e^{-3}	3.8	1.4 e^{-3}	1.6 e^{-3}
Ic [65 -19]	-	-	-	-	-
CAA-N [79 -84]	-5.3 e^{-7}	2.0 e^{-3}	-2.0	0.1 e^{-3}	-0.2 e^{-3}
CAA-S [70 -73]	-4.2 e^{-7}	1.3 e^{-3}	-0.6	4.8 e^{-5}	0.6 e^{-3}

To evaluate the parametrisation of $\dot{h}_l$, the root mean square error (RMSE) of the polynomial fit is calculated as:

$$\mathbf{RMSE} = \sqrt{\frac{\sum (\dot{h}_{p_l} - \dot{h}_l)^2}{n}} \tag{3.13}$$

where n is the number of grid cells. RMSE values vary regionally and range between 0.53 m a^{-1} and 2.43 m a^{-1}.

3.8.4 Validation of the SMB parametrisation

To evaluate the method for partitioning mass imbalance (see Section 3.8.3), the CryoSat-2 derived SMB is compared against SMB from the regional climate model RACMO2.3 using seven glaciological years (10/2010 – 09/2017) over the northern and southern Canadian Arctic glaciers, ice fields and ice caps (Figure 3.17).

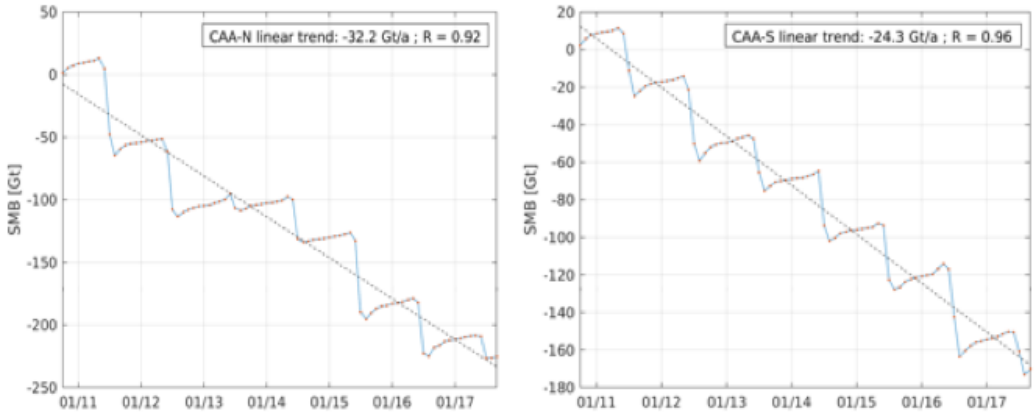


Figure 3.17: RACMO2.3 cumulative SMB between 01/2011 and 12/2017. Northern (CAA-N, left) and the southern (CAA-S, right) Canadian Arctic Archipelagos, (Noël et al., 2018).

Monthly RACMO2.3 data, down sampled to 1×1 km, and corresponding ice and snow masks were provided by Noël et al. (2018) upon request. Additional ice masks at 1 km resolution were produced for marine- and land-terminating basins, separately, for both the southern and the northern archipelagos, based on the RGI 6.0 split between the two types of basins. Annual RACMO2.3 SMB^{yy}

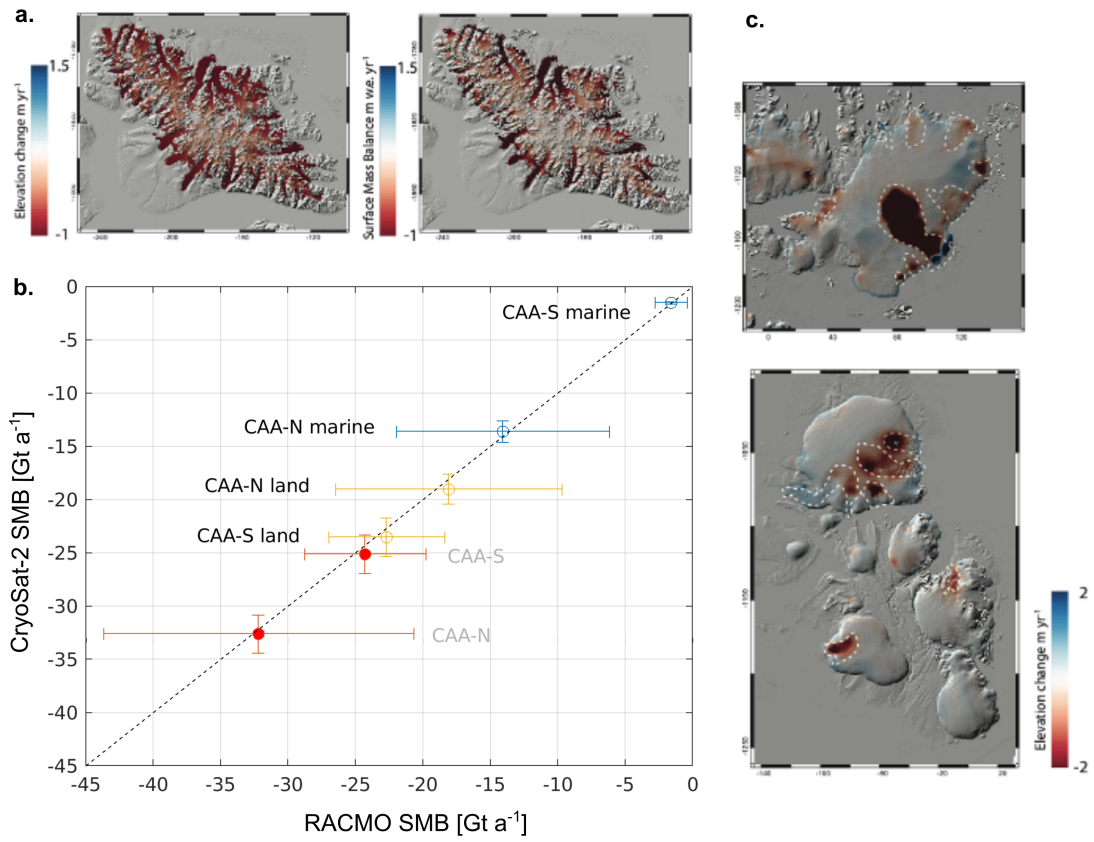


Figure 3.18: CryoSat-2 SMB parametrisation comparison with RACMO2.3. **(a)** CryoSat-2 derived $\dot{h}$ (left) versus RACMO2.3 SMB (right) over Bylot Island, CAA-S; **(b)** SMB from CryoSat-2 versus RACMO2.3 across the Canadian Arctic: all regions (red), land-terminating sectors (yellow), marine-terminating sectors (blue); **(c)** dynamic thinning $\dot{h} - \dot{h}_{pm}$ over major flow units in the Barents and Kara Sea region: Austfonna Ice Cap (upper panel) and Severnaya Zemlya archipelago (lower panel). The white dashed lines delineate the basins characterised by dynamic thinning.

was calculated pixelwise for each glaciological year (2010-2017) as the sum of monthly area specific SMB^{mm} expressed in kg m^{-2} multiplied by the pixel area A_{pix}, which is 1 km^2 for ice covered terrain, and 0 km^2 for land or water:

$$\mathbf{SMB}^{yy} = \mathbf{A}_{pix} \cdot 10^{-6} \cdot \sum_{k=1}^{12} \mathbf{SMB}^{mm} \tag{3.14}$$

Integrated over the entire glaciated area, total SMB by region and terminus type is in excellent agreement with CryoSat-2 derived SMB for all glacial segments in the Canadian Arctic (Figure 3.18b). This highlights the ability of the parametrisation described in Section 3.8.3 to determine bulk SMB_m, and to cap-

ture the first-order SMB dependency on elevation and geographical location, as well as variability in SMB between land- and adjacent marine-terminating sectors (Figure 3.18a,c).

There is significant difference in the range of uncertainties associated with derived SMB from CryoSat-2 and RACMO2.3 (Figure 3.18b). The large uncertainties in the RACMO2.3 model result from large biases between modelled data and observations, while uncertainties in the CryoSat-2 parametrisation could be underestimated by the assumption that all 0.5×0.5 km samples are independent (see Section 3.8.6). In reality, SMB patterns may be correlated over distances of several kilometers depending on the region (e.g. Moholdt et al., 2010; Rolstad et al., 2009), which reduces the number of independent samples and increases the error. This effect may be difficult to quantify using radar altimetry, given the fluctuating nature of radar backscatter with changing surface conditions and topography.

Over Svalbard, parametrised SMB (-7.1 ± 0.6 Gt a^{-1}) compares well with reconciled 2010-2019 estimates from Schuler et al. (2020) (-8 ± 2 Gt a^{-1}) (Table 3.3), although there is a large difference in the estimated discharge D between the two approaches. Nevertheless, Schuler et al.'s estimated dynamic imbalance (-2 ± 6 Gt a^{-1}) is based on two years of additional data, and it is calculated as the residual between total geodetic mass balance and modelled SMB, with a large associated uncertainty of ± 6 Gt a^{-1}, which keeps this estimate within error compared with discharge derived from CryoSat-2 (-6.2 ± 0.9 Gt a^{-1}) (Table 3.3). The latter is also in excellent agreement with calving rates from Blaszczyk et al. (2009) (-6.1 ± 1.5 Gt a^{-1}) (Table 3.3), which to date is the only available study to have quantified frontal ablation of Svalbard's glaciers and ice caps (Schuler et al., 2020). However, given the large increase in dynamic ice loss from Svalbard's tidewater glaciers during the 2010s (Schuler et al., 2020), this comparison suggests that either Blaszczyk's 2000-2006 estimate is too large, or bulk D derived from the CryoSat-2 SMB parametrisation was underestimated.

Only $\sim 10\%$ of Franz Josef Land's glaciated area (1240 km^2) is land-terminating,

Table 3.3: CryoSat-2 SMB parametrisation over Svalbard and comparison with other datasets. MT = marine-terminating basins, LT = land-terminating basins, SMB = surface mass balance, D = ice discharge. Blaszczyk et al. (2009) estimates exclude calving from Kvitøya Ice Cap).

Units [Gt a^{-1}]	MT MB	LT SMB	Total SMB	D	Total MB
CryoSat-2 (2010-2017)	-4.6 ± 0.5	-2.5 ± 0.3	-7.1 ± 0.6	-6.2 ± 0.9	-13.3 ± 0.8
van Pelt et al. (2019) (2010-2017)	-0.4 ± σ	-1.4 ± σ	-1.8 ± σ	-6.1 ± 1.5	-7.9 ± σ
Schuler et al. (2020) (2010-2019)	-	-	-8 ± 2	-2 ± 6	-10 ± 4
Blaszczyk (2009) (2000-2006)	-	-	-	-6.1 ± 1.5	-

which can be considered a limiting factor for the parametrisation in this region, as the number of drainage points is relatively small. Overall, the high density of swath measurements allows to partition regional mass balance, for the first time over the entire extent of Arctic glaciers and ice caps, into losses occurring at the ice surface and via ice discharge. The uncertainties associated with parametrised SMB and bulk D depend on the size of the glaciated area terminating on land and on the spatial correlation in SMB between samples. The latter are difficult to assess in the absence of independent data for comparison.

3.8.5 Contribution to sea level rise (SLR)

Volumetric glacier and ice cap changes were transformed into their water equivalent and multiplied by the total area A_{ocean} of the world's oceans (3.618×10^8 km^2) to obtain the sea level equivalent (SLE) of the ice loss in mm a^{-1}:

$$\mathbf{SLE} = \dot{\mathbf{V}} \cdot \rho_{ice}/\rho_w \cdot \mathbf{A}_{ocean} \tag{3.15}$$

where ρ_w = 997 kg m^{-3} is the density of water and ρ_{ice} = 850 kg m^{-3} the density of ice.

3.8.6 Error calculation

The uncertainty associated with the calculated mass imbalance is the result of unknown fluctuations in near-surface snow/firn/ice densities, gradients in snow accumulation, and errors in elevation trends derived from the satellite measure-

ments. The elevation measurement errors can be attributed to both instrument system errors (intrinsic to *level 1b* data) and to retracking errors in the swath processing algorithm. Here, a representative uncertainty of the mass imbalance is estimated, using the same method as in Foresta et al. (2016). Errors in the measurement are statistically accounted for by extracting from the plane-fit (equation 3.1) covariance matrix C_i the variances $\epsilon_{\dot{h},i}$, which are assigned to the corresponding rates of $\dot{h}$ in each individual grid cell i:

$$\mathbf{C_i} = cov(c_{n,i}) = \mathbf{M}^{-1} cov(h) [\mathbf{M}^{-1}]^T \tag{3.16}$$

where $c_{n,i}$ is the vector of coefficients [c_0 c_1 $\dot{h}$ c_3] of the model in parameters Equation 3.1, h are the input elevations and M = [x y t 1] is the parametrisation matrix (Foresta et al., 2018). The covariance matrix $cov(h_i)$ is a diagonal matrix with elements equal to the squared elevation differences between the observed and parametried elevations in each pixel $(h_i - h'_i)^2$ (Foresta et al., 2018). The square root of each of the elements in C_i is the standard deviation of the corresponding model parameters $c_{n,i}$, with error $\epsilon_{\dot{h},i}$ on surface elevation change extracted from the third element in C_i:

$$\epsilon_{\dot{h},i} = \sqrt{C_{i,33}} \tag{3.17}$$

For a given glaciated raster area of n pixels, this results in a total error on the rates of elevation change $\epsilon_{\dot{h}}$ equal to:

$$\epsilon_{\dot{h}} = \frac{1}{n} \sqrt{\sum_{i}^{n} \epsilon_{\dot{h},i}^2} \tag{3.18}$$

Across the Arctic, 95 % of errors on $\dot{h}$ are below 1 m a^{-1}.

Depending on the type of drainage basin, the error in volume change $\epsilon_{\dot{V}}$ is obtained by propagating $\epsilon_{\dot{h}}$ either via hypsometric averaging (land-terminating basins), or rescaling by the ratio of total-to-measured surface area (marine-terminating basins). In the case of hypsometric averaging, the error associated

with volume change results in:

$$\epsilon_{\dot{V},\,hypso} = \frac{1}{n_j}\sqrt{\sum_{j}^{n_j}\epsilon_{\dot{V},j}^2} = \frac{A_{pixel}}{n_j}\sqrt{\sum_{j}^{n_j}\sum_{i}^{n_i}\epsilon_{\dot{h},i}^2} \tag{3.19}$$

where n_j is the number of elevation bands and n_i the number of pixels in each elevation band j. For scaling, the error on volume change is calculated as:

$$\epsilon_{\dot{V},\,scale} = \frac{n_{total}}{n_k}\cdot\frac{1}{n_k}\cdot\sqrt{\sum_{k}^{n_k}\epsilon_{\dot{V},k}} = \frac{A_{pixel}}{n_k^2}\cdot\sqrt{\sum_{i}^{n_k}\epsilon_{\dot{h},i}^2} \tag{3.20}$$

where n_k is the number of denoised pixels in the $\dot{h}$ map. For the volume-to-mass conversion a constant error on the density $\epsilon_\rho = 60$ kg m^{-3} is assumed following the recommendation by Huss (2013). The error on the mass imbalance is then calculated using uncorrelated Gaussian error propagation as:

$$\epsilon_{\dot{m}} = |\dot{m}|\cdot\sqrt{\left(\frac{\epsilon_{\dot{V}}}{\dot{V}}\right)^2 + \left(\frac{\epsilon_\rho}{\rho_{ice}}\right)^2} \tag{3.21}$$

For land-terminating drainage basins it is assumed that $\epsilon_{\dot{m}} = \epsilon_{SMB}$. SMB uncertainties of marine-terminating basins are estimated by assigning the root mean square deviation of the SMB parametrisation to the error $\epsilon_{\dot{h}}$ on $\dot{h}$, and applying Gaussian error propagation as described above. For discharge D uncertainties ϵ_D are derived from the quadrature of $\epsilon_{\dot{m}}$ and ϵ_{SMB}:

$$\epsilon_D = \sqrt{\epsilon_{\dot{m}}^2 + \epsilon_{SMB}^2} \tag{3.22}$$

In Equations 3.18 and 3.22 the uncertainty is expressed in terms of the variance of the elevation change (SMB) error. It is thereby assumed that 0.5×0.5 km samples are independent, so that integrated errors are uncorrelated. Depending on the location however, elevation change and SMB patterns can be correlated over distances of several (5-10) kilometres (e.g. Moholdt et al., 2010; Rotschky et al., 2004), which is supported by the fact that swath pixels can span multiple pixels. This reduces the number of independent samples, and hence the overall

uncertainty on SMB may actually be considerably higher, potentially by several orders of magnitude (Rolstad et al., 2009, e.g.) than presented here. Because SMB correlation distances are not available at the Arctic scale, they were not accounted for in this thesis.

3.9 Discussion on measurement uncertainty

As described in Section 3.8.6, the error on elevation change $\epsilon_{\dot{h}}$ is extracted from the covariance matrix of the elevation measurement parametrisation (Equation 3.1). Calculated as such, $\epsilon_{\dot{h}}$ represents a statistical estimate of the uncertainty associated with the trend in surface elevation as modelled from the measurements. This approach, often used in the literature (e.g. Foresta et al., 2016, 2018), does not specifically account for the uncertainty related to each individual elevation sample at each step in the measurement and processing stages. From a physical perspective, the uncertainty associated with each elevation measurement can be divided into two categories, namely retrieval errors ϵ_r, and system errors ϵ_s (CryoSat Science Advisory Group, 2001):

$$\epsilon = \epsilon_r + L_r \cdot \epsilon_s \tag{3.23}$$

where L_r are a set of operations in the processing stage by which retrieval errors are introduced to the end-product. For example, physical properties retrieved from the radar signal such as power, phase, coherence and delay time, are processed through phase unwrapping, speckle noise reduction, filtering of echo power and coherence, retracking (POCA), etc. In turn, each of the measured properties carry a specific uncertainty inherent to instrument precision, the sum of which is included in the instrument system error ϵ_s. Finally, retrieval errors, ϵ_r, are introduced with any assumption made on the existing relationship between backscatter fluctuations, surface geometry, and elevation measurements. In simple terms, ϵ_s stem from imperfect engineering of the instruments, and ϵ_r

arise from a flawed description of the scattering from the atmosphere and the ice surface (CryoSat Science Advisory Group, 2001). Both ϵ_r and ϵ_s, as well as L_r, are closely related to the CryoSat-2 processing chain, with ϵ_s equal to the sum of errors introduced during the *level 1b* segment, and ϵ_r the uncertainties introduced mainly during the swath processing (*level 2*) stage.

The estimation of ϵ_r and ϵ_s can be achieved via measurement validation (e.g. OIB airborne or ICESat laser measurements) and instrument calibration, respectively (CryoSat Science Advisory Group, 2001). In the case of CryoSat-2, instrument calibration is regularly performed both remotely (e.g. Foresta, 2015) and via a number of ancillary equipment installed onboard the satellite, whose purpose is to provide independent measurement of ϵ_s. Instrument calibration introduces corrections of the satellite position, rectifies orbital and time measurement errors and adjusts the range bias, including the removal of tropospheric and ionospheric refraction errors and other geophysical biases such as the geocentric polar tide, solid Earth tide, and ocean loading tide errors (e.g. Foresta, 2015).

System errors are more accurately predictable because they form the basis of instrument specifications formulated in advance so that the measurements meet certain performance requirements. These requirements are directly related to the magnitude of ϵ_s. However, even though ϵ_s is determined and corrected for via calibration, the term $L_r \cdot \epsilon_s$, specific to each measurement, remains unknown and needs to be estimated (CryoSat Science Advisory Group, 2001). The same applies to the retrieval error ϵ_r, for which the shape and characteristics of the echo due to both topographic irregularities and variations in the scattering horizon from the air-firn interface to a depth of several meters within the snowpack need to be established through validation experiments.

In interferometric mode, the radar echoes from the ice cap margins come in a great variety of shapes, as these are retrieved over areas characterised by complex topography and rapidly changing ice surface conditions, especially at low elevation. Hence, in order to gain understanding of the extent and magnitude of the retrieval error ϵ_s over Arctic GIC, a comparison with independent laser

altimetry, which retrieve the return signal directly from the ice surface, would be ideally made over locations with the aforementioned attributes. To be efficient, validation data would effectively need to coincide spatially and temporally with the CryoSat-2 measurements. Currently however, validation data from laser instruments are only available from the interior of the ice sheets and from a few larger ice caps and cover relatively short time spans (see Section 3.5). It would make little sense to establish spatial and temporal covariance functions from these limited observations and to extrapolate these to the rest of the Arctic.

In conclusion, although surface elevation change errors are likely underestimated by the statistical approach currently applied, the latter is at the moment the most reasonable error approximation achievable. Considering the information obtained from existing validation exercises, the high spatial and temporal resolution achieved with CryoSat-2, and the general properties of the retrieved signal which is first and foremost, and in particular at low elevation, of very high quality across the Arctic, it is reasonable to believe that the modelled uncertainty $\epsilon_{\dot{h}}$ is relatively accurate where a large volume of data is available (*i.e.* at large spatial and temporal scales), and probably more realistic than the uncertainty on density fluctuations applied for the computation of mass budgets. Density fluctuations could be widely misrepresented at the Arctic scale, in particular in areas with high variability in accumulation rates, and where the firn temperature is close to the melting point (CryoSat Science Advisory Group, 2001). Hence, in order to improve the assessment of the overall error associated with the estimation of mass change from radar altimetry, further densification exercises and modelling experiments are needed, in addition to a rapid expansion of validation and calibration campaigns for satellite measurements.

3.10 Summary of Methods

The methodologies developed in this chapter allowed to make a set of critical advances in the utilisation of interferometric swath altimetry to overcome some of

the key difficulties inherent to large-scale mass balance assessments, and providing new opportunities for the analysis of mass imbalance in relation to climate forcing. These methodological developments were exploited in the result Chapters 4-5 and can be summarised as follows:

- Section 3.1 analysed the current state of Arctic glacier inventories and generated a partitioning, based on RGI metadata and added corrections, between land- and marine-terminating glacier and ice cap basins across all Arctic regions;
- Sections 3.2 - 3.3 layed the foundations for the swath processing of CryoSat-2 measurements at the pan-Arctic scale, and for the first time sampling the surface of all Arctic glaciers and ice caps outside of Greenland and Alaska, including those featuring small glaciated areas and complex topography;
- Section 3.4 tested the capability of an existing algorithm (Foresta et al., 2018) to produce robust, high-resolution time series of surface elevation change over individual catchments at the pan-Arctic scale;
- Section 3.6 utilised validation results from Section 3.5 to introduce a novel and robust procedure, including the use of ROC curves, to identify and remove spurious samples from the gridded swath products;
- Section 3.7 optimised both spatial and temporal sampling density at the ice surface to produce ice cap wide volume changes with drastically reduced associated uncertainties;
- The proposed volume change computation method described in Section 3.7 introduced for the first time an adaptable method aimed at dissociating, based on the predominant mechanism of ice loss in each individual region, between two main regionalisation schemes, that is hypsometric averaging and upscaling;
- Section 3.8 proposed a polynomial parametrisation approach for the partitioning of mass imbalance into dynamic ice loss and anomalous change at the ice surface.

3.11 Appendices

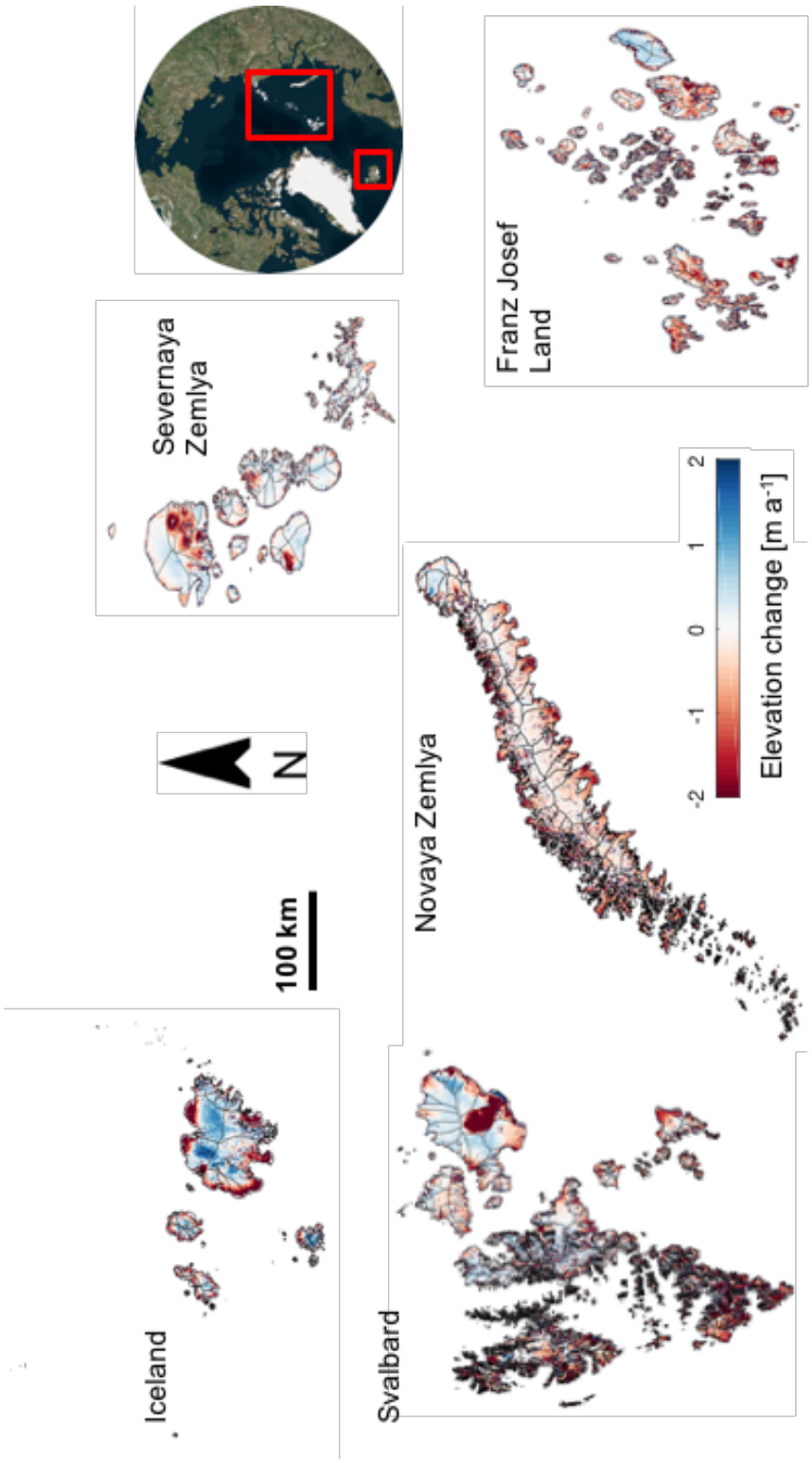


Figure 3.19: Maps of surface elevation change (2010-2017) east of Greenland.

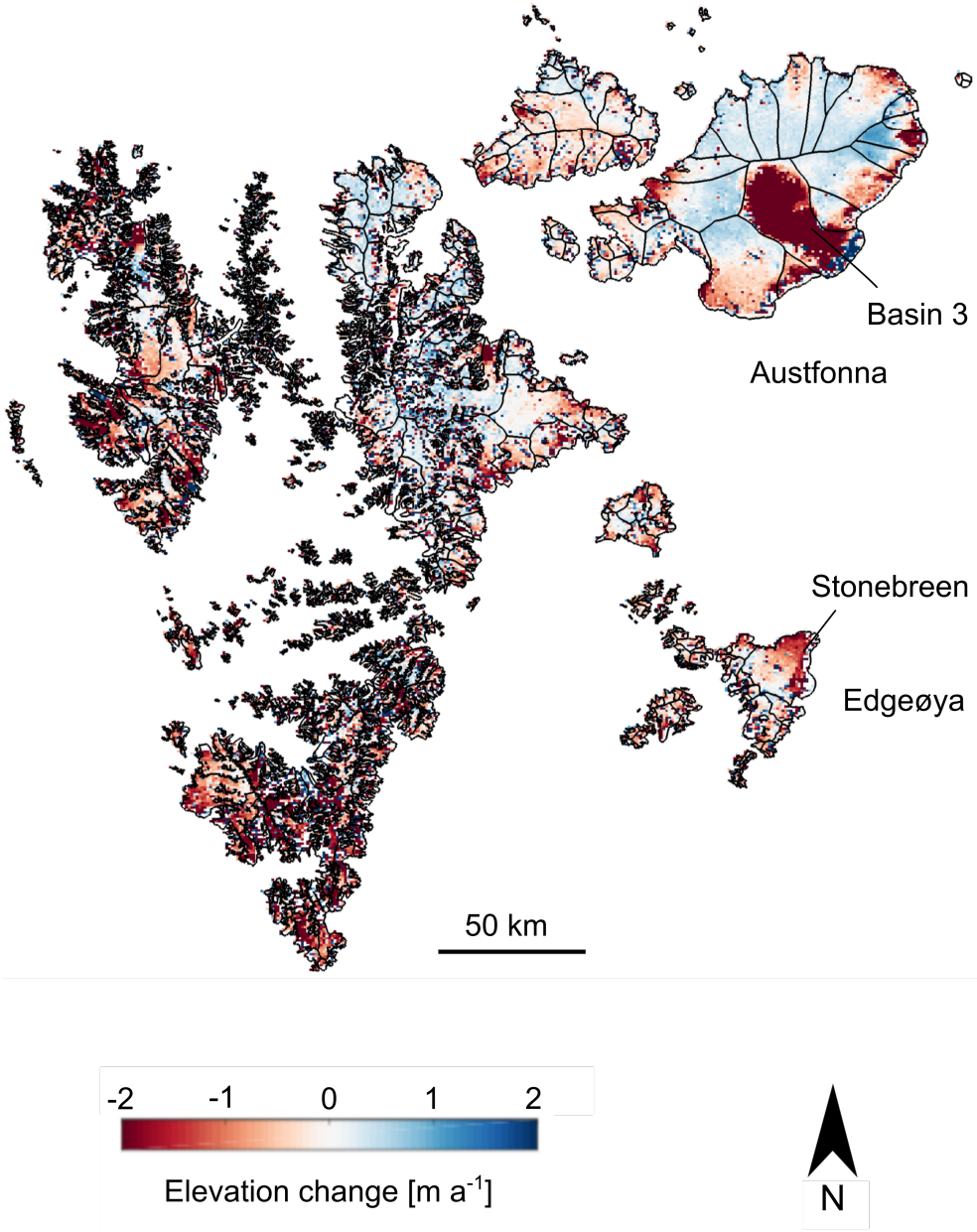


Figure 3.20: Gridded map of surface elevation change (2010-2017) over Svalbard at 500 × 500 m resolution. The map includes all parametrised elevation changes (Equation 3.1), including the spurious samples removed during the subsequent computation of volumetric change (Section 3.7).

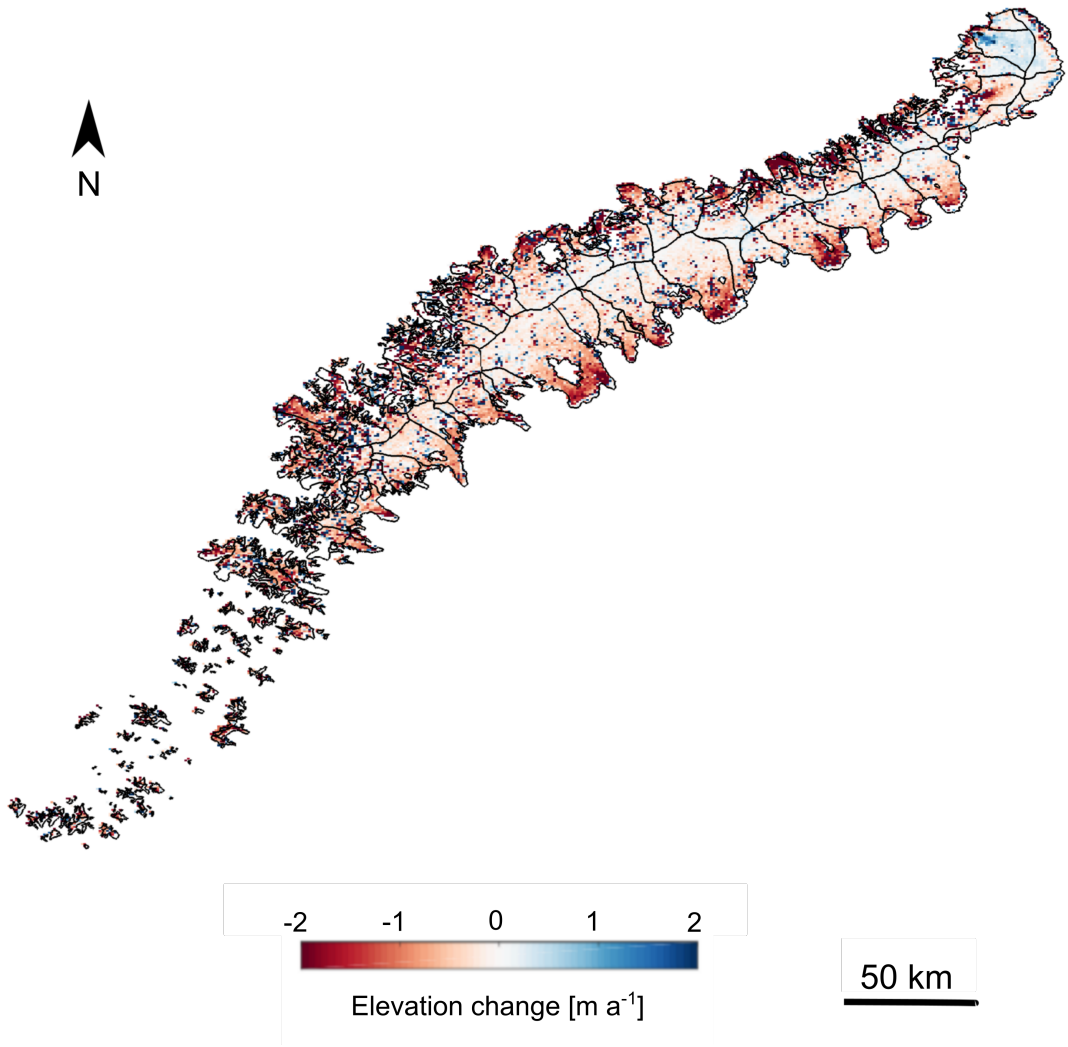


Figure 3.21: Gridded map of surface elevation change (2010-2017) over Novaya Zemlya, Russian Arctic, at 500 × 500 m resolution. The map includes all parametrised elevation changes (Equation 3.1), including the spurious samples removed during the subsequent computation of volumetric change (Section 3.7).

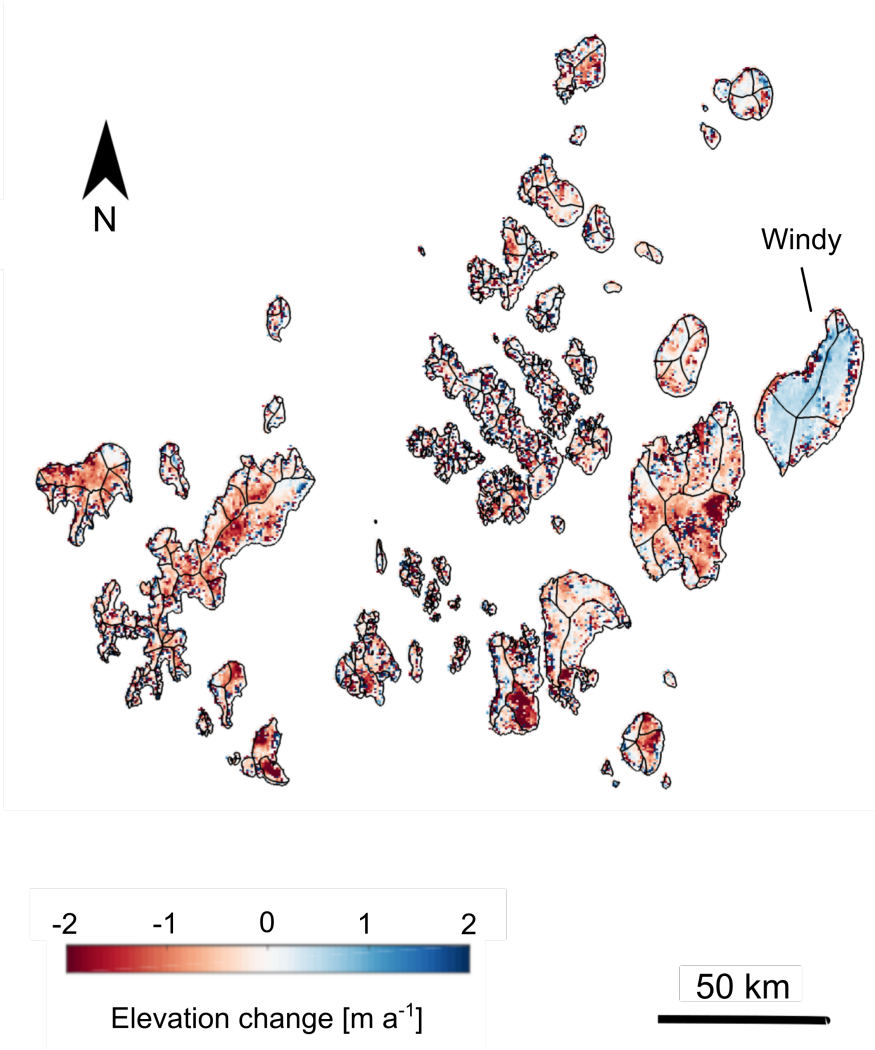


Figure 3.22: Gridded map of surface elevation change (2010-2017) over Franz Josef Land, Russian Arctic, at 500 × 500 m resolution. The map includes all parametrised elevation changes (Equation 3.1), including the spurious samples removed during the subsequent computation of volumetric change (Section 3.7).

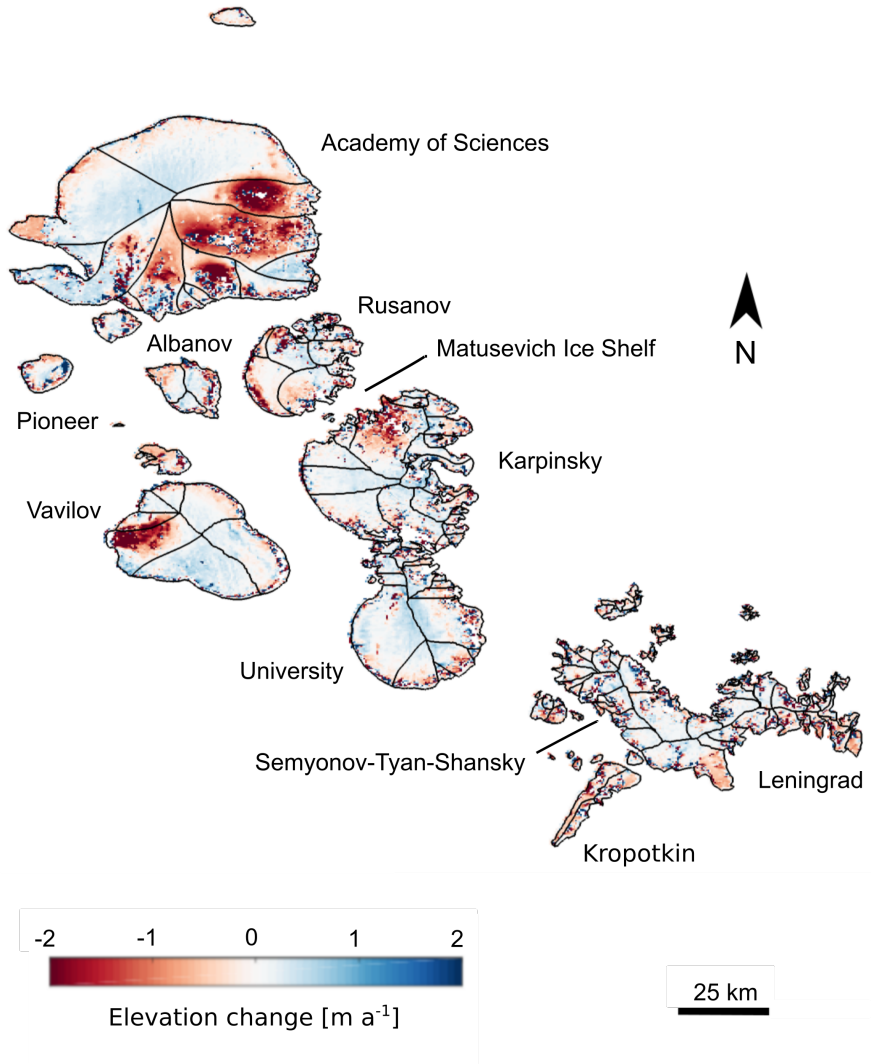


Figure 3.23: Gridded map of surface elevation change (2010-2017) over Severnaya Zemlya, Russian Arctic, at 500 × 500 m resolution. The map includes all parametrised elevation changes (Equation 3.1), including the spurious samples removed during the subsequent computation of volumetric change (Section 3.7).

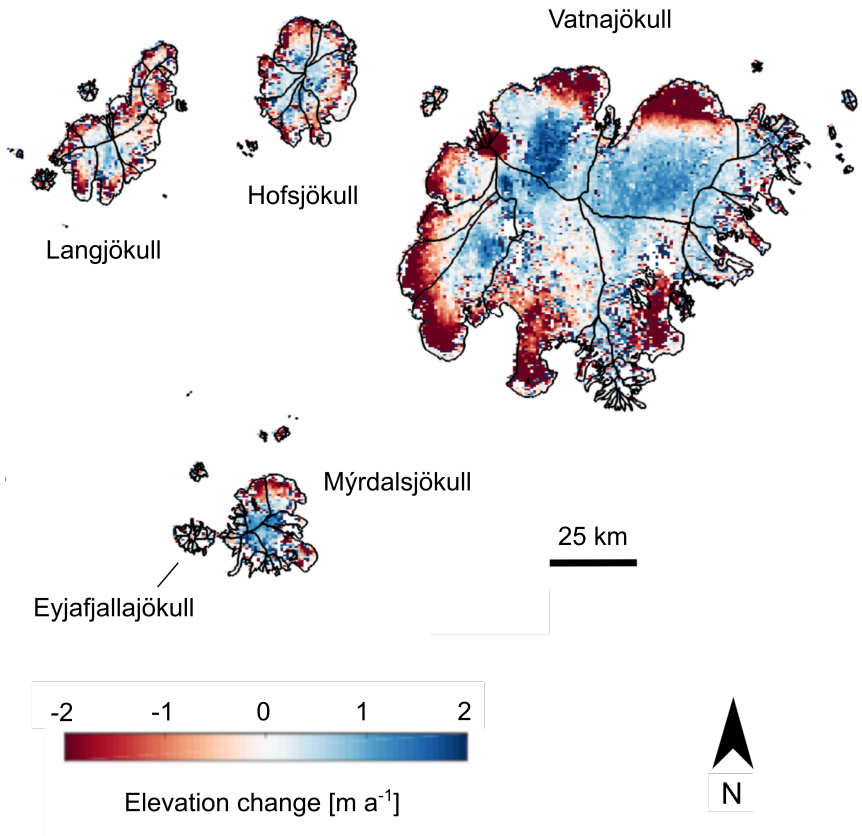


Figure 3.24: Gridded maps of surface elevation change (2010-2017) over Icelandic ice caps, at 500 × 500 m resolution. The maps include all parametrised elevation changes (Equation 3.1), including the spurious samples removed during the subsequent computation of volumetric change (Section 3.7).

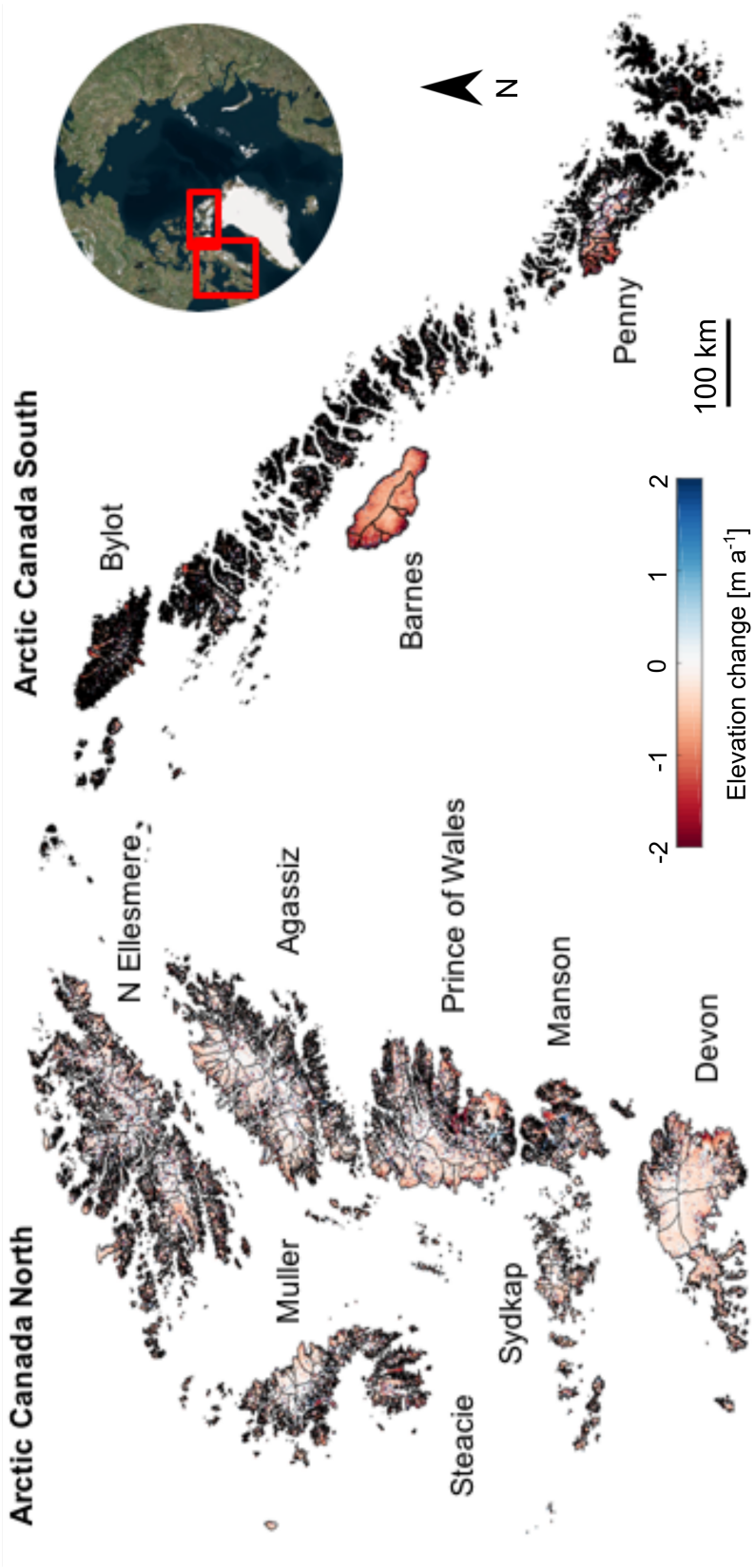


Figure 3.25: Maps of surface elevation change (2010-2017) in the Canadian Arctic.

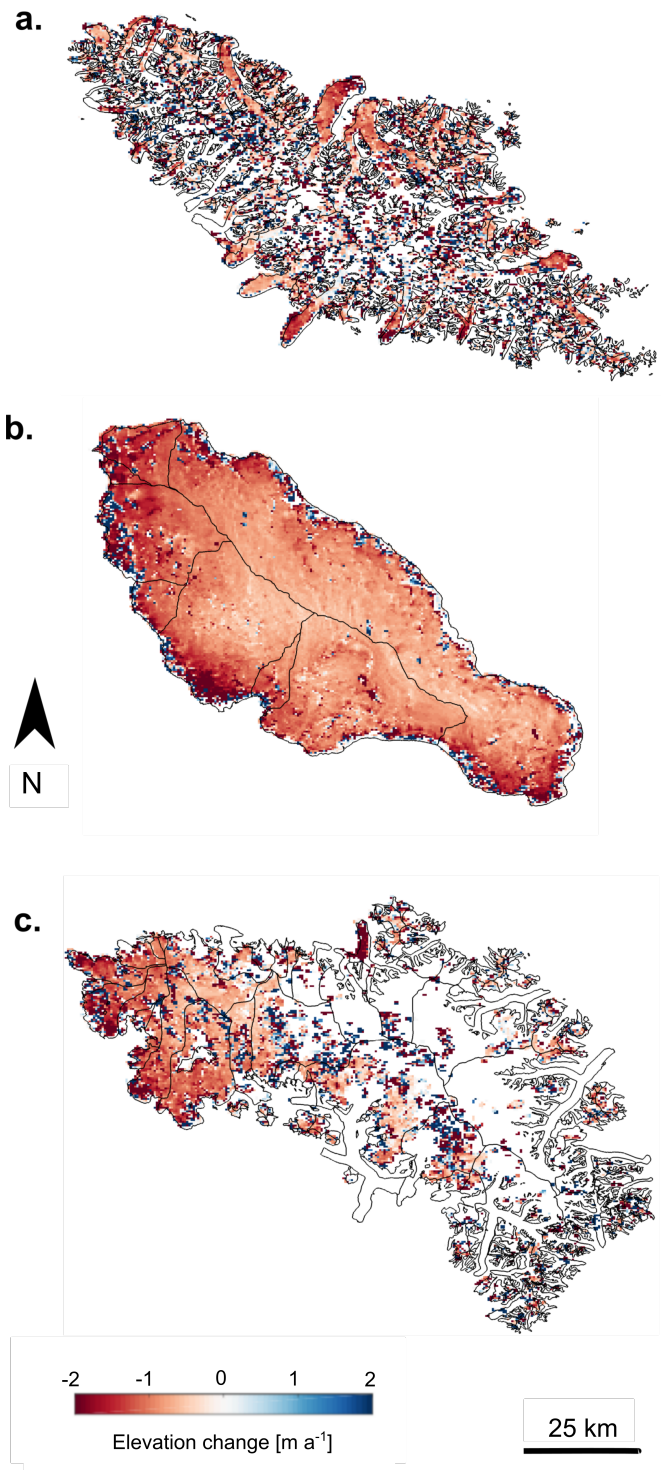


Figure 3.26: Gridded maps of surface elevation change (2010-2017) over Bylot Island (a), and Barnes (b) and Penny (c) Ice Caps, at 500 × 500 m resolution. The maps include all parametrised elevation changes (Equation 3.1), including the spurious samples removed during the subsequent computation of volumetric change (Section 3.7).

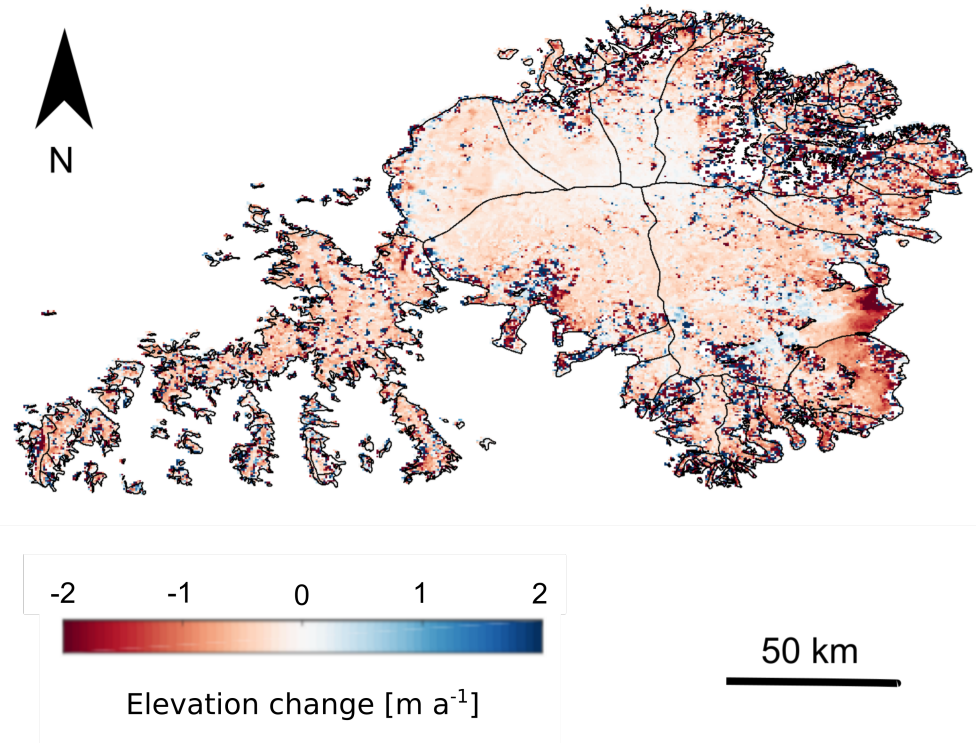


Figure 3.27: Gridded map of surface elevation change (2010-2017) over Devon Ice Cap, at 500 × 500 m resolution. The map includes all parametrised elevation changes (Equation 3.1), including the spurious samples removed during the subsequent computation of volumetric change (Section 3.7).

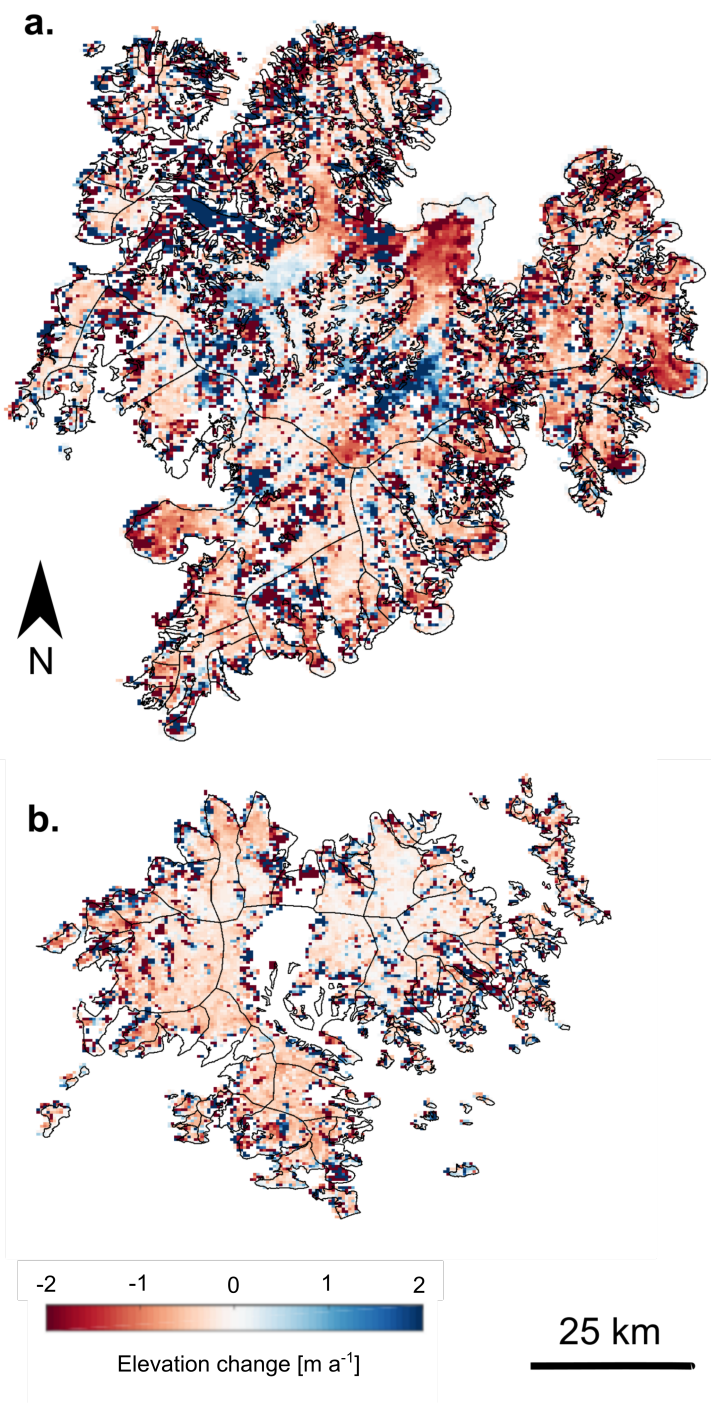


Figure 3.28: Gridded maps of surface elevation change (2010-2017) over Manson (a) and Sydkap (b) Ice Caps, at 500 × 500 m resolution. The maps include all parametrised elevation changes (Equation 3.1), including the spurious samples removed during the subsequent computation of volumetric change (Section 3.7).

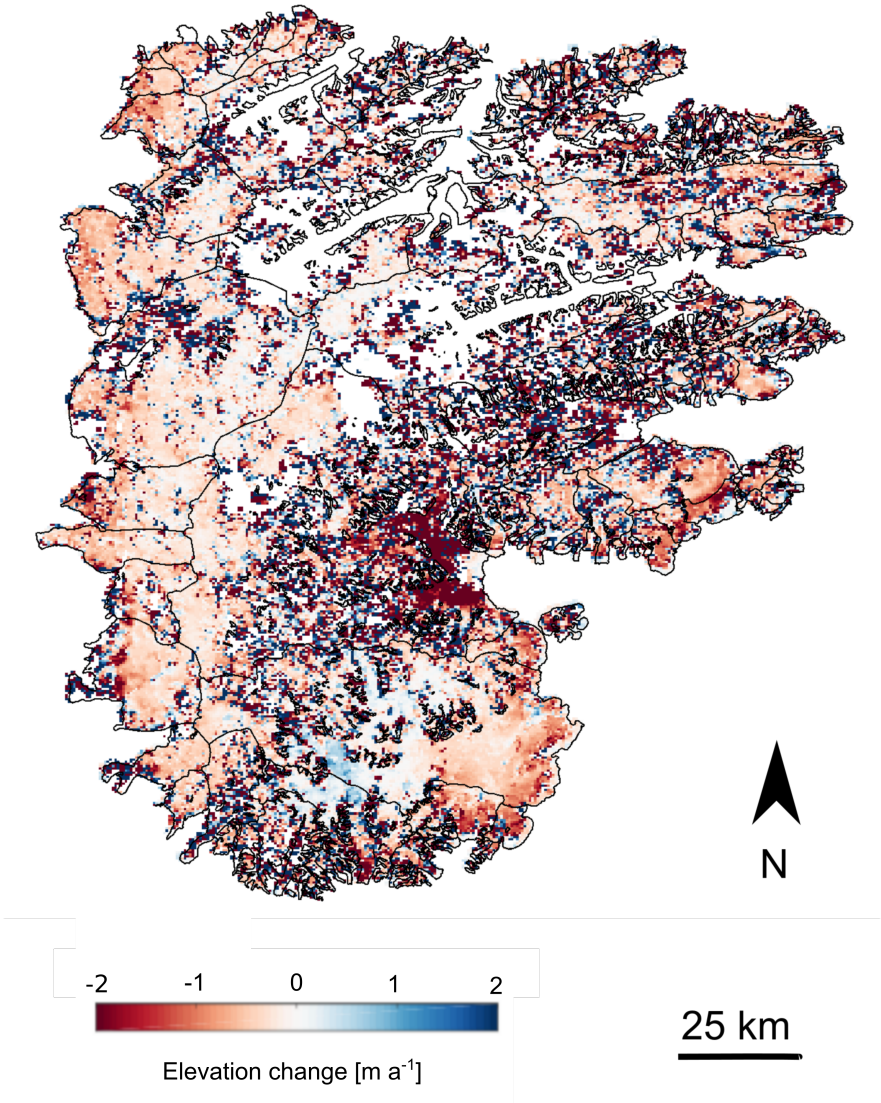


Figure 3.29: Gridded map of surface elevation change (2010-2017) over Prince of Wales Ice Field, at 500 × 500 m resolution. The map includes all parametrised elevation changes (Equation 3.1), including the spurious samples removed during the subsequent computation of volumetric change (Section 3.7).

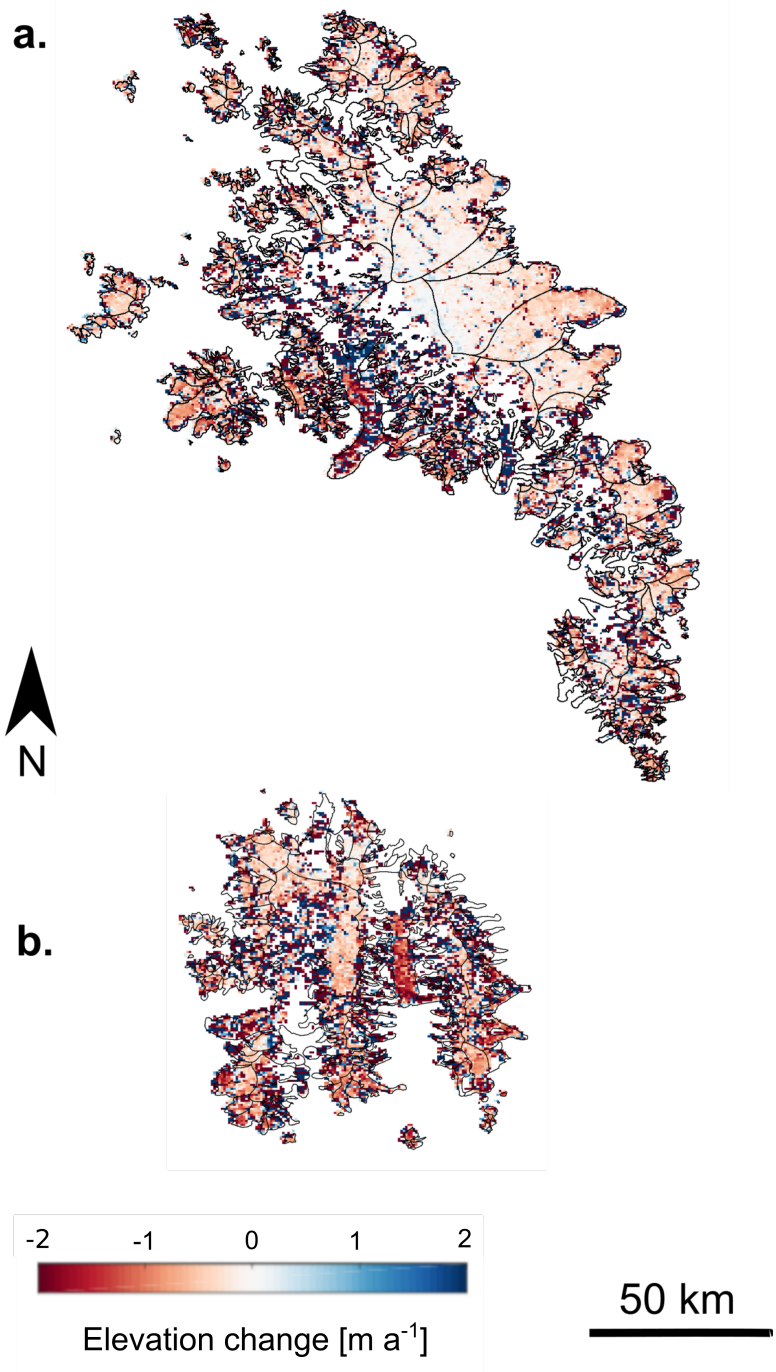


Figure 3.30: Gridded maps of surface elevation change (2010-2017) over Muller (a) and Steacie (b) Ice Caps, at 500 × 500 m resolution. The maps include all parametrised elevation changes (Equation 3.1), including the spurious samples removed during the subsequent computation of volumetric change (Section 3.7).

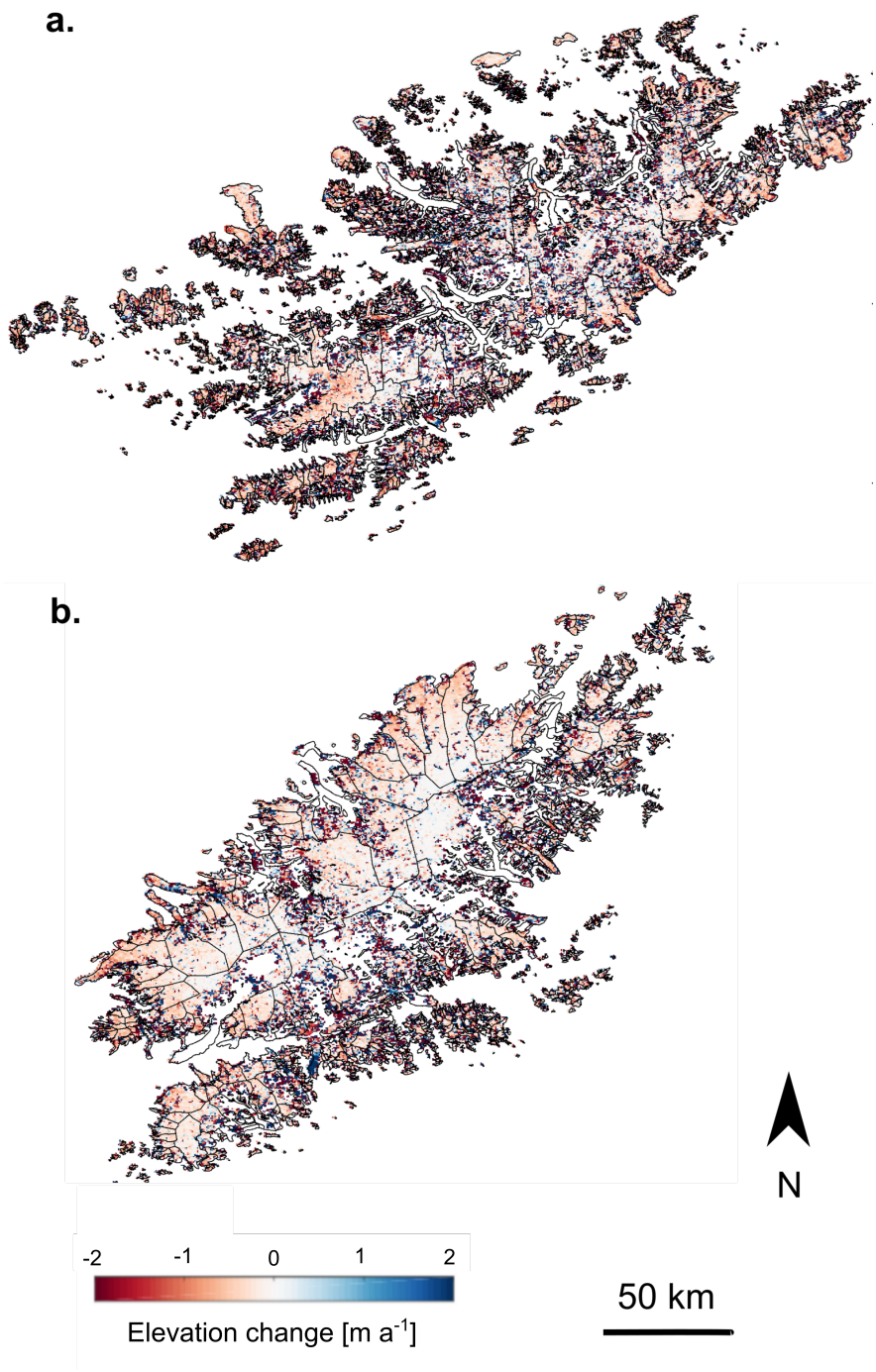


Figure 3.31: Gridded maps of surface elevation change (2010-2017) over Northern Ellesmere ice fields (a) and Agassiz Ice Cap (b), at 500 × 500 m resolution. The maps include all parametrised elevation changes (Equation 3.1), including the spurious samples removed during the subsequent computation of volumetric change (Section 3.7).

Chapter 4

Changes in elevation and mass of Arctic glaciers and ice caps (2010-2017)

4.1 Abstract

Arctic glaciers and ice caps (GIC) are losing mass rapidly, and this process is expected to continue during the 21^{st} century owing to polar amplification of climate warming. Here, we use seven years of CryoSat-2 swath interferometric altimetry to track changes in the volume of Arctic GIC. From these data, we produce a pan-Arctic assessment of GIC mass imbalance, and we partition their losses into signals associated with atmospheric processes and glacier dynamics. Between 2010 and 2017, Arctic GIC lost 609 ± 7 Gt of ice, contributing 0.240 ± 0.007 millimetres per year to global sea level rise. While surface ablation is responsible for 87 % of losses across the Arctic, dynamic imbalance is increasing in the Barents and Kara Sea region where it now accounts for 43 % of total ice loss. Arctic GIC's dynamic imbalance is associated with a northward shift of Atlantic climate, and this effect should be considered in global sea level projections.

4.2 Introduction

Arctic glaciers and ice caps (GIC) are key players in the local freshwater budget, impact thermohaline forcing in the North Atlantic (Thornalley et al., 2018; Yang et al., 2016), and are significant contributors to global eustatic sea level rise (Ciracì et al., 2020; Gardner et al., 2013; Zemp et al., 2019). They store 40 % of the global GIC ice volume, equating to 144 mm of sea level equivalent (Farinotti et al., 2019), and their losses are currently increasing as atmospheric and oceanic forcing intensify (Barton et al., 2018; Ding et al., 2014), and as Arctic sea ice cover shrinks (Onarheim et al., 2018). Furthermore, the dynamic response of land ice to climate forcing constitutes the main uncertainty in global sea level projections for the next century (Church et al., 2013; Martin and Adcroft, 2010). To address this knowledge gap, observations of the relative contribution of both surface mass balance (SMB) and ice dynamics (D) to the total losses are necessary. A recent study finds that between 1972 and 2018, D accounted for 66 % of the total mass imbalance of the Greenland Ice Sheet (Mouginot et al., 2019). For the GIC of the Arctic however, the SMB-to-D ratio is unknown.

SMB is determined by thermodynamic processes at the ice surface, and is modified by shifts in large-scale atmospheric circulation patterns (Delhasse et al., 2018) and by CO_2 - induced radiative forcing (Byrne and Schneider, 2018; Shindell and Faluvegi, 2009). In addition to negative overall SMB, the Arctic GIC mass imbalance was amplified in recent years by the large-scale destabilisation of marine-terminating drainage basins, during which ice acceleration and flux to the ocean was locally increased by several orders of magnitude (McMillan et al., 2014; Nuth et al., 2019; Strozzi et al., 2017a; Willis et al., 2018). The persistent incursion of warm North Atlantic Ocean water into the Arctic Ocean is thought to have direct impact on sea ice extent and tidewater glacier dynamics (Barton et al., 2018; McMillan et al., 2014; Polyakov et al., 2017). The respective role of internal processes, commonly ascribed to glacier surges, and external climatic forcing in driving these dynamic instabilities remains largely unclear (Dunse et

al., 2015; McMillan et al., 2014). The relative impact of atmospheric and oceanic influences on glacier fluctuations at the ice-ocean interface is also uncertain, with potential control from both oceanic heat transport and surface runoff (Cowton et al., 2018). Here, we use CryoSat-2 swath interferometric altimetry (Foresta et al., 2016; Gourmelen et al., 2018) to measure changes in the volume of Arctic GIC with unprecedented spatial resolution and to partition the observed changes into signals associated with meteorology, via SMB, and glacier dynamics.

4.3 Pan-Arctic view of GIC thinning

We derive rates of change in land ice elevation change $\dot{h}$ in all areas of the Arctic beyond Greenland. This includes the southern and northern Canadian Arctic Archipelagos (CAA-S and CAA-N, respectively), Iceland (Ic), Svalbard (Sv), and the Russian Arctic Archipelagos (RAA) of Franz Josef Land (FJL), Novaya Zemlya (NZ) and Severnaya Zemlya (SZ) (Figure 4.1). We apply swath processing to CryoSat-2 altimetry data spanning the period 2010-2017 to retrieve time-dependent elevation measurements over the GIC (Gourmelen et al., 2018). The high density of observations enables us to compute mean $\dot{h}$ over unit areas of 500 by 500 m to ensure sufficient spatial detail while maximising the number of observations in each resolution cell (Foresta et al., 2016) (see Chapter 3, Sections 3.2-3.3). Regionally, this translates into a ratio of measured-to-total glaciated area equal to 83 % over the GIC of the Russian Arctic, 79 % over Svalbard and Iceland, and 60 % over the Canadian Arctic, with good coverage over the ice margins (Appendices, Table 4.4).

Ice thinning is widespread across the Arctic, and the median rate of elevation change is -0.25 m a^{-1}. There is, however, considerable spatial variability, and the 5 % and 95 % quantiles are -1.65 m a^{-1} and +0.70 m a^{-1} respectively, reflecting the diversity of responses of ice masses to forcing across the Arctic (Figure 4.1).

The climate of the southern and northern Canadian Arctic Archipelagos exhibits low interannual variability in precipitation but high variability in summer

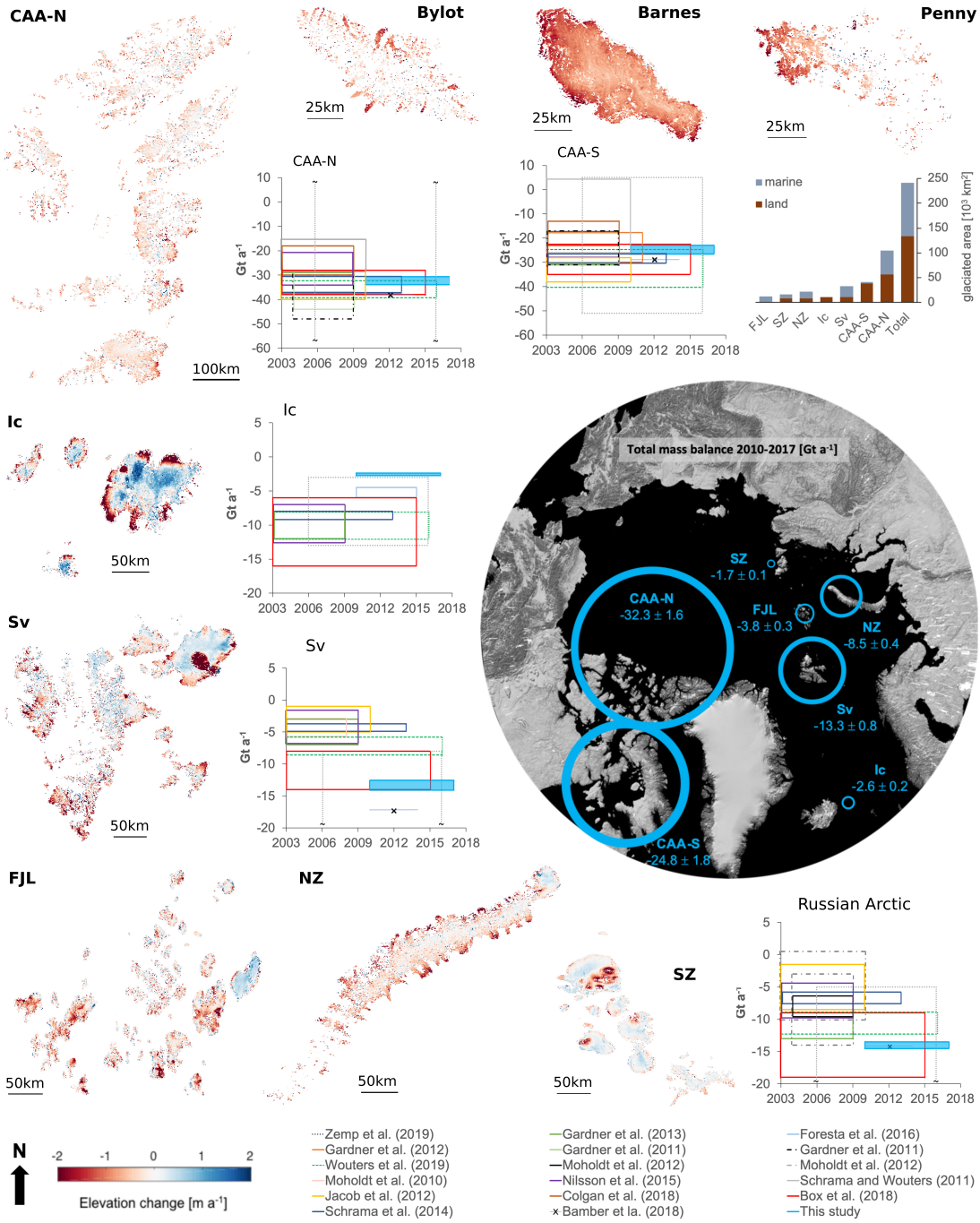


Figure 4.1: CryoSat-2 swath-processed surface elevation change fields and mass balance of Arctic GIC, 2010-2017. Rates of $\dot{h}$, glaciated area of marine- and land-terminating glacier catchments, and Arctic GIC mass balance represented in graphical form as boxes indicating average values over their respective study period (width) with error estimates (height). A map of the Arctic shows the location of GIC and mass balance from the present study represented by circles with size proportional to the mass losses and their width proportional to the error budget.

surface temperatures (Gardner et al., 2012), which results in spatially homogeneous thinning patterns, driven largely by changes in summer surface melt rates (Gardner et al., 2011, 2012). Median thinning rates over CAA-S (0.75 m a^{-1}) are three times larger than over CAA-N (0.24 m a^{-1}), reflecting the latitudinal control on SMB. Rates of thinning of up to 5 m a^{-1} are observed at low elevations and over a limited number of marine-terminating outlet glaciers, including on Devon Ice Cap and Prince of Wales Icefield. The strongest spatially extensive thinning signal across CAA-S is from the ablation zone of Barnes and Penny Ice Caps where thinning rates are in excess of 2.5 m a^{-1} (Figure 4.1). Icelandic ice caps display diverse patterns of glacier change (Figure 4.1), reflecting in part their location over volcanically active terrain, frequent surges, and high variability in weather patterns (Foresta et al., 2016). Nevertheless, between 2010 and 2017, they have mainly experienced SMB-driven ice loss, with strong seasonal trends and high melt rates of up to 6 m a^{-1} along ice cap margins, and thickening in the accumulation zones driven by post-surge dynamic responses and exceptionally large winter accumulation in recent years (Foresta et al., 2016; Wouters et al., 2019).

Complex patterns of change also prevail over the archipelagos of the Barents and Kara Sea (BKS) region where rates of $\dot{h}$ have high spatial variability (Figure 4.1). Pronounced thinning is observed at a large number of marine-terminating glacier catchments, which represent 58 % of the glaciated area of all Arctic archipelagos east of Greenland. Examples of increased thinning associated with dynamic change include an increasing number of marine-terminating basins in Svalbard, such as along the southeastern flanks of Austfonna Ice Cap, including Basin 3 (McMillan et al., 2014), and the frontal destabilisation of Stonebreen, Edgeøya (Strozzi et al., 2017b). In Severnaya Zemlya, six basins are thinning at an average rate (0.85 m a^{-1}) an order of magnitude higher than the rest of the archipelago (0.08 m a^{-1}), all six of which are marine-terminating catchments located primarily around the southern and eastern flanks of the Academy of Sciences Ice Cap (Moholdt et al., 2012a), and one on the western flank of Vavilov Ice

Cap (Willis et al., 2018). Fed by ice streams from the Karpinsky and Rusanov Ice Caps, the collapse of the Matusevich Ice Shelf in 2012 triggered the rapid acceleration of two main outlet glaciers of Karpinsky Ice Cap, one having sped up by up to 200 % at its terminus between 2010 and 2014 (Willis et al., 2015). Windy Ice Cap on Graham Bell Island, the easternmost ice cap in Franz Josef Land, represents a singularity in the archipelago, thickening at an average rate of 0.4 m a^{-1}, thereby maintaining a positive trend since the 1950s (Moholdt et al., 2012b).

4.4 Arctic GIC mass balance

We convert elevation to volume change using glacier area extents from the Randolph Glacier Inventory (RGI 6.0) (see Chapter 3, Section 3.1) and we derive mass budgets (see Chapter 3, Sections 3.7-3.8) using an assumed constant density of ice ρ_{ice} equal to 850 ± 60 kg m^{-3} (Huss, 2013) (Table 4.1). Between 2010 and 2017, Arctic GIC outside of Greenland lost on average 87.0 ± 2.6 Gt of ice per year (Figure 4.1, Table 4.1), corresponding to a mean sea level contribution of $+0.240 \pm 0.007$ mm a^{-1}. The largest losses occurred over the Canadian Arctic, with mass trends of -32.3 ± 1.6 Gt a^{-1} and -24.8 ± 1.8 Gt a^{-1} for CAA-N and CAA-S, respectively. The largest loss per unit area is for CAA-S (606 ± 44 kg m^{-2} a^{-1}), followed by Svalbard (401 ± 24 kg m^{-2} a^{-1}), Novaya Zemlya (385 ± 18 kg m^{-2} a^{-1}), CAA-N (308 ± 15 kg m^{-2} a^{-1}), Franz Josef Land (297 ± 23 kg m^{-2} a^{-1}), and Iceland (234 ± 18 kg m^{-2} a^{-1}). Specific mass loss over Severnaya Zemlya (-106 ± 6 kg m^{-2} a^{-1}) is the lowest in the Arctic, representing $\sim 1/4$ of the rate of loss over Novaya Zemlya and $\sim 1/3$ that of Franz Josef Land.

Our measurements reveal an increase in mean annual ice loss of 7 % between the 2003-2009 ICESat period (Gardner et al., 2013) and our 2010-2017 study period. However, this overall mass loss hides contrasting patterns of change across the regions. While during 2010-2017, the Canadian Arctic has seen a rate of loss comparable to the period between 2003 and 2009, Iceland glaciers have lost

Table 4.1: Summary table of mass budget: total mass balance and cumulative contributions to sea level rise (SLR) of Arctic GIC from 2010 to 2017.* Total glaciated area (RGI 6.0),** mass budgets using a constant density of ice equal to 900 kg m^{-3} (Gardner et al., 2013) for RAA, Sv, Ic, CAA-N and CAA-S, and (Moholdt et al., 2012b) for NZ, SZ and FJL, which cover the period 2004–2009), *** mass budgets using a constant density of ice at 850 kg m^{-3} (900 kg m^{-3} for comparison with the 2003-2009 mass budget estimates).

Region	Total area* [10^3 km^2]	Mass budget** [Gt a^{-1}] 2003-2009	Mass budget*** [Gt a^{-1}] 2010-2017	Mass budget [kg m^{-2} a^{-1}] 2010-2017	SLR [mm a^{-1}] 2010-2017
FJL	12.8	-0.6 ± 0.9	-3.8 (-4.0) ± 0.3	-297 ± 23	+0.010 ± 0.001
NZ	22.1	-7.1 ± 1.2	-8.5 (-9.0) ± 0.4	-385 ± 18	+0.024 ± 0.001
SZ	16.0	-1.4 ± 0.9	-1.7 (-1.8) ± 0.1	-106 ± 6	+0.005 ± 0.000
Sv	33.2	-5 ± 2	-13.3 (-14.1) ± 0.8	-401 ± 24	+0.037 ± 0.002
Ic	11.1	-10 ± 2	-2.6 (-2.8) ± 0.2	-234 ± 18	+0.007 ± 0.001
CAA-N	105.0	-33 ± 4	-32.3 (-34.2) ± 1.6	-308 ± 15	+0.089 ± 0.004
CAA-S	40.9	-27 ± 4	-24.8 (-26.3) ± 1.8	-606 ± 44	+0.068 ± 0.005
RAA	50.9	-11 ± 4	-14.0 (-14.8) ± 0.5	-275 ± 10	+0.039 ± 0.001
BKS	84.1	-16 ± 4	-27.3 (-28.9) ± 0.9	-325 ± 11	+0.075 ± 0.002
CAA	145.9	-60 ± 6	-57.1 (-60.5) ± 2.4	-391 ± 16	+0.186 ± 0.008
Total Arctic	**241.1**	**-86 ± 7**	**-87.0 (-92.1) ± 2.6**	**-361 ± 11**	**+0.240 ± 0.007**

mass at a lower rate, due primarily to recent record rates of winter accumulation leading locally to positive SMB (Foresta et al., 2016; Wouters et al., 2019). The largest increase in rates of mass loss occurred within the BKS sector. Rates of ice loss over Svalbard, for example, almost trebled over the CryoSat-2 measurement period (13.3 ± 0.8 Gt a^{-1}) compared to the previous six years (Gardner et al., 2013). In the Russian Arctic, Franz Josef Land has seen a six-fold increase in mean annual losses during 2010-2017 (3.8 ± 0.3 Gt a^{-1}) compared to the 2004-2009 period (0.6 ± 0.9 Gt a^{-1}, Table 4.1). Novaya Zemlya remained the largest contributor to sea level change in this region, losing 8.5 ± 0.4 Gt a^{-1} between 2010 and 2017. This is 27 % more ice loss per year compared to 2004-2009 (Moholdt et al., 2012b), and 80 % more than the 60-year average (5.1 ± 0.8 Gt a^{-1}) (Melkonian et al., 2016). Severnaya Zemlya's rate of loss was similar (29 % increase) to the previous decade, reaching 1.7 ± 0.1 Gt a^{-1} in 2010-2017 (Table 4.1). Overall, GIC within the BKS sector have released an extra 100 km^3 of freshwater to the

ocean between 2010 and 2017 compared to the previous decade, a volume similar in magnitude to that associated with receding sea ice cover in this region (Labe et al., 2018; Onarheim et al., 2018).

4.5 Surface mass balance and glacier dynamics

Over land-terminating GIC, elevation change rates $\dot{h}$ can be related directly to the local SMB anomaly (Figure 3.18). It is thereby assumed that surface processes dominate the mass loss, and dynamic thickness changes are either negligible, or uniform across the entire area A_l of land-terminating basins, such that $h_l \approx SMB_l/(A_l * \rho_{ice})$. To quantify the relative contribution of SMB and D to the overall mass loss for each of the seven regions listed in Table 4.1, we first parametrise elevation change $\dot{h}_l$ over land-terminating GIC as a function of first-order controls on SMB_l, that is elevation (h_l), and spatial coordinates (x_l, y_l):

$$\dot{\mathbf{h}}_l \approx \mathbf{a}_0\mathbf{h}_l^3 + \mathbf{a}_1\mathbf{h}_l^2 + \mathbf{a}_2\mathbf{h}_l + \mathbf{a}_3\mathbf{x}_l + \mathbf{a}_4\mathbf{y}_l + \mathbf{a}_5 \tag{4.1}$$

We then use our parametrisation to i) estimate bulk SMB_m over marine-terminating sectors, and ii) derive a bulk loss of D by subtracting SMB_m from the total marine-terminating GIC mass balance (see Chapter 3, Section 3.8.3). A comparison between our derived SMB and that of the regional atmospheric climate model RACMO2.3 over land-terminating GIC in the Canadian Arctic (Noël et al., 2018) demonstrates an excellent agreement (Figure 3.18). It also highlights the ability of our parametrisation to capture the first order SMB dependency on elevation and geographical location resulting in SMB variability between land- and adjacent marine-terminating sectors (Figure 3.18a,c).

We observe an increasingly negative area-specific SMB with distance from the pole over the Canadian Arctic (Figure 4.2). In contrast, a simple latitudinal control on SMB is not apparent across the archipelagos east of Greenland, reflecting the more complex interplay between atmospheric and oceanic influences.

Noteworthy are the Sv-FJL-SZ and NZ-SZ gradients of SMB, with less negative values in north-eastward direction resulting from decreasing incursions of hot, moist Atlantic air masses (Moholdt et al., 2012b). Finally, our results confirm that SMB dominates the total mass budget west of Greenland, with decreasing contribution from D since 1990 (Millan et al., 2017; Mortimer et al., 2018).

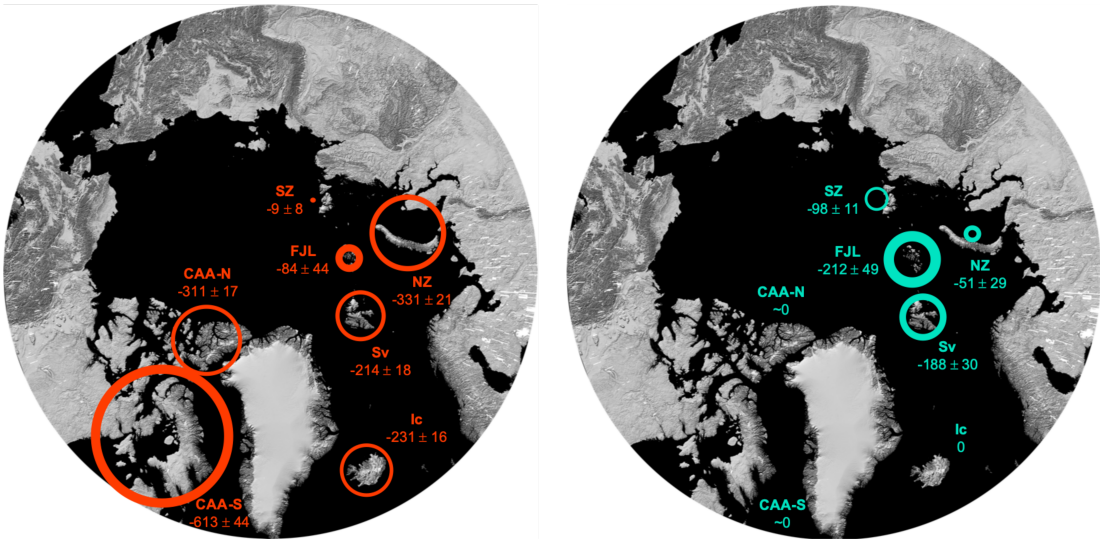


Figure 4.2: Area-specific mass balance in [kg m^{-2} a^{-1}]: SMB (orange, left) and D (cyan, right), derived from CryoSat-2. Circles with size proportional to ice mass losses and their width proportional to the corresponding error budget.

The regional differences in the dynamic component D contrast significantly with SMB, with a pronounced and strong imbalance in the BKS region compared with the rest of the Arctic (Figure 4.2). Between 2010 and 2017, ice losses in the BKS sector were nearly two times larger per unit area from marine-terminating (384 ± 16 kg m^{-2} a^{-1}) than from land-terminating basins (209 ± 10 kg m^{-2} a^{-1}), a disparity that has clearly increased compared to the previous decade, as a result of the acceleration of tidewater glaciers in recent years (Nuth et al., 2019; Strozzi et al., 2017a). This increase can be attributed largely to the rapid deflation of a small number of marine-terminating basins (Dunse et al., 2015; McMillan et al., 2014; Nuth et al., 2019; Strozzi et al., 2017a; Willis et al., 2018). Austfonna Ice Cap alone lost 4.6 ± 0.3 Gt a^{-1} during 2010-2017, a budget dominated by the dynamic activation of Basin 3 since 2012 (McMillan et al., 2014) (Table

Table 4.2: Summary table of discharge D. The dynamic mass budget is calculated with a constant density of ice equal to 850 kg m^{-3}. Area-specific D is computed relative to the total marine-terminating basin area (*) and relative to the total glaciated area (**) of each region. The last column refers to D as a percentage of total mass balance ($\dot{m}$). In parenthesis are uncertainties assuming that SMB patterns correlate over distances of 10 km (Moholdt et al., 2010; Rotschky et al., 2004).

Region	D [Gt a^{-1}]	D_{spec} [kg m^{-2} a^{-1}]*	D_{spec} [kg m^{-2} a^{-1}]**	D / $\dot{m}$
FJL	-2.7 ± 0.6 (± 11.1)	-235 ± 54	-212 ± 49	72 %
NZ	-1.1 ± 0.5 (± 4.5)	-82 ± 37	-51 ± 29	13 %
SZ	-1.6 ± 0.2 (± 1.8)	-205 ± 20	-98 ± 11	94 %
Sv	-6.2 ± 0.9 (± 8.3)	-277 ± 41	-188 ± 30	47 %
Ic	-	-	-	-
CAA-N	+0.3 ± 1.4 (± 7.6)	+7 ± 28	+3 ± 23	1 %
CAA-S	+0.3 ± 0.4 (± 0.9)	+93 ± 137	+7 ± 63	1 %
RAA	-5.4 ± 0.8 (± 12.1)	-164 ± 25	-108 ± 18	38 %
BKS	-11.6 ± 1.2 (± 14.7)	-210 ± 22	-138 ± 16	43 %
Total Arctic	-11.0 ± 1.9 (± 16.6)	-102 ± 17	-46 ± 16	13 %

4.4). In Severnaya Zemlya, where SMB represents only 6 % of total mass loss, ice dynamics were largely responsible for the negative regional losses between 2010 and 2017 (Table 4.2). Elsewhere in the BKS sector, increased ice discharge accounted for 72 %, 47 % and 13 % of the total mass loss for Franz Josef Land, Svalbard and Novaya Zemlya respectively (Table 4.2). By unit area, Franz Josef Land, Svalbard and Severnaya Zemlya exhibit the largest rates of dynamic loss D with 212 ± 49 kg m^{-2} a^{-1}, 188 ± 30 kg m^{-2} a^{-1} and 98 ± 11 kg m^{-2} a^{-1}, respectively (Table 4.2, Figure 4.2). Some of Novaya Zemlya's Barents Sea coast outlet glaciers accelerated during the study period (Carr et al., 2017; Melkonian et al., 2016), contributing to a dynamic imbalance of -51 ± 29 kg m^{-2} a^{-1}. By unit marine-terminating basin area, which highlights the intensity of dynamic instability, Svalbard lost ice via discharge at 277 ± 41 kg m^{-2} a^{-1} owing to Basin 3, followed by Franz Josef Land at 235 ± 54 kg m^{-2} a^{-1}, Severnaya Zemlya at 205 ± 20 kg m^{-2} a^{-1} and Novaya Zemlya at 82 ± 37 kg m^{-2} a^{-1} (Table 4.2).

4.6 Atmospheric and oceanic drivers of ice loss

Although atmospheric warming is the primary cause of ice loss from the surface of Arctic GIC through increased melting (e.g. Gardner et al., 2011), a broad range of factors affect their discharge. Tidewater glacier dynamics are determined by changing boundary conditions such as shifts in the stress balance at the glacier front, as these can trigger instabilities that can propagate inland rapidly (Dunse et al., 2015; McMillan et al., 2014; Nuth et al., 2019; Willis et al., 2018). The influx of Atlantic Ocean waters and recirculation of warm bottom water in Arctic fjords, the rapid drainage of surface meltwater to the base of glaciers, and submarine melting driven by the buoyant advection of subglacial discharge at calving fronts, are all known to affect rates of tidewater glacier flow (Cook et al., 2019; Cowton et al., 2018; Slater et al., 2016). Decreased sea ice concentrations have also been suggested to impact calving rates and promote the acceleration of ice discharge (Robel, 2017). To investigate the drivers of the recent Arctic GIC dynamic imbalance, we analyse trends in regional atmospheric (Dee et al., 2011) and oceanic (Xie et al., 2017) temperatures, and in sea ice concentrations (Comiso, 2017). We use maps of monthly mean sea surface (SST) and air surface temperatures (T_{2m}) on a 0.75° × 0.75° grid from ECMWF Interim Reanalysis (ERA-I) (Dee et al., 2011), with the smallest bias from observations (Lindsay et al., 2014). We extract 200 m depth subsurface ocean temperatures (SOT) from the Arctic Ocean reanalysis TOPAZ (Xie et al., 2017) on a 12-16 km grid, and analysed for the 15^{th} day of each month. The passive microwave NASA Team (Cavalieri et al., 2019) and Bootstrap (Comiso, 2017) sea ice concentration (SIC) data are monthly means on a 25 km × 25 km polar stereographic grid. Annual climate anomalies of all four identified forcings are calculated with reference to 1) a baseline period (1990-1999) (Table 4.3 and Figure 4.3), and 2) an intermediate period that covers sampling by ICESat (2000-2009) (Appendices, Figures 4.4 - 4.7).

The Arctic climate has warmed significantly, and mean air temperatures were

Table 4.3: Arctic climate anomalies during 2010-2017 relative to 1990-2009 means. Anomalies in air surface temperature (T_{2m}), sea surface temperature (SST), subsurface ocean temperature (SOT), and sea ice concentration (SIC) during the survey period (2010-2017) relative to the previous two decades (1990-2009). T_{2m} and SST are from ERA-Interim; SOT is 200 m depth ocean temperature from TOPAZ; SIC data are from NASA bootstrap/team.

Region	T_{2m} [°C]	SST [°C]	SOT [°C]	SIC [%]
FJL	+3.4	+0.3	+0.3	-16.8
NZ	+2.7	+0.8	+0.6	-12.3
SZ	+2.8	+0.2	+0.1	-8.6
Sv	+2.1	+0.9	+0.7	-12.8
Ic	+0.9	+0.1	+0.3	-0.1
CAA-N	+0.9	+0.1	-0.2	-1.4
CAA-S	+2.4	+0.2	-0.2	-2.1
CAA	+1.3	+0.1	-0.2	-1.5
RAA	+2.9	+0.5	+0.4	-12.2
BKS	+2.6	+0.6	+0.5	-12.4

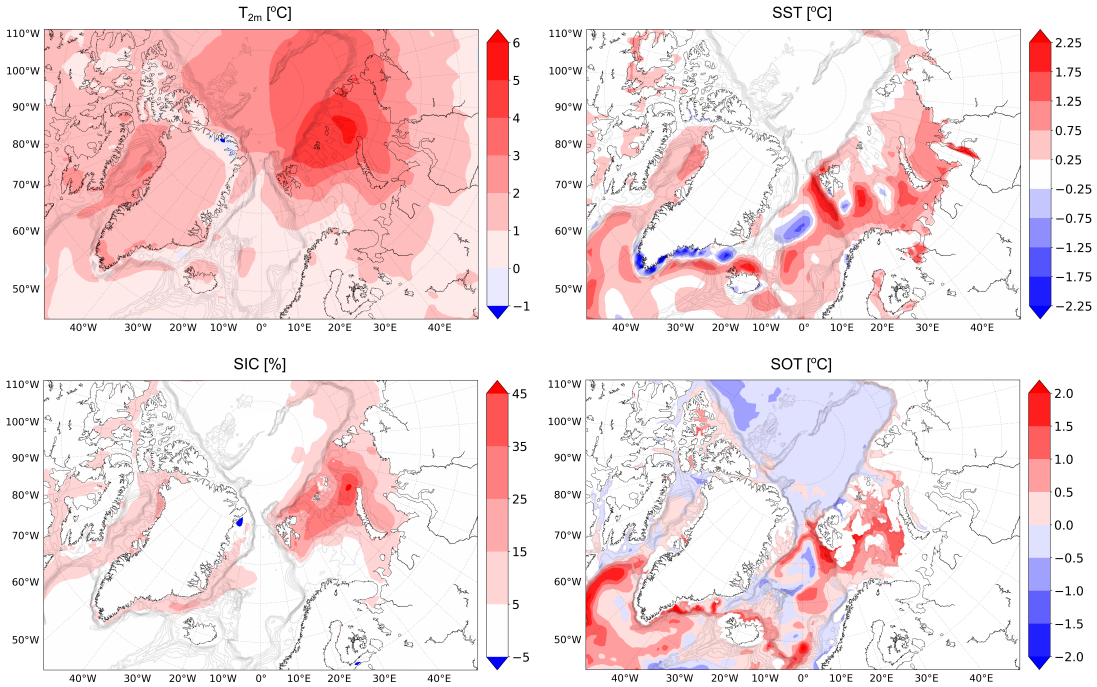


Figure 4.3: Arctic climate forcing anomalies. Air surface temperature (T_{2m}), sea surface temperature (SST), subsurface ocean temperature (SOT), and sea ice concentration (SIC) anomalies during the CryoSat-2 period (2010-2017) with reference to the baseline period (1990-1999). T_{2m} and SST are from ERA-Interim, SOT is 200 m depth ocean temperature from TOPAZ, and SIC are from the NASA Team sea ice algorithm. Positive SIC designate declining sea ice concentrations. Anomalies with reference to an intermediate reference period (2000-2009) are provided in Appendices, Figures 4.4 - 4.7.

0.9°C to 3.4°C higher during our survey period than in the preceding two decades (Table 4.3). However, while atmospheric warming has occurred across the region as a whole, ocean warming and sea ice retreat have been largely restricted to sectors east of Greenland, where GIC have experienced significantly increased glacier discharge (Figure 4.3). For example, across the BKS sector, including Svalbard, Novaya Zemlya, Franz Josef Land, and Severnaya Zemlya, the average rise in sea surface, subsurface ocean, and atmospheric temperatures adjacent to GIC have been 0.6°C, 0.5°C, and 2.6°C, respectively, and the average reduction in sea ice concentration has been 12.4 % (Table 4.3). By comparison, the ocean temperature and sea ice concentration around the Canadian Arctic Archipelagos have changed little.

The warming of the BKS sector has been associated with the combined effects of enhanced storm activity and increased Atlantic Water inflow to the Eurasian and Siberian Shelf seas (Barton et al., 2018; Lind et al., 2018; Polyakov et al., 2017). Farther afield, it has also been shown that the Arctic- and North Atlantic Oscillations are correlated with glacier mass balance (Carr et al., 2017; Ding et al., 2014; Lenaerts et al., 2019; Zeeberg and Forman, 2001), with opposite effects in the eastern and western Hemispheres depending on the position and strength of the Arctic Circumpolar Vortex (Bjørk et al., 2018; Gardner and Sharp, 2006; Wouters et al., 2019). These modes of large-scale atmospheric variability in the North Atlantic are likely to impact not only SMB via surface warming but also trigger dynamic instabilities by affecting sea ice concentrations and ocean warming in addition to changes in meteorology, albeit with possible delayed response times and associated regional heterogeneity (Wouters et al., 2019).

4.7 Conclusions

Using CryoSat-2 swath radar altimetry, we have computed elevation and mass trends for all Arctic GIC outside Greenland with unprecedented (500 m) spatial resolution. Between 2010 and 2017, we estimate they have lost 87.0 ± 2.6 Gt a^{-1}

of snow and ice on average, a 7 % increase relative to the 2003-2009 annual mean (Gardner et al., 2013) but with significant regional differences. By modelling the contribution due to SMB, we isolate the elevation change signal due to anomalous glacier flow. Using this approach, we find that SMB is responsible for the vast majority (87 %) of the observed mass loss, while increased ice discharge has caused the remainder (13 %). However, ice discharge from GIC in the Barents and Kara Sea area has increased since the 2003-2009 period, and now accounts for 43 % of the mass loss from this region. This enhanced dynamic signal has been occurring in conjunction with increased air and ocean temperature, and loss of sea ice.

It is predicted that, even when excluding the mass balance of tidewater glaciers, losses from the Canadian Arctic Archipelagos and the BKS will be dominating glacier change in future climate scenarios (Möller et al., 2016; Radić et al., 2014). Most importantly, while SMB is projected to be the prevalent mechanism of Greenland ice loss in the coming decades (Enderlin et al., 2014; Nick et al., 2013; Price et al., 2011), a recent study finds that D, not SMB has dominated ice losses in Greenland over the past half-century (Mouginot et al., 2019). Our results show that the dynamic response of marine-terminating GIC to climate forcing makes up a significant proportion of the total mass budget in the rest of the Arctic since 2010, with D contributing up to ten times the losses from SMB in some regions, and with rapid and significant temporal fluctuations. This pattern is likely to endure over time, as the large number of Arctic tidewater glaciers will continue to respond to receding sea ice and to the impinging Atlantification of Arctic Ocean basins. We also emphasise the need for caution when extrapolating in space and time observations of glacier changes from a limited number of basins, and encourage the development and use of high-resolution, large-scale observations of surface elevation, ice thickness and velocity to improve the quantitative assessment of ice discharge. This is an essential step towards a more accurate representation of dynamic imbalance in the parametrisation of climate models, and towards reducing uncertainty in the projections of future ice mass loss.

4.8 Appendices

4.8.1 Mass balance of Arctic GIC

Table 4.4: Mass balance of Arctic glaciers and ice caps: split by type of basin (marine- and land-terminating), comparison of upscaling (S) versus hypsometric averaging (H) as alternative regionalisation schemes of land-terminating basins.

Region / GIC	Total MB	Marine-terminating basins		Land-terminating basins		
	[Gt a^{-1}]	S [Gt a^{-1}]	$A_{measured}$ / A_{total}	S [Gt a^{-1}]	H [Gt a^{-1}]	$A_{measured}$ / A_{total}
FJL	**-3.8 ± 0.3**	**-3.7 ± 0.3**	**90%**	**-0.2 ± 0.0**	**-0.1 ± 0.0**	**88%**
Windy	+0.3 ± 0.0	+0.2 ± 0.0	86%	+0.1 ± 0.0	+0.1 ± 0.0	82%
NZ	**-8.5 ± 0.4**	**-5.2 ± 0.4**	**83%**	**-3.0 ± 0.2**	**-3.3 ± 0.2**	**70%**
SZ	**-1.7 ± 0.1**	**-1.6 ± 0.1**	**90%**	**0.1 ± 0.0**	**-0.1 ± 0.0**	**82%**
Sum GIC and upscale	-1.7 ± 0.1	-1.6 ± 0.1		0.1 ± 0.0	-0.1 ± 0.0	
Academy of Sciences	-1.0 ± 0.1	-1.1 ± 0.1	94%	+0.1 ± 0.0	+0.1 ± 0.0	95%
Vavilov	-0.2 ± 0.0	-0.3 ± 0.0	94%	+0.1 ± 0.0	+0.1 ± 0.0	87%
Albanov	0.0 ± 0.0			0.0 ± 0.0	0.0 ± 0.0	83%
Pioneer	0.0 ± 0.0			0.0 ± 0.0	0.0 ± 0.0	82%
Rusanov	-0.2 ± 0.0	-0.1 ± 0.0	87%	-0.1 ± 0.0	-0.1 ± 0.0	76%
Karpinsky	-0.1 ± 0.0	-0.2 ± 0.0	84%	+0.1 ± 0.0	+0.1 ± 0.0	79%
University	+0.1 ± 0.0	0.0 ± 0.0	87%	+0.1 ± 0.0	+0.1 ± 0.0	85%
Semenov-Tyan-Shansky + Kropotkin + Leningradsky	-0.2 ± 0.0	0.0 ± 0.0	75%	-0.2 ± 0.0	-0.2 ± 0.0	76%
Sv	**-13.3 ± 0.8**	**-10.8 ± 0.8**	**85%**	**-2.5 ± 0.2**	**-2.5 ± 0.2**	**69%**
Sum GIC and upscale	-13.8 ± 0.4	-11.2 ± 0.4		-2.6 ± 0.1	-2.6 ± 0.1	
Austfonna	-4.6 ± 0.3	-4.6 ± 0.3	98%	0.0 ± 0.0	0.0 ± 0.0	89%
Vestfonna	-0.4 ± 0.0	-0.4 ± 0.0	95%	0.0 ± 0.0	0.0 ± 0.0	90%
Barentsøya	-0.2 ± 0.0	-0.1 ± 0.0	92%	-0.1 ± 0.0	-0.1 ± 0.0	90%
Edgeøya	-0.9 ± 0.0	-0.5 ± 0.0	90%	-0.4 ± 0.0	-0.4 ± 0.0	84%
NW Spitzbergen	-2.7 ± 0.1	-1.9 ± 0.1	77%	-0.8 ± 0.1	-0.8 ± 0.1	58%
NE Spitzbergen	-0.7 ± 0.0	-0.4 ± 0.0	82%	-0.3 ± 0.0	-0.3 ± 0.0	67%
S Spitzbergen	-4.0 ± 0.2	-3.1 ± 0.2	74%	-0.8 ± 0.1	-0.9 ± 0.1	67%
Ic	**-2.6 ± 0.2**			**-1.2 ± 0.1**	**-2.6 ± 0.2**	**80%**
Sum GIC and upscale	-2.6 ± 0.1			-1.4 ± 0.1	-2.6 ± 0.1	
Vatnajökull	-1.6 ± 0.1			-0.9 ± 0.1	-1.6 ± 0.1	84%
Langjökull	-0.3 ± 0.0			-0.3 ± 0.0	-0.3 ± 0.0	77%
Hofsjökull	-0.2 ± 0.0			-0.1 ± 0.0	-0.2 ± 0.0	84%
Mýrdalsjökull + Eyafjallajökull	-0.1 ± 0.0			+0.1 ± 0.0	-0.1 ± 0.0	63%
Drangajökull	-0.1 ± 0.0			+0.1 ± 0.0	-0.1 ± 0.0	67%
CAA-N	**-32.3 ± 1.6**	**-13.3 ± 0.9**	**63%**	**-17.9 ± 1.3**	**-19.0 ± 1.3**	**62%**
Sum GIC and upscale	-32.6 ± 0.8	-12.9 ± 0.4		-18.0 ± 0.6	-19.7 ± 0.6	
N Ellesmere	-9.4 ± 0.5	-2.7 ± 0.2	56%	-6.0 ± 0.4	-6.7 ± 0.5	57%
Agassiz	-5.0 ± 0.3	-1.5 ± 0.1	52%	-3.1 ± 0.2	-3.5 ± 0.3	64%
Muller	-2.8 ± 0.2	-0.2 ± 0.0	41%	-2.4 ± 0.2	-2.6 ± 0.2	59%
Steacie	-1.8 ± 0.1			-1.6 ± 0.1	-1.8 ± 0.1	50%
Prince of Wales	-5.9 ± 0.3	-4.1 ± 0.3	61%	-1.7 ± 0.1	-1.8 ± 0.1	62%
Sydkap	-0.8 ± 0.0	-0.2 ± 0.0	55%	-0.6 ± 0.0	-0.6 ± 0.0	71%
Manson	-1.7 ± 0.1	-1.4 ± 0.1	71%	-0.3 ± 0.0	-0.3 ± 0.0	53%
Devon	-4.3 ± 0.2	-2.9 ± 0.2	83%	-1.3 ± 0.1	-1.4 ± 0.1	82%
CAA-S	**-24.8 ± 1.8**	**-1.3 ± 0.1**	**37%**	**-23.1 ± 1.6**	**-23.5 ± 1.8**	**56%**
Sum GIC and upscale	-24.5 ± 0.7	-1.5 ± 0.1		-22.7 ± 0.7	-23.0 ± 0.7	
Bylot	-2.3 ± 0.2	-0.2 ± 0.0	67%	-2.2 ± 0.2	-2.1 ± 0.2	54%
Barnes	-4.5 ± 0.3			-4.5 ± 0.3	-4.5 ± 0.3	97%
Penny	-4.3 ± 0.3	-0.8 ± 0.1	11%	-3.5 ± 0.2	-3.5 ± 0.3	44%
N Baffin	-2.3 ± 0.2	-0.2 ± 0.0	39%	-2.0 ± 0.1	-2.1 ± 0.2	51%
Central Baffin	-5.2 ± 0.4	-0.2 ± 0.0	50%	-4.8 ± 0.3	-5.0 ± 0.4	50%
S Baffin	-3.8 ± 0.3			-3.7 ± 0.3	-3.8 ± 0.3	42%
CAA	-57.1 ± 2.4	-14.5 ± 0.9	61%	-41.0 ± 2.1	-42.6 ± 2.2	60%
RAA	-14.0 ± 0.5	-10.5 ± 0.5	87%	-3.1 ± 0.2	-3.5 ± 0.2	77%
BKS	-27.3 ± 0.9	-21.3 ± 0.9	86%	-5.6 ± 0.3	-6.0 ± 0.3	73%
Total Arctic	**-87.0 ± 2.6**	**-35.8 ± 1.3**	**74%**	**-47.8 ± 2.1**	**-51.2 ± 2.3**	**64%**

4.8.2 Atmospheric and oceanic forcing anomalies

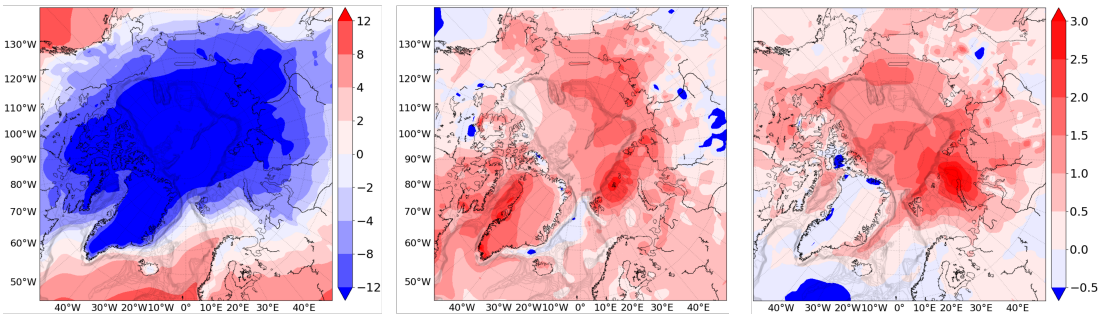


Figure 4.4: T_{2m} decadal anomalies (ERA-Interim). Left: T_{2m} decadal mean of annual means [°] for the 1990-1999 (baseline) period. Middle: T_{2m} anomaly [°] between the 2000-2009 and the baseline period. Right: T_{2m} anomaly [°] between 2010-2017 and 2000-2009.

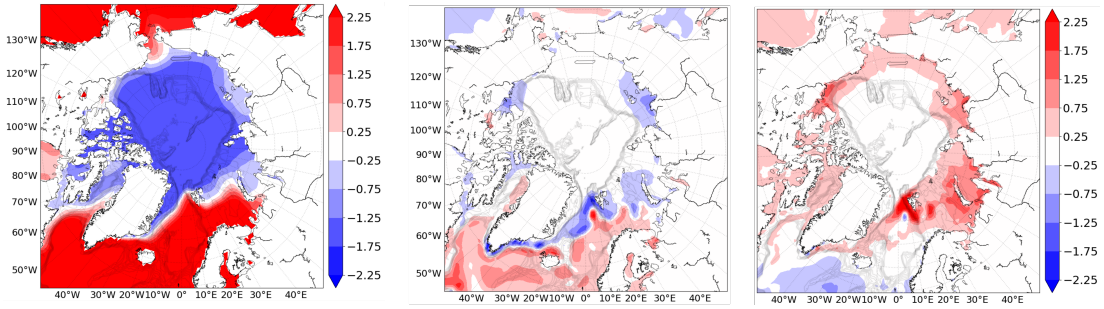


Figure 4.5: SST decadal anomalies (ERA-Interim). Left: SST decadal mean of annual means [°] for the 1990-1999 (baseline) period. Middle: SST anomaly [°] between the 2000-2009 and the baseline period. Right: SST anomaly [°] between 2010-2017 and 2000-2009.

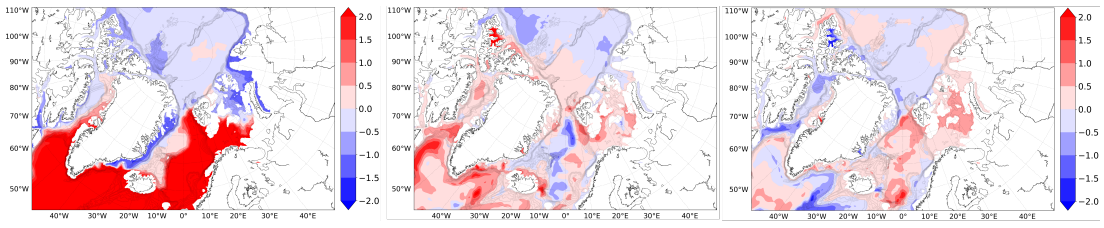


Figure 4.6: SOT decadal anomalies (TOPAZ). Left: SOT decadal mean of annual means [°] for the 1990-1999 (baseline) period. Middle: SOT anomaly [°] between the 2000-2009 and the baseline period. Right: SOT anomaly [°] between 2010-2017 and 2000-2009.

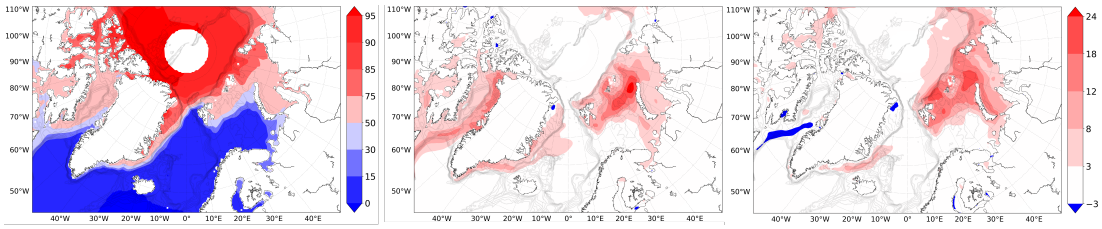


Figure 4.7: SIC decadal anomalies (NASA Team). Left: SIC decadal mean of annual means (%) for the 1990-1999 (baseline) period. Middle: SIC anomaly (%) between the 2000-2009 period and the baseline period. Right: SIC anomaly (%) between 2010-2017 and 2000-2009.

4.8.3 Data availability

Our swath processing algorithm uses SARIn-mode CryoSat-2 Level 1b format data directly downloaded from ftp://science-pds.cryosat.esa.int (accessed on 27/06/2019); NASA Operation Ice Bridge validation data is available for download at https://nsidc.org/data/icebridge (accessed on 27/06/2019); ice and snow masks for all regions except Iceland were taken from https://www.glims.org/RGI/rgi60_dl.html (accessed on 27/06/2019); RACMO data is available for download at https://doi.pangaea.de/10.1594/PANGAEA.881315; the passive microwave NASA Team and Bootstrap concentration data are available respectively from http://nsidc.org/data/nsidc-0051 and http://nsidc.org/data/nsidc-0079; The ARCTIC_REANALYSIS_PHYS_002_003 TOPAZ product is available from http://marine.copernicus.eu/services-portfolio/access-to-produ ERA-Interim monthly means of daily means are available from https://apps.ecmwf.int/datasets/.

4.8.4 Acknowledgements

Chapter 4 was written in a format suitable for publication in a peer-reviewed journal and is currently under review in Remote Sensing of Environment. The work was designed by myself in collaboration with Dr. Noel Gourmelen. I processed all the data and conducted the corresponding analyses. Feedback was provided by Professor Pete Nienow, Dr. Noel Gourmelen., Dr. Flora Weissgerber, Professor

Andrew Shepherd, and Dr. Michel Tsamados. Dr. Michel Tsamados provided, for this chapter, climate data and advice to the segment on climatic drivers of mass loss. Dr. Flora Weissgerber provided input to the method development for the conversion of surface elevation- to volume change at the pan-Arctic scale.

The work in Chapter 4 was performed under the European Space Agency (ESA) Support to Science Elements CryoSat+ CryoTop contract 4000107394/12/I-NB, CS+ Mountain Glaciers contract 4000114224/15/I-SBo to Noel Gourmelen. I would like to thank ESA for providing open access to CryoSat-2 data, the National Aeronautics and Space Administration (NASA) for providing access to measurements from Operation Ice Bridge (OIB), and Dr. B.P.Y. Noël for access to data from the regional ice and climate model RACMO2.3.

Chapter 5

Russian Arctic glacier and ice cap response to accelerated warming (2010-2018)

5.1 Abstract

Glaciers and ice caps of the Russian Arctic are currently experiencing accelerating mass loss as a result of strong atmospheric and ocean warming in the Barents and Kara Sea region. This loss has been driven by increased surface ablation, and dramatic shifts in ice dynamics at individual drainage basins across the entire Eurasian High Arctic since 2010. Here we provide a high-resolution spatial and temporal overview of ice surface elevation changes and mass imbalance across both Novaya Zemlya and Severnaya Zemlya using CryoSat-2 interferometric swath altimetry from 2010 to 2018. We find a total mass imbalance of - 300 kg m^{-2} a^{-1}, marked by a strong west-to-east gradient, with higher rates of loss over Novaya Zemlya (9.7 ± 0.5 Gt a^{-1} at 431 ± 22 kg m^{-2} a^{-1}) in the west compared to Severnaya Zemlya (1.7 ± 0.1 Gt a^{-1} at 97 ± 8 kg m^{-2} a^{-1}) in the east. Correlation between time series of surface elevation change and climate forcing reveals a quasi-linear relationship between coupled ocean-atmospheric forcing and glacier change

over Novaya Zemlya, in agreement with similar findings from east Greenland. We further discern the likely role of ocean warming as the key factor driving dynamic ice loss in Severnaya Zemlya, owing to increasingly warm Atlantic Waters circulating along the Eurasian continental margin. We conclude that simple, linear relationships between environmental forcing and glacier change may be sufficiently accurate to parametrise ice loss in regions where synchronous, coupled ocean-atmosphere forcing prevails.

5.2 Introduction

The Russian Arctic archipelagos of Novaya Zemlya and Severnaya Zemlya are surrounded by the Eurasian Arctic Shelf Seas, which, together with the adjacent Eurasian Basin of the Arctic Ocean, form a contiguous region currently responding to Arctic climate transitions (Lind et al., 2018; Polyakov et al., 2017). The extreme polar warming, relative to the planetary mean, is exacerbated by meridional heat transport via ocean currents (Barton et al., 2018) and atmospheric winds (Stuecker et al., 2018), sustained by a range of climate dynamic feedbacks and processes (Goosse et al., 2018; Serreze et al., 2009). These warming processes are progressively expanding north and eastwards across the Barents and Kara Seas (Figure 5.1), a region highlighted recently as an Arctic warming "hotspot" (Lind et al., 2018). This north-eastward expansion of Atlantic climate (Hwang et al., 2011) into the Eurasian High Arctic, or 'Atlantification' (Årthun et al., 2012), is accompanied by enhanced vertical ocean heat fluxes that affect concurrently ocean stratification (Polyakov et al., 2017), radiative forcing (Held and Soden, 2006), sea ice processes (Stroeve et al., 2018), and glacier dynamics and mass balance (Tepes et al., 2017).

Consistent with these trends, glaciers and ice caps of the BKS have received increasing attention, with observations revealing an acceleration in both ice loss and frontal velocities during the past two decades (Carr et al., 2017; Ciracì et al., 2018; Melkonian et al., 2016; Moholdt et al., 2012b; Strozzi et al., 2017a). While

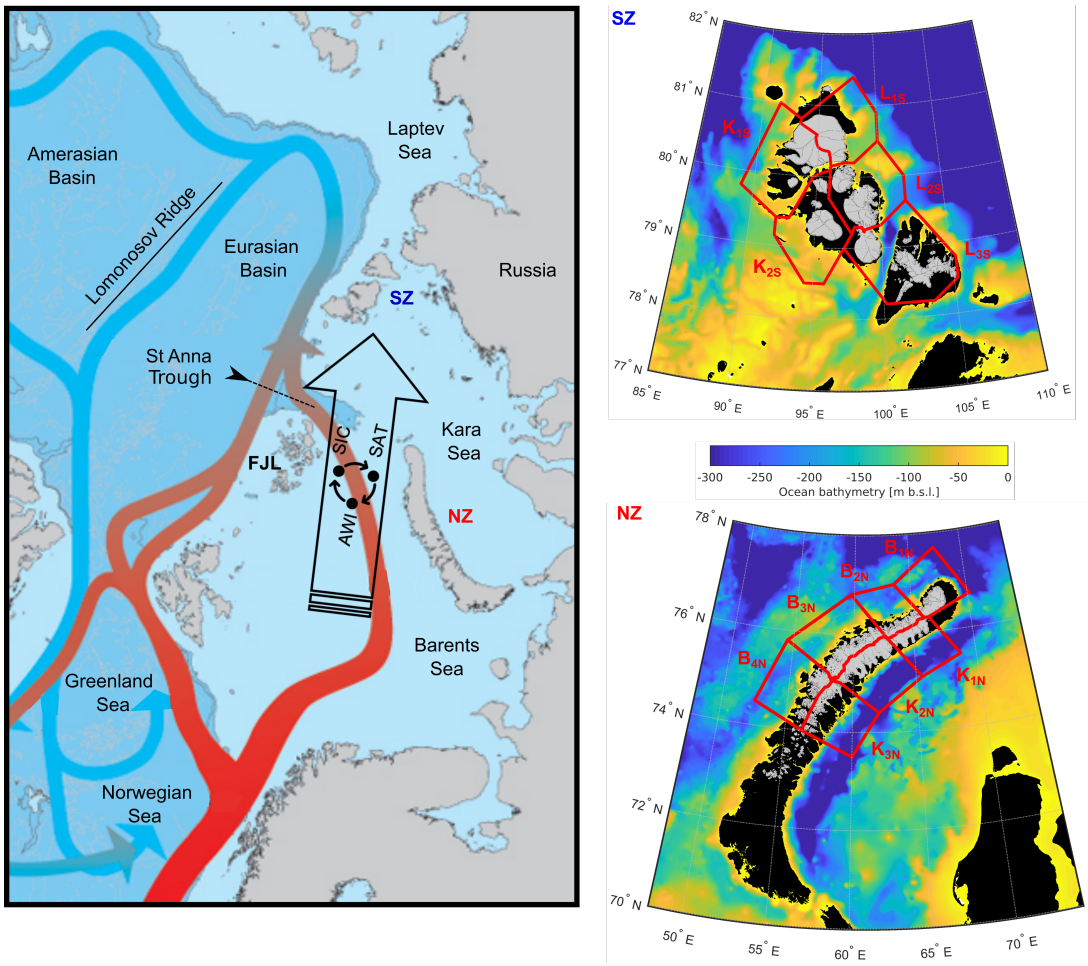


Figure 5.1: Study region: Eurasian Arctic with major ocean currents and ocean bathymetry surrounding the Russian Arctic archipelagos of Novaya Zemlya and Severnaya Zemlya. Left: eastward progressing ocean warming into the Barents and Kara Seas (BKS) and the Eurasian Basin of the Arctic Ocean (red arrows) is accompanied by local climate feedbacks (black arrow) from rising surface air temperatures (SAT), Atlantic Water inflows (AWI), and receding sea ice concentrations (SIC). Prominent features discussed in the text are the St Anna Trough between Franz Josef Land (FJL) and Severnaya Zemlya (SZ), and the continental slope between the shallow shelf seas and the Arctic Ocean Basins. Source: adapted from illustration by Audun Igesund (NPI), available online at: http://www.arcticsystem.no/en/outsideworld/oceancurrents/ (accessed on 20/5/2020). **Right:** ocean bathymetry surrounding the Russian Arctic archipelagos of Novaya Zemlya (NZ) and Severnaya Zemlya (SZ). Glacier outlines are shown as grey shaded areas. Climatic influence on land ice is assessed within control areas that are defined along both regions' seacoasts (see Sections 5.4.2 to 5.4.4): NZ Barents (B_{1N}-B_{4N}), NZ Kara (K_{1N}-K_{3N}), SZ Kara (K_{1S}-K_{2S}) and SZ Laptev (L_{1S}-L_{3S}) coasts.

the region's mass imbalance is attributed primarily to surface processes (Tepes et al., 2017), a growing number of glacier catchments and ice cap margins are

disintegrating rapidly, indicating the increased role of dynamic processes in controlling total mass loss (Willis et al., 2015; Willis et al., 2018; Zheng et al., 2019). The mechanisms by which amplified warming generates such diverse patterns of glacial response, such as those observed across the Eurasian High Arctic, however, remain unclear (e.g. Carr et al., 2017; Ciracì et al., 2018; Sánchez-Gámez et al., 2019). Understanding these mechanisms is essential for addressing current knowledge gaps to help improve the parametrisation of processes occurring at the ice-ocean interface, and thus critical for achieving more robust global sea level projections.

Here we use high-density CryoSat-2 swath altimetry to produce estimates of volume and mass loss over the glaciers and ice caps of the Russian Arctic for the period 2010-2018, and compute time series of surface elevation change at 90-day time steps for single glaciers and ice cap basins. We use our results to investigate across Novaya Zemlya and Severnaya Zemlya how interannual and decadal variability in ice thinning, contrasting spatial and temporal patterns of ice loss and rapidly shifting ice flow regimes are related to trends in atmospheric warming, ocean forcing and sea ice concentrations. In particular, we review decadal ice-climate linkages in the BKS beyond the 2010-2018 timeframe and examine footprints of 'Atlantification' on Russian Arctic glacier mass balance and ice cap dynamic regimes since 2010.

5.3 Methods

We sample CryoSat-2 radar altimetry from 2010 to 2018 using a novel swath processing algorithm (Foresta et al., 2018; Gourmelen et al., 2018), and derive gridded rates of surface elevation change ($\dot{h}$, or dh) over the glaciers and ice caps of Novaya Zemlya and Severnaya Zemlya in the Russian Arctic. After removing outliers, we obtain a ratio of measured-to-total glaciated area equal to 90 % for both regions. We further partition $\dot{h}$ according to basin and terminus type into marine- and land-terminating catchments, which represent respectively 62 %

and 38 % of the total glaciated area for Novaya Zemlya, and 47 % and 53 % for Severnaya Zemlya (Figure 5.2). We use the swath elevations and surface elevation change fields to derive, following the methodology described in Chapter 3, time series of surface elevation change and mass budgets for all land- and marine-terminating glacier and ice cap basins of the two archipelagos. For a detailed description of this methodology, and more complete information on CryoSat-2 altimetry, swath processing, error budgets, and data validation, please refer to Chapter 3.

To investigate potential causal mechanisms driving the observed spatial variability in Arctic glacier and ice cap mass loss, trends in sea surface (SST), subsurface ocean (SOT), and air surface temperatures (T_{2m}), as well as changes in sea ice concentrations (SIC) were jointly examined over the CryoSat-2 period (2010-2018). Longer-term trends were also considered to account for possible delays in glacier response to environmental forcing. The underlying methodology was guided by a similar style of analysis undertaken on West Antarctica's Marie Byrd Land Sector by (Christie et al., 2018). It represents a step increase in granularity compared to the pan-Arctic study in Chapter 4, thanks to the additional analysis of seasonal climate variability, in conjunction with time series of glacier change at 90-day time intervals. A more exhaustive enquiry of ocean forcing in the Barents and Kara Seas has also been completed and is described in the following.

The climate data used for the Russian Arctic case study consist of 1/4° monthly mean T_{2m} and SST atmospheric reanalysis from the (ECMWF) ERA5 covering the period from 1978 to 2018 (Copernicus Climate Change Service, 2017), and global 1/12° monthly mean SIC, potential temperature θ and salinity S from the global ocean eddy-resolving reanalysis GLORYS12v1, available from 1993 to 2018. Compared with ERA-Interim reanalysis used in Chapter 4, ERA5 has been publicly available since 2017, offers much higher spatial resolution (1/4° versus 3/4°), and provides more consistent tropospheric and sea surface temperature data (Copernicus Climate Change Service, 2017). Subsurface ocean thermal forcing (SOTF) is a function of depth z and is defined as the difference between

in situ potential temperature θ and in situ freezing temperature θ_f (Slater et al., 2019), with a linear expression for the freezing point (Jenkins, 2011):

$$\mathbf{SOTF} = \theta - \theta_{\mathbf{f}} = \theta - (\lambda_{\mathbf{1}}\mathbf{S} + \lambda_{\mathbf{2}} + \lambda_{\mathbf{3}}\mathbf{z}) \tag{5.1}$$

where λ_1 = - 5.73 $\times$ 10^{-2} °C is the seawater freezing point slope, λ_2 = 8.32 $\times$ 10^{-2} °C is the seawater freezing point offset, and λ_3 = 7.61 $\times$ 10^{-4} °C m^{-1} is the depth dependence of the freezing point.

The GLORYS12v1 dataset provides ocean temperature and salinity at 50 depth levels, ranging from 0.5m to 5700 meters below sea level (m b.s.l.). Mean ocean forcing is calculated for three depth ranges, namely: 0.5 - 55 m b.s.l. ($SOTF_1$), 55 - 110 m b.s.l. ($SOTF_2$), and 110 - 155 m b.s.l. ($SOTF_3$). This choice is based on visual inspection of ocean bathymetry immediately offshore the glacier and ice cap frontal margins, using data from the General Bathymetric Chart of the Oceans (GEBCO), and assuming that ice thickness at glacier termini largely falls within the chosen depth ranges (Carr et al., 2014; Moholdt et al., 2012a). Nonetheless, it needs to be emphasised, that marginal ice thicknesses of marine-terminating glaciers are poorly constrained in the Russian Arctic (Sharov, 2010).

To achieve a more appropriate comparison between the climate forcing data and the 90-day segmented time-series of ice surface elevation change, monthly means from the reanalysis datasets are converted into seasonal means, with seasons defined as follows: June-August (JJA) - 'summer', September-November (SON) – 'fall', December-February (DJF) – 'winter', and March-May (MAM) – 'spring'. Seasonal anomalies in a given year are calculated by subtracting from the seasonal observations the seasonal mean calculated over the full time series for each individual season. Anomaly trends are equal to the slope of a linear polynomial fit (MATLAB *polyfit* function) that is used as an approximation of anomaly variations over time. All climatologies and anomalies are derived for the entire Barents and Kara Sea region, in addition to each of the control domains

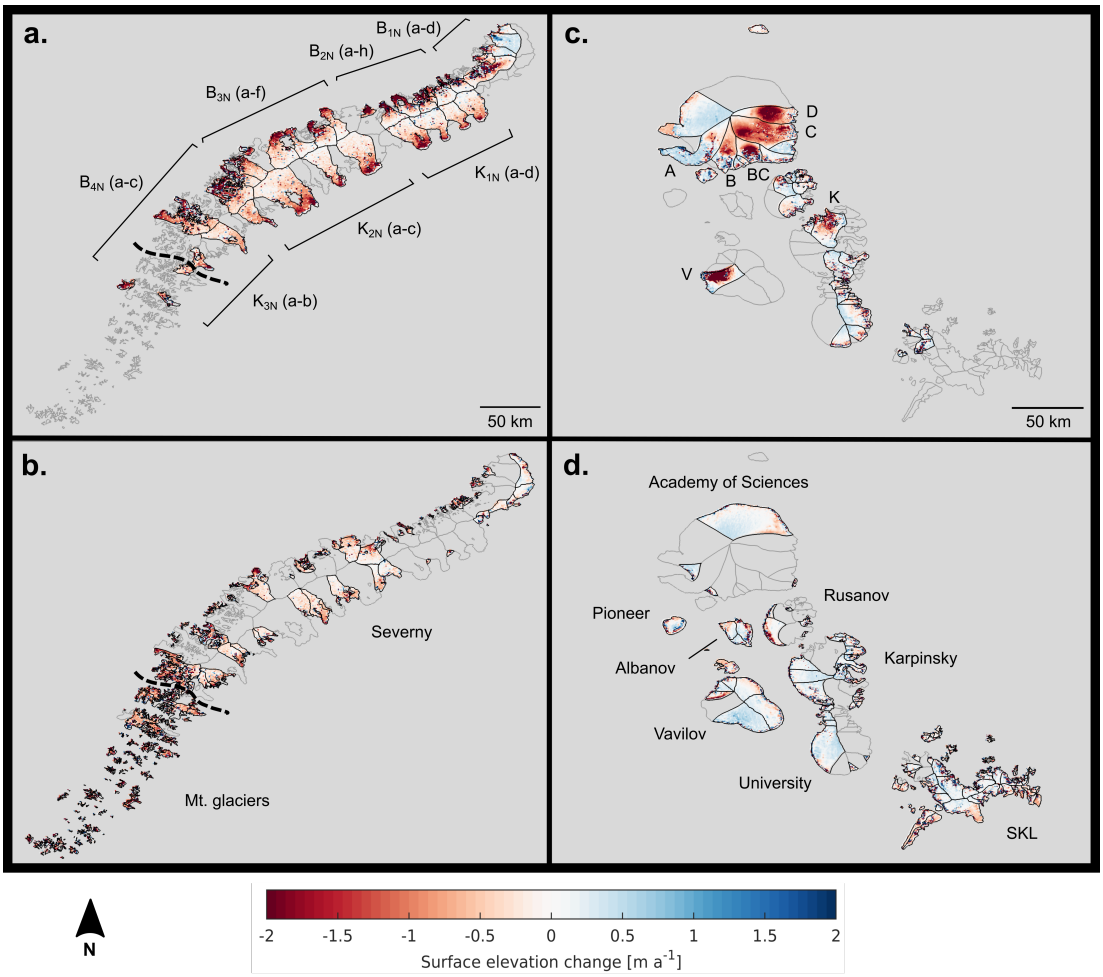
defined in Figure 5.1 for both Novaya Zemlya and Severnaya Zemlya. To account for long-term trends in forcing and possible time lags in glacier response, climate anomalies are computed with reference to a baseline covering the longest period of data available, that is 1978-2018 for ERA5, and 1993-2018 for GLORYS12v1. For an in-depth analysis of more recent trends in ice-climate interactions, anomalies are also calculated based on a 15-year baseline from 2003 to 2018.

5.4 Results

5.4.1 Spatial patterns of surface elevation change

Land ice extending over Novaya Zemlya and Severnaya Zemlya covers a total of 38,135 km^2, representing 75 % of the total Russian Arctic's glaciated area and an estimated 87 % of its volume (Radić and Hock, 2010). This equates to 27.9 ± 7.2 mm potential sea level change representing 19 % of the entire Arctic glaciers and ice caps and 9 % of the global total, including glaciers and ice caps peripheral to the Greenland and Antarctic Ice Sheets (Farinotti et al., 2019). Both archipelagos are surrounded by the shallow Arctic Ocean coastal shelf where the Barents Sea is the deepest with an average depth of 230 m (Oziel et al., 2016). The two islands forming Novaya Zemlya separate the Barents and Kara Seas, while Severnaya Zemlya forms a natural boundary between the Kara and Laptev Seas, with the continental slope to the east (Figure 5.1).

Ice loss in Severnaya Zemlya is dominated by a small number of marine terminating basins while thinning in Novaya Zemlya prevails over almost the entire extent of the glaciated area (Figure 5.2). Tidewater glaciers drain ice from large parts of Novaya Zemlya's ice cap on Severny Island along both the Barents and Kara coasts, where their termini end in relatively shallow fjords or embayments (Figures 5.1 and 5.2). Thinning rates across these basins are highest below 200 m a.s.l. where they reach up to 4 m a^{-1} locally. On average thinning is 50-60 % greater along the Barents coast compared to the Kara coast. Slight thickening



NZ	MT	LT	SZ	MT	LT
Area coverage [% of total]	62%	38%	**Area coverage** [% of total]	47%	53%
Mass budget [Gt a^{-1}]	-5.9 ± 0.4	-3.8 ± 0.2	**Mass budget** [Gt a^{-1}]	-1.9 ± 0.1	+0.2 ± 0.0
Specific mass budget [kg m^{-2} a^{-1}]	-425 ± 30	-441 ± 31	**Specific mass budget** [kg m^{-2} a^{-1}]	-234 ± 17	+27 ± 2

Figure 5.2: Mean 2010-2018 $\dot{h}$ for Novaya Zemlya (NZ) (a, b) and Severnaya Zemlya (SZ) (c, d), and mass budgets (table). Data is partitioned into marine-terminating (MT) (a, c) and land-terminating (LT) basins (b, d). Letters in panels a and c denote single basins keeping the same nomenclature as in Dowdeswell et al. (2002) and Sánchez-Gámez et al. (2019). Names of single ice caps are given in panels b and d. SKL designates the Semyonov-Tyan-Shansky, Kropotkin and Leningrad glacier complex on Bolshevik Island (SZ). The thick dashed line in panels a and b indicates the location of the southern fringe of the contiguous Severny Island Ice Cap.

(< 1 m a^{-1}) is limited to the northernmost basins of the ice cap (B_{1N} a-c), with Bunge Glacier (B_{1N} b) accumulating ice above the equilibrium line and along the central flow line to lower elevations (Figure 5.2a). Thinning across the land-

terminating ice masses of Novaya Zemlya is less pronounced compared to their marine-terminating counterparts, although there is a notable north-south gradient with higher rates of thinning in the south compared to the north suggesting latitudinal control on surface mass balance (Figure 5.2b).

Nearly half of the total glaciated area of Severnaya Zemlya is marine-terminating (Figure 5.2c), 58 % of which is found within the Academy of Sciences Ice Cap in the north of the archipelago. The remaining marine-terminating basins face east along the Laptev coast with the exception of one draining the western margin of Vavilov Ice Cap (Figure 5.2c). Pronounced thinning is observed in six marine-terminating catchments (B, BC, C, D, K and V), with surface lowering from 2 to 30 m across these basins over the entire measurement period, and reaching up to 100 m locally in basin V within a single year (Willis et al., 2018). As a result of their recent dynamic behavior, these basins have all been classified as ice streams in the literature (Sánchez-Gámez et al., 2019; Willis et al., 2015; Zheng et al., 2019). The remaining marine-terminating ice cap basins on Severnaya Zemlya have not exhibited dramatic recent changes in ice dynamics, instead revealing large areas close to balance or thickening in response to long-term net accumulation (Moholdt et al., 2012a). Thinning at these glaciers is confined to narrow sections along the ice cap margins below 200 m a.s.l., with mean rates < 1 m a^{-1}, a pattern that is repeated across all of Severnaya Zemlya's land-terminating ice cap basins.

5.4.2 Time series of surface elevation change

Owing to the high-density of CryoSat-2 swath elevations, we are able to produce statistically robust time series of surface elevation change for individual catchments using 90-day time steps (see Section 3.4). We compute individual time series for the sum of all marine and land-terminating basins located within each of the twelve control domains (B_{1N}-B_{4N}, K_{1N}-K_{3N}, K_{1S}-K_{2S} and L_{1S}-L_{3S}) defined in Figure 5.1 (Figure 5.3). Because tidewater glaciers are likely to exhibit

a more variable response to forcing owing to the additional complexities of ice-ocean interactions and varying boundary conditions (Cowton et al., 2018), we also compute time series for each individual tidewater glacier basin in Novaya Zemlya's seven control areas. We exclude only basins previously identified as surge type (Anuchina, B_{2N}, and Serp i Molot, K_{3N}, see Carr et al., 2017), and two smaller basins (< 150 km^2) that have very few measurements thereby reducing the robustness of their time series, which are Pavlova (B_{1N}) and Krivosheina Glaciers (B_{3N}). For Severnaya Zemlya, we generate time series over basins that dominate total mass loss, namely basins B, BC, C and D on Academy of Sciences Ice Cap, basin V on Vavilov Ice Cap, and basin K on Karpinsky Ice Cap. We also compute time series for basin A, which was previously identified as dynamically active (Moholdt et al., 2012a).

We observe consistent temporal patterns of change along the Barents Sea coast of Novaya Zemlya, with a gradual shift towards more negative thinning trends from north to south (Figure 5.3). The sum of all ice masses within B_{1N} has remained relatively stable during the measurement period ($+0.1 \pm 0.1$ m a^{-1}), although single outlet glaciers display contrasting behaviour, from slight thickening in the northern areas (Bunge Glacier, B_{1N} b and Vera Glacier, B_{1N} c) to thinning of Inostrantseva Glacier (B_{1N} d) further south (Figures 5.2 and 5.3). Ice within B_{2N} thinned on average 0.4 ± 0.1 m a^{-1}, although differences in trends between single basins reach one order of magnitude, ranging from -0.1 ± 0.1 m a^{-1} (Vize Glacier, B_{2N} a) to -1.2 ± 0.1 m a^{-1} (Shokal'skogo Glacier, B_{1N} h) over the study period. This likely reflects differences in dynamic flow characteristics influenced by surface slope, basin hypsometry or variable boundary conditions such as fjord depth and shape (Carr et al., 2017). In comparison, the southernmost control areas of the Barents (B_{3N} and B_{4N}) and the Kara coasts (K_{2N} and K_{3N}) exhibit more consistent trends across basins, with smaller differences in long-term thinning rates between single catchments, and similar seasonal patterns of change (Figure 5.3). The region that experienced the largest losses is B_{4N} (-0.6 ± 0.1 m a^{-1}), with surface lowering locally exceeding 4 m on

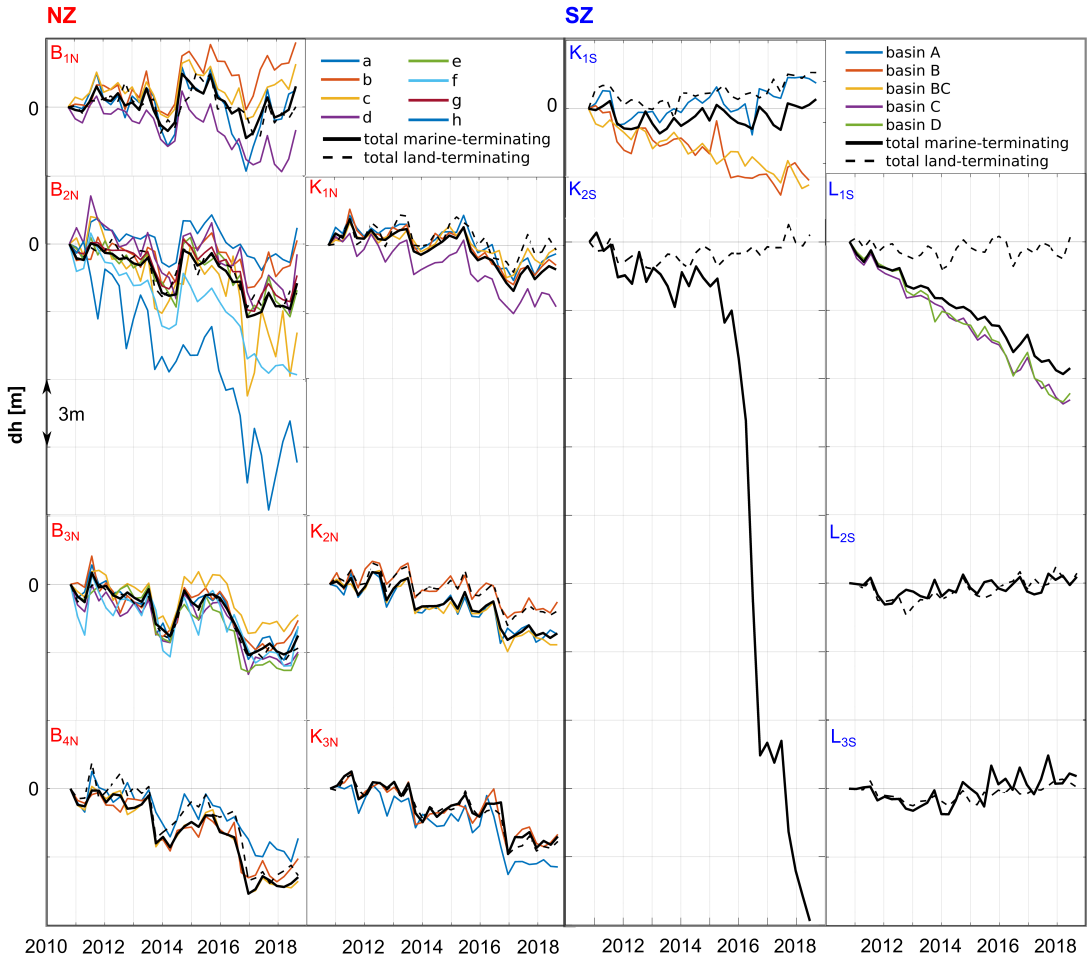


Figure 5.3: Time series of cumulative surface elevation change. Elevation change ($\dot{h}$) is generated over the twelve control areas (B_{1N} – B_{4N}, K_{1N}-K_{3N}, K_{1S}-K_{2S}, L_{1S}-L_{3S}) defined in Figure fig:BKSMap: total glaciated area of marine- and land-terminating (black) and single basins (marine-terminating only, coloured). For Novaya Zemlya, a is the northernmost basin in each control area, other basins are numbered in alphabetical order moving southwards (see Figure 5.2c). For Severnaya Zemlya, the nomenclature of all Academy of Sciences Ice Cap basins (see Figure 5.2d) is based on (Moholdt et al., 2012a) and (Sánchez-Gámez et al., 2019).

average since 2010. Mean rates of thinning along the Kara coast were -0.3 ± 0.0 m a^{-1} in K_{1N} and -0.4 ± 0.0 m a^{-1} in K_{2N} and K_{3N}.

The slowdown in retreat rate, or in some cases advance, of tidewater glacier termini during the period 2013-2015, documented by Carr et al. (2017) and Ciracì et al. (2018), is reflected in our $\dot{h}$ time series, and is particularly visible along the Barents coast, with more pronounced thickening of up to 2 m in the northern areas (B_{1N}) compared to the south (B_{4N}) during the winter of 2014-2015 (Figure

5.3).

The temporal pattern of ice mass change over Severnaya Zemlya is characterised by two distinctive modes of imbalance. The first mode is represented by spatially widespread, uniform, and slow mass gains, which are evidenced by 0.1 ± 0.1 m a^{-1} mean surface elevation increase across all land-terminating basins as well as at all marine-terminating catchments not affected by dynamic thinning (Figure 5.3). This mass gain reflects an ongoing long-term net positive trend in surface mass balance across the archipelago (Dowdeswell et al., 2002; Moholdt et al., 2012a), and contrasts with a second state of imbalance characterised by the confined and rapid offshore advection of ice from the six maritime basins B, BC, C, D, K, and V identified in the previous section. Basins B, C, and D on Academy of Sciences Ice Cap have been subject to multidecadal dynamic thinning (Dowdeswell et al., 2002), with mean annual thinning rates from 2010 to 2018 of 0.3 ± 0.1 m a^{-1} in basin B, and 0.9 ± 0.0 m a^{-1} in basins C and D. Basin BC accelerated at the end of the 2000s (Sánchez-Gámez et al., 2019), with average thinning rates identical to those observed in the neighbouring basin B (0.3 ± 0.1 m a^{-1}), although Sánchez-Gámez et al. (2019) report rates up to 1.21 ± 0.24 m a^{-1} between 2012/13 and 2016. We note that our derived rates of loss from basin BC are likely underestimated due to poor coverage by CryoSat-2 over this particular basin at low elevation (Figure 5.2c). The dramatic losses in region K_{2S} are the result of changes in Basin V on Vavilov Ice Cap, which started to accelerate and thin dramatically after 2015. Two outlet glaciers in basin K (L_{2S}) also accelerated after the breakup of the Matusevich Ice Shelf in 2012 (Willis et al., 2015), but corresponding losses are largely compensated by thickening elsewhere in L_{2S} (Figure 5.2c).

5.4.3 Mass balance

We convert rates of surface elevation change to volume change using glacial area from the Randolph Glacier Inventory (RGI 6.0) and derive mass budgets assuming no spatial or temporal changes in ice density ($\rho_{ice} = 850 \pm 60$ kg m^{-3} = constant) following Huss (2013). We calculate mass balance regionally, according to basin type (marine- or land-terminating) and subdivided into glaciers and ice caps located within the single control areas defined in Figure 5.1.

From 2010 to 2018, Novaya Zemlya lost ice at an average rate of 9.7 ± 0.5 Gt a^{-1} (Table 5.1). Our estimate is marginally higher than the short-term (2012-2013/14) rate of -8.5 Gt a^{-1}) obtained by Melkonian et al. (2016) using stereo-pair WorldView imagery. Applying a point-of-closest-approach sampling using CryoSat-2 altimetry, Ciracì et al. (2018) estimated Novaya Zemlya's losses at 13.3 ± 5 Gt a^{-1} over the period 2010-2016. Our data indicate no mass gains during 2016-2018 (Figure 5.3), hence there seems to be some disagreement between our results and the higher estimates of Ciracì et al. (2018), although differences remain within error, and our estimate is consistent with their 2002-2016 mean of -8 ± 4 Gt a^{-1}. Marine-terminating basins on the Barents coast account for 39 % of Novaya Zemlya's total loss (3.8 ± 0.3 Gt a^{-1}) and sustain the highest local area-specific loss rate across the archipelago, with rates below 500 m a.s.l. up to 1439 ± 32 kg m^{-2} a^{-1}, and a mean rate across catchments of 523 ± 37 kg m^{-2} a^{-1}. These mean rates of loss are 72 % (59 %) higher than those observed within the same elevation band on land-terminating basins along the Barents (Kara) coast (Table 5.1). Losses from land-terminating basins along the Barents coast represent 24 % (2.3 ± 0.1 Gt a^{-1} at 492 ± 22 kg m^{-2} a^{-1}) of total loss, followed by the Kara coasts marine- and land-terminating basins which exhibit losses of 22 % (2.1 ± 0.2 Gt a^{-1} at 329 ± 23 kg m^{-2} a^{-1}) and 10 % (1.0 ± 0.1 Gt a^{-1} at 324 ± 17 kg m^{-2} a^{-1}), respectively. The remaining 5 % of losses (0.5 ± 0.1 Gt a^{-1} at 560 ± 99 kg m^{-2} a^{-1}) come from the mountain glaciers south of Severny Ice Cap (Table 5.1).

Overall, our results reveal a latitudinal gradient in area-specific mass balance

Table 5.1: Glacier and ice cap mass balance and area for regional aggregates and single marine-terminating basins across Novaya Zemlya (NZ) and Severnaya Zemlya (SZ). Mountain glaciers (*) relate to those located south of Severny Island Ice Cap (Figure 5.2b).

	Area [km^2]			Mass budget [Gt a^{-1}]			Mass budget [kg m^{-2} a^{-1}]		
				Total	MT	LT	Total	MT	LT
NZ	**22128**	**13714**	**8414**	**-9.7 ± 0.5**	**-5.9 ± 0.4**	**-3.8 ± 0.2**	**-431 ± 22**	**-425 ± 30**	**-441 ± 31**
> 500m a.s.l.	11094	7727	3367	*-2.1 ± 0.4*	*-1.1 ± 0.3*	*-1.0 ± 0.1*	-197 ± 15	-156 ± 20	-272 ± 22
< 500m a.s.l.	10124	5987	4137	*-7.6 ± 0.1*	*-4.8 ± 0.1*	*-2.8 ± 0.0*	-699 ± 18	-843 ± 23	-543 ± 24
Barents Coast	**11836**	**7263**	**4573**	**-6.1 ± 0.3**	**-3.8 ± 0.3**	**-2.3 ± 0.1**	**-511 ± 24**	**-523 ± 37**	**-492 ± 22**
> 500m a.s.l.	5665	3966	1698	*-1.2 ± 0.3*	*-0.7 ± 0.3*	*-0.5 ± 0.1*	-223 ± 20	-194 ± 10	-287 ± 24
< 500m a.s.l.	6171	3297	2875	*-4.9 ± 0.1*	*-3.1 ± 0.1*	*-1.8 ± 0.0*	-788 ± 25	-978 ± 58	-567 ± 30
B_{1N}	**2568**	**1530**	**1037**	**-0.6 ± 0.1**	**-0.4 ± 0.1**	**-0.2 ± 0.0**	**-241 ± 20**	**-268 ± 33**	**-203 ± 10**
> 500m a.s.l.	*1138*	*705*	*433*	*-0.0 ± 0.0*	*-0.0 ± 0.0*	*-0.0 ± 0.0*	*-53 ± 20*	*-57 ± 28*	*-46 ± 7*
< 500m a.s.l.	*1430*	*825*	*604*	*-0.6 ± 0.0*	*-0.4 ± 0.0*	*-0.2 ± 0.0*	*-434 ± 17*	*-533 ± 22*	*-298± 5*
B_{2N}	**2155**	**1641**	**514**	**-1.3 ± 0.1**	**-1.0 ± 0.1**	**-0.3 ± 0.0**	**-575 ± 38**	**-603 ± 49**	**-486 ± 39**
> 500m a.s.l.	*1289*	974	316	*-0.2 ± 0.1*	*-0.1 ± 0.1*	*-0.1 ± 0.0*	-147 ± 12	-134 ± 25	-190 ± 21
< 500m a.s.l.	*866*	667	198	*-1.1 ± 0.0*	*-0.9 ± 0.0*	*-0.2 ± 0.0*	-1305 ± 39	-1439 ± 32	-857 ± 33
B_{3N}	**4202**	**3172**	**1030**	**-2.2 ± 0.1**	**-1.7 ± 0.1**	**-0.5 ± 0.0**	**-523 ± 30**	**-533 ± 38**	**-495 ± 39**
> 500m a.s.l.	*2435*	1924	511	*-0.5 ± 0.1*	*-0.4 ± 0.2*	*-0.1 ± 0.0*	-205 ± 6	-208 ± 12	-196 ± 7
< 500m a.s.l.	*1767*	1248	519	*-1.7 ± 0.0*	*-1.3 ± 0.0*	*-0.4 ± 0.0*	-939 ± 32	-1026 ± 28	-732 ± 78
B_{4N}	**2911**	**920**	**1992**	**-2.0 ± 0.1**	**-0.7 ± 0.1**	**-1.3 ± 0.1**	**-673 ± 37**	**-739 ± 65**	**-643 ± 45**
> 500m a.s.l.	*802*	363	439	*-0.5 ± 0.1*	*-0.2 ± 0.1*	*-0.3 ± 0.1*	-631 ± 24	-523 ± 18	-547 ± 41
< 500m a.s.l.	*2109*	556	1553	*-1.5 ± 0.0*	*-0.5 ± 0.0*	*-1.0 ± 0.0*	-648 ± 33	-863 ± 58	-752 ± 39
Kara Coast	**9382**	**6451**	**2931**	**-3.1 ± 0.2**	**-2.1 ± 0.2**	**-1.0 ± 0.1**	**-327 ± 17**	**-329 ± 23**	**-324 ± 17**
> 500m a.s.l.	5429	3761	1668	*-0.7 ± 0.2*	*-0.4 ± 0.1*	*-0.3 ± 0.1*	-138 ± 14	-117 ± 14	-186 ± 12
< 500m a.s.l.	3953	2690	1263	*-2.4 ± 0.0*	*-1.7 ± 0.0*	*-0.7 ± 0.0*	-600 ± 11	-681 ± 18	-427 ± 13
K_{1N}	**2499**	**2224**	**275**	**-0.6 ± 0.0**	**-0.6 ± 0.0**	**-0.0 ± 0.0**	**-248 ± 16**	**-270 ± 18**	**-73 ± 9**
> 500m a.s.l.	*1224*	1100	125	*-0.0 ± 0.0*	*-0.0 ± 0.0*	*-0.0 ± 0.0*	-49 ± 8	-55 ± 9	-14 ± 2
< 500m a.s.l.	*1275*	1124	150	*-0.6 ± 0.0*	*-0.6 ± 0.0*	*-0.0 ± 0.0*	-533 ± 16	-578 ± 18	-199 ± 12
K_{2N}	**4729**	**3344**	**1385**	**-1.6 ± 0.1**	**-1.2 ± 0.1**	**-0.4 ± 0.0**	**-336 ± 20**	**-359 ± 27**	**-282 ± 22**
> 500m a.s.l.	*2994*	2168	826	*-0.4 ± 0.1*	*-0.3 ± 0.1*	*-0.1 ± 0.0*	-117 ± 6	-120 ± 8	-109 ± 9
< 500m a.s.l.	*1736*	1177	559	*-1.2 ± 0.0*	*-0.9 ± 0.0*	*-0.3 ± 0.0*	-703 ± 39	-807 ± 21	-483 ± 48
K_{3N}	**2154**	**883**	**1271**	**-0.9 ± 0.1**	**-0.3 ± 0.0**	**-0.6 ± 0.0**	**-399 ± 23**	**-362 ± 34**	**-425 ± 31**
> 500m a.s.l.	*1211*	494	718	*-0.3 ± 0.1*	*-0.1 ± 0.1*	*-0.2 ± 0.1*	-281 ± 13	-243 ± 16	-307 ± 22
< 500m a.s.l.	*942*	389	553	*-0.6 ± 0.0*	*-0.2 ± 0.0*	*-0.4 ± 0.0*	-509 ± 35	-617 ± 41	-434 ± 25
Mt. glaciers*	**910**	**-**	**910**	**-0.5 ± 0.1**	**-**	**-0.5 ± 0.1**	**-560 ± 99**	**-**	**-560 ± 99**
> 500m a.s.l.	*324*	-	324	*-0.2 ± 0.1*	-	*-0.2 ± 0.1*	-419 ± 76	-	-419 ± 76
< 500m a.s.l.	*586*	-	586	*-0.3 ± 0.0*	-	*-0.3 ± 0.0*	-598 ± 102	-	-598 ± 102
	Area [km^2]			Mass budget [Gt a^{-1}]			Mass budget [kg m^{-2} a^{-1}]		
				Total	MT	LT	Total	MT	LT
SZ	**15957**	**7592**	**8365**	**-1.7 ± 0.1**	**-1.9 ± 0.1**	**+0.2 ± 0.0**	**-97 ± 8**	**-234 ± 17**	**+27 ± 2**
Kara Coast	**5203**	**2992**	**2211**	**-0.8 ± 0.1**	**-0.9 ± 0.1**	**+0.1 ± 0.0**	**-158 ± 18**	**-331 ± 30**	**+77 ± 5**
K_{1S}	2952	2637	315	+0.1 ± 0.0	+0.1 ± 0.0	+0.0 ± 0.0	+24 ± 3	+15 ± 4	+95 ± 0
K_{2S}	2251	355	1896	-0.9 ± 0.1	-1.0 ± 0.1	+0.1 ± 0.0	-395 ± 40	-2901 ± 254	+74 ± 5
Laptev Coast	**10754**	**4600**	**6154**	**-0.9 ± 0.1**	**-1.0 ± 0.1**	**+0.1 ± 0.0**	**-77 ± 7**	**-204 ± 15**	**+18 ± 2**
L_{1S}	2979	1735	1244	-0.9 ± 0.1	-1.0 ± 0.1	+0.1 ± 0.0	-302 ± 24	-576 ± 40	+80 ± 8
L_{2S}	3460	1756	1704	-0.1 ± 0.0	-0.1 ± 0.0	-0.0 ± 0.0	-9 ± 3	-34 ± 6	-2 ± 0
L_{3S}	4315	1109	3206	+0.1 ± 0.0	+0.1 ± 0.0	+0.0 ± 0.0	+23 ± 2	+108 ± 9	+6 ± 0

across Novaya Zemlya's ice cap, which is clearest above 500 m a.s.l. and applies to both marine and land-terminating basins along both coasts. Area-specific losses generally increase southwards, although below 500 m a.s.l. the gradient is less evident, likely due to the complexities of ice-ocean interactions, which lead to more diverse responses across tidewater glacier basins (Table 5.1). There is also a clear longitudinal mass loss gradient between the east and west coasts of Novaya Zemlya, with marine- (land-) terminating basins along the Barents coast deflating on average 59 % (52 %) more intensively per unit area compared to the Kara coast (Table 5.1).

The 2010-2018 mass imbalance of Severnaya Zemlya was dominated by the acceleration of ice flow from basin V in region K_{2S} in 2015-2016 (Willis et al., 2018). During 2010-2018, the basin lost on average 2901 ± 254 kg m^{-2} annually (Table 5.1). This estimate includes large areas situated along the southern and eastern margins of the catchment where surface elevation remained stable during our CryoSat-2 monitoring period. We also confirm significant losses from four ice streams draining the Academy of Sciences Ice Cap (Sánchez-Gámez et al., 2019), in particular basins C and D, which dominate the overall loss rate of 576 ± 40 kg m^{-2} a^{-1} within control domain L_{1S}. Ice discharge from these two basins was estimated by Sánchez-Gámez et al. (2019) at 1.13 ± 0.09 Gt a^{-1} for the period 11/2016 - 11/2017. This compares well with our longer-term 2010-2018 mean of 1.0 ± 0.1 Gt a^{-1} for the marine-terminating segment of domain L_{1S} (Table 5.1), which in addition to the ice streams C and D also incorporates two relatively small southwestern basins that are close to balance (Figure 5.2c).

5.4.4 Climatic trends in the BKS region

Glaciers and ice caps of the Eurasian High Arctic have been exposed to multidecadal atmospheric and ocean warming, and associated high rates of sea ice decline, with increased intensity in the western compared to the eastern parts of the region (Dowdeswell et al., 2002; Moholdt et al., 2012b). This exposure

has triggered extensive acceleration of ice loss (Strozzi et al., 2017a) and induced widespread thermal and dynamic regime shifts across the entire BKS (Dunse et al., 2015; Nuth et al., 2019; Willis et al., 2018). Amidst this fast-changing environment, identifying the main controls on glacier change has proven challenging (Carr et al., 2017; Ciracì et al., 2018; Sánchez-Gámez et al., 2019). Here, we investigate regional and synoptic climate variability, in an attempt to identify potential forcing mechanisms and their interannual to decadal impact on glaciers and ice cap mass loss across the Russian Arctic.

For the BKS region as a whole, and for each of the control domains defined earlier for Novaya Zemlya and Severnaya Zemlya, we analyse changes in air surface temperature (T_{2m}), sea surface temperature (SST), subsurface ocean thermal forcing (SOTF), and sea ice concentrations (SIC) over the satellite period (1970s-2010s), with variable temporal coverage depending on data availability for each parameter (Figures 5.4 and 5.5). To capture possible control mechanisms at the ice-ocean interface, we calculate mean $SOTF_{1-3}$ as the ocean potential temperature expressed relative to the in situ freezing point (see Methods and Slater et al., 2019) at three different depth levels ($SOTF_1$, 0-55 m; $SOTF_2$, 55-110 m; $SOTF_3$, 110-155 m). Because the various forcings can influence glacier dynamics and surface mass balance over different time scales, we consider ice-climate interactions over multidecadal timescales at seasonal (90-day) resolution. Seasonal climate anomalies are calculated with reference to the entire measurement period that corresponds to each climate variable, and annual anomaly trends are with reference to a 15-year (2003-2018) baseline, which coincides with ice surface altimetry from both ICESat and CryoSat-2 (Figures 5.4 and 5.5).

Time series of T_{2m}, SST, SOTF and SIC seasonal forcing anomalies reveal trends disrupted by a discernible climatic shift that started in the early-to-mid 2000s, with positive temperature- and negative SIC anomalies largely prevailing in all seasons after this change (Figures 5.4b,d and 5.5b,d). Segmented regression of the time series suggests a shift towards accelerated warming starting in the western parts of the BKS, with highest rates of increase in T_{2m} and SST (0.1°C

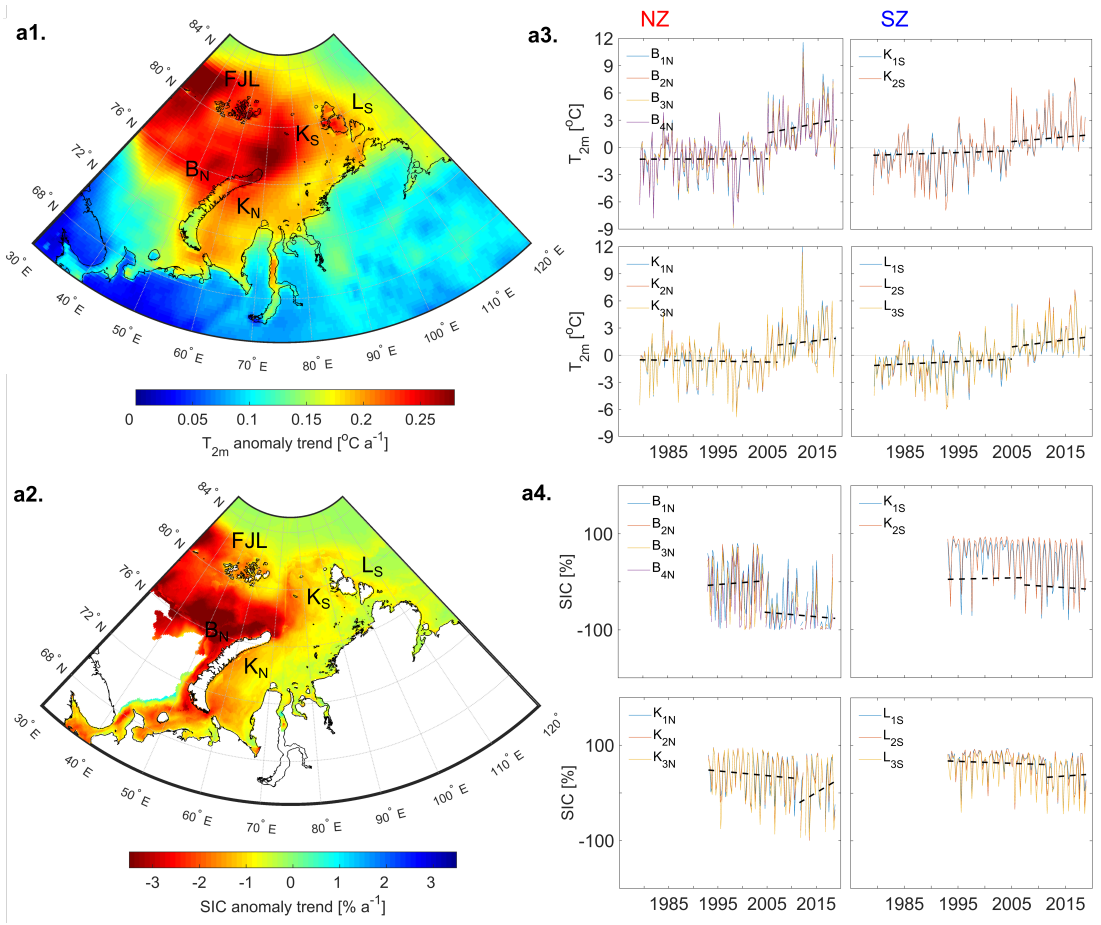


Figure 5.4: T_{2m} (ERA5) and SIC (GLORYS) annual anomaly trends over the baseline period 2003-2018 **(a,c)** and long-term seasonal anomalies time series **(b,d)** relative to 1978-2018 (T_{2m}) and 1993-2018 (SIC) means. The latter two reference periods correspond to the maximum temporal coverage of the ERA5 (T_{2m}) and GLORYS (SIC) reanalysis products. Dashed lines are derived from segmented best fit analysis using a single break point.

a^{-1}) along the Novaya Zemlya Barents coast after 2003 and 2005 (Figures 5.4b and 5.5b upper left panels), and locally > 0.3 °C a^{-1} (Figures 5.4a and 5.5a). By the time of the first CryoSat-2 measurements in 2010, all forcings, including SOTF and SIC, reveal accelerating trends compared to the pre-CryoSat-2 period, with maximum rates of change (> 0.1 °C a^{-1}) occurring in the areas B_{1N}-B_{4N} (Figures 5.4b,d and 5.5b,d all panels).

Maps of anomaly trends between 2003-2018 provide a spatial overview of climate warming amplification in the Eurasian High Arctic (Figures 5.4a,c and 5.5a,c), from the early 2000s, when acceleration in glacier frontal retreat began

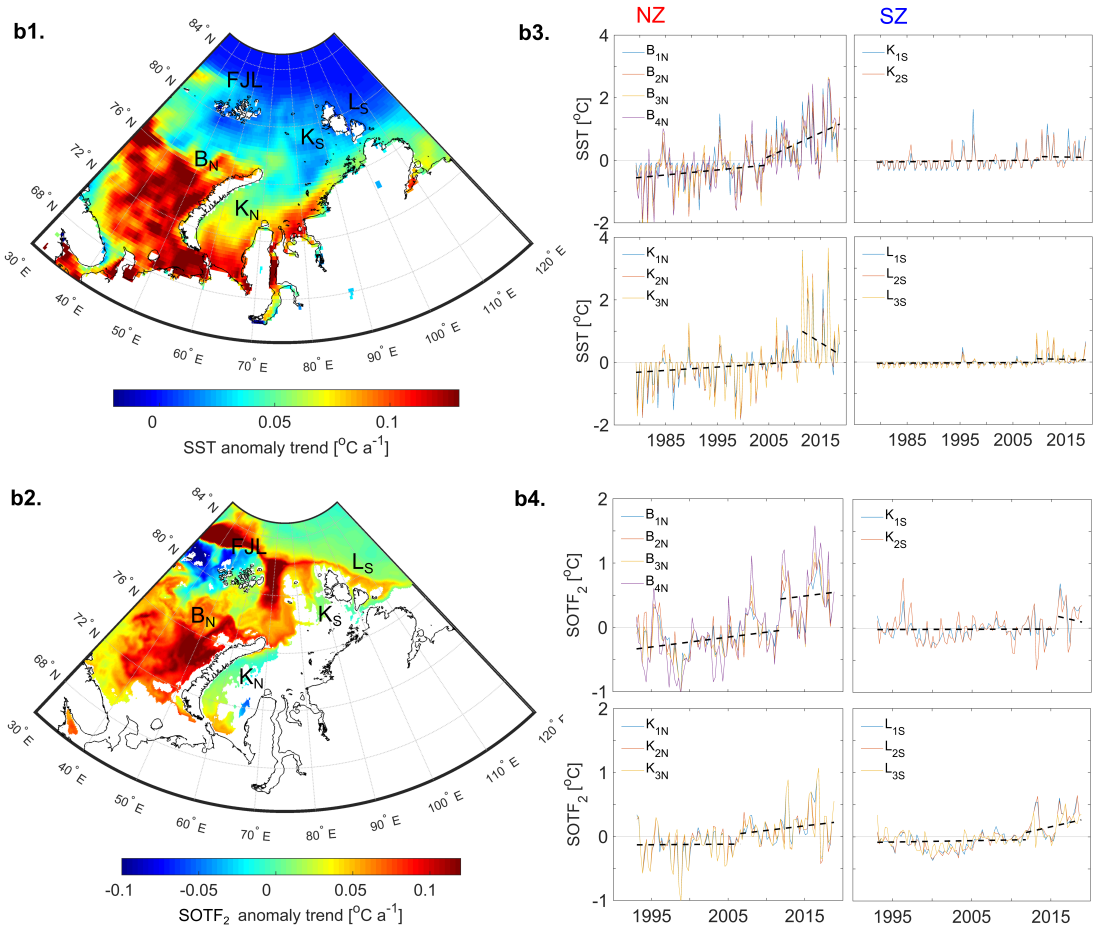


Figure 5.5: SST (ERA5) and SOTF$_2$ (GLORYS) annual anomaly trends between 2003 and 2018 (a,c) and seasonal anomalies over the reference period (b,d). Anomalies are calculated with reference to 1978-2018 (SST) and 1993-2018 (SOTF$_2$) long-term means corresponding to the maximum temporal coverage of each reanalysis product (note different time axes). SOTF$_2$ is the mean ocean forcing computed over 19 depth levels between 55 m and 110 m below sea level. Dashed lines are derived from segmented best-fit analysis using a single break point.

(Carr et al., 2017), and throughout the CryoSat-2 period. The T_{2m} map (Figure 5.4a) reveals extensive and intense regional surface warming, from west of Franz Josef Land to Severnaya Zemlya, and from the central Barents Sea to the continental shelf break north of Franz Josef Land. Maximum T_{2m} (> 0.3 °C a^{-1}) and SIC (< -1 % a^{-1}) anomalies within this hotspot are concentrated in the northeast Barents Sea, and extend into a relatively well-defined area north of Novaya Zemlya, coinciding with the location of the St Anna Trough between Franz Josef Land and Severnaya Zemlya (Figure 5.1). This is a region where, in

addition to high rates of surface warming and sea ice decline, SOTF anomalies are particularly high compared to zonal means (Figure 5.5c). SOTF anomalies > 0.1 °C a^{-1} are also present along the southern periphery of the Eurasian Basin of the Arctic Ocean, suggesting the presence of Atlantic Water entering the Arctic via the Fram Strait, and propagating along the continental slope in the form of a geostrophic current (Lien et al., 2013) (Figures 5.1 and 5.5c). Steep, positive SST anomaly trends can be observed in the central, southern and eastern parts of the Barents Sea (Figure 5.5a), where weak ocean stratification and strong vertical mixing are dominant features (Barton et al., 2018; Oziel et al., 2016). This is further reflected in similar subsurface ocean warming signatures, with steep SOTF anomaly trends in the same regions (Figure 5.5c). High rates of change in SST are restricted in the north by the polar front, a narrow oceanic convergence zone, where warm and saline Atlantic Water entering the southern Barents Sea meets fresher and colder Arctic Water (Oziel et al., 2016). The east and northward migration of the polar front, forced by "impinging Atlantification" (Polyakov et al., 2017), has led to sea ice decline, weakened ocean stratification, and increased vertical heat flux through the water column (Årthun et al., 2012; Barton et al., 2018). We infer that this eastward progression of Atlantic climate has also increasingly affected tidewater glacier dynamics and land ice loss in the BKS region.

5.5 Discussion

5.5.1 Novaya Zemlya's ice mass response to atmospheric and oceanic warming

Our CryoSat-2 measurements confirm previous findings by Carr et al., 2017; Ciracì et al., 2018; Melkonian et al., 2016 suggesting that Novaya Zemlya's mass loss is greatest from marine-terminating basins located along the Barents coast (Table 5.1). These and other studies (e.g. Wouters et al., 2019) have made a range

of inferences linking observations of glacier change to external forcing. Carr et al. (2017), for example, found a correlation between SST, SIC and accelerated glacier retreat across Novaya Zemlya from 2000 to 2012. Here, we expand these analyses and include subsurface ocean temperature data to elucidate differences in response patterns over Novaya Zemlya's ice masses.

Climate reanalyses reveal a clear difference in SIC, SST and SOTF anomaly trends between the Barents and Kara coasts since the early 2000s. Between 2003 and 2018, SST and $SOTF_{1-3}$ increased on average by 0.1 - 0.3 °C a^{-1} along the Barents coast, while ocean temperatures remained relatively stable along the Kara coast (Figure 5.5a,c and Appendices, Figures 5.12 - 5.14). During the same time period, sea ice concentration decreased at rates > 3 % a^{-1} off the Barents coast, compared to just ~ 1 % a^{-1} along the Kara coast (Figure 5.4c,d). We also note that SIC and SST warming anomaly trends along the Barents coast are steepest during MAM and JJA, respectively (Appendices, Figures 5.10 - 5.11). Along the main paths of Atlantic Water inflow, SOTF anomalies appear large at all depths, and rates of subsurface warming > 0.1 °C a^{-1} are pervasive in all seasons in the eastern Barents Sea, the St Anna Trough, and along the continental margin, with slightly stronger ocean warming in the upper 110 m layer during SON and DJF (Appendices, Figures 5.12 - 5.13). This sustained ocean forcing is consistent with the high frontal velocities reported for Barents coast marine-terminating outlet glaciers in all seasons (Melkonian et al., 2016). At the same time, T_{2m} anomaly trends are > 0.4 °C a^{-1} during winter (DJF) around the central and northern part of Severny Ice Cap, with also a significant warming trend of 0.3 – 0.4 °C a^{-1} in the Barents coastal region during spring (MAM) (Appendices, Figure 5.9). Collectively, these forcing patterns suggest that high surface melt rates in spring and summer coincide with strong ocean forcing at the calving front, forming a concomitant driver of rapid dynamic thinning along the western margins of Severny Ice Cap. Furthermore, evidence suggests persistent, decadal upwelling of relatively warm subsurface ocean water through vertical Ekman transport around Novaya Zemlya (Ma et al., 2017), in particular in the

eastern Barents Sea (Appendices, Figure 5.15, left panel), with the potential to enhance glacier calving and submarine melting. Based on these observations, we infer that, in addition to ubiquitous net surface losses, ocean forcing is a key parameter that explains: **1)** the 59 % difference in mass loss from west-coast- compared to east-coast-facing tidewater glaciers, and **2)** the 72 % (59 %) higher rates of loss below 500 m a.s.l. on Barents (Kara) coast tidewater glaciers compared to adjacent land-terminating glaciers Ciracì et al., 2018; Melkonian et al., 2016 (Table 5.1).

5.5.2 Atlantic Ocean fingerprints on Severnaya Zemlya's dynamic imbalance

The highly heterogenous response of Severnaya Zemlya's glaciers and ice caps to external forcing (Figures 5.2 and 5.3) suggests either a more varied and complex set of control mechanisms on glacier change compared to Novaya Zemlya, or a more dramatic dynamic response to the same set of forcings. While ice streams B, C and D in the Academy of Sciences Ice Cap (Figure 5.2) are known to have continuously drawn down ice for multiple decades (Moholdt et al., 2012a), and without any signs of associated surge-type activity (Dowdeswell and Williams, 1997), three further catchments have dynamically activated across the archipelago during the 2010s. These are basin BC on Academy of Sciences Ice Cap (Sánchez-Gámez et al., 2019), basin K on Karpinsky Ice Cap (Willis et al., 2015) and basin V on Vavilov Ice Cap (Willis et al., 2018). To explain the increasing number of dynamic instabilities and formation of ice streams across the Eurasian Arctic, including Svalbard, a number of recent studies have argued for the role of ocean-driven frontal ablation, which can trigger instabilities that propagate inland rapidly (McMillan et al., 2014; Strozzi et al., 2017b). Another commonly postulated driver of ice velocity variations is through the supply of summer surface melt to the glacier bed, which temporarily increases water pressure thereby initiating rapid ice-flow by partially releasing underlying resistive stresses (Dunse

et al., 2015; Nuth et al., 2019). In Severnaya Zemlya, the dynamically thinning and relatively fast flowing (> 200 m a^{-1}) ice streams exhibit monthly ice flow variability not only during the summer months, but also in winter (Sánchez-Gámez et al., 2019; Strozzi et al., 2017a; Willis et al., 2015; Willis et al., 2018), with no significant correlation between summer surface temperatures and ice dynamics (Sánchez-Gámez et al., 2019). This suggests that active supply of supraglacial meltwater to the glacier bed is not likely to play a leading role in the variability of ice flow in this region (Willis et al., 2018). Although intrinsic, catchment-specific processes triggering dynamic imbalances need to be considered (Sánchez-Gámez et al., 2019; Willis et al., 2018), it is striking that all ice stream formations and glacier accelerations in Severnaya Zemlya are marine-terminating. We examine therefore the possibility of ocean forcing as a potential overarching driver that may at least partially explain both summer and winter velocity variations, as well as Severnaya Zemlya's global dynamic mass imbalance.

A net decrease in Atlantic influence over Severnaya Zemlya compared to Novaya Zemlya is evident in the less pronounced T_{2m} and SIC anomaly trends, on average < 0.1 °C a^{-1} and < 1 %, respectively between 2003 and 2018, and hence a less dramatic shift towards more rapid warming in the 2000s (Figure 5.4 all panels). Furthermore, ocean warming around Severnaya Zemlya is delayed with respect to warming in the Barents Sea, with steeper trends emerging only in the 2010s, in particular along the Laptev coast (Figure 5.5b,d). The most prominent climatic signal in the vicinity of the archipelago, however, is the persistent positive SOTF anomaly warming trend along the Eurasian continental slope, which affects locally the L_{1S}-L_{3S} domains in all seasons (Figure 5.5c and Appendices, Figures 5.12 - 5.14). This feature is characterised by ocean temperature anomalies up to 0.2 °C a^{-1}, and as noted previously, is an expression of the eastward flowing Fram Strait branch of Atlantic Water (Figure 5.1), a geostrophic current adjacent to the continental margin between the Laptev Sea and the Eurasian Basin (Zhurbas and Kuzmina, 2020). It was previously shown that ocean stratification in the Eurasian Basin has weakened over recent decades (Polyakov et al., 2010), which

facilitates upward heat transfer across ocean layers and to the surface (McMillan et al., 2014; Polyakov et al., 2017). Furthermore, rates of upwelling along the east coast of Severnaya Zemlya have increased over the past four decades as a result of enhanced Ekman pumping in the Laptev Sea (Appendices, Figures 5.15 - 5.16; Ma et al., 2017). We therefore infer, in line with observations elsewhere (Nick et al., 2013) that this long-term, enhanced oceanic heat supply represents a potential control on glacier dynamics in the region. A sustained upward movement of relatively warm subsurface water, assisted by coastal surface currents and tides, may result in these warm waters reaching some of the fronts of Severnaya Zemlya's glaciers and ice caps, in particular the eastern and southern basins of the Academy of Sciences Ice Cap (L_{1S}), and the east-facing marine-terminating segments of Rusanov (L_{2S}), Karpinsky (L_{2S}) and University Ice Caps (L_{3S}) (Figure 5.1). Taking into account that the bed topography adjacent to the Academy of Science Ice Cap's ice streams is characterised by deep troughs 100-300 m below sea level (Dowdeswell et al., 2002), it is likely that ocean water with temperatures above freezing not only impacts submarine melting at the glacier front, but also flows into ocean cavities beneath the floating tongues which tend to form at marine ice cap margins (Straneo and Heimbach, 2013). This is the case for example in the frontal area of basin K (Issledovateley Glacier) on Karpinsky Ice Cap, and basins C and D on Academy of Science Ice Cap (Williams and Dowdeswell, 2001). Marine subglacial water incursions may perpetuate or initiate dynamic instability by increasing rates of submarine melting at the grounding line (Slater et al., 2016), thereby reducing resistive stress forces and possibly weakening subglacial sediment layers (Sánchez-Gámez et al., 2019; Willis, 1995).

5.5.3 Coupled versus decoupled climatic forcing

To further examine the sensitivity of the Russian Arctic's glacier response to climatic change, we perform a quantitative assessment of the relationship between CryoSat-2 90-day surface elevation change, $\dot{h}$, and seasonal forcing anomalies be-

tween 2003 and 2018, with a particular focus on the established west-east forcing gradient between Novaya Zemlya and Severnaya Zemlya. We first calculate cross-correlations between $\dot{h}$ and T_{2m}, SIC, SST and $SOTF_{1-3}$ using sequential 90-day shifts along the time axis to identify the length of any delay, based on statistics, between the observed changes in elevation and the underlying forcings in each of the twelve control areas defined in Figure 5.1 (Appendices, Figure 5.17a-c). The best fit is obtained with an average time lag between all forcings and regions of 1.5-year (6×90 days), indicating an equivalent delay in response to forcing (Appendices, Figure 5.17d). To the best of our knowledge, no previous estimates have been made regarding glacier response times in the Russian Arctic, but our result is consistent with the recent dynamic response (slow-down) to ocean cooling at Jakobshavn Isbrae Glacier in west Greenland (Khazendar et al., 2019).

After taking into account the 1.5-year delay in response, we perform a regression analysis between $\dot{h}$ and each of the forcings using both original and detrended time series for comparison. The latter are calculated by subtracting the linear forcing trends over the full length of the dataset to avoid establishing spurious relationships between the non-stationary dynamic processes involved (Hanna et al., 2013; Santer et al., 2000; Slater et al., 2019). These analyses reveal a significant link ($p < 0.01$) between ocean forcing and $\dot{h}$ along Novaya Zemlya's Barents coast, with maximum values of R^2 ranging between 0.23 and 0.63, and between 0.19 and 0.41 when using detrended time series (Appendices, Figure). Correlations between $\dot{h}$ and T_{2m} and SIC are generally weaker, which may be explained in part by high seasonal variability in these forcings, with a tendency to increase the magnitude of short-term noise in the long-term trends (Cowton et al., 2018), and leading to a more dispersed delay window of ice mass response to these forcings compared to ocean forcing across regions. Furthermore, the statistical significance of the correlations between $\dot{h}$ and all climate forcings decreases from west to east across the BKS, with p-values > 0.01 over Severnaya Zemlya, where a consistent delay in response is not evidenced, as a result of large shifts in mass balance, strong discrepancies in response between land- and marine-terminating basins

(Figure 5.3), and different climate dynamics with respect to Novaya Zemlya.

Because the observed trends in glacier mass imbalance are caused by interannual and decadal climate variability, we investigate the ice-climate relationships at timescales of the order of the average response delay, and perform regression analysis again with a 1.5-year moving average filter applied to both $\dot{h}$ and forcings, and with all variables normalised over their respective minimum/maximum range within each control area (Figure 5.6). The smoothed forcing patterns highlight the general warming trend discussed in Chapter 2, Section 2.4, on which are superimposed 4-5-year cycles during which T_{2m}, SIC, SST and $SOTF_{1-3}$ anomalies oscillate in phase over Novaya Zemlya (Figure 5.6, B_{1N}-B_{4N} and K_{1N}-K_{3N}), and increasingly out of phase when moving eastward (areas K_{1S}-K_{4S} and L_{1S}-L_{3S}). This overarching oscillating pattern is possibly associated with leading modes of hemispheric climate variability such as the Arctic- or the North Atlantic Oscillation (see Appendices, Figure 5.19 and accompanying text for further discussion). Over Novaya Zemlya, the smoothed and normalised forcing anomalies are in phase with the corresponding time-lagged $\dot{h}$ responses in all domains, with higher $\dot{h}$ rates prevailing over the southern- compared to the northern areas due to meridional air- and sea surface temperature gradients (Appendices, Figure 5.20).

Regression performed on the smoothed time series confirm significant correlations between $\dot{h}$ and all of the forcings in the areas along the Barents coast of Novaya Zemlya (Figure 5.7), with R^2 values varying between 0.25 and 0.83 depending on the forcing. We report these correlations with a high level of confidence ($p < 0.005$), although we note that the fits and their statistical significance are possibly enhanced by the low-pass filtering of the time series. The level of significance in the correlation decreases in the areas K_{1N}-K_{3N} along the Kara coast of Novaya Zemlya, where only $SOTF_{1-3}$ exhibit a significant relationship to ice thinning (Figure 5.7). Over Severnaya Zemlya, the correspondence between different forcings and thinning rates is less clear and more variable between regions (Figures 5.6 and 5.7). Nevertheless, ice loss in this region is most consistently correlated significantly with $SOTF_2$, in particular in the regions K_{2S}, L_{1S} and L_{2S},

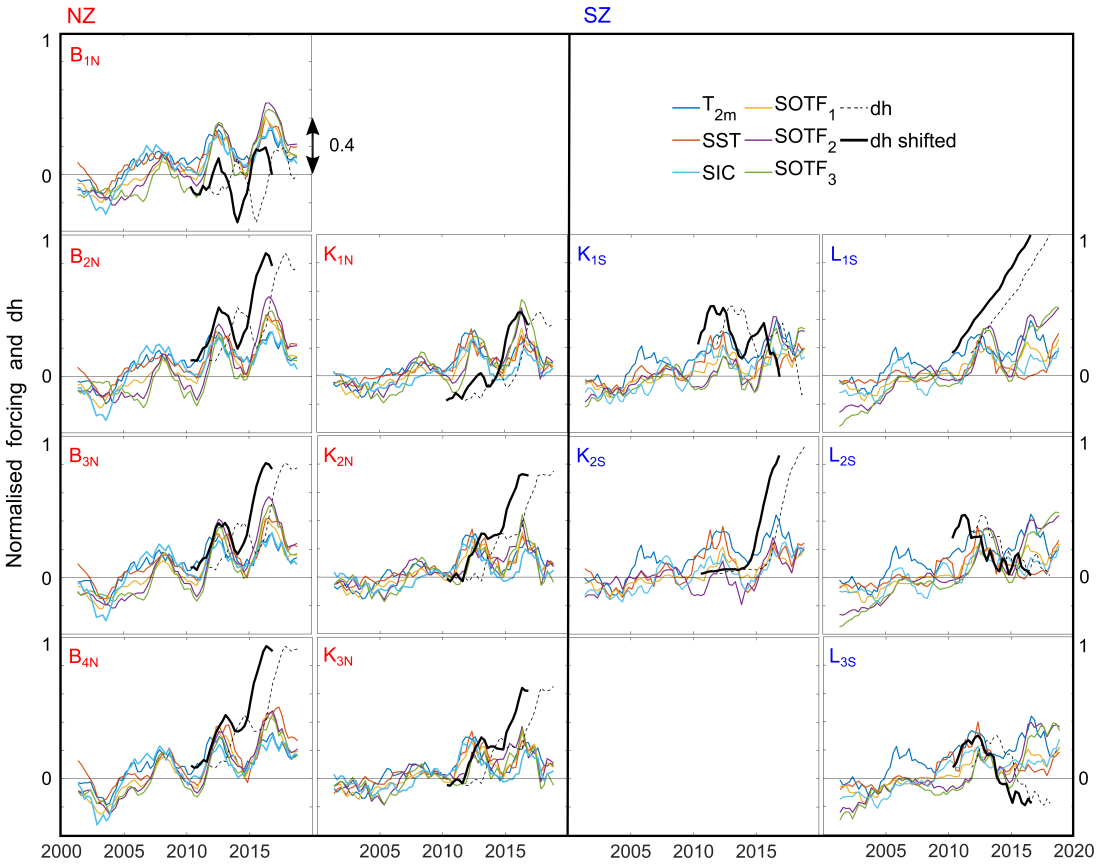


Figure 5.6: Forcing anomalies and $\dot{h}$ time series over marine-terminating basins plotted for each of the twelve control areas: Novaya Zemlya's Barents- (left) and Kara coasts (middle-left), and Severnaya Zemlya's Kara- (middle-right) and Laptev coasts (right). To average out short-term climatic fluctuations, $\dot{h}$ and all forcing anomalies are represented by their 1.5-year moving mean. For an improved visual interpretation of the results, $\dot{h}$ and SIC are shown inverted over the time axis (i.e. positive $\dot{h}$ and SIC represent thinning and reduction, respectively). Rates of $\dot{h}$ are displayed both with and without applying the 1.5-year response delay to forcing (see text). Anomalies are expressed over their long-term means and normalized over their respective minimum/ maximum range.

where dynamic thinning has been most intensive over the study period (Figure 5.7).

We infer that changes in mass loss over Novaya Zemlya from 2010 to 2018 were modulated by a coupled atmosphere (T_{2m}) - ocean (SIC, SST, $SOTF_{1-3}$) forcing mechanism, with all controls displaying a non-stationary oscillatory forcing pattern with a 4-5-year periodicity, and with decreasing strength from west to east between the two coasts. According to this supposition, the 2013 slow-

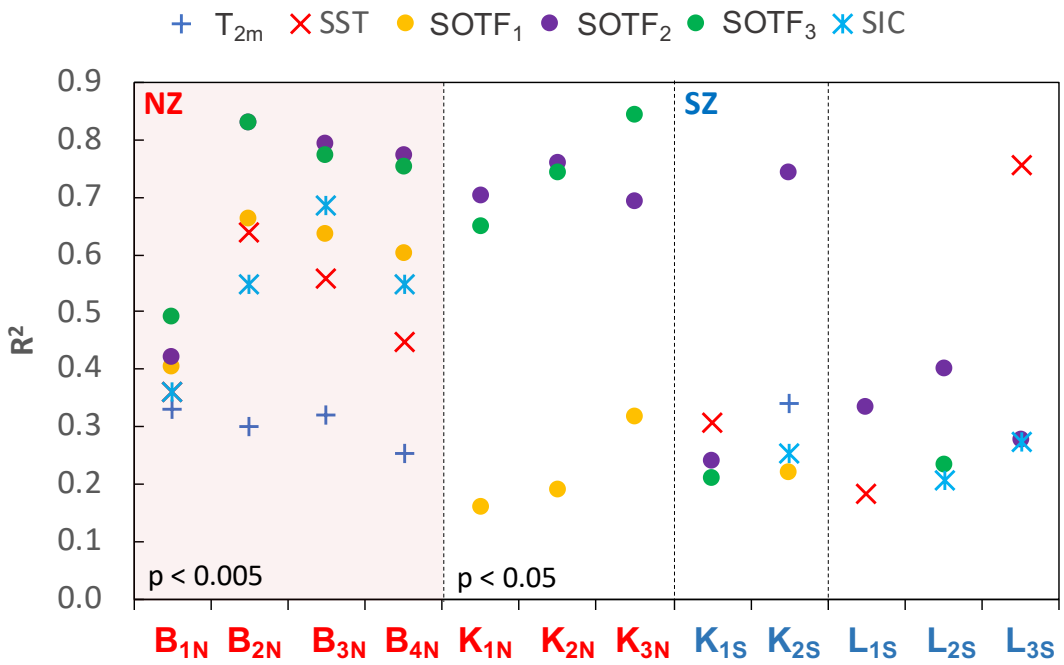


Figure 5.7: R^2 statistics as a measure of linear fit between environmental forcing and surface elevation change $\dot{h}$. A significant correlation ($p < 0.005$) is found between $\dot{h}$ and all forcings (T_{2m}, SST, $SOTF_{1-3}$, SIC) within the areas B_{1N}-B_{4N}. For the remaining control domains in Novaya Zemlya and Severnaya Zemlya the results are only shown for $p < 0.05$.

down in frontal retreat rates reported by Carr et al. (2017) would have occurred in response to a slowdown in atmospheric and ocean warming between 2011 and 2013 (Figure 5.6), followed by a dynamic response during the period 2014-2015. This inference is evidenced by thickness gains in Novaya Zemlya's $\dot{h}$ time series from 2014 to 2015 (Figure 5.3). Similarly, we infer that the periods of accelerated ice loss between 2011 and 2013 and after 2016 were in response to a preceding acceleration in warming during the periods 2009-2011 and 2014-2016, respectively. Hence, in this region, and particularly along the Barents coast, we argue that the Atlantic supply of oceanic heat controls frontal ablation via submarine melting and calving and drives the inland-propagating dynamic imbalance of tidewater glaciers, as revealed by intense thinning over large areas at low elevation of marine-terminating catchments (Figure 5.2a). At the same time, receding sea ice in the eastern and northern Barents Sea (Appendices, Figure 5.10) allows for

heat fluxes to rise vertically through the water column and into the atmospheric boundary layer (Årthun et al., 2012). This increases both sea- and air surface temperatures locally, further enhancing sea ice loss and the already pervasive surface melt across Novaya Zemlya.

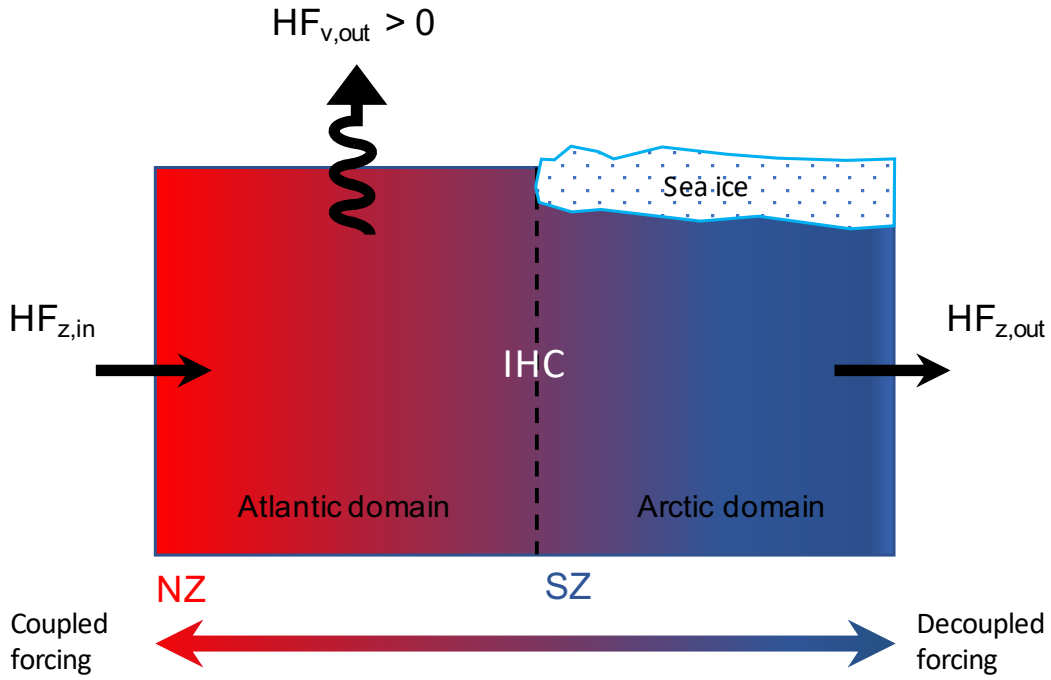


Figure 5.8: Schematic illustrating heat fluxes in the BKS region. IHC is the integrated ocean heat content, with horizontal arrows symbolising lateral ocean heat fluxes (HF_z). Vertical heat fluxes (HF_v) across the water column and into the atmospheric boundary layer lead to synchronous, coupled atmosphere-ocean forcing on land ice (Novaya Zemlya, Barents Sea coast). Higher sea ice concentrations around Severnaya Zemlya decouple potential atmosphere-ocean interactions and divide their impact on land ice mass change. Schematic adapted from Årthun et al. (2012).

Coupled atmosphere-ocean forcing is less prevalent in the eastern BKS, where a more pronounced ocean stratification (Polyakov et al., 2017) impedes the propagation of vertical heat fluxes, and higher sea ice concentrations inhibit the efficient ocean-to-atmosphere heat transfer (Figure 5.8). Upwelling of relatively warm subsurface water with Atlantic signature is nonetheless sustained by vertical Ekman transport along the continental slope, an occurrence that is likely to have an effect on submarine melting and calving of the east-facing glacier fronts of Severnaya Zemlya. Hence, atmospheric and oceanic forcings over the

archipelago drove differing mass changes via contrasting behaviours reflecting decoupled environmental forcing (Figure 5.8). Under these conditions low annual mean air temperatures and precipitation rates led to slight and almost ubiquitous mass gains distributed across the surface of the ice caps (Moholdt et al., 2012a; Zhao et al., 2014), but with ocean forcing contributing locally to sustained ice discharge and calving from a number of marine-terminating catchments, some of which have only been recently activated.

5.6 Summary and conclusions

We used eight years of high-resolution CryoSat-2 interferometric altimetry to generate maps of surface elevation change $\dot{h}$ and derive mass balance from 2010 to 2018 over the glaciers and ice caps of Novaya Zemlya and Severnaya Zemlya in the Russian Arctic. The high-density swath elevation fields were used further to generate, for the first time, robust time series of $\dot{h}$ at 90-day time steps over single tidewater glacier basins at regional scale. We analysed the time series in conjunction with climate data reanalyses to establish links between the Russian Arctic's glaciers and ice caps mass imbalance and environmental change.

We find that Novaya Zemlya continues to dominate sea level input in the BKS region, with total ice loss of 9.7 ± 0.5 Gt a^{-1} driven by similar area-specific rates of loss from both land (441 ± 31 kg m^{-2} a^{-1}) and marine terminating glaciers (425 ± 30 kg m^{-2} a^{-1}). Along Novaya Zemlya's Barents coast, both surface melt and ice dynamics form and strong coupled mechanism leading to enhanced tidewater glacier mass imbalance, due to dramatic thinning in the lower tidewater terminus regions. Ice loss in Severnaya Zemlya (1.7 ± 0.1 Gt a^{-1} at 97 ± 8 kg m^{-2} a^{-1}) is predominantly driven by six marine-terminating ice streams, whereas elsewhere in the archipelago, the ice at the basin scale is slightly thickening. Of the six ice streams, the acceleration of basin V on Vavilov Ice Cap in spring 2015 has led to the most significant shift in mass balance in the BKS region since 2010.

Our results reveal a clear and significant link between amplified, coupled

atmosphere-ocean forcing and ice thinning over Novaya Zemlya, with a ∼1.5-year delay in the response of the ice masses to the onset of forcing. This linear response is particularly strong along the Barents Sea coast, where ongoing Atlantification is driving the climate dynamics and the subsequent ice mass response. Calving rates in Severnaya Zemlya are also controlled by Atlantic Ocean heat transfer, in this instance along the Eurasian continental slope, and assisted by Ekman vertical transport enabling warmer waters to reach tidewater glacier termini. However, over Severnaya Zemlya, oceanic and atmospheric forcing are decoupled, the former sustaining or activating ice dynamics at individual marine-terminating basins, and the latter sustaining a positive surface mass balance over the entire archipelago.

A linear relationship between ice loss and oceanic and atmospheric forcing has been demonstrated previously over parts of Greenland (Cowton et al., 2018; Slater et al., 2019, 2020). In the Eurasian High Arctic, a coupled atmosphere-ocean warming feedback is currently expanding eastwards in response to the northward shift of Atlantic climate (Polyakov et al., 2017), sea ice decline (Stroeve et al., 2018), and positive climate feedbacks (Goosse et al., 2018). Our detailed temporal and spatial observations of patterns of glacier thinning suggests that this progression is already significantly impacting glacier and ice cap stability in the eastern Russian Arctic, with the potential for future dynamic regime changes and enhanced mechanisms of ice loss.

Despite the complexities of climate variability in the BKS sector and a range of dynamic responses specific to the Russian High Arctic, our study confirms that relatively simple, linear relationships are sufficient to describe regional ice-climate interactions and future ice loss in this region. These relationships provide considerable potential for improving global sea level predictions through the incorporation of parametrisations in coupled ice-atmosphere-ocean modelling work (Slater et al., 2020).

5.7 Appendices

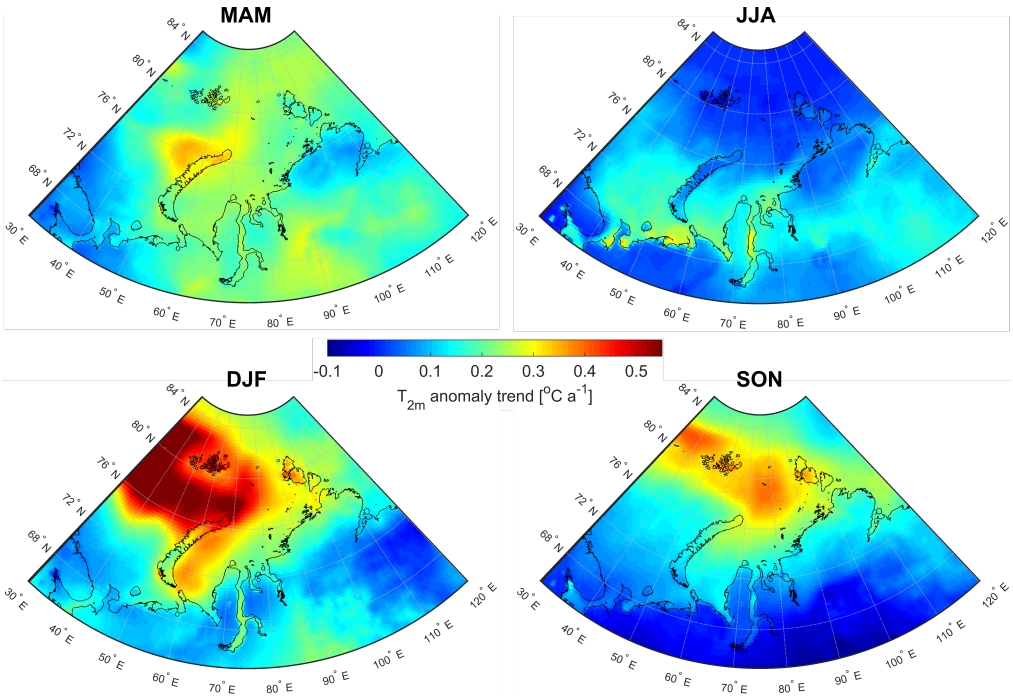


Figure 5.9: T_{2m} (ERA5) seasonal anomaly trends 2003-2018.

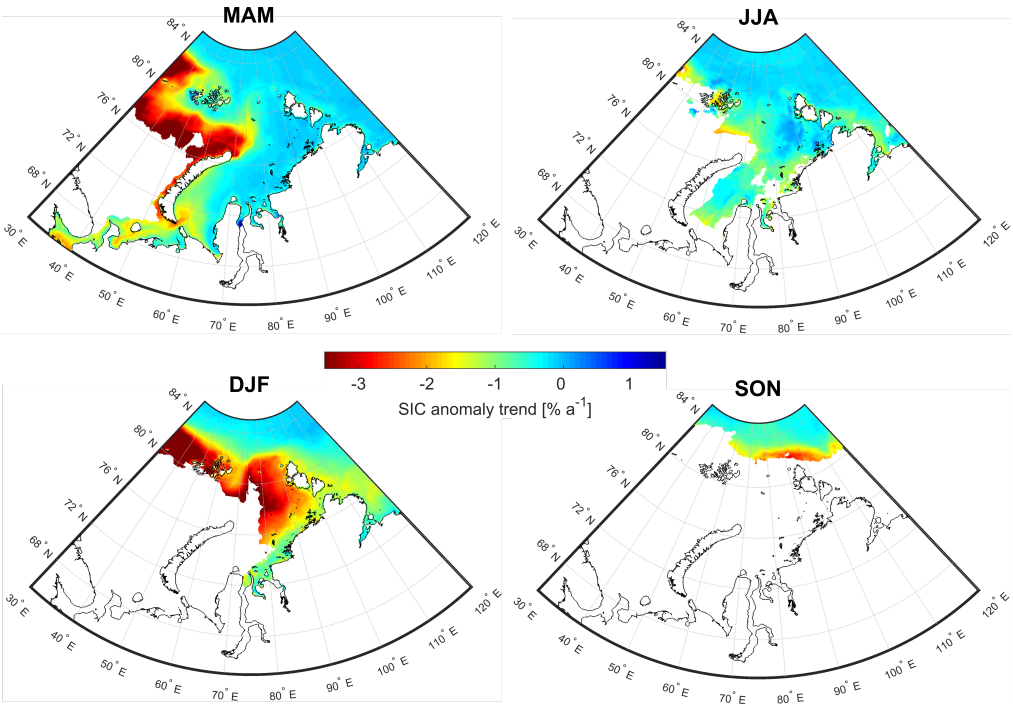


Figure 5.10: SIC (GLORYS) seasonal anomaly trends 2003-2018.

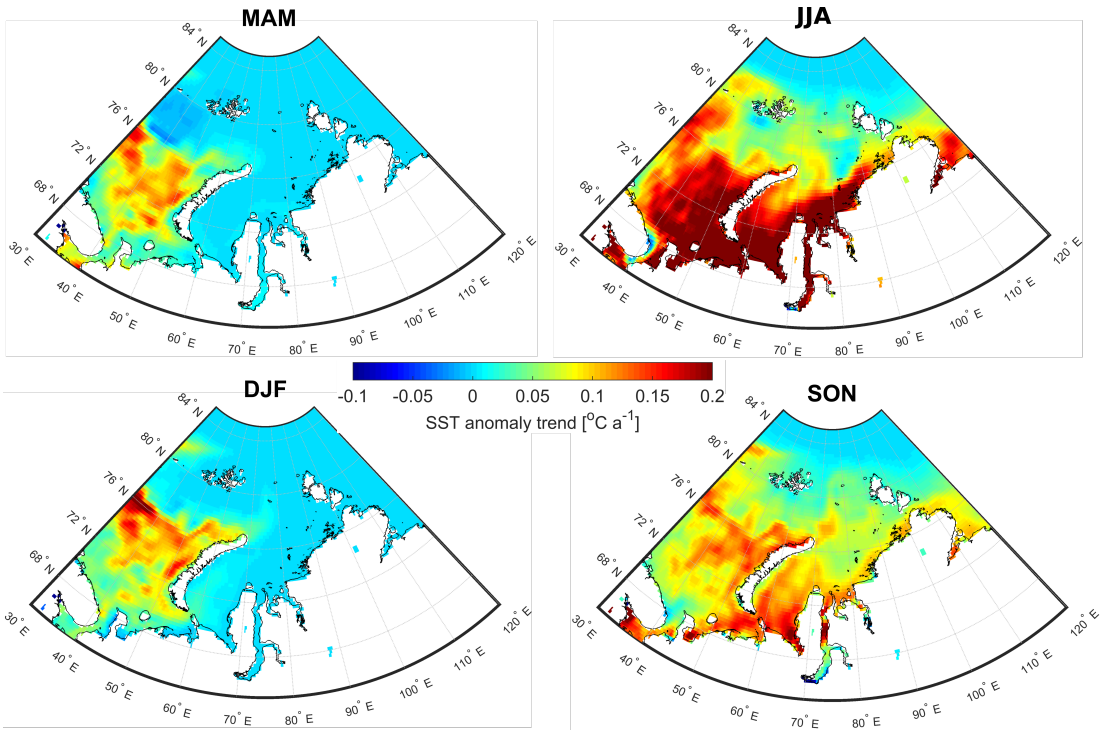


Figure 5.11: SST (ERA5) seasonal anomaly trends 2003-2018.

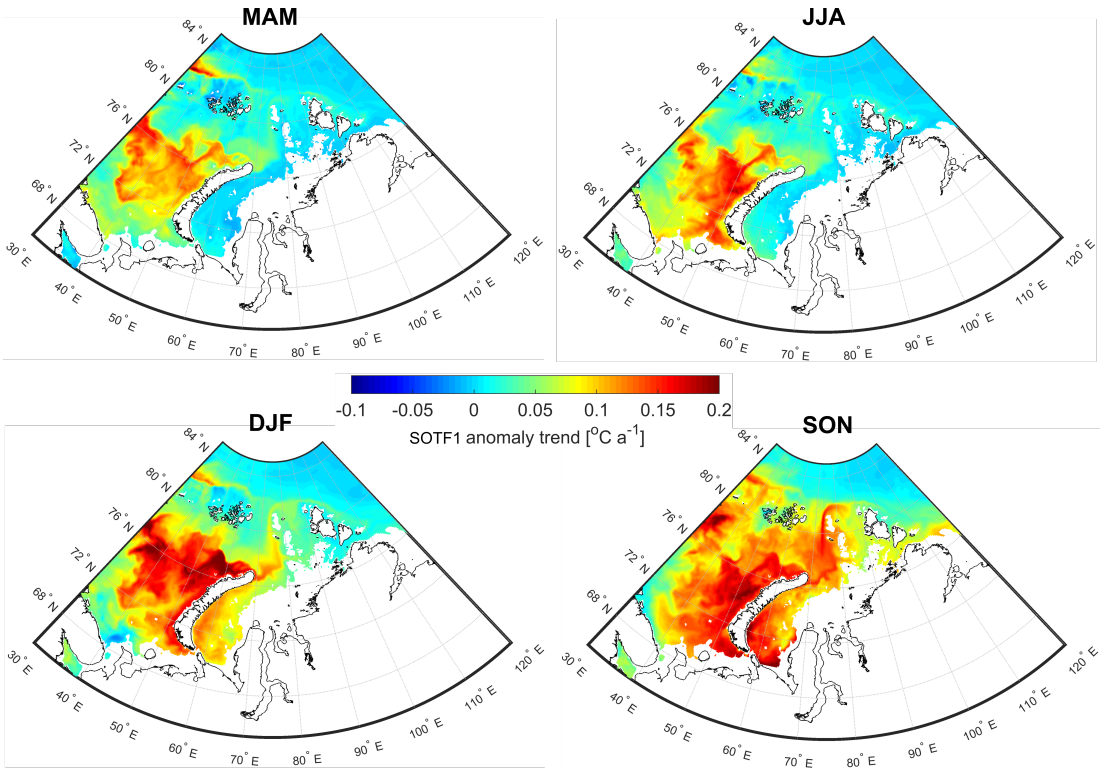


Figure 5.12: Mean (0.5 – 55 m b.s.l.) $SOTF_1$ (GLORYS) seasonal anomaly trends 2003-2018.

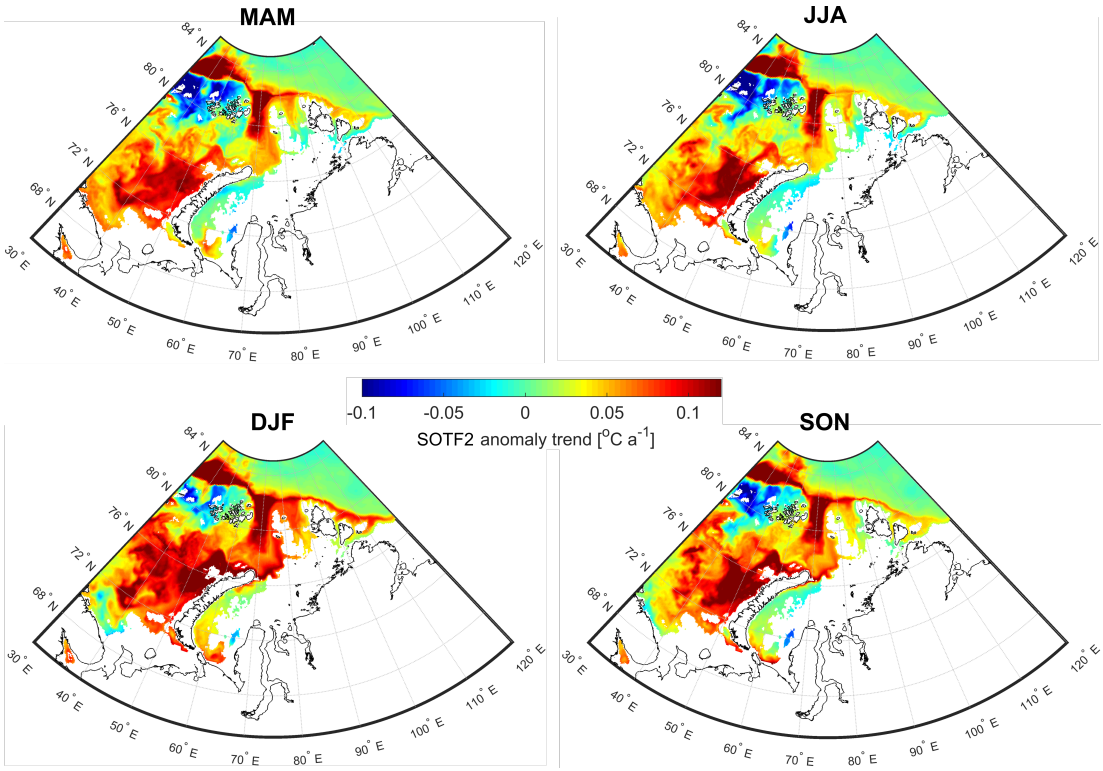


Figure 5.13: Mean (55 – 110 m b.s.l.) $SOTF_2$ seasonal anomaly trends 2003-2018.

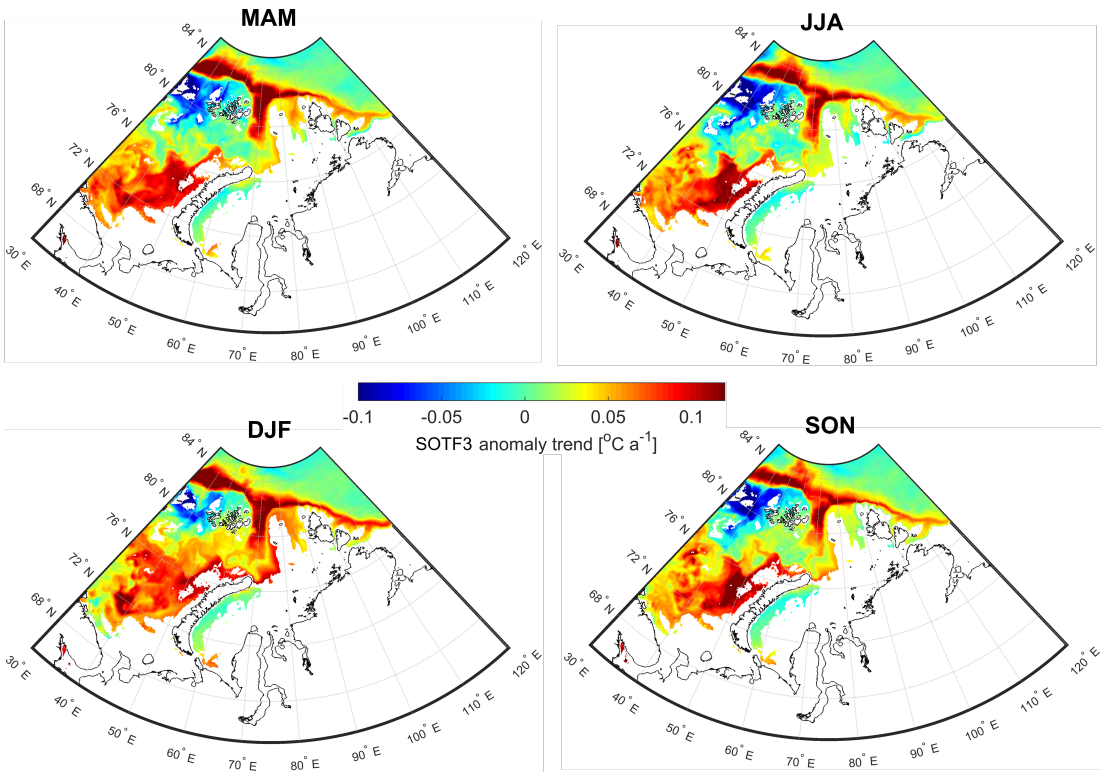


Figure 5.14: Mean (110 – 155 m b.s.l.) $SOTF_3$ seasonal anomaly trends 2003-2018.

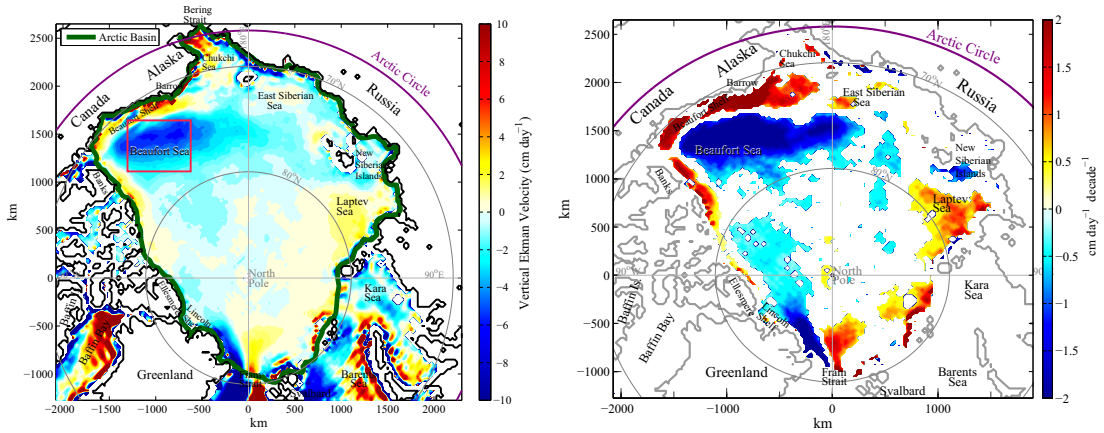


Figure 5.15: Arctic Ocean mean annual (1979-2014) vertical Ekman transport (left) and linear trends in vertical Ekman velocity (1979-2014) with significance level p $\leq$ 0.05 (right). Source: (Ma et al., 2017)

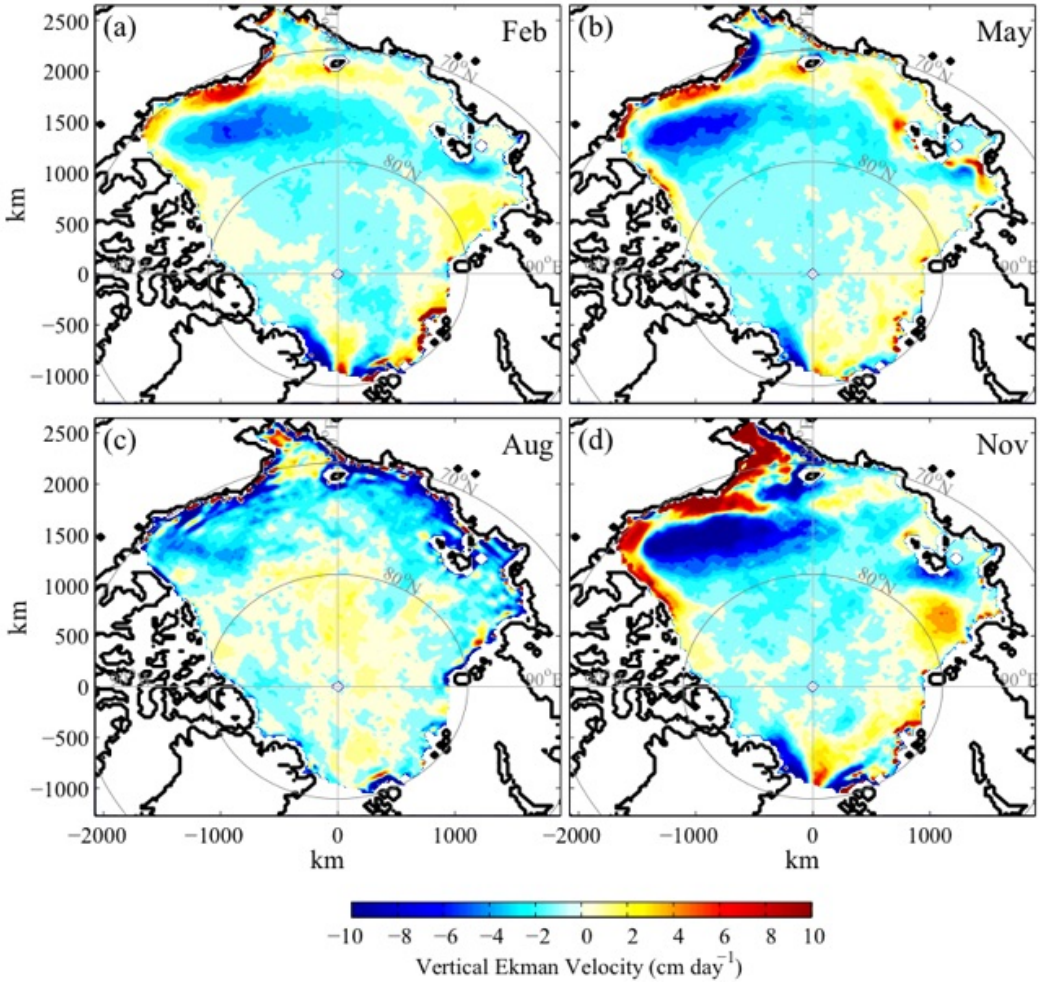


Figure 5.16: Maps of annual mean vertical Ekman velocity for (a) 1979-1989), (b) (1990-1999), (c) (2000-2009), (2010-2014). Source: (Ma et al., 2017)

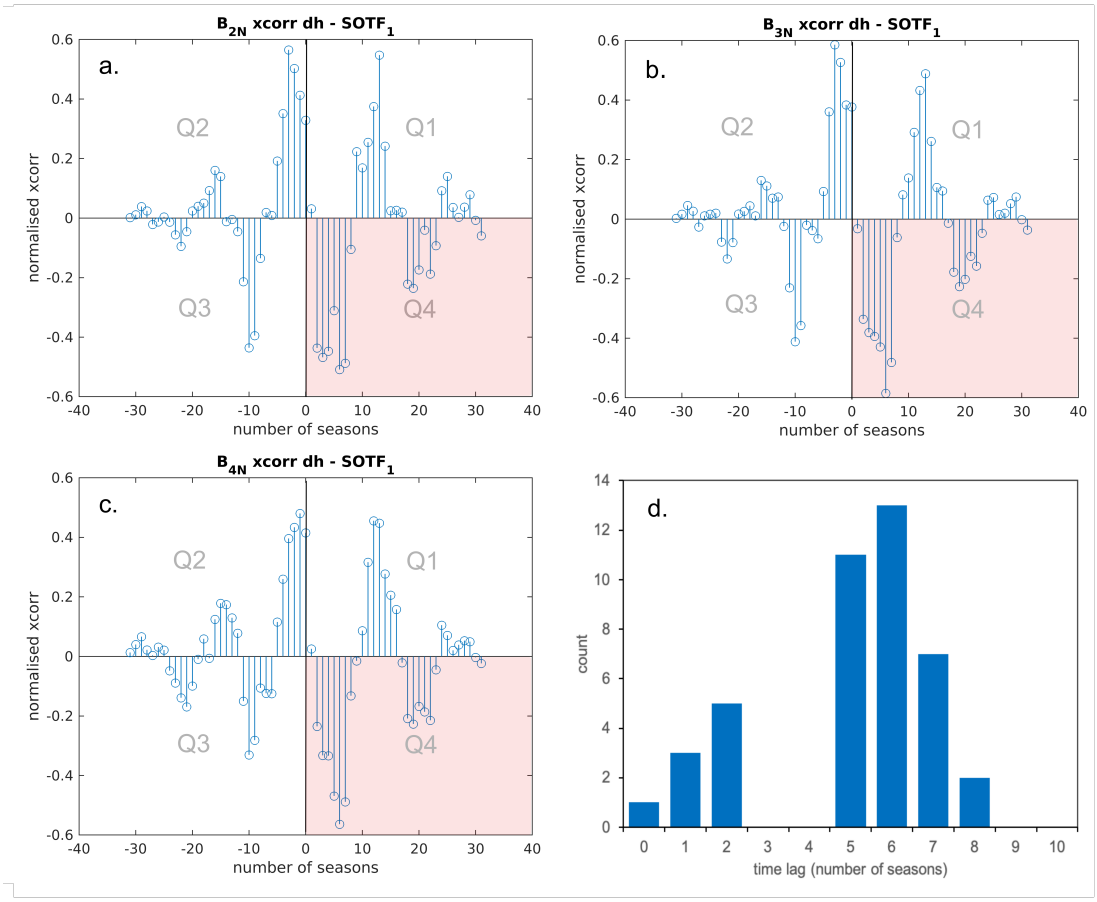
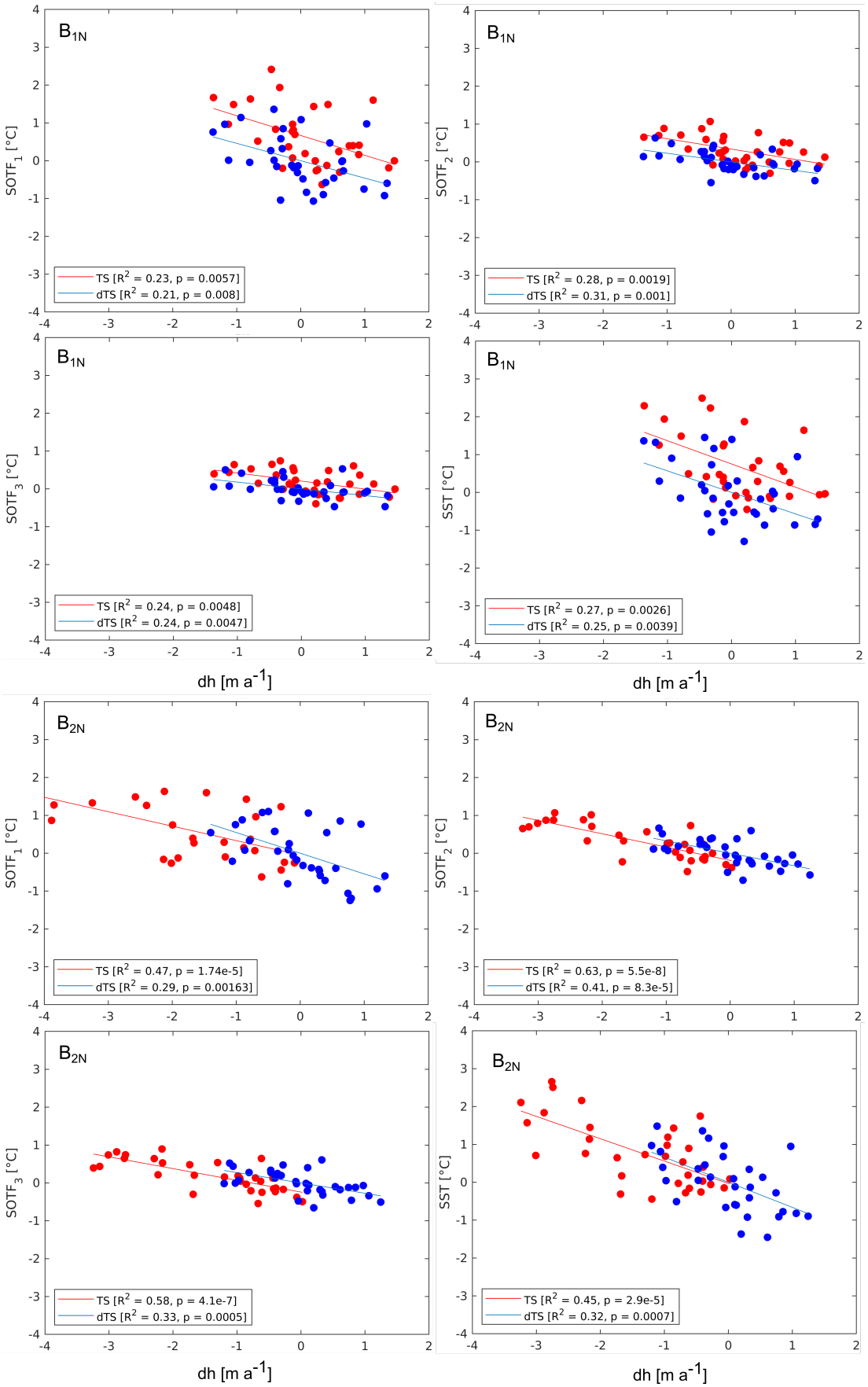
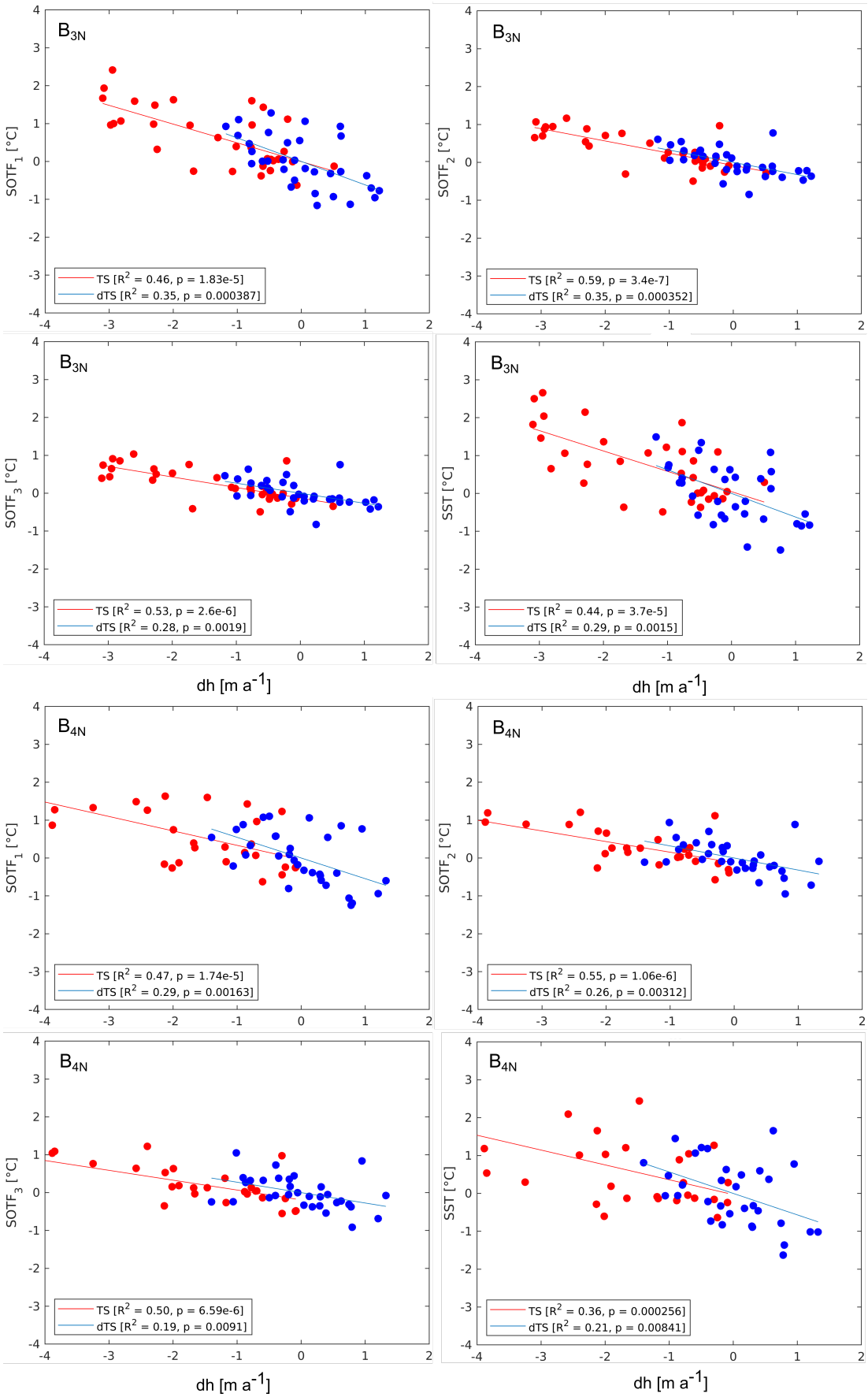


Figure 5.17: Cross-correlation analysis (*xcorr*) to identify a potential mean time lag between dh and different environmental forcings: example of $SOTF_1$ cross-correlated with dh over Novaya Zemlya's control areas B_{2N}- B_{4N} **(a-c)** and a histogram accounting for all the statistically strongest cross-correlations between dh and forcings T_{2m}, SIC, SST and $SOTF_{1-3}$ within the seven control areas of Novaya Zemlya **(d)**. The *xcorr* function (MATLAB) returns the cross-correlation of two discrete time sequences, with each unit in the time sequence equating to 90 days. It measures the similarity between each time-dependent forcing F(t) and shifted (lagged) copies of dh as a function of the lag. Cross-correlations in the first and second graphic quandrants (Q1 & Q2) represent inverse relationships between F and dh (e.g. thickening in response to rising temperatures). Similarly, cross-correlations in the second and third quadrants (Q2 & Q3) represent inverted time lags, implying that the climate response is preceding the forcing. Assuming that no other forcing, such as for example post-surge activity, is significantly influencing dh, all cross-correlations in quadrants Q1-Q3 therefore describe cases of physical aberrancy and thus need to be discarded. The histogram in (d) therefore only accounts for cross-correlation maxima occurring within the fourth quadrant (Q4) in each of the plots. The median time lag in the histogram is 6 seasons or 1.5 years.

Figure 5.18: Linear regressions of $\dot{h}$ and ocean forcings for areas along Novaya Zemlya's Barents coast using the original, non-stationary time series (red dots), and detrended time series (blue dots). Weaker correlations between $\dot{h}$ and T_{2m} and SIC, and for the rest of the control areas are not shown.




B3N
SOTF1 [°C]
TS [R2 = 0.46, p = 1.83e-5]
dTS [R2 = 0.35, p = 0.000387]
B3N
SOTF2 [°C]
TS [R2 = 0.59, p = 3.4e-7]
dTS [R2 = 0.35, p = 0.000352]
B3N
SOTF3 [°C]
TS [R2 = 0.53, p = 2.6e-6]
dTS [R2 = 0.28, p = 0.0019]
B3N
SST [°C]
TS [R2 = 0.44, p = 3.7e-5]
dTS [R2 = 0.29, p = 0.0015]
dh [m a-1]
dh [m a-1]
B4N
SOTF1 [°C]
TS [R2 = 0.47, p = 1.74e-5]
dTS [R2 = 0.29, p = 0.00163]
B4N
SOTF2 [°C]
TS [R2 = 0.55, p = 1.06e-6]
dTS [R2 = 0.26, p = 0.00312]
B4N
SOTF3 [°C]
TS [R2 = 0.50, p = 6.59e-6]
dTS [R2 = 0.19, p = 0.0091]
B4N
SST [°C]
TS [R2 = 0.36, p = 0.000256]
dTS [R2 = 0.21, p = 0.00841]
dh [m a-1]
dh [m a-1]

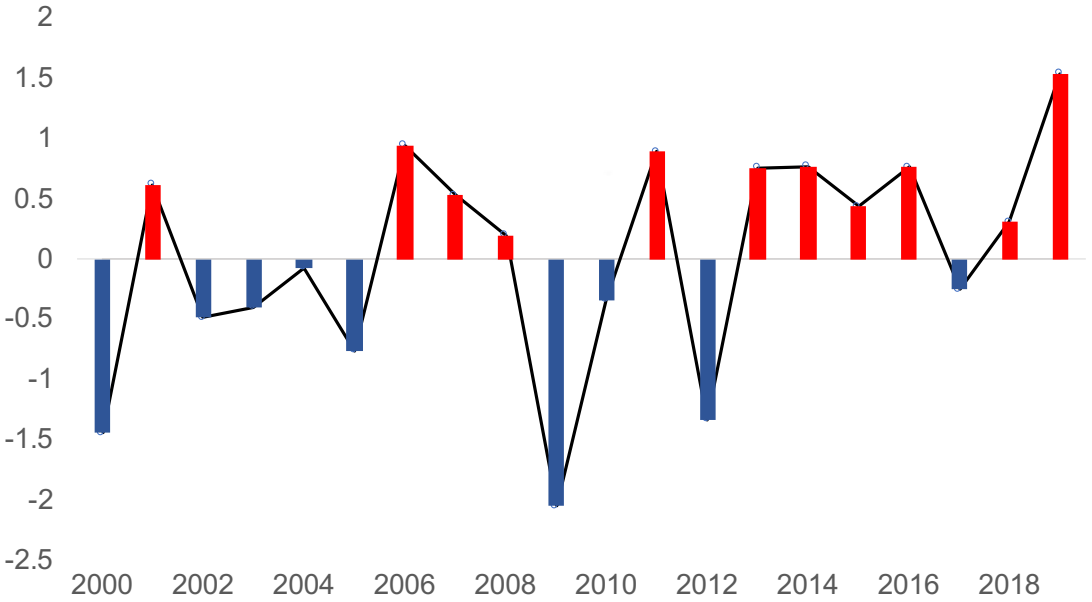


Figure 5.19: Arctic Oscillation (AO) Index for the months of November to March (NOAA).

The Arctic Oscillation (AO) is defined as the leading empirical orthogonal function of the wintertime sea level pressure field (Thompson and Wallace, 1998). It is the dominant pattern of atmospheric interannual and decadal variability in the Arctic, while the North Atlantic Oscillation (NAO), a regional manifestation of AO, is the main mode of circulation variability in the North Atlantic (Ding et al., 2014). To capture Arctic-wide correlations between climate variability and changes in the mass balance of glaciers and ice caps, the AO is a relevant index as it captures hemispheric in addition to regional (i.e. North Atlantic for the NAO index) variability in the atmospheric circulation (Rigor et al., 2002; Thompson and Wallace, 1998). Described by variations in the sea-level pressure field between the polar cap/ North Atlantic region and the Azores (midlatitude Atlantic), AO/NAO indices are associated with changes in SST, T_{2m}, SIC, cyclonic activity and associated winds and precipitation patterns in the North Atlantic and the Arctic (Oziel et al., 2016; Thompson and Wallace, 1998). Negative AO/NAO indices are associated with high sea-ice concentrations, low surface temperatures, and increased vertical heat fluxes in winter in the Barents- (Oziel et al., 2016)

and the Kara (Rigor et al., 2002) Seas. The Atlantic Multi-Decadal Oscillation (AMO) referred to by (Carr et al., 2017), is a mode of natural climate variability based on SST anomalies in the North Atlantic. There is generally a strong correlation between the AMO and AO/NAO indices (e.g. Yashayaev and Seidov, 2015.

According to Ding et al. (2014), inter-annual variability in surface temperatures over north-eastern Canada and Greenland are largely modulated by changes in the NAO index, while warming in the BKS region are strongly correlated with sea-ice reduction. Correlations between NAO and ice mass changes in the Russian Arctic, particularly Novaya Zemlya, have been often found in the past (Carr et al., 2017; Ciracì et al., 2018; Zeeberg and Forman, 2001). Zeeberg and Forman (2001), for example, associate positive mass balance over Novaya Zemlya with high rates of winter precipitation and positive summer surface temperature anomalies during prolonged periods of positive NAO, with T_{2m} responding to NAO phases with a time lag of 3-5 years. Oziel et al. (2016), for example, discuss how AMO and NAO impact variability of Atlantic Water inflow into the Barents Sea through atmospheric forcing (westerlies). Yashayaev and Seidov (2015) observe that Atlantic Water transport into the Arctic follows a multidecadal warming trend that is superimposed by successive intervals of relatively high and low rates of thermal advection that correlate with periods of relatively low and high NAO values, respectively, with a response time of the warm water flux to NAO phases of 4-5 years. This seems to coincide and may be a viable explanation for the patterns discussed here and described in Figure 5.6 of this thesis chapter.

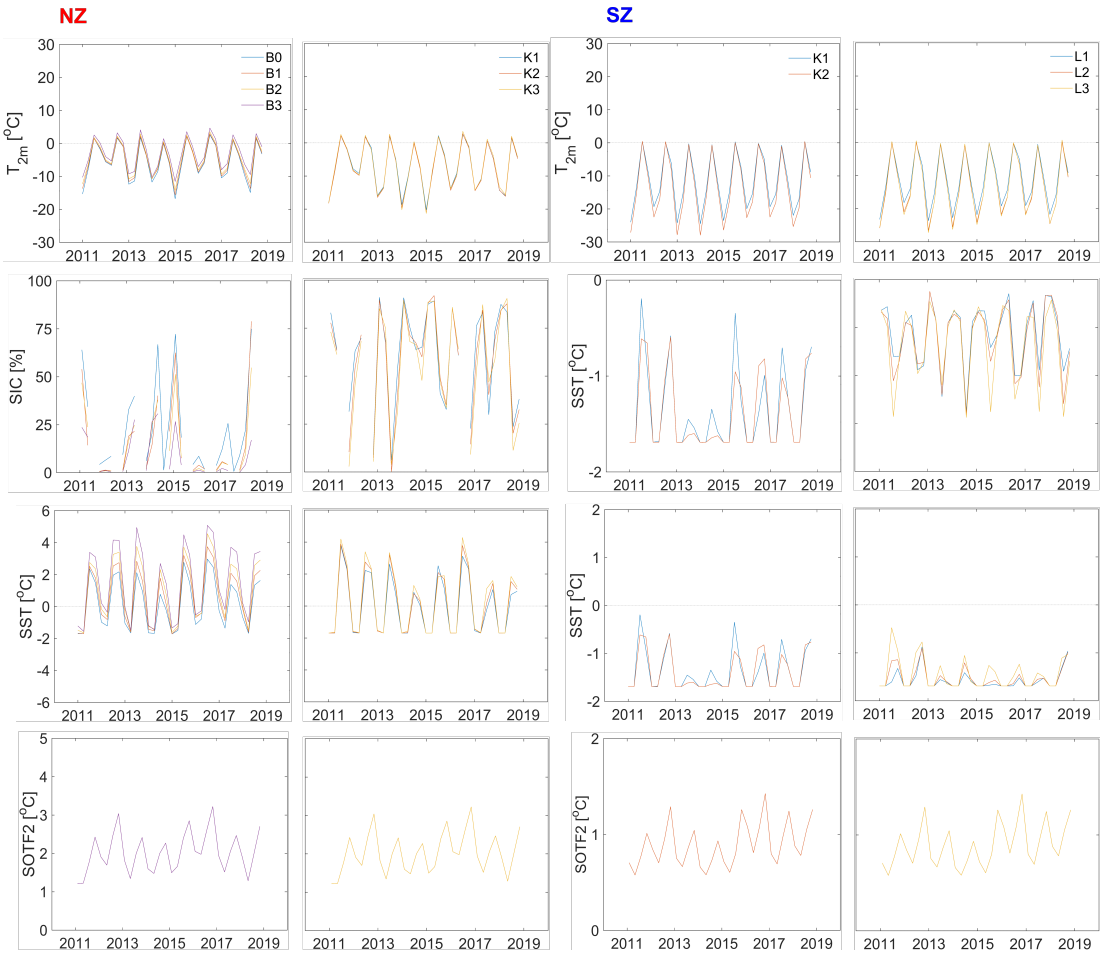


Figure 5.20: Time series of mean seasonal T_{2m}, SIC, SST and $SOTF_2$ by region and control domain.

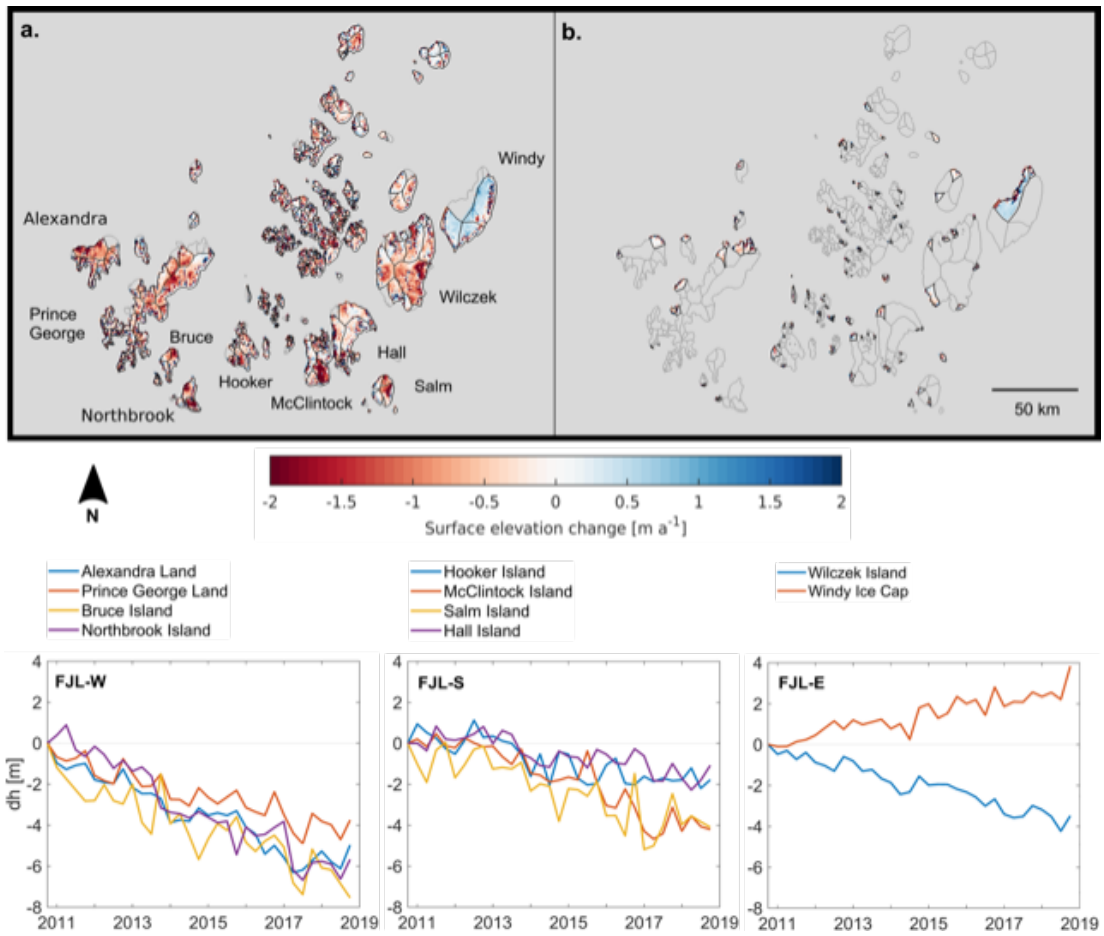


Figure 5.21: Mean 2010-2018 $\dot{h}$ for Franz Josef Land's marine-terminating (a) and land-terminating (b) glaciers and ice caps, and $\dot{h}$ time series for the main ice caps.

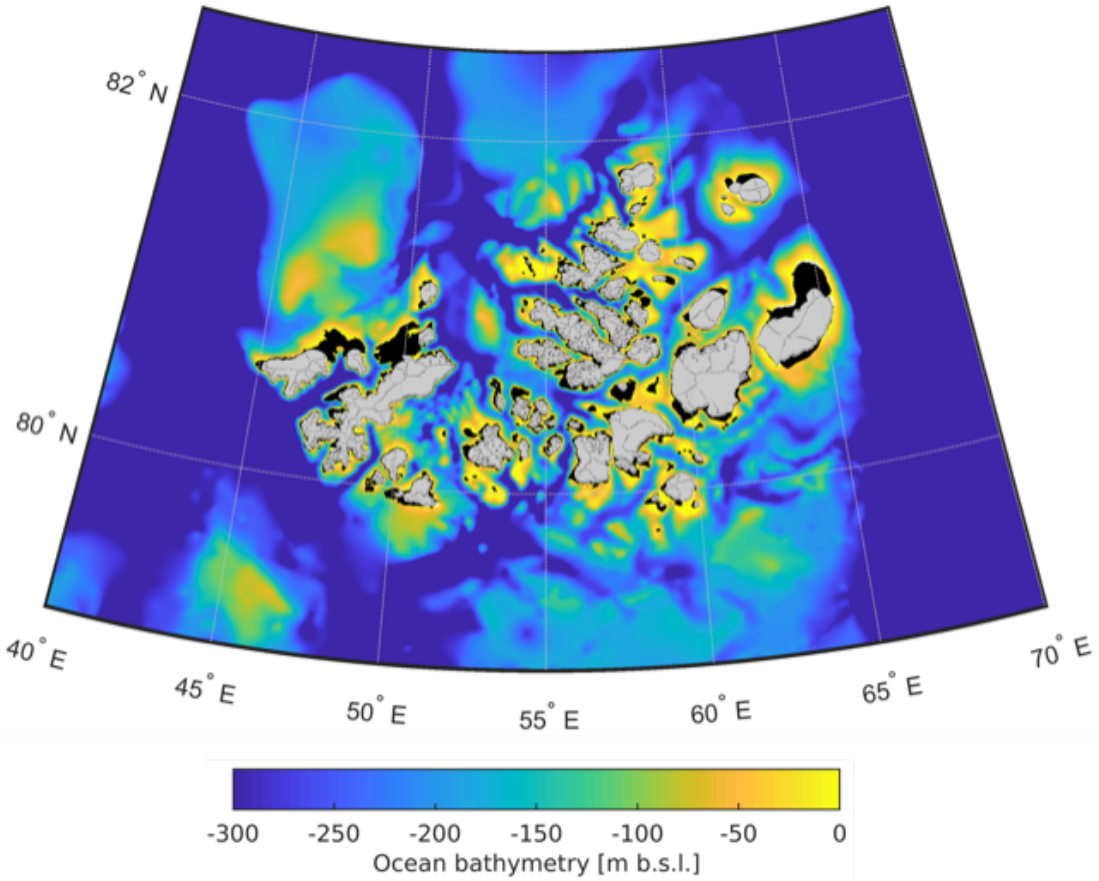


Figure 5.22: Ocean bathymetry around Franz Josef Land. Source: GEBCO.

For the purpose of complementarity, tme series of $\dot{h}$ spanning the time period between 2010 and 2018 were produced over ten of Franz Josef Land's larger ice caps (Figure 5.21). According to the results in Chapter 4 (Tepes et al., 2017), ice loss between 2010 and 2017 in the archipelago was 72 % through dynamic thinning and 28 % through negative surface mass balance. At decadal scale, we observe relatively steady, ice-stream like patterns of thinning (Figure 5.21). Windy Ice Cap on Graham Bell Island has been thickening at ~ 0.4 m a^{-1} during 2010-2018, and as such forms an exception to this overall trend. Rates of surface elevation change vary progressively from the western to the eastern regions of the archipelago, with more pronounced average thinning in the west (0.5 - 1 m a^{-1}) compared to the east (0.25 - 0.5 m a^{-1}). Franz Josef Land's geographic location north of the polar front (Barton et al., 2018) means that Arctic water masses are predominant in the areas around the ice caps, with much less exposure to Atlantic Water incursions compared to Novaya Zemlya's Barents coast. This is reflected in the positive but relatively low SST anomalies around the archipelago, particularly during spring and summer (Figure 5.11). Furthermore, downwelling resulting from negative Ekman transport just south of the archipelago (Figure 5.15, left) is hampering influx of deeper and warmer Atlantic and Barents Sea Waters near the archipelago's ice cap margins. This is in strong contrast to the ubiquitous presence of warm subsurface currents further south, which, in conjunction with coastal upwelling has a much stronger ocean forcing potential on the tidewater glaciers along Novaya Zemlya's Barents coast (Figure 5.15, left). Finally, the relatively short distance between Franz Josef Land's large number of relatively small islands may enhance buttressing forces in the presence of sea ice (Vieli and Nick, 2011), and this may play an important role in controlling ice discharge and calving rates. The strong acceleration of ice loss after 2010 compared to the 2000s (Tepes et al., 2017) may be therefore caused by a combination of both rapid atmospheric warming and sea ice retreat (Figures 5.9 and 5.10).

5.8 Data availability statement

There are no restrictions to access the data used within this manuscript. Data sources are cited in the main text, with access information summarised here. CryoSat-2 Level-1b, baseline C altimetry was downloaded from the European Space Agency's CryoSat-2 Science Server (https://science-pds.cryosat.esa.int/, accessed on 20/10/2020). Reference digital elevation models at 3 arc second resolution from Viewfinder Panoramas are available at http://viewfinderpanoramas.org/dem3.html (accessed on 20/10/2020). Ice masks were taken from the Randolph Glacier Inventory (RGI 6.0) (https://www.glims.org/RGI/rgi60_dl.html, accessed on 20/10/2020). Gridded bathymetry from the International Bathymetric Chart of the Arctic Ocean (IBCAO) can be accessed online via the General Bathymetric Chart of the Oceans (GEBCO) data portal (https://www.gebco.net/data_and_products/gridded_bathymetry_data/arctic_ocean/, accessed on 20/10/2020). The European Centre for Medium-Range Weather Forecasts' (ECMWF) ERA5 monthly averaged air and ocean surface temperature data from 1979 to present are available online via the E.U. Copernicus Climate Change Service (https://cds.climate.copernicus.eu/cdsapp#!/dataset/reanalysis-era5-single-leve tab=overview, accessed on 20/10/2020). Global Ocean Physics Reanalysis can be accessed online via the E.U. Copernicus Marine Service Information data repository (https://resources.marine.copernicus.eu/?option=com_csw&view=details&product_id=GLOBAL_REANALYSIS_PHY_001_030, accessed on 20/10/2020). Processed data used to generate the figures and tables presented in this article are available at https://zenodo.org/record/4419925.

5.9 Acknowledgments

The work in Chapter 5 was performed under the European Space Agency (ESA) Support to Science Elements CryoSat+ CryoTop contract 4000107394/12/I-NB, CS+ Mountain Glaciers contract 4000114224/15/I-SBo to N.G. P.T. acknowl-

edges a PhD scholarship grant from the University of Edinburgh. We thank Frazer Christie (Scott Polar Research Institute) for guidance on climate trends analysis and George Malczyk (University of Edinburgh) for improving CryoSat-2 swath time-series computations.

Chapter 6

Conclusions

The primary aim of this thesis was to use spaceborne radar altimetry from CryoSat-2 together with novel processing methods to produce a multi-year, high-resolution measurement of geometric change and mass balance of glaciers and ice caps across the Arctic between 2010 and 2017. In conjunction with this Arctic-wide assessment, the second main objective consisted of investigating patterns of glacier imbalance in relation to climate forcing. The work presented in Chapters 3-5 has addressed these two objectives as follows:

- Chapter 3 described in detail the methodological steps that were developed and implemented in order to generate the proposed pan-Arctic mass balance assessment;
- Chapter 4 produced high-resolution surface elevation maps over single ice caps and glaciated regions of the Arctic outside of Greenland for the period 2010 to 2017. From these products, mass balance was derived for seven individual Arctic regions and their main ice caps, and was partitioned into losses at the glacier surface and as ice discharge into the ocean. The chapter concluded with a synoptic overview of Arctic climate trends and their impact on glacier change, and identified the glaciated archipelagos of the Eurasian Arctic as undergoing critical transitions due to accelerated atmospheric and oceanic warming;

- Chapter 5 built on the results from Chapter 4 to analyse in more detail the mass balance trends and ice-climate interactions that are taking place across the glaciers and ice caps of Novaya Zemlya and Severnaya Zemlya in the Russian Arctic. It proposed a simple mathematical relationship to describe the regions' glacier and ice cap sensitivity to climate warming.

A synthesis of the principle findings of the thesis is presented in Section 6.1 of this concluding chapter. Section 6.2 critically discusses how the thesis met the knowledge gaps identified in Section 2.7. Section 6.3 provides an overview of the potential limitations associated with the main findings of the thesis and recommends avenues for future research. Finally, Section 6.4 offers a number of concluding remarks regarding the overall significance of the work presented in this thesis.

6.1 Synthesis of findings

This thesis used a novel interferometric swath algorithm to process 1.7×10^9 elevation measurements at the surface of glaciers and ice caps across the Arctic outside of Greenland. These measurements included the southern and northern Canadian Arctic Archipelagos, Iceland, Svalbard, and the archipelagos of Franz Josef Land, Novaya Zemlya, and Severnaya Zemlya in the Russian Arctic. The high density of observations enabled the statistical computation of mean rates of elevation change, over unit areas of 500×500 m, and associated with relatively small residual error (1 m a^{-1} at the 95^{th} percentile) at regional scale.

The methodology subsequently developed in Chapter 3 used these gridded maps of surface elevation change, in order to estimate changes in the volume and mass across all seven Arctic regions. The methodology was designed in such a way that painstaking quality control, essential in handling large datasets and in producing accurate quantitative mass balance assessments at the global scale, was reduced to a minimum, and without loss of data quality. This was achieved primarily by an automated, robust procedure aimed at identifying and

removing spurious elevation change estimates in the swath products. In doing so, uncertainty in the mass balance estimates was further reduced by optimising the trade-off between area coverage and signal-to-noise ratio. This methodology proved very effective when applied over the entire Arctic, yielding ratios of measured-to-total glaciated area of 60 % on average over the Canadian Arctic, 80 % over the Eurasian Arctic, and up to 95 % over single ice caps such as Austfonna (Svalbard), and the Academy of Sciences Ice Cap (Russian Arctic). The exceptionally high coverage achieved in the Eurasian High Arctic is of utmost importance, since this is a region where critical dynamical imbalances and climate transitions are taking place (e.g. Lind et al., 2018; McMillan et al., 2014; Polyakov et al., 2017; Willis et al., 2018).

Overall, swath processing of CryoSat-2 data, as reported in Chapter 4, showed that at a regional scale, ice thinning is ubiquitous across the entire Arctic, with a median rate of elevation change between 2010 and 2017 equal to -0.25 m a^{-1}, albeit with considerable spatial variability. A strong dichotomy was evidenced between spatially homogeneous ice losses in the Canadian Arctic, driven largely by surface processes, and much more variable patterns of change in the archipelagos east of Greenland. This heterogeneity in the Eurasian Arctic was inferred to reflect a range of process driven glacier and ice cap responses to the region's complex climate dynamics.

From the swath products, the thesis produced a detailed mass balance assessment revealing that over the measurement period, Arctic glaciers and ice caps lost 609 $\pm$ 7 Gt of ice, contributing 1.7 $\pm$ 0.1 millimetres to global sea level rise. The large volume of data from CryoSat-2 was used to partition the mass balance from each of the seven glaciated regions into land- and marine-terminating ice losses, and to differentiate for all of the tidewater glacier basins in each region between losses through net surface ablation and ice discharge (Chapter 4). A comparison between surface mass balance from CryoSat-2 and the RACMO2.3 regional climate model revealed an excellent agreement between the two datasets over both the southern and northern Canadian Arctic (Noël et al., 2018). This demon-

strates that dense swath elevation fields can be used effectively to parametrise non-dynamical changes in surface height as a function of elevation, latitude and longitude, and to infer regional variability in surface mass balance between land- and adjacent marine-terminating sectors across large regions. The analysis revealed that 87 % of total ice loss across the Arctic is due to net surface ablation, while dynamically driven imbalance increased significantly in the Eurasian Arctic where it accounted for 43 % of total regional ice loss.

Climate data analyses conducted in Chapter 4 revealed positive ocean temperature anomalies during the CryoSat-2 period relative to the previous two decades, indicating strong ocean warming, particularly around the archipelagos of the Eurasian Arctic. The trend was reversed around Greenland and the Canadian Arctic in response to a slowdown in meridional ocean heat transport in the subpolar North Atlantic and via the Greenland and Irminger Currents (Myers et al., 2007). Large air- and sea surface temperature anomalies over the Eurasian Arctic confirmed the significant warming associated with the combined effects of atmospheric heat transport due to enhanced storm activity, and increased Atlantic Water inflow to the Barents and Kara Seas (Årthun et al., 2012; Barton et al., 2018). Chapter 4 highlighted the importance of elucidating the complexities inherent in the Eurasian Arctic's climate system, in order to determine the mechanisms responsible for driving the large and sustained dynamical imbalances observed across the region between 2010 and 2017. This formed the underlying foundations of the research conducted in Chapter 5, including the choice of the Russian Arctic as a critical study region.

The analysis in Chapter 5 found that the contrasting patterns of mass loss between Novaya Zemlya and Severnaya Zemlya in the Russian Arctic are essentially controlled by the degree of influence of Atlantic climate on each of the regions' ice masses. Novaya Zemlya, in the western section of the Russian Arctic, dominates the entire region's contribution to sea level rise, with mean rates of loss of 9.7 ± 0.5 Gt a^{-1}, and similar area specific losses from basins terminating both on land (441 ± 31 kg m^{-2} a^{-1}) and in the ocean (425 ± 30 kg m^{-2} a^{-1}). Intensive thin-

ning at low elevations at a large number of west-facing tidewater glaciers along Novaya Zemlya's Barents Sea coast indicated strong and widespread dynamic imbalance coupled with high rates of net surface ablation. Severnaya Zemlya's slightly negative mass balance (-1.7 ± 0.1 Gt a^{-1}) was largely driven by ice discharge from just six marine-terminating basins. Overall, Severnaya Zemlya's tidewater basins exhibited rates of loss equal to 243 ± 17 kg m^{-2} a^{-1}, whereas ice caps terminating on land gained mass on average at 27 ± 2 kg m^{-2} a^{-1}.

CryoSat-2 swath elevation fields were finally used in this last chapter to generate, for the first time, robust time series of surface elevation change at 90-day time steps over the sum of all individual tidewater glacier basins and larger land-terminating glacier clusters in Novaya Zemlya and Severnaya Zemlya. The seasonal resolution of the time series allowed for a detailed investigation in to the potential links between ice mass fluctuations and climate variability in the Russian Arctic. Statistical analyses revealed that Novaya Zemlya's ice masses responded linearly, and with a delay of $\sim$ 1.5 years, to a coupled atmosphere-ocean forcing, driven by a strong and increasing Atlantic ocean-and-weather influence (or 'Atlantification' – Polyakov et al., 2017). This response pattern is less pronounced further east, although warm Atlantic Water incursions along the continental margin were inferred to be responsible for Severnaya Zemlya's recent dynamic imbalance.

6.2 Advances on key knowledge gaps

This section provides a critical overview of the thesis' findings with respect to the critical knowledge gaps highlighted at the start of the project, and which guided the research rationale.

6.2.1 High-definition swath interferometry for the direct assessment of global ice mass balance

Before the launch of CryoSat-2 in 2010, global sea level assessments were unable to account accurately for the inputs from glaciers and ice caps due to the lack of observational data at a suitable spatial coverage. The World Glacier Inventory (WGI), conceived during the International Geophysical Year 1957/58, included until 2009 approximately just half of the glaciated area outside the two ice sheets (Cogley, 2009). It was only after the Randolph Glacier Inventory (RGI) database was developed, to meet the needs of the Fifth Assessment Report (AR5) of the Intergovernmental Panel on Climate Change (IPCC) for estimating present and future glacier mass balance, that coverage of glaciers and ice caps could be substantially improved at the global level (Pfeffer et al., 2014). Nevertheless, these glacier outline collections provided only a very basic data framework for undertaking mass balance computations. As the results presented in AR5 have shown, individual measurement techniques were additionally faced with significant sampling limitations that translated into large uncertainties in the glaciers and ice caps' mass balance assessments (Gardner et al., 2013; Vaughan et al., 2013). The main issues were related to the large satellite footprints of gravimetric instruments, relative to the size of glaciers, and substantial data gaps resulting from insufficient coverage by altimetric sensors over extreme topography, such as over glaciated mountain ranges and rugged ice cap margins. Hence, to this day, global assessments of mass change still rely on laborious collaborative efforts, involving a vast array of resources aimed at reconciling quantitatively the ice losses determined using different observational techniques and covering different regions of the world (e.g. Gardner et al., 2013; The IMBIE Team, 2018, 2020). This thesis has demonstrated the strong potential offered by interferometric swath altimetry as a single spaceborne sampling and processing technique to overcome these key difficulties. This is achieved through the continuous supply of large volumes of measurements, which can generate, over the lifetime of an orbiting radar al-

timeter, high-precision mass budgets at the global scale, that include the more challenging assessment of glaciers and ice caps.

6.2.2 Partitioning between surface mass balance anomalies and dynamic imbalance

Another important development, addressed in this thesis, was the use of a polynomial parametrisation scheme to describe non-dynamical surface elevation changes as a function of their main drivers, that is elevation and geographical location. This development made it possible to quantify anomalous mass changes at the ice surface, and to extract subsequently the proportion of the signal related to dynamic ice discharge from the total mass balance. The most accurate way to estimate surface mass balance traditionally is by deploying sophisticated regional climate models, downscaling them, and enhancing them with coupled snow and firn modelling segments and albedo parametrisations (e.g. Lenaerts et al., 2019). The most commonly applied method for estimating dynamic imbalance is by calculating changes in ice discharge through flux gates at the ice margins (e.g. Mouginot et al., 2019). To calculate ice flux, data on ice thickness at the grounding line is needed, as well as ice surface velocities, which are generally based on satellite stereo image pairs (e.g. Dehecq et al., 2019). At present, ice thickness is available for fewer than 1 % of the world's glaciers (Radić et al., 2014), while generating ice velocity fields is very computer-intensive, requires large data storage capacity, and cannot be produced on a continuous time frame. As a result, ice discharge was not accounted for at all in IPCC's AR4 global sea level projections (Church et al., 2013), and in AR5, there was only *medium* confidence in the ability of coupled ice sheet–climate models to project sea level contributions from dynamic changes, which moreover could only be estimated for the Greenland and the Antarctic Ice Sheets.

The parametrisation using CryoSat-2 swath measurements presented in this thesis proposes an alternative solution for determining both surface mass balance

and ice discharge statistically, and for the first time for the entire population of Arctic glaciers and ice caps. The parametrisation was successfully validated against modelling results over the Canadian Arctic using RACMO2.3 regional climate model (Noël et al., 2018). Given the increased dynamic instability of Arctic land ice, in particular in the Eurasian Arctic (Chapter 4), quantifying dynamic fluctuations in response to different forcings is becoming ever more important, not only for global mass balance assessments, but also for identifying and predicting areas of potential instability, that may be susceptible to the sudden destabilisation of an entire glacier or ice cap basin. Accelerated warming and rapid environmental change requires the continuous monitoring of such fluctuations and this has been demonstrably achieved using the statistical approach developed in this thesis.

6.2.3 Climate sensitivity of glaciers and ice caps in an Arctic warming 'hotspot'

The thesis further showed that the high-definition products available from swath processing provide powerful data support that enables analysis of ice-climate processes on a broad range of spatial and temporal scales, and at the necessary detail required for elucidating the complex responses of the world's glaciers to climate forcing. Multiple studies have focused previously on specific regions, reporting that environmental forcings such as near surface air temperatures, sea ice concentrations and sea surface and subsurface temperatures are key controls on glacier dynamics (e.g. Cook et al., 2019; Cowton et al., 2018). The work presented in this thesis extended this analysis to the entire Arctic and showed that there is a strong spatial and temporal correlation between forcing anomalies and ice discharge, with a distinct asymmetry to the east and west of Greenland. Although covariance between the different potential forcings makes it hard to identify conclusively the most dominant of the four controlling factors on glacier change at the pan-Arctic scale (Chapter 4), a more detailed, regional investigation

of the processes in Chapter 5 revealed important climatic controls on decadal mass imbalance in the archipelagos of the Eurasian Shelf. This is a region undergoing critical transitions and is one of the Arctic's climatic 'hotspots' in the face of ongoing 'Atlantification' (Polyakov et al., 2017).

The analysis in Chapter 5 used high-resolution time series of surface elevation change and climate reanalyses over the Russian Arctic, the most understudied glaciated region in the Arctic at the start of this thesis (Moholdt et al., 2012b). The results reveal the important role of receding sea ice in the formation of strong, coupled atmosphere-ocean mechanisms of ice loss, leading to a quasi-linear response of the ice masses in regions where this type of forcing prevails. Coupled atmosphere-ocean forcing occurs when synchronous air- and ocean warming form a strong mechanism of ice loss on tidewater glacier basins through both high rates of surface melt and enhanced ice dynamics and frontal ablation driven by submarine melt. This is the case in the western section of the Eurasian Arctic where Atlantic climatic influence is strongest, and low sea ice concentrations allow heat to be transferred vertically between the ocean and the atmosphere. This effect is clearly visible along Novaya Zemlya's Barents Sea coast where high melt rates at the surface of Severny Ice Cap together with intense dynamic thinning near the tidewater glacier termini lead to dramatic ice loss overall. In contrast, vertical heat fluxes and ocean-atmosphere exchange processes are reduced in the eastern Eurasian Arctic around Severnaya Zemlya where mean annual sea ice concentrations are high, impeding near-surface warming and glacier melting. Arctic Ocean circulation along the continental margin of the Siberian Shelf draws in warm Atlantic Water that finds its way the termini of glaciers in the eastern part of the Russian Arctic, thereby sustaining ice discharge from single ice cap basins, and activating new ice streams in Severnaya Zemlya. Hence through these processes, the rapid changes observed throughout the Eurasian Arctic's glacier and ice caps are currently strongly linked with the encroaching nature of 'Atlantification' and its effects on sea- and land ice depletion. Overall, these new findings improve the understanding of some important aspects of the ice-climate interactions prevailing

in the Arctic beyond Greenland, and provide compelling support for new paths in the parametrisation of dynamic ice loss and its underlying forcing mechanisms in climate models.

6.3 Limitations and opportunities for future research

Considering the scale of the undertaking to estimate mass balance and climate forcing mechanisms at the pan-Arctic scale, the difficulties encountered during this thesis were many. The main challenges were to: **1)** provide a robust methodological framework for the processing of large data volumes at the pan-Arctic scale; **2)** accurately estimate surface mass balance anomalies and dynamic imbalance by region, and **3)** describe and analyse the complex interactions taking place between land ice and climate in the Eurasian Arctic.

While overall the methodology proposed in this project, starting from *Level 1b* data processing to mass balance calculation has proven efficient, in particular the critical procedures removing spurious measurements and proposing adapted regionalisation schemes according to the different patterns of ice loss, some limitations remain that are important to consider further.

Primarily, although the high coverage and signal-to-noise ratio obtained from swath altimetry across the Arctic reduces uncertainties significantly, the mass budgets derived from the swath products still rely on very broad assumptions about snow, firn, and ice density. While applying a constant density scheme across glaciated regions is still considered a standard approach for global mass balance assessments (e.g. Gardner et al., 2013; Huss, 2013; Zemp et al., 2019), the associated error also represents the majority (> 90 %) of the uncertainty associated with the estimated mass budgets in Chapters 4 and 5. In order to reduce these uncertainties significantly, better constrained density schemes are necessary. Moreover, knowledge about ice, snow and firn conditions at the ice

surface are important for the correct interpretation of radar return echoes, as these conditions strongly influence the location of the scattering horizon, potentially introducing large elevation biases (0.5 – 1 m) in the measurements (Nilsson et al., 2015b).

Geospatial statistical analysis is needed to determine region-specific autocorrelation ranges in the swath measurements and to better quantify the integrated uncertainty in surface elevation changes by including spatial correlation between samples (Rolstad et al., 2009). This can be achieved, for example, through the analysis of semivariograms of surface elevation change for each individual Arctic region (e.g. Nilsson et al., 2015a; Rolstad et al., 2009). Spatial correlations in elevation change also depend on fluctuations in backscatter and surface conditions and therefore, alternative measurement records are needed for comparison. More generally, the quality assessment of CryoSat-2 swath altimetry presented in this thesis relies heavily on validation data from only two ice caps. Considering the extremely variable ice surface conditions across the Arctic, this underscores the urgent need for more surface elevation and elevation change measurements from other Arctic regions, and using alternative sampling techniques, for example laser altimetry.

The European Space Agency Cryo2Ice campaign is currently deploying a maneuvering scheme aimed at synchronising the CryoSat-2 and ICESat-2 orbits (see portal online at https://earth.esa.int/eogateway/missions/cryosat/cryo2ice, accessed on 29/07/2020). ICESat's laser altimeter is less sensitive to ground conditions compared with CryoSat (e.g. Smith et al., 2020), and the expectation is that it can be used to expand and strengthen the validation of CryoSat-2 elevation estimates. The planned orbital adjustment will enable a detailed investigation of the complementarity of the two satellite missions, with likely benefits to the application of swath processing over Arctic land ice through the provision of coverage over previously unmeasured areas (Shepherd 2020, Cryolist). In this context, it is also worth mentioning that the CryoSat-2 SARIn mask would benefit from an update to include the relatively large Kvitøya (Svalbard),

Schmidt (Severnaya Zemlya), and Ushakov (Russian High Arctic) Ice Caps in the Eurasian High Arctic.

Uncertainties in grounding line locations in the RGI 6.0 database have been estimated to be $\sim$ 5 % (Pfeffer et al., 2014), but were not taken into account in this thesis' pan-Arctic mass balance calculation since a regional breakdown of this error is not available. The significant inaccuracies in the RGI metadata record, providing information on the type of basin, need to be addressed and in particular for Svalbard.

Tracking volume changes from swath altimetry over small catchments remains challenging in some instances due to limitations in data coverage. For example, estimating volumetric change over individual basins that experienced substantial losses, such as Vavilov Basin in Severnaya Zemlya (Willis et al., 2018), or Basin 3 in Austfonna (McMillan et al., 2014) is a laborious task and an undertaking of its own in an Arctic-wide mass balance assessment.

Partitioning surface elevation change into signals associated with atmospheric processes and ice dynamics was demonstrated over all seven Arctic regions studied in this thesis. The accuracy, as inferred from the statistical significance of the results, depended on both the spatial coverage and measurement density obtained over the land-terminating segments of each individual region. The dynamic imbalance however of each of the Arctic region's land-terminating segments, and the spatial correlation ranges applicable to surface mass balance need careful consideration in any future developments of these parametrisation. Additionally, alternative measurement and modelling methods are required to validate the partitioning at the global scale.

Finally, the complexities of the existing interactions between rapid climatic transitions and ice dynamics in the Eurasian Arctic require extensive climate data analyses. The analyses provided in this thesis would undoubtedly benefit from a more detailed consideration of climate variables such as windspeed and Ekman transport, precipitation, and a more in-depth analysis of overarching atmospheric circulation patterns such as the North Atlantic Oscillation. Enhanced bathymetry

and a more detailed description of ocean currents in the Barents-Kara Sea coastal areas is generally missing in the literature, and would also greatly improve the analysis of the processes at the ice-ocean interface.

6.4 Final remarks

The high density measurement fields and high-definition products, potentially made available by the CryoSat-2 mission, and developed during this thesis at the pan-Arctic scale provide a glimpse of the new perspectives that are currently emerging for the continuous monitoring of cryospheric change at the planetary scale, and for the global assessment of glacier, ice cap and ice sheet contributions to future sea level rise change. The methodology developed during the thesis, from swath processing to estimating mass budgets and conducting climate data analysis in conjunction with temporal records of ice volume change, has been shown to be mature enough to expand to the global level, including the Greenland and Antarctic Ice Sheets and the glaciers and ice caps at their periphery. Measuring change in regions of extreme topography remains a major challenge yet to overcome. Nevertheless, further exploitation of the echo waveforms, in particular the analysis of the interferometric phase of the return signal, has already shown promising results over Jakobshavn Isbrae Glacier in Greenland (Weissgerber and Gourmelen, 2017), and could be developed further to achieve improved coverage over key mountain regions such as Alaska and the Himalayas, thereby increasing confidence in global estimates of sea level rise.

The results presented here demonstrate that large volumes of earth observation data, when available at fine spatial and temporal resolution, can be used to explain, using simple mathematical relationships and statistical analysis, the complex mechanisms of ice loss and their relationships with a range of environmental forcings. Further optimisation of these parametrisations, and in particular, partitioning of the mass budgets into surface mass balance and ice dynamics, the computation of time series of mass change for individual catchments at the

global level, and enhanced observation from joint, complementary satellite missions, lay the foundation for promising and exciting new opportunities for polar research in the near future.

Bibliography

Agosta, C., C. Amory, C. Kittel, A. Orsi, V. Favier, H. Gallée, et al. (2019). "Estimation of the Antarctic surface mass balance using the regional climate model MAR (1979-2015) and identification of dominant processes". In: *The Cryosphere* 13.1, pp. 281–296. DOI: 10.5194/tc-13-281-2019.

AMAP (2017). *Snow, Water, Ice and Permafrost in the Arctic (SWIPA)*. Tech. rep. Oslo, Norway: Arctic Monitoring and Assessment Programme (AMAP), pp. 137–168.

Årthun, M., T. Eldevik, L. H. Smedsrud, Ø. Skagseth, and R. B. Ingvaldsen (2012). "Quantifying the Influence of Atlantic Heat on Barents Sea Ice Variability and Retreat". In: *Journal of Climate* 25.13, pp. 4736–4743. DOI: 10.1175/jcli-d-11-00466.1.

Barber, D. G., W. N. Meier, S. Gerland, C. J. Mundy, M. Holland, S. Kern, et al. (2017). *Snow, Water, Ice and Permafrost in the Arctic (SWIPA) 2017, Arctic Monitoring and Assessment Programme (AMAP) - Arctic sea ice*. Tech. rep. Oslo, Norway, pp. 103–136.

Bartels, M., J. Titschack, K. Fahl, R. Stein, M. S. Seidenkrantz, C. Hillaire-Marcel, et al. (2017). "Atlantic Water advection vs. glacier dynamics in northern Spitsbergen since early deglaciation". In: *Climate of the Past* 13, pp. 1717–1749. DOI: 10.5194/cp-13-1717-2017.

Barton, B. I., Y.-D. Lenn, and C. Lique (2018). "Observed atlantification of the Barents Sea causes the Polar Front to limit the expansion of winter sea ice". In: *Journal of Physical Oceanography* 48.8, pp. 1849–1866. DOI: 10.1175/jpo-d-18-0003.1.

Benn, D. and D. J. A. Evans (2010). *Glaciers and Glaciation*. 2nd. London: Hodder Education, p. 802. ISBN: 0340584319,

Berton, P. (1988). *The Arctic Grail: The Quest for the North West Passage and the North Pole, 1818-1909*. Viking, p. 629. ISBN: 978-0-670-82491-5.

Bezeau, P., M. Sharp, and G. Gascon (2015). "Variability in summer anticyclonic circulation over the canadian arctic archipelago and west greenland in the late 20th/early 21st centuries and its effect on glacier mass balance". In: *International Journal of Climatology* 35.4, pp. 540–557. DOI: 10.1002/joc.4000.

Bjørk, A. A., S. Aagaard, A. Lütt, S. A. Khan, J. E. Box, K. K. Kjeldsen, et al. (2018). "Changes in Greenland's peripheral glaciers linked to the North Atlantic Oscillation". In: *Nature Climate Change* 8.1, pp. 48–52. DOI: 10.1038/s41558-017-0029-1.

Björnsson, H., A. F. Glazovskiy, J. O. Hagen, P. Holmlund, J. Jania, E. Josberger, et al. (1996). *International Arctic Science Committee - Working Group on Arctic Glaciology, Mass Balance Of Arctic Glaciers, IASC Report No. 5*. Tech. rep. 5.

Sosnowiec-Oslo: University of Silesia/ Faculty of Earth Sciences, pp. 1–54. URL: http://nag.iasc.info/images/publications/magics/iasc_mb1996.pdf.

Björnsson, H., F. Pálsson, S. Gudmundsson, E. Magnússon, G. Adalgeirsdõttir, T. Jõhannesson, et al. (2013). "Contribution of Icelandic ice caps to sea level rise: Trends and variability since the Little Ice Age". In: *Geophysical Research Letters* 40.8, pp. 1546–1550. DOI: 10.1002/grl.50278.

Blaszczyk, M., J. A. Jania, and J. O. Hagen (2009). *Tidewater glaciers of Svalbard: Recent changes and estimates of calving fluxes*. Vol. 30. 2, pp. 85–142. ISBN: 2007905507.

Bouffard., J., R. Manner, and D. Brockley (2015). *CryoSat-2 Level 2 product evolutions and quality improvements in Baseline C*. Tech. rep. European Space Agency, p. 18. URL: http://cryosat.mssl.ucl.ac.uk/qa/docs/CS-Evolution-Baseline-C-L2-v2.pdf.

Bouzinac, C. (2012). *CryoSat Product Handbook, European Space Agency and Mullar Space Science Laboratory (University College London)*. Tech. rep. European Space Agency, p. 150. URL: https://earth.esa.int/documents/10174/125272/CryoSat_Product_Handbook.

Box, J. E. and M. Sharp (2017). "Snow, Water, Ice and Permafrost in the Arctic (SWIPA) 2017, Arctic Monitoring and Assessment Programme (AMAP) - Changes to Arctic land ice". In: pp. 137–168.

Box, J. E. and W. T. Colgan (2017). "Snow, Water, Ice and Permafrost in the Arctic (SWIPA) 2017, Arctic Monitoring and Assessment Programme (AMAP) - Sea level rise contribution from Arctic land ice: 1850-2100". In: pp. 219–230.

Brigham-Grette, J., M. Melles, P. Minyuk, A. Andreev, P. Tarasov, R. DeConto, et al. (2013). "Pliocene warmth, polar amplification, and stepped Pleistocene cooling recorded in NE Arctic Russia". In: *Science* 340, pp. 1421–1427. DOI: 10.1126/science.1233137.

Byrne, M. P. and T. Schneider (2018). "Atmospheric dynamics feedback: concept, simulations and climate implications". In: *Journal of Climate* 31.2011, pp. 3249–3264. DOI: 10.1175/JCLI-D-17-0470.1.

Caesar, A. L., S. Rahmstorf, A. Robinson, G. Feulner, and V. Saba (2018). "Observed fingerprint of a weakening Atlantic Ocean overturning circulation". In: *Nature* 556, pp. 191–196. DOI: 10.1038/s41586-018-0006-5.

Carr, J. R., H. Bell, R. Killick, and T. Holt (2017). "Exceptional retreat of Novaya Zemlya's marine-terminating outlet glaciers between 2000 and 2013". In: *The Cryosphere* 11.5, pp. 2149–2174. DOI: 10.5194/tc-11-2149-2017.

Carr, J. R., C. Stokes, and A. Vieli (2014). "Recent retreat of major outlet glaciers on Novaya Zemlya, Russian Arctic, influenced by fjord geometry and sea-ice conditions". In: *Journal of Glaciology* 60.219, pp. 155–170. DOI: 10.3189/2014JoG13J122.

Cavalieri, D., C. Parkinson, P. Gloersen, and J. H. Zwally (2019). *Sea ice concentrations from Nimbus-7 SMMR and DMSP SSM/I-SSMIS passive microwave data, Version 1*. Tech. rep. Boulder, Colorado USA: NASA DAAC at the National Snow and Ice Data Center.

Christie, F. D., R. G. Bingham, N. Gourmelen, S. F. B. Tett, and A. Muto (2016). "Four-decade record of pervasive grounding line retreat along the Bellingshausen margin of West Antarctica". In: *Geophysical Research Letters* 43, pp. 5741–5749. DOI: 10.1002/2016GL068972.

Christie, F. D., R. G. Bingham, N. Gourmelen, E. J. Steig, R. R. Bisset, H. D. Pritchard, et al. (2018). "Glacier change along West Antarctica's Marie Byrd Land Sector and links to inter-decadal atmosphere-ocean variability". In: *The Cryosphere* 12, pp. 2461–2479. DOI: 10.5194/tc-12-2461-2018.

Church, J. a., P. U. Clark, A. Cazenave, J. M. Gregory, S. Jevrejeva, A. Levermann, et al. (2013). *AR5 - Sea level change*. Tech. rep., pp. 1137–1216.

Ciracì, E., I. Velicogna, and S. Swenson (2020). "Continuity of the Mass Loss of the World ' s Glaciers and Ice Caps From the GRACE and GRACE Follow-On Missions". In: *Geophysical Research Letters* 47, pp. 1–11. DOI: 10.1029/2019GL086926.

Ciracì, E., I. Velicogna, and T. C. Sutterley (2018). "Mass Balance of Novaya Zemlya Archipelago, Russian high arctic, using time-variable gravity from GRACE and altimetry data from ICESat and CryoSat-2". In: *Remote Sensing* 10.11. DOI: 10.3390/rs10111817.

Cogley, J. G. (2009). "A more complete version of the World Glacier Inventory". In: *Annals of Glaciology* 50.53, pp. 32–38.

Cohen, J., J. A. Screen, J. C. Furtado, M. Barlow, D. Whittleston, D. Coumou, et al. (2014). "Recent Arctic amplification and extreme mid-latitude weather". In: *Nature Geoscience* 7.August, pp. 627–637. DOI: 10.1038/ngeo2234.

Comiso, J. C. (2017). *Bootstrap sea ice concentrations from Nimbus-7 SMMR and DMSP SSM/I-SSMIS, Version 3*. Tech. rep. Boulder, Colorado USA: NASA National Snow and Ice Data Center Distributed Active Archive Center.

Cook, A. J., L. Copland, B. P. Y. Noël, C. R. Stokes, M. J. Bentley, M. J. Sharp, et al. (2019). "Atmospheric forcing of rapid marine-terminating glacier retreat in the Canadian Arctic Archipelago". In: *Science Advances* 5.3, p. 8507. DOI: 10.1126/sciadv.aau8507.

Copernicus Climate Change Service, C. (2017). *ERA5: Fifth generation of ECMWF atmospheric reanalyses of the global climate*. URL: https://cds.climate.copernicus.eu/cdsapp#!/home.

Cowton, T. R., A. J. Sole, P. W. Nienow, D. A. Slater, and P. Christoffersen (2018). "Linear response of east Greenland's tidewater glaciers to ocean/atmosphere warming". In: *Proceedings of the National Academy of Sciences* 115, pp. 7907–7912. DOI: 10.1073/pnas.1801769115.

CryoSat Science Advisory Group (2001). *CryoSat Calibration & Validation Concept*. Tech. rep. 1. London: Centre for Polar Observation & Modelling, Department of Space & Climate Physics, University College London, pp. 1–96. URL: https://earth.esa.int/web/guest/-/cryosat-calibration-and-validation-concept-4471.

Cuffey, K. M. and W. S. B. Paterson (2010). *The Physics of Glaciers*. 4th ed. Amsterdam: Elsevier.

Das, S. B., I. Joughin, M. D. Behn, I. M. Howat, M. A. King, D. Lizarralde, et al. (2008). "Fracture Propagation to the Base of the Greenland Ice Sheet During Supraglacial Lake Drainage". In: *Science* 320.May, pp. 778–782.

Dee, D. P., S. M. Uppala, A. J. Simmons, P. Berrisford, P. Poli, S. Kobayashi, et al. (2011). "The ERA-Interim reanalysis: Configuration and performance of the data assimilation system". In: *Quarterly Journal of the Royal Meteorological Society* 137.656, pp. 553–597. DOI: 10.1002/qj.828.

Dehecq, A., N. Gourmelen, A. Shepherd, R. Cullen, and E. Trouve (2013). "Evaluation of Cryosat-2 for Height Retrieval Over the Himalayan". In: *CryoSat-2 third user workshop*. Dresden, Germany.: HAL, pp. 1–4. URL: https://hal.archives-ouvertes.fr/hal-00973393.

Dehecq, A., N. Gourmelen, and E. Trouve (2015). "Deriving large-scale glacier velocities from a complete satellite archive: Application to the Pamir–Karakoram–Himalaya". In: *Remote Sensing of Environment* 162, pp. 55–66. DOI: 10.1016/j.rse.2015.01.031.

Dehecq, A., N. Gourmelen, A. S. Gardner, F. Brun, D. Goldberg, P. W. Nienow, et al. (2019). "Twenty-first century glacier slowdown driven by mass loss in High Mountain Asia". In: *Nature Geoscience* 12.1, pp. 22–27. DOI: 10.1038/s41561-018-0271-9.

Delhasse, A., X. Fettweis, C. Kittel, C. Amory, and C. Agosta (2018). "Brief communication: Impact of the recent atmospheric circulation change in summer on the future surface mass balance of the Greenland Ice Sheet". In: *The Cryosphere* 12.11, pp. 3409–3418. DOI: 10.5194/tc-12-3409-2018.

Ding, Q., J. M. Wallace, D. S. Battisti, E. J. Steig, A. J. E. Gallant, H.-J. Kim, et al. (2014). "Tropical forcing of the recent rapid Arctic warming in northeastern Canada and Greenland". In: *Nature* 509, pp. 209–212. DOI: 10.1038/nature13260.

Dowdeswell, J. A. and M. Williams (1997). "Surge-type glaciers in the Russian High Arctic identified from digital satellite imagery". In: *Journal of Glaciology* 43.145, pp. 489–494. DOI: 10.3189/S0022143000035097.

Dowdeswell, J. A., J. Ove Hagen, A. F. Glazovsky, W. D. Harrison, P. Holmlund, J. Jania, et al. (1997). "The Mass Balance of Circum-Arctic Glaciers and Recent Climate Change". In: *Quaternary Research* 48.48, pp. 1–14. DOI: 10.1006/qres.1997.1900.

Dowdeswell, J. A., R. P. Bassford, M. R. Gorman, M. Williams, A. F. Glazovsky, Y. Y. Macheret, et al. (2002). "Form and flow of the Academy of Sciences Ice Cap, Severnaya Zemlya, Russian High Arctic". In: *Journal of Geophysical Research-Solid Earth* 107.B4, pp. 1–10. DOI: 10.1029/2000JB000129.

Dunse, T., T. Schellenberger, J. O. Hagen, A. Kääb, T. V. Schuler, and C. H. Reijmer (2015). "Glacier-surge mechanisms promoted by a hydro-thermodynamic feedback to summer melt". In: *The Cryosphere* 9.1, pp. 197–215. DOI: 10.5194/tc-9-197-2015.

Elachi, C. and J. van Zyl (2006). *The Science and Engineering of Remote Sensing - Theory and Applications*. 2nd. Wiley, p. 616. ISBN: 0471475696.

Enderlin, E. M., I. M. Howat, S. Jeong, M.-J. Noh, J. H. van Angelen, and M. R. van den Broeke (2014). "An improved mass budget for the Greenland ice sheet". In: *Geophysical Research Letters* 41, pp. 866–872.

Farinotti, D., M. Huss, J. J. Fürst, J. Landmann, H. Machguth, F. Maussion, et al. (2019). "A consensus estimate for the ice thickness distribution of all glaciers on Earth". In: *Nature Geoscience* 12, pp. 168–173. DOI: 10.1038/s41561-019-0300-3.

Farnsworth, W. R., L. Allaart, Ó. Ingólfsson, H. Alexanderson, M. Forwick, R. Noormets, et al. (2020). "Holocene glacial history of Svalbard: Status, perspectives and challenges". In: *Earth-Science Reviews* 208.April (103249), pp. 1–28. DOI: 10.1016/j.earscirev.2020.103249.

Ferranti, J. de (2014). *Viewfinder panoramas*. Tech. rep. URL: http://www.viewfinderpanoramas.org/%20dem3.html.

Fettweis, X., B. Franco, M. Tedesco, J. H. V. Angelen, J. T. M. Lenaerts, M. R. V. D. Broeke, et al. (2013). "The Cryosphere Estimating the Greenland ice sheet surface mass balance contribution to future sea level rise using the regional atmospheric climate model MAR". In: *The Cryosphere* 7, pp. 469–489. DOI: 10.5194/tc-7-469-2013.

Fisher, D., J. Zheng, D. Burgess, C. Zdanowicz, C. Kinnard, M. Sharp, et al. (2012). "Recent melt rates of Canadian arctic ice caps are the highest in four millennia". In: *Global and Planetary Change* 84-85, pp. 3–7. DOI: 10.1016/j.gloplacha.2011.06.005.

Foresta, L. (2015). *Support to Science Element (STSE) CryoSat + Cryosphere Theme 3: CryoSat Glacier and Ice Sheet Margins Topography (CryoTop) Algorithm Theoretical Basis Document (ATBD)*. Tech. rep. The University of Edinburgh, University College London, isardSat, University of Leeds, p. 18. URL: https://files.isardsat.co.uk/cryotop-evolution/D4.1_UE-ESA-STSE_CryoTop_ATBD_02_signed.pdf.

Foresta, L., N. Gourmelen, F. Pálsson, P. Nienow, H. Björnsson, and A. Shepherd (2016). "Surface elevation change and mass balance of Icelandic ice caps derived from swath mode CryoSat-2 altimetry". In: *Geophysical Research Letters* 43, pp. 12138–12145. DOI: 10.1002/2016GL071485.

Foresta, L., N. Gourmelen, F. Weissgerber, P. Nienow, J. J. Williams, A. Shepherd, et al. (2018). "Heterogeneous and rapid ice loss over the Patagonian Ice Fields revealed by CryoSat-2 swath radar altimetry". In: *Remote Sensing of Environment* 211, pp. 441–455. DOI: 10.1016/j.rse.2018.03.041.

Gardner, A. S. and M. Sharp (2006). "Influence of the Arctic Circumpolar Vortex on the mass balance of Canadian High Arctic glaciers". In: *Journal of Climate* 20, pp. 4586–4598. DOI: 10.1175/JCLI4268.1.

Gardner, A. S., G. Moholdt, B. Wouters, G. J. Wolken, D. O. Burgess, M. J. Sharp, et al. (2011). "Sharply increased mass loss from glaciers and ice caps in the Canadian Arctic Archipelago". In: *Nature* 473, pp. 357–360. DOI: 10.1038/nature10089.

Gardner, A. S., G. Moholdt, A. Arendt, and B. Wouters (2012). "Accelerated contributions of Canada's Baffin and Bylot Island glaciers to sea level rise over the past half century". In: *The Cryosphere* 6, pp. 1103–1125. DOI: 10.5194/tc-6-1103-2012.

Gardner, A. S., G. Moholdt, J. G. Cogley, B. Wouters, A. a. Arendt, J. Wahr, et al. (2013). "A reconciled estimate of glacier contributions to sea level rise: 2003 to 2009". In: *Science* 340, pp. 852–857. DOI: 10.1126/science.1234532.

Glazovskiy, A. F. (1996). *Mass Balance of Arctic Glaciers, IASC Report No. 5*. Tech. rep. University of Silesia, Sosnowiec-Oslo, Norway: International Arctic Science Committee (Working Group on Arctic Glaciology), pp. 32–38.

Goosse, H., J. E. Kay, K. C. Armour, A. Bodas-Salcedo, H. Chepfer, D. Docquier, et al. (2018). "Quantifying climate feedbacks in polar regions". In: *Nature Communications* 9.1, pp. 1–13. DOI: 10.1038/s41467-018-04173-0.

Gourmelen, N., M. J. Escorihuela, A. Shepherd, L. Foresta, A. Muir, A. Garcia-Mondéjar, et al. (2018). "CryoSat-2 swath interferometric altimetry for mapping ice elevation and elevation change". In: *Advances in Space Research* 62, pp. 1226–1242. DOI: 10.1016/j.asr.2017.11.014.

Gray, L., D. Burgess, L. Copland, R. Cullen, N. Galin, R. Hawley, et al. (2013). "Interferometric swath processing of Cryosat data for glacial ice topography". In: *The Cryosphere* 7.6, pp. 1857–1867. DOI: 10.5194/tc-7-1857-2013.

Gray, L., D. Burgess, L. Copland, M. N. Demuth, T. Dunse, K. Langley, et al. (2015). "CryoSat-2 delivers monthly and inter-annual surface elevation change for Arctic ice caps". In: *The Cryosphere* 9.3, pp. 1895–1913. DOI: 10.5194/tcd-9-2821-2015.

Gray, L., D. Burgess, L. Copland, T. Dunse, K. Langley, and G. Moholdt (2017). "A revised calibration of the interferometric mode of the CryoSat-2 radar altimeter improves ice height and height change measurements in western Greenland". In: *The Cryosphere* 11, pp. 1041–1058. DOI: 10.5194/tc-11-1041-2017.

Grove, J. (1988). *The Little Ice Age*. 2nd. Taylor & Francis Ltd, p. 500. ISBN: 041509948X.

Hanna, E., J. M. Jones, J. Cappelen, S. H. Mernild, L. Wood, K. Steffen, et al. (2013). "The influence of North Atlantic atmospheric and oceanic forcing effects on 1900-2010 Greenland summer climate and ice melt/runoff". In: *International Journal of Climatology* 33, pp. 862–880. DOI: 10.1002/joc.3475.

Harcourt, W. D., S. J. Palmer, D. T. Mansell, A. L. Brocq, O. Bartlett, N. Gourmelen, et al. (2019). "Subglacial controls on dynamic thinning at Trinity- Wykeham Glacier , Prince of Wales Ice Field , Canadian Arctic". In: *International Journal of Remote Sensing* 00.00, pp. 1–23. DOI: 10.1080/01431161.2019.1658238.

Hawley, R. L., a. Shepherd, R. Cullen, V. Helm, and D. J. Wingham (2009). "Ice-sheet elevations from across-track processing of airborne interferometric radar altimetry". In: *Geophysical Research Letters* 36.22, pp. 1–5. DOI: 10.1029/2009GL040416.

Held, I. M. and B. J. Soden (2006). "Robust Responses of the Hydrological Cycle to Global Warming". In: *Journal of Climate* 19.21, pp. 5686–5699. DOI: 10.1175/JCLI3990.1.

Henderson, K. A. (2002). "An ice core paleoclimate study of Windy Dome, Franz Josef Land (Russia): Development of a recent climate history for the Barents Sea". PhD thesis, p. 274. ISBN: 061239378X.

Huss, M. (2013). "Density assumptions for converting geodetic glacier volume change to mass change". In: *The Cryosphere* 7, pp. 877–887. DOI: 10.5194/tcd-7-219-2013.

Hwang, Y. T., D. M. Frierson, and J. E. Kay (2011). "Coupling between Arctic feedbacks and changes in poleward energy transport". In: *Geophysical Research Letters* 38, pp. 1–5. DOI: 10.1029/2011GL048546.

Ignéczi, Á., A. J. Sole, S. J. Livingstone, A. A. Leeson, X. Fettweis, N. Selmes, et al. (2016). "Northeast sector of the Greenland Ice Sheet to undergo the greatest inland expansion of supraglacial lakes during the 21st century". In: *Geophysical Research Letters* 43.18, pp. 9729–9738. DOI: 10.1002/2016GL070338.

Iken, A. and R. A. Bindschadler (1986). "Combined Measurements of Subglacial Water Pressure and Surface Velocity of Findelengletscher, Switzerland: Conclusions About Drainage System and Sliding Mechanism". In: *Journal of Glaciology* 32.110, pp. 101–119.

Immerzeel, W. W., L. P. H. van Beek, and M. F. P. Bierkens (June 2010). "Climate change will affect the Asian water towers." In: *Science* 328.5984, pp. 1382–1385. DOI: 10.1126/science.1183188.

Isaksson, E., V. Pohjola, T. Jauhiainen, J. Moore, J. F. Pinglot, R. Vaikmäe, et al. (2001). "A new ice-core record from Lomonosovfonna, Svalbard: Viewing the 1920-97 data in relation to present climate and environmental conditions". In: *Journal of Glaciology* 47.157, pp. 335–345. DOI: 10.3189/172756501781832313.

Jacob, T., J. Wahr, W. T. Pfeffer, and S. Swenson (2012). "Recent contributions of glaciers and ice caps to sea level rise." In: *Nature* 482, pp. 514–518. DOI: 10.1038/nature10847.

James, G., D. Witten, T. Hastie, and R. Tibshirani (2015). *An Introduction to Statistical Learning*. Springer, p. 426. ISBN: 978-1-4614-7137-0.

Jenkins, A. (2011). "Convection-driven melting near the grounding lines of ice shelves and tidewater glaciers". In: *Journal of Physical Oceanography* 41, pp. 2279–2294. DOI: 10.1175/JPO-D-11-03.1.

Kaufman, D. S., T. A. Ager, N. J. Anderson, P. M. Anderson, J. T. Andrews, P. J. Bartlein, et al. (2004). "Holocene thermal maximum in the western Arctic (0-180°W)". In: *Quaternary Science Reviews* 23, pp. 529–560. DOI: 10.1016/j.quascirev.2003.09.007.

Khazendar, A., I. G. Fenty, D. Carroll, A. Gardner, C. M. Lee, I. Fukumori, et al. (2019). "Interruption of two decades of Jakobshavn Isbrae acceleration and thinning as regional ocean cools". In: *Nature Geoscience* 12.4, pp. 277–283. DOI: 10.1038/s41561-019-0329-3.

Labe, Z., G. Magnusdottir, and H. Stern (2018). "Variability of Arctic sea ice thickness using PIOMAS and the CESM Large Ensemble". In: *Journal of Climate* 31.8, pp. 3233–3247. DOI: 10.1175/JCLI-D-17-0436.1.

Lenaerts, J. T., J. H. Van Angelen, M. R. Van Den Broeke, A. S. Gardner, B. Wouters, and E. Van Meijgaard (2013). "Irreversible mass loss of Canadian Arctic Archipelago glaciers". In: *Geophysical Research Letters* 40.5, pp. 870–874. DOI: 10.1002/grl.50214.

Lenaerts, J. T., M. R. Van Den Broeke, J. M. Van Wessem, W. J. Van De Berg, E. Van Meijgaard, L. H. Van Ulft, et al. (2014). "Extreme precipitation and climate gradients in patagonia revealed by high-resolution regional atmospheric climate modeling". In: *Journal of Climate* 27.12, pp. 4607–4621. DOI: 10.1175/JCLI-D-13-00579.1.

Lenaerts, J. T., B. Medley, M. R. Broeke, and B. Wouters (2019). "Observing and Modeling Ice-Sheet Surface Mass Balance". In: *Reviews of Geophysics*, pp. 1–45. DOI: 10.1029/2018rg000622.

Lien, V. S., F. B. Vikebø, and O. Skagseth (2013). "One mechanism contributing to covariability of the Atlantic inflow branches to the Arctic". In: *Nature Communications* 4, pp. 1–6. DOI: 10.1038/ncomms2505.

Lind, S., R. B. Ingvaldsen, and T. Furevik (2018). "Arctic warming hotsopt in the northern Barents Sea linked to declining sea-ice import". In: *Nature Climate Change* 8.7, pp. 634–639. DOI: 10.1038/s41558-018-0205-y.

Lindsay, R., M. Wensnahan, A. Schweiger, and J. Zhang (2014). "Evaluation of seven different atmospheric reanalysis products in the Arctic*". In: *Journal of Climate* 27, pp. 2588–2606. DOI: 10.1175/JCLI-D-13-00014.1.

Ma, B., M. Steele, and C. M. Lee (2017). "Ekman circulation in the Arctic Ocean: Beyond the Beaufort Gyre". In: *Journal of Geophysical Research: Oceans* 122, pp. 3358–3374. DOI: 10.1002/2016JC012486.Received.

Malczyk, G., N. Gourmelen, D. Goldberg, J. Wuite, and T. Nagler (2019). "Repeat Subglacial Lake Drainage and Filling Beneath Thwaites Glacier, West-Antarctic Ice Sheet". In: *AGU 2019 Fall Meeting*. San Francisco, CA, USA, 9-13 Dec. 2019.

Martin, C. F., W. B. Krabill, S. S. Manizade, R. L. Russel, J. G. Sonntag, R. N. Swift, et al. (2012). *Airborne topographic mapper calibration procedures and accuracy assessment*. Tech. rep. Greenbelt, MD, USA: National Aeronautics and Space Administration, Goddard Space Flight Center, p. 42. URL: https://ntrs.nasa.gov/archive/nasa/casi.ntrs.nasa.gov/20120008479.pdf.

Martin, T. and A. Adcroft (2010). "Parameterizing the fresh-water flux from land ice to ocean with interactive icebergs in a coupled climate model". In: *Ocean Modelling* 34.3-4, pp. 111–124. DOI: 10.1016/j.ocemod.2010.05.001.

Marzeion, B., P. W. Leclercq, J. G. Cogley, and A. H. Jarosch (2015). "Brief Communication: Global reconstructions of glacier mass change during the 20th century are consistent". In: *The Cryosphere* 9.6, pp. 2399–2404. DOI: 10.5194/tc-9-2399-2015.

Marzeion, B., J. G. Cogley, K. Richter, and D. Parkes (2014). "Attribution of global glacier mass loss to anthropogenic and natural causes". In: *Science* 345, pp. 919–922.

Matthews, J. a. and K. R. Briffa (2005). "the 'Little Ice Age': Re-Evaluation of an Evolving Concept". In: *Geografiska Annaler: Series A, Physical Geography* 87.1, pp. 17–36. DOI: 10.1111/j.0435-3676.2005.00242.x.

McLeod, J. T. and T. L. Mote (2016). "Linking interannual variability in extreme Greenland blocking episodes to the recent increase in summer melting across the Greenland ice sheet". In: *International Journal of Climatology* 36, pp. 1484–1499. DOI: 10.1002/joc.4440.

McMillan, M., A. Shepherd, N. Gourmelen, A. Dehecq, A. Leeson, A. Ridout, et al. (2014). "Rapid dynamic activation of a marine-based Arctic ice cap". In: *Geophysical Research Letters* 41.24, pp. 8902–8909. DOI: 10.1002/2014GL062255.

McMillan, M., A. Leeson, A. Shepherd, K. Briggs, T. W. K. Armitage, A. Hogg, et al. (2016). "A high-resolution of Greenland mass balance". In: *Geophysical Research Letters* 43, pp. 7002–7010. DOI: 10.1002/2016GL069666.Received.

Meier, M. F., M. B. Dyurgerov, U. K. Rick, S. O'neel, W. T. Pfeffer, R. S. Anderson, et al. (2007). "Glaciers dominate eustatic sea-level rise in the 21st century." In: *Science* 317.August, pp. 1064–1067. DOI: 10.1126/science.1143906.

Melkonian, A. K., M. J. Willis, M. E. Pritchard, and A. J. Stewart (2016). "Recent changes in glacier velocities and thinning at Novaya Zemlya". In: *Remote Sensing of Environment* 174, pp. 244–257. DOI: 10.1016/j.rse.2015.11.001.

Millan, R., J. Mouginot, and E. Rignot (2017). "Mass budget of the glaciers and ice caps of the Queen Elizabeth Islands, Canada, from 1991 to 2015". In: *Environmental Research Letters* 12, p. 024016.

Miller, G. H., S. J. Lehman, K. A. Refsnider, J. R. Southon, and Y. Zhong (2013). "Unprecedented recent summer warmth in Arctic Canada". In: *Geophysical Research Letters* 40.21, pp. 5745–5751. DOI: 10.1002/2013GL057188.

Moholdt, G., C. Nuth, J. O. Hagen, and J. Kohler (2010). "Recent elevation changes of Svalbard glaciers derived from ICESat laser altimetry". In: *Remote Sensing of Environment* 114, pp. 2756–2767. DOI: 10.1016/j.rse.2010.06.008.

Moholdt, G., T. Heid, T. Benham, and J. A. Dowdeswell (2012a). "Dynamic instability of marine-terminating glacier basins of Academy of Sciences Ice Cap, Russian High Arctic". In: *Annals of Glaciology* 53.60, pp. 193–201. DOI: 10.3189/2012AoG60A117.

Moholdt, G., B. Wouters, and A. S. Gardner (2012b). "Recent mass changes of glaciers in the Russian High Arctic". In: *Geophysical Research Letters* 39.10, p. L10502. DOI: 10.1029/2012GL051466.

Möller, M., F. Navarro, and A. Martín-Español (2016). "Monte Carlo modelling projects the loss of most land-terminating glaciers on Svalbard in the 21st century under RCP 8.5 forcing". In: *Environmental Research Letters* 11.9, p. 094006. DOI: 10.1088/1748-9326/11/9/094006.

Mortimer, C. A., M. Sharp, and W. Van Wychen (2018). "Influence of recent warming and ice dynamics on glacier surface elevations in the Canadian High Arctic, 1995–2014". In: *Journal of Glaciology* 64, pp. 450–464. DOI: 10.1017/jog.2018.37.

Mouginot, J., E. Rignot, A. A. Bjørk, M. van den Broeke, R. Millan, M. Morlighem, et al. (2019). "Forty-six years of Greenland Ice Sheet mass balance from 1972 to 2018". In: *Proceedings of the National Academy of Sciences* 116, pp. 9239–9244. DOI: 10.1073/pnas.1904242116.

Myers, P. G., N. Kulan, and M. H. Ribergaard (2007). "Irminger water variability in the West Greenland Current". In: *Geophysical Research Letters* 34.17, p. L17601. DOI: 10.1029/2007GL030419.

Nick, F. M., A. Vieli, M. L. Andersen, I. Joughin, A. Payne, T. L. Edwards, et al. (2013). "Future sea-level rise from Greenland's main outlet glaciers in a warming climate". In: *Nature* 497.7448, pp. 235–238. DOI: 10.1038/nature12068.

Nicolussi, K. and C. Schlüchter (2012). "The 8.2 ka event - Calendar - dated glacier response in the Alps". In: *Geology* 40, pp. 819–822. DOI: 10.1130/G32406.1.

Nilsson, J., L. S. Sørensen, V. R. Barletta, and R. Forsberg (2015a). "Mass changes in Arctic ice caps and glaciers: Implications of regionalizing elevation changes". In: *The Cryosphere* 9.1, pp. 139–150. DOI: 10.5194/tc-9-139-2015.

Nilsson, J., P. Vallelonga, S. B. Simonsen, L. S. Sørensen, R. Forsberg, D. Dahl-Jensen, et al. (2015b). "Greenland 2012 melt event effects on CryoSat-2 radar altimetry". In: *Geophysical Research Letters* 42.10, pp. 3919–3926. DOI: 10.1002/2015GL063296.

Noël, B., W. Jan Van De Berg, H. MacHguth, S. Lhermitte, I. Howat, X. Fettweis, et al. (2016). "A daily, 1 km resolution data set of downscaled Greenland ice sheet surface mass balance (1958-2015)". In: *The Cryosphere* 10.5, pp. 2361–2377. DOI: 10.5194/tc-10-2361-2016.

Noël, B., W. J. van de Berg, S. Lhermitte, B. Wouters, N. Schaffer, and M. R. van den Broeke (2018). "Six decades of glacial mass loss in the Canadian Arctic Archipelago". In: *Journal of Geophysical Research: Earth Surface* 123.6, pp. 1430–1449. DOI: 10.1029/2017JF004304.

Nuth, C., G. Moholdt, J. Kohler, J. O. Hagen, and A. Kääb (2010). "Svalbard glacier elevation changes and contribution to sea level rise". In: *Journal of Geophysical Research: Earth Surface* 115.1, pp. 1–16. DOI: 10.1029/2008JF001223.

Nuth, C., A. Gilbert, A. Köhler, R. McNabb, T. Schellenberger, H. Sevestre, et al. (2019). "Dynamic vulnerability revealed in the collapse of an Arctic tidewater glacier". In: *Scientific Reports* 9.1, p. 5541. DOI: 10.1038/s41598-019-41117-0.

Öberg, L. and L. Kullman (2011). "Recent glacier recession - A new source of postglacial treeline and climate history in the Swedish Scandes". In: *Landscape Online* 26, pp. 1–38. DOI: 10.3097/LO.201126.

Onarheim, I. H., T. Eldevik, L. H. Smedsrud, and J. C. Stroeve (2018). "Seasonal and regional manifestation of Arctic sea ice loss". In: *Journal of Climate* 31, pp. 4917–4932. DOI: 10.1175/JCLI-D-17-0427.1.

Opel, T., D. Fritzsche, H. Meyer, R. Schu, K. Weiler, U. Ruth, et al. (2009). "115 year ice-core data from Akademii Nauk ice cap , Severnaya Zemlya : high-resolution

record of Eurasian Arctic climate change". In: *Journal of Glaciology* 55.189, pp. 21–31.

Opel, T., D. Fritzsche, and H. Meyer (2013). "Eurasian Arctic climate over the past millennium as recorded in the Akademii Nauk ice core (Severnaya Zemlya)". In: *Climate of the Past* 9.5, pp. 2379–2389. DOI: 10.5194/cp-9-2379-2013.

Overland, J., J. Walsh, and V. Kattsov (2017). *Snow, Water, Ice and Permafrost in the Arctic (SWIPA) 2017, Arctic Monitoring and Assessment Programme (AMAP) - Trends and feedbacks*. Tech. rep., pp. 9–24.

Oziel, L., J. Sirven, and J. C. Gascard (2016). "The Barents Sea frontal zones and water masses variability (1980-2011)". In: *Ocean Science* 12.1, pp. 169–184. DOI: 10.5194/os-12-169-2016.

Park, K., S. M. Kang., D. Kim, M. F. Stuecker, and F. Jin (2018). "Contrasting Local and Remote Impacts of Surface Heating on Polar Warming and Amplification". In: *Journal of Climate* 31, pp. 3155–3166. DOI: 10.1175/JCLI-D-17-0600.1.

Pfeffer, W. T., J. T. Harper, and S. O'Neel (2008). "Kinematic constraints on glacier contributions to 21st-century sea-level rise." In: *Science* 321.5894, pp. 1340–1343. DOI: 10.1126/science.1159099.

Pfeffer, W. T., A. A. Arendt, A. Bliss, T. Bolch, J. G. Cogley, A. S. Gardner, et al. (2014). "The Randolph Glacier Inventory: a globally complete inventory of glaciers". In: *Journal of Glaciology* 60.221, pp. 537–552. DOI: 10.3189/2014JoG13J176.

Polyakov, I. V., L. A. Timokhov, V. A. Alexeev, S. Bacon, I. A. Dmitrenko, L. Fortier, et al. (2010). "Arctic ocean warming contributes to reduced polar ice cap". In: *Journal of Physical Oceanography* 40, pp. 2743–2756. DOI: 10.1175/2010JPO4339.1.

Polyakov, I. V., A. V. Pnyushkov, M. B. Alkire, I. M. Ashik, T. M. Baumann, E. C. Carmack, et al. (2017). "Greater role for Atlantic inflows on sea-ice loss in the Eurasian Basin of the Arctic Ocean". In: *Science* 356, pp. 285–291. DOI: 10.1126/science.aai8204.

Porter, C., P. Morin, I. Howat, M.-J. Noh, B. Bates, K. Peterman, et al. (2018). *ArcticDEM*. DOI: 10.7910/DVN/OHHUKH.

Price, S. F., A. J. Payne, I. M. Howat, and B. E. Smith (2011). "Committed sea-level rise for the next century from Greenland ice sheet dynamics during the past decade". In: *Proceedings of the National Academy of Sciences* 108.22, pp. 8978–8983. DOI: 10.1073/pnas.1017313108.

Qiu, J. (2008). "The Third Pole". In: *Nature* 454.July, pp. 393–396.

Radić, V. and R. Hock (2010). "Regional and global volumes of glaciers derived from statistical upscaling of glacier inventory data". In: *Journal of Geophysical Research: Earth Surface* 115.1, pp. 1–10. DOI: 10.1029/2009JF001373.

Radić, V., A. Bliss, A. C. Beedlow, R. Hock, E. Miles, and J. G. Cogley (2014). "Regional and global projections of twenty-first century glacier mass changes in response to climate scenarios from global climate models". In: *Climate Dynamics* 42.1-2, pp. 37–58. DOI: 10.1007/s00382-013-1719-7.

Rajewicz, J. and S. J. Marshall (2014). "Variability and trends in anticyclonic circulation over the Greenland ice sheet, 1948–2013". In: *Geophysical Research Letters* 41, pp. 2842–2850. DOI: 10.1002/2014GL059255.

Raper, S. C. B. and R. J. Braithwaite (2006). "Low sea level rise projections from mountain glaciers and icecaps under global warming." In: *Nature* 439, pp. 311–313. DOI: 10.1038/nature04448.

Rigor, I. G., J. M. Wallace, and R. L. Colony (2002). "Response of Sea Ice to the Arctic Oscillation". In: *Journal of Climate* 15.18, pp. 2648–2663. DOI: 10.1175/1520-0442(2002)015<2648:ROSITT>2.0.CO;2.

Robel, A. A. (2017). "Thinning sea ice weakens buttressing force of iceberg mélange and promotes calving". In: *Nature Communications* 8, p. 14596. DOI: 10.1038/ncomms14596.

Roemmich, D., W. J. Gould, and J. Gilson (2012). "135 years of global ocean warming between the Challenger expedition and the Argo Programme". In: *Nature Climate Change* 2.April, pp. 425–428. DOI: 10.1038/nclimate1461.

Rolstad, C., T. Haug, and B. Denby (2009). "Spatially integrated geodetic glacier mass balance and its uncertainty based on geostatistical analysis: Application to the western Svartisen ice cap, Norway". In: *Journal of Glaciology* 55.192, pp. 666–680. DOI: 10.3189/002214309789470950.

Rotschky, G., O. Eisen, F. Wilhelms, U. Nixdorf, and H. Oerter (2004). "Spatial distribution of surface mass balance on Amundsenisen plateau, Antarctica, derived from ice-penetrating radar studies". In: *Annals of Glaciology* 39, pp. 265–270. DOI: 10.3189/172756404781814618.

Sánchez-Gámez, P., F. J. Navarro, T. J. Benham, A. F. Glazovsky, R. P. Bassford., and J. A. Dowdeswell (2019). "Intra- and inter-annual variability in dynamic discharge from the Academy of Sciences Ice Cap, Severnaya Zemlya, Russian Arctic, and its role in modulating mass balance". In: *Journal of Glaciology* 65, pp. 780–797. DOI: 10.1017/jog.2019.58.

Santer, B. D., T. M. Wigley, J. S. Boyle, D. J. Gaffen, J. J. Hnilo, D. Nychka, et al. (2000). "Statistical significance of trends and trend differences in layer-average atmospheric temperature time series". In: *Journal of Geophysical Research Atmospheres* 105, pp. 7337–7356. DOI: 10.1029/1999JD901105.

Schuler, T. V., J. Kohler, N. Elagina, J. O. M. Hagen, A. J. Hodson, J. A. Jania, et al. (2020). "Reconciling Svalbard Glacier Mass Balance". In: *Frontiers in Earth Science* 8, pp. 1–16. DOI: 10.3389/feart.2020.00156.

Screen, J. and I. Simmonds (2010). "The central role of diminishing sea ice in recent Arctic temperature amplification." In: *Nature* 464, pp. 1334–1337. DOI: 10.1038/nature09051.

Screen, J., C. Deser, and I. Simmonds (May 2012). "Local and remote controls on observed Arctic warming". In: *Geophysical Research Letters* 39.10, pp. 1–5. DOI: 10.1029/2012GL051598.

Serreze, M. C., A. P. Barrett, J. C. Stroeve, D. N. Kindig, and M. M. Holland (2009). "The emergence of surface-based Arctic amplification". In: *The Cryosphere* 3, pp. 11–19. DOI: 10.5194/tc-3-11-2009.

Sharov, A. (2010). *SMARAGD: Satellite Monitoring and Regional Analysis of Glacier Dynamics in the Barents-Kara Region*. Ed. by A. Sharov. Graz, Austria: JOANNEUM RESEARCH Forschungsgesellschaft mbH, p. 105. ISBN: 9783200016187.

Shepherd, A. and D. Wingham (2007). "Recent Sea-Level Contributions of the Antarctic and Greenland Ice Sheets". In: *Science* 315.5818, pp. 1529–1532. DOI: 10.1126/science.1136776.

Shepherd, A., E. R. Ivins, A. Gerudo, V. R. Barletta, M. J. Bentley, S. Bettadpur, et al. (Nov. 2012). "A reconciled estimate of ice-sheet mass balance." In: *Science* 338.6111, pp. 1183–1189. DOI: 10.1126/science.1228102.

Shindell, D. and G. Faluvegi (2009). "Climate response to regional radiative forcing during the twentieth century". In: *Nature Geoscience* 2, pp. 294–300. DOI: 10.1038/ngeo473.

Slater, D. A., D. N. Goldberg, P. W. Nienow, and T. R. Cowton (2016). "Scalings for submarine melting at tidewater glaciers from buoyant plume theory". In: *Journal of Physical Oceanography* 46.6, pp. 1839–1855. DOI: 10.1175/jpo-d-15-0132.1.

Slater, D. A., F. Straneo, D. Felikson, C. M. Little, H. Goelzer, X. Fettweis, et al. (2019). "Estimating Greenland tidewater glacier retreat driven by submarine melting". In: *The Cryosphere* 13.9, pp. 2489–2509. DOI: 10.5194/tc-13-2489-2019.

Slater, D. A., D. Felikson, F. Straneo, H. Goelzer, C. M. Little, M. Morlighem, et al. (2020). "Twenty-first century ocean forcing of the Greenland ice sheet for modelling of sea level contribution". In: *The Cryosphere* 14.3, pp. 985–1008. DOI: 10.5194/tc-14-985-2020.

Slater, T., I. R. Lawrence, I. N. Otosaka, A. Shepherd, N. Gourmelen, L. Jakob, et al. (2021). "Review Article: Earth's ice imbalance". In: *The Cryosphere* 15, pp. 233–246. DOI: 10.5194/tc-15-233-2021.

Slaymaker, O. and R. E. J. Kelly (2007). *The Cryosphere*. Blackwell, p. 280. ISBN: 978-1-405-12976-3.

Smith, B. E., N. Gourmelen, A. Huth, and I. Joughin (2017). "Connected subglacial lake drainage beneath Thwaites Glacier, West Antarctica". In: *The Cryosphere* 11, pp. 451–467. DOI: 10.5194/tc-11-451-2017.

Smith, B., H. A. Fricker, A. S. Gardner, B. Medley, J. Nilsson, F. S. Paolo, et al. (2020). "Pervasive ice sheet mass loss reflects competing ocean and atmosphere processes". In: *Science* 368, pp. 1239–1242. DOI: 10.1126/science.aaz5845.

Solomina, O. N., R. S. Bradley, D. A. Hodgson, S. Ivy-Ochs, V. Jomelli, A. N. Mackintosh, et al. (2015). "Holocene glacier fluctuations". In: *Quaternary Science Reviews* 111, pp. 9–34. DOI: 10.1016/j.quascirev.2014.11.018.

Sørensen, L. S., S. B. Simonsen, K. Langley, L. Gray, V. Helm, J. Nilsson, et al. (2018). "Validation of CryoSat-2 SARIn data over Austfonna ice cap using airborne laser scanner measurements". In: *Remote Sensing* 10.9, pp. 1–12. DOI: 10.3390/rs10091354.

Straneo, F. and P. Heimbach (2013). "North Atlantic warming and the retreat of Greenland's outlet glaciers." In: *Nature* 504, pp. 36–43. DOI: 10.1038/nature12854.

Stroeve, J. C., D. Schroder, M. Tsamados, and D. Feltham (2018). "Warm winter, thin ice?" In: *The Cryosphere* 12, pp. 1791–1809. DOI: 10.5194/tc-12-1791-2018.

Strozzi, T., F. Paul, A. Wiesmann, T. Schellenberger, and A. Kääb (2017a). "Circum-arctic changes in the flow of glaciers and ice caps from satellite SAR data between the 1990s and 2017". In: *Remote Sensing* 9.947. DOI: 10.3390/rs9090947.

Strozzi, T., A. Kääb, and T. Schellenberger (2017b). "Frontal destabilization of Stonebreen, Edgeøya, Svalbard". In: *The Cryosphere* 11.1, pp. 553–566. DOI: 10.5194/tc-11-553-2017.

Studinger, M. (2014). *IceBridge ATM L4 Surface Elevation Rate of Change, Version 1*. Tech. rep. Boulder, Colorado USA: NASA National Snow and Ice Data Center Distributed Active Archive Center. DOI: https://doi.org/10.5067/BCW6CI3TXOCY.

Stuecker, M. F., C. M. Bitz, K. C. Armour, C. Proistosescu, S. M. Kang, S. P. Xie, et al. (2018). "Polar amplification dominated by local forcing and feedbacks". In: *Nature Climate Change* 8, pp. 1076–1081. DOI: 10.1038/s41558-018-0339-y.

Tapley, B. D., S. Bettadpur, J. C. Ries, P. F. Thompson, and M. M. Watkins (2004). "GRACE Measurements of Mass Variability in the Earth System". In: *Science* 305, pp. 503–505.

Tedstone, A. J., P. W. Nienow, N. Gourmelen, A. Dehecq, D. Goldberg, and E. Hanna (2015). "Decadal slowdown of a land-terminating sector of the Greenland Ice Sheet despite warming". In: *Nature* 526.7575, pp. 692–695. DOI: 10.1038/nature15722.

Tepes, P., N. Gourmelen, F. Weissgerber, M. J. Escorihuela, J. Wuite, T. Nagler, et al. (2017). "Changes of Arctic Marine Glaciers and Ice Caps from CryoSat Swath Altimetry". In: *AGU 2017 Fall Meeting*. New Orleans, LA, USA, 11-15 Dec. 2017.

The IMBIE Team (2018). "Mass balance of the Antarctic ice sheet". In: *Nature* 558, pp. 1627–1635. DOI: 10.1098/rsta.2006.1792.

The IMBIE Team (2020). "Mass balance of the Greenland Ice Sheet from 1992 to 2018". In: *Nature* 579.March, pp. 233–239. DOI: 10.1038/s41586-019-1855-2.

Thompson, D. W. and J. M. Wallace (1998). "The Arctic oscillation signature in the wintertime geopotential height and temperature fields". In: *Geophysical Research Letters* 25.9, pp. 1297–1300. DOI: 10.1029/98GL00950.

Thornalley, D. J. R., W. Delia, P. Ortega, J. I. Robson, C. M. Brierley, R. Davis, et al. (2018). "Atlantic overturning during the past 150 years". In: *Nature* 556, pp. 227–230. DOI: 10.1038/s41586-018-0007-4.

Vaughan, D. G., J. C. Comiso, I. Allison, J. Carrasco, G. Kaser, R. Kwok, et al. (2013). *AR5 - Observations: Cryosphere*. Tech. rep., pp. 317–382. DOI: 10.1017/CBO9781107415324.012.

Vieli, A. and F. M. Nick (2011). "Understanding and Modelling Rapid Dynamic Changes of Tidewater Outlet Glaciers: Issues and Implications". In: *Surveys in Geophysics* 32, pp. 437–458. DOI: 10.1007/s10712-011-9132-4.

Watanabe, O., H. Motoyama, M. Igarashi, K. Kamiyama, S. Matoba, K. Goto-Azuma, et al. (2001). "Studies on climatic and environmental changes during the last few hundred years using ice cores from various sites in Nordaustlandet, Svalbard". In: *Memoirs of National Institute of Polar Research Special Issue* 54, pp. 227–242.

WCRP Global Sea Level Budget Group (2018). "Global sea-level budget 1993-present". In: *Earth Syst. Sci. Data* 10, pp. 1551–1590. DOI: 10.3929/ethz-b-000287786.

Weaver, a. J., C. M. Bitz, a. F. Fanning, and M. M. Holland (May 1999). "Thermohaline Circulation: High-Latitude Phenomena and the Difference Between the Pacific and Atlantic". In: *Annual Review of Earth and Planetary Sciences* 27.1, pp. 231–285. DOI: 10.1146/annurev.earth.27.1.231.

Weissgerber, F. (2016). "Traitements cohérents d'images RSO multi-modes multi-resolutions pour la caractérisation du milieu urbain". PhD thesis. Télécom ParisTech, p. 299. URL: https://hal.archives-ouvertes.fr/tel-01481528.

Weissgerber, F. and N. Gourmelen (2017). "CryoTop Evolution: utiliser la pseudo-fauchée de CryoSat-2 pour rafiner la résolution des MNE et des cartes de taux de changements d'élévation". In: *Gretsi*, pp. 2–5. DOI: hal.archives-ouvertes.fr/hal-01647175.

Williams, M. and J. A. Dowdeswell (2001). "Historical Fluctuations of the Matusevich Ice Shelf, Severnaya Zemlya, Russian High Arctic". In: *Arctic, Antarctic, an Alpine Research* 33.2, pp. 211–222. DOI: 10.2307/1552222.

Willis, I. C. (1995). "Intra-annual variations in glacier motion: a review". In: *Progress in Physical Geography: Earth and Environment* 19, pp. 61–106. DOI: 10.1177/030913339501900104.

Willis, M. J., A. K. Melkonian, and M. E. Pritchard (2015). "Outlet glacier response to the 2012 collapse of the Matusevich Ice Shelf, Severnaya Zemlya, Russian Arctic". In: *Journal of Geophysical Research: Earth Surface* 120, pp. 2040–2055. DOI: 10.1002/2015JF003544.

Willis, M. J., W. Zheng, W. J. Durkin, M. E. Pritchard, J. M. Ramage, J. A. Dowdeswell, et al. (2018). "Massive destabilization of an Arctic ice cap". In: *Earth and Planetary Science Letters* 502, pp. 146–155. DOI: 10.1016/j.epsl.2018.08.049.

Wingham, D., C. Francis, S. Baker, C. Bouzinac, D. Brockley, R. Cullen, et al. (2006). "CryoSat: A mission to determine the fluctuations in Earth's land and marine ice fields". In: *Advances in Space Research* 37.4, pp. 841–871. DOI: 10.1016/j.asr.2005.07.027.

Wouters, B., A. S. Gardner, and G. Moholdt (2019). "Global glacier mass loss during the GRACE satellite mission (2002-2016)". In: *Frontiers in Earth Science* 7.96, pp. 1–11. DOI: 10.3389/feart.2019.00096.

Xie, J., L. Bertino, L. Knut, and P. Sakov (2017). "Quality assessment of the TOPAZ4 reanalysis in the Arctic over the period 1991-2013". In: *Ocean Science* 13.1, pp. 123–144. DOI: 10.5194/os-13-123-2017.

Yang, Q., T. H. Dixon, P. G. Myers, J. Bonin, D. Chambers, and M. R. Van Den Broeke (2016). "Recent increases in Arctic freshwater flux affects Labrador Sea convection and Atlantic overturning circulation". In: *Nature Communications* 7.10525. DOI: 10.1038/ncomms10525.

Yashayaev, I. and D. Seidov (2015). "The role of the Atlantic Water in multidecadal ocean variability in the Nordic and Barents Seas". In: *Progress in Oceanography* 132.December 2014, pp. 68–127. DOI: 10.1016/j.pocean.2014.11.009.

Zeeberg, J. and S. L. Forman (2001). "Changes in glacier extent on north Novaya Zemlya in the twentieth century". In: *The Holocene* 11.2, pp. 161–175. DOI: 10.1191/095968301676173261.

Zeeberg, J. J., S. L. Forman, and L. Polyak (2003). "Glacier extent in a Novaya Zemlya fjord during the "Little Ice Age" inferred from glaciomarine sediment records". In: *Polar Research* 22.2, pp. 385–394. DOI: 10.3402/polar.v22i2.6467.

Zemp, M., M. Huss, E. Thibert, N. Eckert, R. McNabb, J. Huber, et al. (2019). "Global glacier mass balances and their contributions to sea-level rise from 1961 to 2016". In: *Nature* 568, pp. 382–386. DOI: 10.1038/s41586-019-1071-0.

Zhao, M., J. Ramage, K. Semmens, and F. Obleitner (2014). "Recent ice cap snowmelt in Russian High Arctic and anti-correlation with late summer sea ice extent". In: *Environmental Research Letters* 9.4, p. 045009. DOI: 10.1088/1748-9326/9/4/045009.

Zheng, W., M. E. Pritchard, M. J. Willis, P. Tepes, N. Gourmelen, T. J. Benham, et al. (2018). "Accelerating glacier mass loss on Franz Josef Land, Russian Arctic". In: *Remote Sensing of Environment* 211.November 2017, pp. 357–375.

Zheng, W., M. E. Pritchard, M. J. Willis, and L. A. Stearns (2019). "The Possible Transition From Glacial Surge to Ice Stream on Vavilov Ice Cap". In: *Geophysical Research Letters* 46.23, pp. 13892–13902. DOI: 10.1029/2019GL084948.

Zhurbas, N. and N. Kuzmina (2020). "Variability of the thermohaline structure and transport of Atlantic water in the Arctic Ocean based on NABOS (Nansen and Amundsen Basins Observing System) hydrography data". In: *Ocean Science* 16, pp. 405–421. DOI: 10.5194/os-16-405-2020.